UNIVERSIDAD PÚBLICA DE NAVARRA
Departamento de Ingeniería Eléctrica y Electrónica

NAFARROAKO UNIBERTSITATE PUBLIKOA
Ingeniaritza Elektriko eta Elektroniko Saila

PHOTONIC BANDGAP STRUCTURES IN MICROSTRIP TECHNOLOGY:

STUDY USING THE COUPLED MODE FORMALISM AND APPLICATIONS

Tesis Doctoral realizada por / Doctoral Thesis by
José María Lopetegui Beregaña

dirigida por / supervised by
Dr. Mario Sorolla Ayza

Pamplona-Iruña, 2002

UNIVERSIDAD PÚBLICA DE NAVARRA
Departamento de Ingeniería Eléctrica y Electrónica

Título de la tesis doctoral:

Photonic Bandgap structures in Microstrip Technology:
Study using the Coupled Mode Formalism and Applications.

Autor:

José María Lopetegui Beregaña, Ingeniero de Telecomunicación

Director:

Mario Sorolla Ayza
Doctor Ingeniero de Telecomunicación, Catedrático de Universidad UPNa

Tribunal nombrado para juzgar la tesis doctoral citada:

Presidente

....

Vocales

....

....

....

Secretario

....

Acuerdan otorgarle la calificación de..

En Pamplona a ....

A Mercedes y a mis padres,
gracias por todo.

Acknowledgements

The author would like to thank to Miguel Ángel Gómez Laso for all the research work realized in collaboration, and for his help in the final redaction of several sections of this Thesis.

The author would like to thank also to Francisco Falcone for his kind revision of the English in the manuscript, and for his enthusiastic research work.

The author wants to express his deep gratitude to his supervisor, Mario Sorolla, and to our collaborators, David Benito, María José Garde, and María José Erro. With their always smart advise, their willingness to help and their encouragement, they have made possible this Doctoral Thesis.

The author is also very grateful to Iñigo Ederra, for the kind help provided in the earlier stages of the work in the cross section method.

Finally, the author wants to thank the generous assistance provided by Marco Guglielmi, Viktor Vasilyevich Shevchenko, Manfred Thumm and Didier Lippens. It has been really a privilege to receive their advice.

CONTENTS

Chapter 3. Approximate analytical solutions for PBG structures in microstrip technology 83

CHAPTER 1

INTRODUCTION

1.1. Background

In the last years the field of periodic structures for electromagnetic waves has received an important impulse with the introduction of the novel and fruitful concepts of Photonic Bandgap (PBG) and Photonic/Electromagnetic Crystal. These novel concepts were originally developed by Yablonovitch [YAB 87] and John [JOH 87] in the latest 1980s, in the optical wavelength region. The idea was to design materials so that they can affect the properties of photons, in much the same way that ordinary semiconductor crystals affect the properties of electrons. Both Yablonovitch and John suggested that structures with periodic variations in dielectric constant, resembling the self-organized structure of atoms in a semiconductor, could influence the nature of photonic modes in a material, creating forbidden frequency bands in certain directions (partial photonic bandgaps) or in all the directions (complete photonic bandgaps). These new materials were called Photonic Crystals or Photonic Bandgap (PBG) Crystals. Figure 1.1 shows schematics of Photonic Crystals with one-dimensional (1D), two-dimensional (2D), and three-dimensional (3D) periodic variations of the dielectric constant.

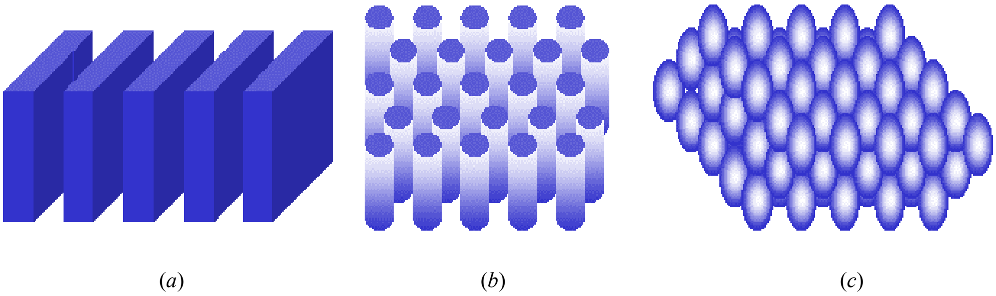

Figure 1.1: *Photonic Crystals or Photonic Bandgap (PBG) Crystals showing periodicity in several dimensions. From left to right, (a) one-dimensional (1D), (b) two-dimensional (2D), and (c) three-dimensional (3D) periodic arrangements of implants of a dielectric constant (or refractive index) embedded in a host with another dielectric constant.*

This way, PBG crystals can be defined as one- two- or three-dimensional periodic structures in which the propagation of electromagnetic waves is not allowed in some frequency bands or directions, behaving in a similar way as electronic crystals (e. g. semiconductors) do for the flow of electrons [JOA 95]. Their operation rely, however, on the well-known Bragg reflection effect, but in this case one- two- or three-dimensional periodic structures can be involved, and hence the term 'generalized Bragg reflection' is sometimes used.

Of special importance to establish and extend the knowledge on these novel concepts and materials was the edition of ‘Photonic Crystals’, by Joannopoulos et al. [JOA 95]. It was the first book entirely devoted to the topic, and it is indeed a very valuable reference.

Although the research was initially focused on the optical wavelength region, PBG crystals and properties are scalable and applicable to a wide frequency range. This happens because Maxwell’s equations have no fundamental length scale. Actually, the implications for the microwave and millimeter wave domains became soon apparent and multiple interesting and promising structures and applications were developed.

It is worth saying that far from the optical frequency range, ‘*Photonic* Crystal’ could be an ambiguous term, and the denomination ‘*Electromagnetic* Crystal’ seems to be natural and has been also proposed at those non-optical frequency ranges. However, and although it was somehow controversial, they are also frequently termed simply as PBG (i.e. *Photonic* Bandgap) structures, regardless of the frequency regime of operation. Here, ‘*Photonic*’ should be understood neither with the meaning of referring to optical frequencies, nor considered as underlining any kind of process related to the wave-particle duality. Here, ‘*Photonic*’ only enhances the relationship of all these structures with those in the optical range where they first appeared, as well as, owing to the scaling property of the solution of Maxwell’s equations, it makes apparent that many concepts and ideas developed for them in the optical range can be directly transposed to other frequency ranges. Additionally the term ‘*Photonic* Crystal’ reminds the fact that a fruitful analogy can be established between the operation of these structures and the way in which ordinary semiconductor crystals affect the properties of electrons.

Specially significant from the point of view of nomenclature in the framework of this thesis is the term employed by the pioneers in the introduction of PBG structures in microstrip circuits and in their applications. This pioneering and leading role has been carried out by Prof. Tatsuo Itoh and his group at the University of California in Los Angeles , using the term ‘PBG structure’.

PBG structures at microwave frequencies were initially realized by scaling the structures used at optical frequencies. That implied micromachining holes into dielectric slabs to create a 2D [GAU 97] periodic variation of the material dielectric constant. Machined slabs could be also stacked to create a 3D periodic variation of the dielectric constant [SMI 99]. Specially famous is the ‘woodpile’ structure, Fig. 1.2, a layer-by-layer PBG crystal made of stacked alumina rods, of the Iowa State University [HO 94, OZB 96].

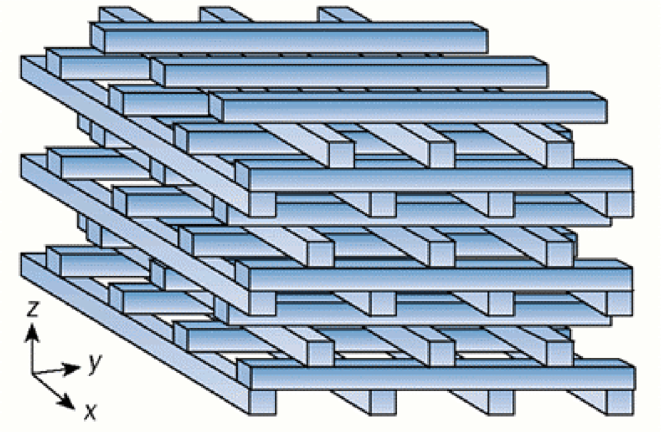

Figure 1.2: *The 'woodpile' 3D PBG crystal made by stacking alumina rods*

The main applications proposed for these microwave PBG structures were their use as substrates for planar antennas (to improve their efficiency and radiation pattern by forbidding surface wave excitation) [GAU 97, SMI 99] the implementation of reflectors (since they provide wide and deep reflected frequency bands) [KES 96], and the implementation of resonant cavities and waveguides [TEM 99].

However these configurations, while useful, have two main drawbacks: firstly, they are not easy to fabricate and, secondly, they are big in terms of wavelength. To reduce the PBG crystal dimensions the use of metallodielectric configurations was proposed [BRO 95, FAN 96, SIE 98]. An effective example of metallodielectric crystal is given by the high-impedance ground plane described in [SIE 98a], and employed to improve a patch antenna performance in [QIA 98]. It is comprised of a grounded dielectric slab periodically loaded with a square lattice of square metallic pads. The edges of the pads are a few millimeters apart, realizing a 2D periodic network of capacitors. Each pad is connected to the ground through one via at its center, which provides the inductive part of the LC-network.

These approaches, although very effective, require a non-planar fabrication process. In the latest 1990s, Prof. Tatsuo Itoh's group at the University of California in Los Angeles, focused on the development of planar PBG crystals that do not need vias and that can be easily integrated in conventional planar microwave and millimeter-wave circuits. His achievements constituted a real breakthrough in the application of PBG structures in the microwave and millimeter wave filed, since the planar circuit technology is the driving force for modern microwave and millimeter wave applications, because of its enormous advantages including greatly reduced hardware size and weight, lower profile, easier integration with solid state devices, low power consumption, conformal implementation on moving platforms, and greatly reduced fabrication cost since they can be simply printed on a circuit board or semiconductor wafer in large quantities instead of being machined piece by piece. However, one of the fundamental disadvantages of planar circuits when used at high frequencies is their relatively high loss or low quality factor (Q), in comparison to the classical and bulky metallic waveguide systems. It is therefore extremely interesting to explore novel ideas, concepts and structures, like the PBG crystals, to try to improve the performance of planar microwave and millimeter wave systems. Actually, this thesis will be devoted specifically to the study PBG structures in the most popular microwave planar circuit technology: the microstrip technology.

The first approach proposed by Prof. Itoh to produce a PBG structure in microstrip technology consisted in drilling a periodic pattern of cylinders in the substrate of the microstrip line to locate implants of different materials within them, or to leave them filled by air [QIA 97]. A photograph of a prototype is shown in Fig. 1.3. However, it was soon found that PBG structures with even deeper and wider stopbands could be simply achieved by etching a periodic pattern of circles in the ground plane along the microstrip line. This approach is simpler to fabricate, compatible with the monolithic

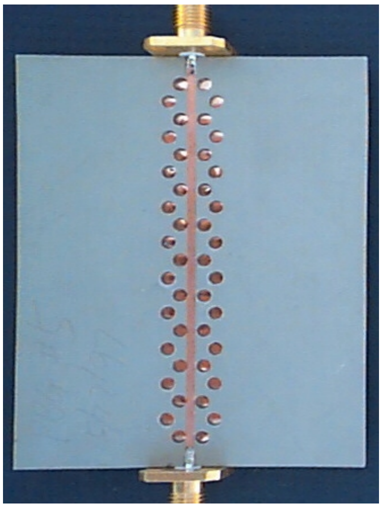

Figure 1.3: *PBG crystal in microstrip technology obtained by drilling a periodic pattern in the dielectric substrate, as it was originally proposed by Prof. Itoh at UCLA. (Source: http://www.cwc.nus.edu.sg/news/seminar/arch1.shtml, speaker's notes on 'Photonic Bandgap structures for microwave circuits', by Dr A. Alphones at the Center for Wireless Communications, National University of Singapore).*

technology, and permits the PBG structure to be integrated with other microstrip components in the upper plane. As a first approximation, a PBG microstrip structure with three rows of same-size and equidistant circles, one of them etched in the ground plane just below the upper-plane conductor strip and the two others at both sides of it, was designed [RAD 98]. A photograph of a prototype is shown in Fig. 1.4.

An also very interesting PBG structure for planar microwave circuits was later proposed. It is a more compact crystal referred to as Uniplanar Compact PBG (UC-PBG) structure, which realizes a 2D periodic network of LC circuits without introducing vias. It is also very attractive for applications to MICs and MMICs because of the easy and low cost realization as well as compatibility with standard fabrication techniques, although the rejection level provided by it in the forbidden band is not as predictable and regular as in the previous structures [QIA 98a, YAN 98]. A sketch of the PBG crystal structure can be seen in Fig. 1.5.

The range of applications proposed for these PBG structures in microstrip technology in the last years has been very wide. Among them we can include broadband harmonic tuning in power amplifiers [RAD 98a, RAD 98b, RAD 98c, HAN 99, YOO 01], oscillators [XUE 01] and mixers [YAN 99a], to increase the output power and the efficiency, and to reduce the spurious harmonics of these active devices; the implementation of microstrip lowpass filters with a wide high-frequency rejection

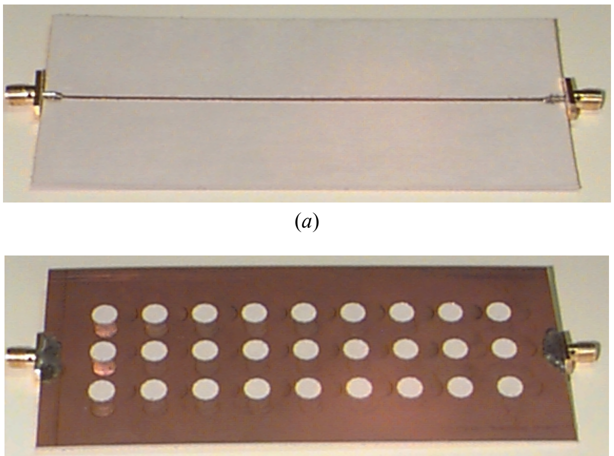

(*a*)

(*b*)

Figure 1.4: *PBG crystal in microstrip technology obtained by etching a 2D lattice of holes in the ground plane (b), while the upper plane is unperturbed (a), as it was originally proposed by Prof. Itoh at UCLA. The photograph shows a prototype fabricated at the Public University of Navarre, Spain.*

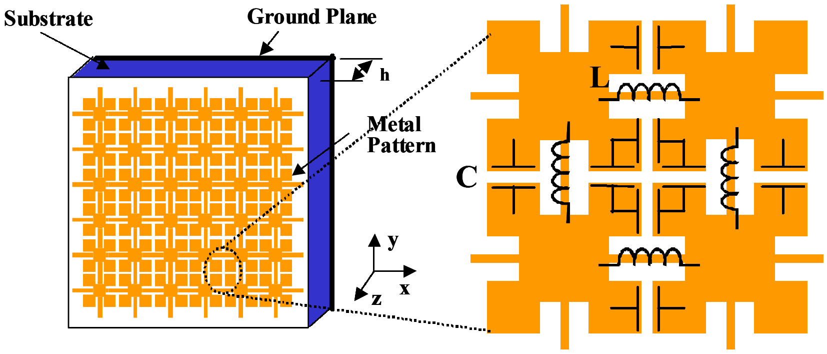

Figure 1.5: *Uniplanar Compact PBG (UC-PBG) structure proposed by Prof. Itoh at UCLA. This more compact crystal realizes a 2D periodic network of LC circuits without introducing vias, as it is shown in the sketch.*
(Source: http://www.cwc.nus.edu.sg/news/seminar/arch1.shtml, speaker's notes on 'Photonic Bandgap structures for microwave circuits', by Dr A. Alphones at the Center for Wireless Communications, National University of Singapore).

bandwidth [RUM 98, YAN 99a, KIM 00]; the implementation of microstrip bandpass filters with intrinsic spurious suppression [YAN 98a, YAN 99, YAN 00, JI 00]; and suppression of radiation at harmonic frequencies in microstrip patch antennas with PBG ground plane [HOR 99], or reduction of their power losses and improvement of their radiation pattern due to the inhibition of surface wave excitation [COC 98, COC 99].

Other more sophisticated applications that are also interesting to mention include the reduction of parallel-plate mode leakage in conductor-backed coplanar waveguide and in stripline [MA 98, MA 99, YAN 99], the suppression of the coupling between adjacent microstrip lines [LEO 02], and the implementation of TEM waveguides [YAN 99b]. It is also interesting to note that other different periodic patterns have been proposed by several groups to implement PBG crystals in microstrip technology [XUE 00, KIM 00a], and even PBG structures for coplanar waveguides have been lately proposed [FU 01].

Actually, the topic of PBG structures for planar microwave circuits (particularly microstrip circuits) has attracted an increasing interest among the researchers in the last years, that has led to an important number of journal articles devoted to them, and to the introduction of sections dedicated to the topic in the latest books about microstrip technology that have been published [EDW 00, HON 01, ITO 01]. It can be said that the topic is growing very quickly and becoming quite popular in the microwave planar circuit community, due to the promising and exciting applications envisaged. However, the new terminology, concepts, ideas and applications must not fade the fact that these devices are intimately related to the historically known microwave and millimeter wave periodic structures [COL 91]. In fact, microwave applications of periodic structures can be dated back to the early days of radar, with such examples as one-dimensional (1-D) slotted-waveguide array antennas, as well as two-dimensional (2-D) frequency selective surfaces (FSSs) and polarization diplexers. The emphasis of recent research efforts, however, is on 1-D or 2-D PBG structures that are compatible with modern planar circuit fabrication technology. Applying the PBG concept allows one to greatly extend the horizon of imagination when conceiving novel structures to control the behavior of electromagnetic waves, whether it is a guided wave, surface wave, or radiation wave. For example, as it has been previously commented, microstrip-based lowpass (rejected band) filters can be achieved by modifying the dielectric substrate [QIA 97] and/or the ground plane [RAD 98, YAN 99], rather than following the traditional high-low impedance line approach. In the same way, surface wave and leaky wave suppression can be achieved by the same means.

1.2. Overview of the thesis

The work presented in this thesis is focused on the study of PBG structures in microstrip technology for circuit applications. The starting point will be the PBG structure for microstrip lines proposed by Prof. Itoh in 1998, and obtained by etching a periodic pattern of circles, following a square lattice, in the ground plane of a microstrip line. The frequency response of this structure was very promising, since it included a low-loss passband, together with a wide and deep rejected band whose central frequency is fixed by the periodicity of the perturbation. However, the analysis and design of the structure was troublesome, since it features a ground plane perturbation of distributed nature, that is difficult to fit in the models customarily employed to analyze microwave periodic structures. Actually, the analysis and design of these devices was carried out with no more tools than time-consuming full-wave electromagnetic simulations, and a trial method was used to adjust the structure parameters to satisfy the required specifications. In order to surpass these difficulties, and to have a better insight into the operation of the structure, a very convenient way to model Photonic Bandgap structures for planar microwave and millimeter wave circuits that suits very well distributed perturbations is proposed: the use of the coupled mode theory. Here we have applied it to PBG structures in microstrip technology, but it could be easily extended to other planar waveguides.

In order to formulate an accurate coupled mode theory suitable for microwave and millimeter wave devices, the cross-section method will be used in the chapter 2 of this thesis. The method will be rigorously applied to open waveguides that can include perturbed ground planes and strip conductors, covering all of our cases of interest. As a result of it, the system of coupled mode equations that characterizes the nonuniform waveguide of interest will be obtained. It is interesting to remark that there are no approximations involved in this process. However, as it is explained in chapter 3, the problem can be notably simplified by realizing several reasonable approximations that will eventually lead to a simplified system of coupled mode equations that allows us to obtain a fast numerical solution of the general problem, and that features analytical solutions for the case of uniform PBG structures. In this way, a comprehensive set of analytical expressions for the most important design parameters of PBG microstrip structures will be furnished. The set of analytical expressions available cover a wide scope, ranging from the S parameters to the Bloch wave analysis, and constitutes a very useful and unique set of tools for the analysis and design of these devices.

The study of PBG structures in microstrip technology using the coupled mode theory provides also physical insight about the operation of the structure, and reveals a direct and fruitful link with the well established topic of Fiber Bragg Gratings (FBGs) in the optical regime. As a consequence, several ideas and techniques that are widely employed in the field of FBGs, can be transposed to the novel and emergent field of PBG structures for microstrip lines, to improve their performance. In this way, in chapter 4, optimization techniques to enhance the performance of PBG structures in microstrip technology will be proposed and tested. Using them, the ripple that appears in the passband can be eliminated, wider rejected bandwidths can be obtained, the circuit layout area required can be reduced, and non-periodic frequency responses as well as multiple frequency tuned devices, can be achieved.

To finish this work, in chapter 5 several examples of practical applications of PBG structures in microstrip technology are proposed and tested. The range of applications considered is quite wide, including the suppression of spurious bands and harmonics in passive and active circuits for enhanced out of band behaviour and higher efficiency, the implementation of enhanced lowpass filers and high rejection bandpass filters, the implementation of high-Q fully planar resonators, and the design of chirped delay lines to realize quadratic-phase filters with applications like real-time Fourier analysis. All of the examples presented show successfully the feasibility of the applications proposed and, in general, the high potential of these novel structures.

CHAPTER 2

COUPLED MODE THEORY THE CROSS-SECTION METHOD

The basic idea of the cross-section method is that the electromagnetic fields at any cross section of a nonuniform waveguide can be represented as a superposition of the forward and backward travelling waves associated to the different modes of an auxiliary uniform waveguide that has the same cross section and identical distribution of ε *and* μ *as the considered cross section. The coefficients of this superposition can be seen as the complex amplitudes of the modes along the nonuniform waveguide, and satisfy a set of first order linear ordinary differential equations, that turn into integro-differential equations for open waveguides, known as the coupled mode equations. In this way, the general problem of field derivation in a nonuniform waveguide (i.e. the three-dimensional (3D) electromagnetic problem) is reduced to the two-dimensional (2D) problem of mode field calculation in a uniform waveguide, and to the one-dimensional problem (1D) of solution of the coupled mode equations.*

In this chapter the method described will be developed for general nonuniform straight waveguides, and the specific details of its application to PBG structures in microstrip technology will be given.

2.1. Introduction

The first works that gave rise to the cross-section method were driven by research for the waveguide telecommunications projects [MIL 54, KAZ 59]. These projects dealt with the construction of pipes several kilometers length for information transmission using circular oversized waveguides and the low loss TE_{01} mode operating at millimeter wavelengths. Finally, metallic waveguide communications were not widely applied mainly due to the emergence of the optical fibers. Actually an important number of specialists that had been working in metallic waveguides migrated to the optical communications field transferring the acquired knowledge and the developed techniques.

The initial ideas relating to the cross-section method belong to the book of Kisun'ko [KIS 49] and the papers of Gutman, published in the former Soviet Union. The first paper published in the western countries was Stevenson's article [STE 51]. However, the extensive application of the method did not start until after the publication of Schelkunoff [SCH 55]. In his paper the cross-section method is proposed again and studied in detail, and it is illustrated by several examples.

Reiter [REI 59], Katsenelenbaum [KAT 57] and Unger [UNG 58] made significant contributions to develop the method. Of special importance is the book of Katsenelenbaum [KAT 61] (in Russian). It is the first book devoted specifically to the cross-section method and studies the problem for closed waveguides in great detail and depth.

The problem of nonuniform open waveguides was first studied applying the cross-section method by Shevchenko in his also very important book [SHE 71]. It is interesting to note that the referenced book is actually a translation of the original one published by the author in Russian in 1969.

The coupled mode theory was later applied to nonuniform optical dielectric waveguides by various authors and using various methods. We want to make reference here in particular to Marcuse [MAR 74], who studied optical dielectric slab waveguides and to Snyder [SNY 71, SNY 72, SNY 83] who formulated the coupled mode theory for nonuniform optical fibers. We want to highlight also, in the context of this thesis, the work of Yariv [YAR 73, YAR 84] who applied the coupled mode theory to optical gratings. However, it is important to note that due to the weakness of the perturbation customarily present in the nonuniform optical dielectric waveguides, they can be most of the times studied using a simplified coupled mode theory that performs the expansion of the fields in terms of “ideal modes” (the modes of the unperturbed uniform waveguide). However, Marcuse and Snyder have also formulated

the coupled mode theory for optical dielectric waveguides realizing the expansion in terms of “local modes” and hence applying in fact the cross-section method.
To finish this quick historical review we want to mention two books that deal with the cross-section method for closed metallic waveguides and study it in great detail and depth including numerous examples and applications. The first one is the book of Sporleder and Unger [SPO 79]. It is a very serious work and was during decades the only book available in English on this topic. The second one is a new and improved version in English of the previously mentioned book of Katsenelenbaum [KAT 61]. It contains very solid foundations on the theory of the cross-section method, analyzes a lot of examples and special cases, and includes the new material that appeared until the moment of its publication in 1998, constituting an excellent reference on the topic [KAT 98].

In this chapter we are going to apply the cross section method to analyze nonuniform open waveguides using the coupled mode theory formalism. The organization of the chapter will be the following: we will start in section (2.2) studying the properties of the modes in uniform waveguides. Both closed and open waveguides will be considered. We will continue in section (2.3) centering our attention in the nonuniform waveguides and in the mode coupling phenomena that take place at them. The cross section method will be used to study them. First, in section (2.3.1), the coupled mode equations and the coupling coefficient expressions will be deduced for nonuniform waveguides with ε and μ variable in the propagation direction. It is assumed, however, that in this case the metals present at the waveguide do not vary in the propagation direction, i.e. that the metals have constant cross section. The study will be extended to nonuniform waveguides that include metals with variable cross section, in section (2.3.2). There, it will be demonstrated that the same coupled mode equations are still valid for these last waveguides, and the new expressions for the coupling coefficients will be obtained. To finish, in section (2.3.2.3), a very useful expression for the coupling coefficient $C_{m,-m}$ as a function of the characteristic impedance of the mode will be obtained and its accuracy will be discussed.

2.2. Uniform waveguides: modes

As it has been seen in the abstract of the chapter, the modes of the uniform waveguides (waveguides that have a cross-section and a ε and μ profile that does not vary with distance along the waveguide axis, i.e. that are translationally invariant) will be the building blocks used by the cross-section method to expand the total field present in the nonuniform waveguide. In this section we are going to review the form of these modes and the properties that they satisfy.

In first place it is important to note that we are going to assume steady-state sinusoidal time dependence of the fields, and we are going to use their phasor representation. Hence the form of the fields is assumed to be:

$$\begin{aligned}\vec{E}(x,y,z,t) &= \vec{E}(x,y,z)\cdot e^{j\cdot\omega\cdot t}\\ \vec{H}(x,y,z,t) &= \vec{H}(x,y,z)\cdot e^{j\cdot\omega\cdot t}\end{aligned} \tag{2.1}$$

and to obtain the value of the field that actually exists we have to take the real or the imaginary part of the previous quantities.

As it is well known, Fourier analysis allows us to express any field $\vec{E}(x,y,z,t)$ or $\vec{H}(x,y,z,t)$ as a superposition of fields with steady-state sinusoidal time dependence of different frequencies, of the form given by eqn. (2.1). Therefore, the analysis that we are going to realize assuming that form for the fields, imposes no restrictions.

The vectors $\vec{E}(x,y,z)$ and $\vec{H}(x,y,z)$ are known as phasors of the electric and magnetic field, respectively, and we are going to work with them throughout this thesis. Using phasors, Maxwell equations have the following form:

$$\begin{aligned}&\nabla\vec{D} = \rho\\ &\nabla\vec{B} = 0\\ &\nabla\times\vec{E} = -j\cdot\omega\cdot\vec{B}\\ &\nabla\times\vec{H} = \vec{J} + j\cdot\omega\cdot\vec{D}\end{aligned} \tag{2.2}$$

To take into account the interaction between the fields and the media we have to add the following auxiliary relations:

$$\begin{aligned}&\vec{J} = \sigma\cdot\vec{E}\\ &\vec{D} = \varepsilon\cdot\vec{E} = \varepsilon_0\cdot\varepsilon_r\cdot\vec{E}\\ &\vec{B} = \mu\cdot\vec{H} = \mu_0\cdot\mu_r\cdot\vec{H}\end{aligned} \tag{2.3}$$

The MKS (or international) system of units is used throughout this work. With it, the involved quantities are defined as follows:

$\vec{E}$ is the electric field intensity, in V/m
$\vec{H}$ is the magnetic field intensity, in A/m
$\vec{D}$ is the electric flux density, in Coul/m^2
$\vec{B}$ is the magnetic flux density, in Wb/m^2

$\vec{J}$ is the electric current density, in A/m^2

ρ is the electric charge density, in Coul/m^3

σ is the conductivity of the medium, in S/m

$\varepsilon_0 \approx 8.854 \cdot 10^{-12}$ F/m , is the dielectric constant (or permittivity) of vacuum

ε is the dielectric constant (or permittivity) of the medium, in F/m

$\mu_0 = 4 \cdot \pi \cdot 10^{-7}$ H/m , is the permeability of vacuum

μ is the permeability of the medium, in H/m

In order to obtain the modes of a waveguide we are going to assume that the waveguide region is source-free. Hence it is assumed that there are no external current sources in the waveguide section ($\vec{J} = 0$), and that the fields are excited by waves incident on this section. Taking advantage of this assumption the third and fourth Maxwell equations (eqn. (2.2)) can be rewritten as:

$$\begin{aligned} \nabla \times \vec{E} &= -j \cdot \omega \cdot \mu \cdot \vec{H} \\ \nabla \times \vec{H} &= j \cdot \omega \cdot \varepsilon \cdot \vec{E} \end{aligned} \tag{2.4}$$

It is interesting to note that in these equations the existence of a medium with conductivity σ can be taken into account defining a complex ε with value:

$$\varepsilon_{comp} = \varepsilon - j \cdot \frac{\sigma}{\omega} = \varepsilon \cdot \left(1 - j \cdot \frac{\sigma}{\omega \cdot \varepsilon} \right) \tag{2.5}$$

that in the case of a good conductor ($\sigma >> \omega \cdot \varepsilon$) can be rewritten as:

$$\varepsilon_{comp} \approx -j \cdot \frac{\sigma}{\omega} \tag{2.6}$$

Let us define a Cartesian coordinate system (*x, y, z*) where the *z* axis is parallel to the waveguide axis. The type of solution sought for the waveguide modes is that corresponding to a wave that propagates along the *z* axis and has the following form:

$$\begin{aligned} \hat{\vec{E}}(x,y,z) &= \vec{E}(x,y) \cdot e^{-j \cdot \beta \cdot z} \\ \hat{\vec{H}}(x,y,z) &= \vec{H}(x,y) \cdot e^{-j \cdot \beta \cdot z} \end{aligned} \tag{2.7}$$

where $\hat{\vec{E}}(x,y,z)$ and $\hat{\vec{H}}(x,y,z)$ are the total electric and magnetic field of the mode, $\vec{E}(x,y)$ and $\vec{H}(x,y)$ are the (*x,y*) dependent part of the electric and magnetic field of the mode, i.e. they are the factors that describe the mode field dependence in the cross-section plane, and β is known as the phase constant, propagation constant or wavenumber of the mode. In this work we are going to assume that there are no dissipative losses in the waveguide, so there will be no attenuation constant together with the phase constant. For a frequency of operation a mode can be in the waveguide in propagation (it happens if $\beta^2 > 0$, and in this case power flows through the waveguide) or cut-off (it happens if $\beta^2 < 0$ and in this case it will have evanescent behaviour, suffering reactive attenuation along the waveguide without carrying power).

For a given uniform waveguide there exists a set of solutions of the form expressed by eqn. (2.7) that are known as the modes of the waveguide. Let us numerate all modes of the waveguide with a superscript i, where i is an integer that can take positive and negative values.

$$\begin{aligned} \hat{\vec{E}}^i(x,y,z) &= \vec{E}^i(x,y)\cdot e^{-j\cdot\beta_i\cdot z} \\ \hat{\vec{H}}^i(x,y,z) &= \vec{H}^i(x,y)\cdot e^{-j\cdot\beta_i\cdot z} \end{aligned} \tag{2.8}$$

As it can be seen each mode is characterized by the (*x,y*) dependent part of the of the electric and magnetic field, $\vec{E}^i(x,y)$ and $\vec{H}^i(x,y)$, and by its phase constant, β_i. These parameters must satisfy the following relations:

$$\begin{aligned} &\frac{\partial E_z^i}{\partial y} + j\cdot\beta_i\cdot E_y^i = -j\cdot\omega\cdot\mu\cdot H_x^i \\ &-j\cdot\beta_i\cdot E_x^i - \frac{\partial E_z^i}{\partial x} = -j\cdot\omega\cdot\mu\cdot H_y^i \\ &\frac{\partial E_y^i}{\partial x} - \frac{\partial E_x^i}{\partial y} = -j\cdot\omega\cdot\mu\cdot H_z^i \end{aligned} \tag{2.9}$$

$$\begin{aligned} &\frac{\partial H_z^i}{\partial y} + j\cdot\beta_i\cdot H_y^i = j\cdot\omega\cdot\varepsilon\cdot E_x^i \\ &-j\cdot\beta_i\cdot H_x^i - \frac{\partial H_z^i}{\partial x} = j\cdot\omega\cdot\varepsilon\cdot E_y^i \\ &\frac{\partial H_y^i}{\partial x} - \frac{\partial H_x^i}{\partial y} = j\cdot\omega\cdot\varepsilon\cdot E_z^i \end{aligned} \tag{2.10}$$

that are obtained by substituting the form of the modes (eqns. (2.8)) in the Maxwell equations for a source-free region (eqns. (2.4)).

The above six equations (eqns. (2.9) and (2.10)) can be solved for the four transverse fields components in terms of the longitudinal field components (E_z^i , H_z^i), obtaining:

$$\begin{aligned}
H_x^i &= \frac{j}{k^2-\beta_i^2}\cdot\left(\omega\cdot\varepsilon\cdot\frac{\partial E_z^i}{\partial y}-\beta_i\cdot\frac{\partial H_z^i}{\partial x}\right)\\
H_y^i &= \frac{-j}{k^2-\beta_i^2}\cdot\left(\omega\cdot\varepsilon\cdot\frac{\partial E_z^i}{\partial x}+\beta_i\cdot\frac{\partial H_z^i}{\partial y}\right)\\
E_x^i &= \frac{-j}{k^2-\beta_i^2}\cdot\left(\beta_i\cdot\frac{\partial E_z^i}{\partial x}+\omega\cdot\mu\cdot\frac{\partial H_z^i}{\partial y}\right)\\
E_y^i &= \frac{j}{k^2-\beta_i^2}\cdot\left(-\beta_i\cdot\frac{\partial E_z^i}{\partial y}+\omega\cdot\mu\cdot\frac{\partial H_z^i}{\partial x}\right)
\end{aligned} \tag{2.11}$$

where

$$k=\omega\cdot\sqrt{\mu\cdot\varepsilon}$$

(see, for instance, [POZ 98]).

The fields of the modes can have arbitrary normalization and consequently, in general, $\vec{E}^i(x,y)$ and $\vec{H}^i(x,y)$ are complex. However, in our case of a nonabsorbing waveguide (i.e. a waveguide without dissipative losses) ε and μ are real, and eqns. (2.11) (together with (2.10) and (2.9)) show that for a mode in propagation ($\beta_i^2>0\Rightarrow\beta_i$ real) it is consistent to choose the components of $\vec{E}^i(x,y)$ and $\vec{H}^i(x,y)$ so that the transverse components are real and the longitudinal components are imaginary. We will adopt this convention throughout this work and thus a mode in propagation will satisfy:

$$\begin{aligned}
&E_x^i, E_y^i, H_x^i, H_y^i \text{ are real}\\
&E_z^i, H_z^i \text{ are imaginary}
\end{aligned} \tag{2.12}$$

As it will be shown later, this convention will be very convenient because it makes very simple the relation between the normalization of the mode fields and the power carried by the propagating mode [SNY 83].

Until now we have formulated the mode problem in such a way that it could seem that the modes with positive superscripts and the modes with negative superscripts are totally independent between them. This is not true. Rigorously speaking, we have

developed the waves associated to the modes. Actually each mode (characterized by a positive index *i*) has two associated waves: one forward travelling wave (with a superscript +*i*) and one backward travelling wave (with a superscript –*i*).
The relation between their phase constants is:

$$\beta_{-i} = -\beta_i \tag{2.13}$$

where, for $i > 0$ (forward travelling wave) , $\beta_i > 0$ if the mode is in propagation, and $\beta_i = -j \cdot |\beta_i|$ if the mode is cut-off.
On the other hand the relation between the (*x,y*) dependent part of the fields of the forward and backward travelling waves associated to the *i* mode is taken as:

$$\begin{aligned} E_x^{-i} &= -E_x^i \; ; \; E_y^{-i} = -E_y^i \; ; \; E_z^{-i} = E_z^i \\ H_x^{-i} &= H_x^i \; ; \; H_y^{-i} = H_y^i \; ; \; H_z^{-i} = -H_z^i \end{aligned} \tag{2.14}$$

In this case eqns. (2.9) , (2.10) and (2.11) are invariant to the superscript sign, that is, if the fields of the forward wave satisfy them, then the fields of the backward wave also satisfy the same equations (if eqns. (2.13) and (2.14) are applied). However it is important to notice that the relation between the (*x,y*) dependent part of the fields (2.14) has been taken following [KAT 98]. Actually the relation could be also taken with $\vec{E}^i$ and $\vec{H}^i$ exchanged, as it is done in [SPO 79], [SNY 83] and [MAR 91], for example.

2.2.1. Closed waveguide

In a uniform closed waveguide (i.e. a uniform waveguide that includes a metallic cover that surrounds it) the set of modes proposed in the previous section, both propagating and evanescent, forms a complete and orthogonal system. They can be numerated with a superscript *i* (see eqn. (2.8)), and for a given uniform closed waveguide the set is composed by an infinite number of discrete modes [SHE 71], [ROZ 97].

2.2.1.1. Expansion of the fields

Any electromagnetic field distribution that can exist in the uniform closed waveguide can be expanded in a unique way as a linear combination of its modes (including the forward and backward travelling waves). The expansion has the following form:

$$\begin{aligned}\hat{\vec{E}}(x,y,z) &= \sum_{i=-\infty}^{\infty} A_i \cdot \vec{E}^i(x,y) \cdot e^{-j\cdot\beta_i\cdot z} = \sum_{i=-\infty}^{\infty} a_i \cdot \vec{E}^i(x,y) \\ \hat{\vec{H}}(x,y,z) &= \sum_{i=-\infty}^{\infty} A_i \cdot \vec{H}^i(x,y) \cdot e^{-j\cdot\beta_i\cdot z} = \sum_{i=-\infty}^{\infty} a_i \cdot \vec{H}^i(x,y)\end{aligned} \qquad (2.15)$$

where the coefficients A_i have in general constant complex values in our case of uniform lossless waveguides.

2.2.1.2. Orthogonality relations and normalization

As we have previously stated, in a uniform closed waveguide the fields of the different modes are mutually orthogonal. The orthogonality relationship will be formulated for any combination of modes, superscript signs and in particular for the forward and backward travelling waves of the same mode (same superscript but with different sign). The expression for the orthogonality relationship in a closed waveguide (with isotropic materials, i.e. with ε and μ scalars) can be easily obtained applying the Lorentz lemma to the fields $\hat{\vec{E}}^i, \hat{\vec{H}}^i$ and $\hat{\vec{E}}^m, \hat{\vec{H}}^m$ in a waveguide section defined between two planes $z=z_1$ and $z=z_2$, [KAT 98], [COL 91], obtaining:

$$\iint_S \left(\left(\vec{E}^i \times \vec{H}^m\right) + \left(\vec{E}^m \times \vec{H}^i\right)\right) \cdot \hat{z} \cdot dS = 0 \quad , \quad m \neq i \qquad (2.16)$$

where $\hat{z}$ is the unitary vector in the z direction (waveguide axis), and the integral is performed over the cross section surface, S.

Rigorously speaking the orthogonality integral (2.16) is identically equal to zero if $\beta_m \neq \beta_i$. Actually, if two modes are degenerate (i.e. their phase constants are equal, $\beta_m = \beta_i$), then the orthogonality relationship (2.16) could be not satisfied between them. However, for any subset of n degenerate modes we can customarily choose suitable linear combinations of them in such a way that the subset of n degenerate modes can be converted into a new subset of n mutually orthogonal modes. Thus we may, generally speaking, assume that the orthogonality relationship (2.16) is always satisfied for $m \neq i$ [COL 91].

Other orthogonality relationship that can be obtained in the same way as the previous one (and hence is valid for closed waveguides with isotropic materials) has the following form [COL 91]:

$$\iint_S \left(\vec{E}^i \times \vec{H}^m\right) \cdot \hat{z} \cdot dS = 0 \quad , \quad m \neq i \ \text{ and } \ m \neq -i \qquad (2.17)$$

where $\hat{z}$ is again the unitary vector in the z direction (waveguide axis), and the integral is performed over the cross section surface, S.
As it can be seen, this last orthogonality relation is not satisfied between the forward and backward travelling waves of the same mode, $+i$, $-i$.

Let us normalize the electromagnetic fields of the i mode, $\vec{E}^i$ and $\vec{H}^i$, in the following way:

$$\iint_S \left(\vec{E}^i \times \vec{H}^i\right) \cdot \hat{z} \cdot dS = N_i \tag{2.18}$$

It is interesting to note that due to the relation taken between the fields of the forward and backward travelling waves associated to the same i mode (see eqn. (2.14)), the normalization factor will satisfy:

$$N_i = -N_{-i} \tag{2.19}$$

The orthogonality condition of eqn. (2.16) and the normalization of eqn. (2.18) can be written in the same equation giving rise to the following expression:

$$\iint_S \left(\left(\vec{E}^i \times \vec{H}^m\right) + \left(\vec{E}^m \times \vec{H}^i\right)\right) \cdot \hat{z} \cdot dS = \delta_{im} \cdot 2 \cdot N_i \tag{2.19}$$

where the Kronecker symbol is $\delta_{im}=0$ for $i \neq m$, whereas $\delta_{ii}=1$.

2.2.1.3. Power flow

As it was previously discussed, the modes in propagation in a closed waveguide transport power along the waveguide, whereas the modes in cutoff have evanescent behaviour, suffering reactive attenuation without carrying power. For our case of nonabsorbing waveguides power flows parallel to the waveguide axis (z direction) and is distributed over the cross-section with density given by the magnitude of the time-averaged Poynting vector. Integrating it over the cross-section for a propagating i mode, the total power carried by the mode is calculated as:

$$\begin{aligned} P_i &= \frac{1}{2} \cdot \mathrm{Re}\left(\iint_S \hat{E} \times \hat{H}^* \cdot \hat{z} \cdot dS\right) = \frac{1}{2} \cdot |a_i|^2 \cdot \mathrm{Re}\left(\iint_S \vec{E}^i \times \vec{H}^{i^*} \cdot \hat{z} \cdot dS\right) = \\ &= \frac{1}{2} \cdot |a_i|^2 \cdot \mathrm{Re}\left(\iint_S \left(E_x^i \cdot H_y^{i^*} - H_x^{i^*} \cdot E_y^i\right) \cdot dS\right) = \frac{1}{2} \cdot |a_i|^2 \cdot \left(\iint_S \vec{E}^i \times \vec{H}^i \cdot \hat{z} \cdot dS\right) \end{aligned}$$

where the convention for the mode fields given by eqn. (2.12) has been applied, and

$$\hat{E}(x,y,z) = a_i \cdot \bar{E}^i(x,y)$$
$$\hat{H}(x,y,z) = a_i \cdot \bar{H}^i(x,y)$$

being a_i the complex amplitude of the mode.
Taking advantage of the normalization of the mode fields (eqn. (2.18)), the expression for the power carried by the propagating *i* mode becomes:

$$P_i = \frac{1}{2} \cdot |a_i|^2 \cdot N_i \tag{2.20}$$

This last expression reveals that in our case where the convention for the mode fields given by eqn. (2.12) has been taken, the normalization factor, N_i , for the propagating modes must be a positive real number for $i > 0$ (forward propagating waves, and hence positive power flow), and a negative real number for $i < 0$ (backward propagating waves, and hence negative power flow). This is coherent with the relationship that the normalization factors must satisfy, eqn. (2.19).

Regarding the total power carried by the closed waveguide (in the increasing *z* direction), it is given by the total Poynting vector integrated over the cross-section. Its value is:

$$P_{tot} = \frac{1}{2} \cdot \mathrm{Re}\left(\iint_S \hat{E}_{tot} \times \hat{H}_{tot}^{\ *} \cdot \hat{z} \cdot dS\right)$$

Expanding $\hat{E}_{tot}$ and $\hat{H}_{tot}$ as in eqn. (2.15), applying the convention for the mode fields given by eqn. (2.12), using the orthogonality and normalization conditions of eqns. (2.17) and (2.18), and recalling the definition for the power carried by a propagating mode of eqn. (2.20), we have that for our case of a nonabsorbing waveguide:

$$P_{tot} = \sum_i \frac{1}{2} \cdot |a_i|^2 \cdot N_i = \sum_i P_i \tag{2.21}$$

where the summation is performed for all the propagating modes (with both signs). Thus, the total power carried by the waveguide (in the increasing *z* direction) is equal to the power in all forward propagating modes, minus the power in all backward propagating modes (since the later will have a normalization factor with negative sign, and the power carried by them will be negative, i.e. in the opposite direction).

2.2.2. Open waveguide

Unlike the modes of a closed waveguide, the discrete modes of an open waveguide do not form a complete system. Actually, the radiated field can not be represented by them. Moreover it can be demonstrated that, in contrast to the case of closed waveguides, the system of discrete modes of an open waveguide will be formed by a finite number of modes, all of them in propagation.

To obtain a complete system of modes for an open waveguide, able to represent any field distribution that can exist in the open waveguide (including the radiated fields), we must complement the well known system of discrete modes (that exist also in the closed waveguides and has a discrete spectrum), adding a system of modes with a continuous spectrum. This additional system allows us to represent the radiated field, and together with the traditional system of modes with discrete spectrum forms a complete system for the open waveguide. The modes of this complete system will be also mutually orthogonal and hence will propagate independently of each other in the case of a nonabsorbing uniform open waveguide.

The basic idea to construct the complete system of modes is the following. If we apply Maxwell equations, eqns. (2.4), to an open waveguide, we impose solutions that imply propagation (or reactive attenuation) in the z direction (waveguide axis) (i.e. we impose the mode solutions, eqn. (2.8)), and we impose the boundary conditions, including the so called “radiation condition” (the fields must vanish as the distance from the waveguide increases to infinity), then we will obtain the well known system of modes with discrete spectrum of the open waveguide. This system of modes will not be complete though. The “radiation condition” imposed is very reasonable at first sight, because it simply implies that the power carried by the mode is finite. However, in order to obtain the system of modes with continuous spectrum of the open waveguide we must relax this last condition. We must impose a weaker condition: the fields of the mode must be finite when the distance from the waveguide goes to infinity. In this way we will obtain the sought system of modes with continuous spectrum that together with the system of modes with discrete spectrum forms the complete orthogonal system for the open waveguide that can be used for the representation of any physically realizable field distribution in the waveguide. It is important to note that the fact that the modes with continuous spectrum do not vanish at infinity, and hence have infinite power, does not lead to non physical results. The reason is that no physically realizable source generates only one of these modes. A set of them is always excited. Since the spectrum of these modes is continuous, the field is always expressed as an integral of them, and this integral will always satisfy the radiation condition (the value of the integral will vanish as the distance from the waveguide increases to infinity), [SHE 71].

A very interesting point of view to understand the success of the method proposed and the properties of the continuous spectrum modes of an open waveguide, is to consider each of them as the limit of a mode of a closed waveguide (formed by surrounding the open waveguide with a metal clad) when the metal clad goes to infinity. Actually, an open waveguide can be always regarded as a waveguide closed at infinity, and hence the condition to obtain the continuous spectrum modes of having finite fields at infinity is not so strange. [SHE 71], [SNY 83], [ROZ 97].

2.2.2.1. Expansion of the fields

Any electromagnetic field distribution that can exist in a uniform open waveguide can be expanded in a unique way as a linear combination of its modes with discrete spectrum and its modes with continuous spectrum (including the forward and backward travelling waves). In this work we are going to center our attention on open waveguides that are essentially constituted by a ground plane with perturbations (i.e. they are formed by a ground plane and customarily include a single dielectric and other conductors, and are surrounded by air). This case includes the microstrip line, the slotline, the coplanar waveguide... , and the structures produced by etching the ground plane in these planar technologies. So it includes all our cases of interest. For this kind of open waveguides the expansion of the fields has the following form [ROZ 97], [ROZ 92], [MON 93]:

$$\begin{aligned}
\hat{\vec{E}}(x,y,z) &= \sum_{i=-M}^{M} A_i \cdot \vec{E}^i(x,y) \cdot e^{-j\cdot\beta_i\cdot z} + \sum_{i=-Q}^{Q} \int_0^{\infty} A_i(k_t)\cdot\vec{E}^i(x,y,k_t)\cdot e^{-j\cdot\beta_i(k_t)\cdot z}\cdot dk_t = \\
&= \sum_{i=-M}^{M} a_i \cdot \vec{E}^i(x,y) + \sum_{i=-Q}^{Q} \int_0^{\infty} a_i(k_t)\cdot\vec{E}^i(x,y,k_t)\cdot dk_t \\
\hat{\vec{H}}(x,y,z) &= \sum_{i=-M}^{M} A_i \cdot \vec{H}^i(x,y) \cdot e^{-j\cdot\beta_i\cdot z} + \sum_{i=-Q}^{Q} \int_0^{\infty} A_i(k_t)\cdot\vec{H}^i(x,y,k_t)\cdot e^{-j\cdot\beta_i(k_t)\cdot z}\cdot dk_t = \\
&= \sum_{i=-M}^{M} a_i \cdot \vec{H}^i(x,y) + \sum_{i=-Q}^{Q} \int_0^{\infty} a_i(k_t)\cdot\vec{H}^i(x,y,k_t)\cdot dk_t
\end{aligned} \tag{2.22}$$

where

$$k_t^{\,2} = k_0^{\,2} - \beta_i^2(k_t) \quad , \quad \text{with} \quad \begin{array}{ll} \beta_i(k_t) = +\sqrt{k_0^{\,2} - k_t^{\,2}} & \text{for } i > 0 \\ \beta_i(k_t) = -\sqrt{k_0^{\,2} - k_t^{\,2}} & \text{for } i < 0 \end{array}$$

$$k_0 = \omega \cdot \sqrt{\mu_0 \cdot \varepsilon_0}$$

The first summation is performed over the system of modes with discrete spectrum (there will be *M* discrete modes, all of them in propagation, with their corresponding forward and backward travelling waves, and $\beta_i^2 > k_0^{\,2}$).

The second summation and the integral are performed over the modes with continuous spectrum. The summation is necessary due to the existence of degenerate modes that share the same propagation constant $\beta_i(k_t)$ (the *i* index of the propagation constant of the continuous spectrum modes only selects the sign). As it can be seen the propagation constant of these modes of the continuous spectrum can take a continuous set of values. When the k_t parameter is in the range $0 < k_t < k_0$, then the propagation constant will be in the range $0 < \beta_i^2(k_t) < k_0^{\,2}$, giving rise to propagating (radiative) modes. On the other hand, when the k_t parameter is in the range $k_0 < k_t < \infty$, then the propagation constant will be in the range $-\infty < \beta_i^2(k_t) < 0$, giving rise to attenuating modes (modes having evanescent behaviour and suffering reactive attenuation).

The coefficients A_i (corresponding to the discrete spectrum modes), and $A_i(k_t)$ (corresponding to the continuous spectrum modes) have in general constant complex values in our case of uniform nonabsorbing open waveguides.

It is important to note that for other types of open waveguides (like for example the dielectric rib waveguide [ROZ 97] or the optical fiber [SNY 83]) the expansion corresponding to the continuous spectrum can have slightly different forms, although it will always include the integral of the mode fields over a continuous parameter.

2.2.2.2. Orthogonality relations and normalization

As we have previously stated, in a uniform open waveguide the fields of the different modes are mutually orthogonal. The orthogonality relationship will be formulated for any combination of modes (including the modes with discrete spectrum and the modes with continuous spectrum), superscript signs, and, in particular, for the forward and backward travelling waves of the same mode (same superscript but with different sign). The expressions for the orthogonality relationships in an open waveguide (with isotropic materials, i.e. with ε and μ scalars) will have the form:

$$\iint_S \left(\left(\vec{E}^i \times \vec{H}^m\right) + \left(\vec{E}^m \times \vec{H}^i\right)\right)\cdot \hat{z} \cdot dS = 0 \quad , \quad m \neq i \tag{2.23a}$$

$$\iint_S \left(\left(\vec{E}^i \times \vec{H}^m(k_t)\right) + \left(\vec{E}^m(k_t) \times \vec{H}^i\right)\right)\cdot \hat{z} \cdot dS = 0 \tag{2.23b}$$

$$\iint_S \left(\left(\vec{E}^i(k_t) \times \vec{H}^m(\tilde{k}_t)\right) + \left(\vec{E}^m(\tilde{k}_t) \times \vec{H}^i(k_t)\right)\right)\cdot \hat{z} \cdot dS = 0 \ , \ \tilde{k}_t \neq k_t \ \text{ or } \ m \neq i \tag{2.23c}$$

where $\hat{z}$ is the unitary vector in the z direction (waveguide axis), and the integral is performed over the infinite cross section surface, S.

Eqn. (2.23a) accounts for the orthogonality relationship existent between each pair of modes of the discrete spectrum, and eqn. (2.23b) for the orthogonality relationship between a mode of the discrete spectrum and a mode of the continuous spectrum. These equations can be easily obtained by applying the Lorentz lemma to the mode fields in a waveguide section defined between two planes $z=z_1$ and $z=z_2$. [COL 91].

On the other hand, eqn. (2.23c) accounts for the orthogonality relationship existent between each pair of modes of the continuous spectrum. An easy way to obtain it is to consider each mode of the continuous spectrum as the limit of a mode of a closed waveguide (formed by surrounding the open waveguide with a metal clad) when the metal clad goes to infinity. Another point of view is to consider the open waveguide as a waveguide closed at infinity. In this way the orthogonality relationship can be easily obtained by applying the Lorentz lemma to the mode fields, as in the previous cases. [SNY 83], [ROZ 97], [ROZ 92].

It is important to note that, rigorously speaking, the orthogonality integrals (2.23) are identically equal to zero if $\beta_m \neq \beta_i$. Actually, if two modes are degenerate (i.e. their phase constants are equal, $\beta_m = \beta_i$), then the orthogonality relationships (2.23) could be not satisfied between them. This could be specially troublesome in eqn. (2.23c). However, for any subset of n degenerate modes we can customarily choose suitable linear combinations of them in such a way that the subset of n degenerate modes can be converted into a new subset of n mutually orthogonal modes. Thus we may, in a general discussion, assume that the orthogonality relationships (2.23) are always satisfied for $m \neq i$ or $\tilde{k}_t \neq k_t$ [COL 91].

Other orthogonality relationships that can be obtained in the same way as the previous ones (and hence are valid for open waveguides with isotropic materials) have the following form [COL 91], [SNY 83], [ROZ 97], [ROZ 92]:

$$\iint_S \left(\vec{E}^i \times \vec{H}^m\right)\cdot \hat{z}\cdot dS = 0 \quad , \quad m \neq i \text{ and } m \neq -i \tag{2.24a}$$

$$\iint_S \left(\vec{E}^i \times \vec{H}^m(k_t)\right)\cdot \hat{z}\cdot dS = 0 \tag{2.24b}$$

$$\iint_S \left(\vec{E}^i(k_t) \times \vec{H}^m(\tilde{k}_t)\right)\cdot \hat{z}\cdot dS = 0 \quad , \quad \tilde{k}_t \neq k_t \text{ or } m \neq i \text{ and } m \neq -i \tag{2.24c}$$

where $\hat{z}$ is again the unitary vector in the z direction (waveguide axis), and the integral is performed over the infinite cross section surface, S.

As it can be seen, this last orthogonality relation is not satisfied between the forward and backward travelling waves of the same mode.

Let us normalize the electromagnetic fields of the modes, in the following way [SNY 83], [ROZ 97], [ROZ 92]:

$$\iint_S \left(\vec{E}^i \times \vec{H}^i\right)\cdot \hat{z}\cdot dS = N_i \tag{2.25a}$$

$$\iint_S \left(\vec{E}^i(k_t) \times \vec{H}^i(\tilde{k}_t)\right)\cdot \hat{z}\cdot dS = N_i(k_t)\cdot \delta(k_t - \tilde{k}_t) \tag{2.25b}$$

where $\delta(x)$ is the Dirac delta function. As it can be seen, eqn. (2.25a) refers to the discrete spectrum modes, and eqn. (2.25b) corresponds to the continuous spectrum modes.

It is interesting to note that due to the relation taken between the fields of the forward and backward travelling waves associated to the same mode (see eqn. (2.14)), the normalization factor will satisfy:

$$N_i = -N_{-i} \tag{2.26a}$$

$$N_i(k_t) = -N_{-i}(k_t) \tag{2.26b}$$

The orthogonality conditions of eqns. (2.23) and the normalizations of eqns. (2.25) can be written together giving rise to the following expressions:

$$\iint_S \left(\left(\vec{E}^i \times \vec{H}^m\right) + \left(\vec{E}^m \times \vec{H}^i\right)\right)\cdot \hat{z}\cdot dS = \delta_{im}\cdot 2\cdot N_i \tag{2.27a}$$

$$\iint_S \left(\left(\vec{E}^i \times \vec{H}^m(k_t)\right) + \left(\vec{E}^m(k_t) \times \vec{H}^i\right)\right)\cdot \hat{z}\cdot dS = 0 \tag{2.27b}$$

$$\iint_S \left(\left(\vec{E}^i(k_t) \times \vec{H}^m(\tilde{k}_t)\right) + \left(\vec{E}^m(\tilde{k}_t) \times \vec{H}^i(k_t)\right)\right)\cdot \hat{z}\cdot dS = \delta_{im}\cdot \delta(k_t - \tilde{k}_t)\cdot 2\cdot N_i(k_t) \tag{2.27c}$$

where δ_{im} is the Kronecker symbol, and $\delta(x)$ is the Dirac delta function.

2.2.2.3. Power flow

As it has been previously stated, in an open waveguide all the modes with discrete spectrum are in propagation, i.e. all of them can transport power along the waveguide. These modes are also known as the bound modes of the open waveguide. On the other hand, part of the modes of the continuous spectrum will be cut-off (i.e. they will have evanescent behavior, suffering reactive attenuation along the open waveguide without carrying power) and part of them will be in propagation, accounting for the radiated power. As a result, the modes of the continuous spectrum are often referred to as the radiation modes.

For our case of nonabsorbing open waveguides the power of the bound modes (discrete spectrum modes) flows parallel to the waveguide axis (z direction) and is distributed over the cross-section with density given by the magnitude of the time-averaged Poynting vector. Integrating it over the cross-section for an i mode, the total power carried by the bound mode is calculated as [SNY 83]:

$$\begin{aligned} P_i &= \frac{1}{2}\cdot \mathrm{Re}\left(\iint_S \hat{\vec{E}} \times \hat{\vec{H}}^* \cdot \hat{z} \cdot dS\right) = \frac{1}{2}\cdot |a_i|^2 \cdot \mathrm{Re}\left(\iint_S \vec{E}^i \times \vec{H}^{i^*} \cdot \hat{z} \cdot dS\right) = \\ &= \frac{1}{2}\cdot |a_i|^2 \cdot \mathrm{Re}\left(\iint_S \left(E_x^i \cdot H_y^{i^*} - H_x^{i^*} \cdot E_y^i\right) \cdot dS\right) = \frac{1}{2}\cdot |a_i|^2 \cdot \left(\iint_S \vec{E}^i \times \vec{H}^i \cdot \hat{z} \cdot dS\right) \end{aligned}$$

where the convention for the mode fields given by eqn. (2.12) has been applied, and

$$\begin{aligned} \hat{\vec{E}}(x,y,z) &= a_i \cdot \vec{E}^i(x,y) \\ \hat{\vec{H}}(x,y,z) &= a_i \cdot \vec{H}^i(x,y) \end{aligned}$$

being a_i the complex amplitude of the discrete spectrum mode.

Taking advantage of the normalization of the fields for the discrete spectrum modes (eqn. (2.25a)), the expression for the power carried by the i bound mode becomes:

$$P_i = \frac{1}{2}\cdot |a_i|^2 \cdot N_i \tag{2.28}$$

Regarding the continuous spectrum modes (or radiation modes), the total time-averaged power flow carried by them parallel to the waveguide axis can be calculated as:

$$P_{rad} = \frac{1}{2} \cdot \mathrm{Re}\left(\iint_S \hat{E}_{rad} \times \hat{H}_{rad}^{\ *} \cdot \hat{z} \cdot dS \right)$$

Expanding the total field of the continuous spectrum, $\hat{E}_{rad}$ and $\hat{H}_{rad}$, as a function of the continuous spectrum modes as in eqns. (2.22):

$$\hat{E}_{rad} = \sum_{i=-Q}^{Q} \int_0^{\infty} a_i(k_t) \cdot \bar{E}^i(x,y,k_t) \cdot dk_t$$

$$\hat{H}_{rad} = \sum_{i=-Q}^{Q} \int_0^{\infty} a_i(k_t) \cdot \bar{H}^i(x,y,k_t) \cdot dk_t$$

being $a_i(k_t)$ the complex amplitude of the continuous spectrum modes, applying the convention for the mode fields given by eqn. (2.12), and using the orthogonality and normalization conditions of eqns. (2.24c) and (2.25b), it can be obtained [SNY 83]:

$$P_{rad} = \sum_{i=-Q}^{Q} \int_0^{k_0} \frac{1}{2} \cdot \left| a_i(k_t) \right|^2 \cdot N_i(k_t) \cdot dk_t \qquad (2.29)$$

As it can be seen to calculate the power flow the integral is performed over the range $0 < k_t < k_0$, i.e. the range corresponding to the propagating or radiative modes. The range $k_0 < k_t < \infty$ is not included in the calculation because it corresponds to the attenuating or evanescent modes, which do not propagate power.

It is interesting to note that individual radiation modes, like bound modes, propagate energy parallel to the waveguide axis. The total radiated power (in the positive z direction) is the summed power of individual radiation modes, as expressed by eqn. (2.29). However, because of the interference between the fields of different radiation modes, the continuum of modes expressed by integral in eqn. (2.29), represents the expected behavior of the total radiation field, i.e. a flow of power away from the waveguide. Clearly, an individual radiation mode is not physically meaningful and is only a convenient building block for describing radiation mathematically.

The expressions for the power carried by the propagating modes, eqns. (2.28) and (2.29), reveal that in our case where the convention for the mode fields given by eqn. (2.12) has been taken, the normalization factors, N_i for the discrete spectrum modes, and $N_i(k_t)$ for the continuous spectrum modes in propagation, must be positive real numbers for $i > 0$ (forward propagating waves, and hence positive power flow), and negative real numbers for $i < 0$ (backward propagating waves, and hence negative power flow). This is coherent with the relationship that the normalization factors must satisfy, eqn. (2.26).

Regarding the total power carried by the open waveguide (in the increasing *z* direction), including the guided power and the radiated power, it is given by the total time-averaged Poynting vector integrated over the cross-section. Its value is:

$$P_{tot} = \frac{1}{2} \cdot \mathrm{Re}\left(\iint_S \hat{E}_{tot} \times \hat{H}_{tot}^{\;*} \cdot \hat{z} \cdot dS \right)$$

Expanding $\hat{E}_{tot}$ and $\hat{H}_{tot}$ as in eqns. (2.22), applying the convention for the mode fields given by eqn. (2.12), using the orthogonality and normalization conditions of eqns. (2.24) and (2.25), and recalling the definitions for the power carried by a bound mode (or discrete spectrum mode) of eqn. (2.28), and the power carried by the radiation modes (or continuous spectrum modes) of eqn. (2.29), we have that for our case of a nonabsorbing waveguide:

$$\begin{aligned} P_{tot} &= \sum_{i=-M}^{M} \frac{1}{2} \cdot \left|a_i\right|^2 \cdot N_i + \sum_{i=-Q}^{Q} \int_0^{k_0} \frac{1}{2} \cdot \left|a_i(k_t)\right|^2 \cdot N_i(k_t) \cdot dk_t = \\ &= \sum_{i=-M}^{M} P_i \; + \; P_{rad} \end{aligned} \qquad (2.30)$$

where the summations are performed for all the propagation modes, with both signs, and including the discrete spectrum modes and the propagating continuous spectrum modes. Thus, the total power carried by the open waveguide (in the increasing *z* direction) is equal to the power in all forward propagating modes, minus the power in all backward propagating modes (since the later will have a normalization factor with negative sign, and the power carried by them will be negative, i.e. in the opposite direction).

It is important to note that if we want to calculate the total power radiated by an open waveguide, we have to take into account the power radiated in the positive z direction and the power radiated in the negative z direction, and we have to count all of it as positive. For example, if a nonuniform open waveguide placed between *z*=0 and *z=L* is excited by bound modes at *z*=0 and is matched at *z=L*, then the total power lost in it due to radiation can be calculated as [MAR 91]:

$$
\begin{aligned}
P_{loss} = & \sum_{i=-Q}^{-1} \int_0^{k_0} \frac{1}{2} \cdot \left| a_i(k_t, z=0) \right|^2 \cdot \left| N_i(k_t, z=0) \right| \cdot dk_t + \\
& + \sum_{i=1}^{Q} \int_0^{k_0} \frac{1}{2} \cdot \left| a_i(k_t, z=L) \right|^2 \cdot N_i(k_t, z=L) \cdot dk_t
\end{aligned}
\qquad (2.31)
$$

where the modes with positive superscripts account for power outflow at $z=L$, and the modes with negative superscripts carry power away from the nonuniform waveguide through the plane at $z=0$.

2.2.3. Calculation of the modes

In the last sections we have studied the general form and properties of the modes of closed and open waveguides. However, when we have to solve an specific problem we have to calculate the exact expressions for the modes. Several techniques have been developed in order to calculate the modes of an specific waveguide. In general, if the problem is somewhat complex it will be necessary to resort to numerical methods.

If the cross-section of the waveguide is one-dimensional or two-dimensional and separable, the complete spectrum (including the discrete and continuous spectrum in the case of open waveguides) can be obtained using classical procedures, giving rise to more or less simple solutions, and even to analytical solutions in certain cases. [FRI 56], [FEL 73], [SHE 71].

If the waveguide cross-section is two-dimensional and non-separable, the application of the transverse resonance method in the spectral [ITO 80] or in the space domain [ROZ 87] or in the equivalent network form [KOS 86] can always, in principle, yield its discrete spectrum (for the case of closed and open waveguides).

Regarding the continuous spectrum of open waveguides with two-dimensional non-separable cross-section, to our knowledge there are very few approaches proposed to calculate it. One interesting method that could be used is proposed in [ROZ 92], [ROZ 97]. It constitutes a modified transverse resonance method to allow for the calculation of both, the continuous spectrum modes and the discrete spectrum modes.

The application of a similar method to calculate the continuous spectrum of open microstrip lines is developed in [ROZ 95], and to calculate the continuous spectrum of open slotlines is described in [ROZ 92a].

2.3. Nonuniform waveguides: mode coupling. Application of the cross-section method

As it is well known, in a loss-less waveguide that is uniform in the longitudinal direction, the modes propagate (or attenuate) along it independently, i.e. without transferring power between them. If the waveguide is, on the other hand, nonuniform in the longitudinal direction the modes will no longer propagate along it independently, but will transfer power between them. The mode coupling phenomenon will take place.

2.3.1. Waveguides with ε and μ variable in the propagation direction

Let us consider a straight waveguide, nonuniform in the propagation direction (the longitudinal direction), where ε and μ vary not only with x and y (in the transversal direction) but also with z (in the longitudinal direction). To start, it will be assumed that $\varepsilon(x,y,z)$ and $\mu(x,y,z)$ are functions that are continuous with z, i.e. that evolve with z without discontinuities. This condition can be expressed mathematically as:

$$\begin{aligned} &\varepsilon(x_0,y_0,z) \quad \text{continuous} \quad \forall\ (x_0,y_0)\in S \\ &\mu(x_0,y_0,z) \quad \text{continuous} \quad \forall\ (x_0,y_0)\in S \end{aligned} \tag{2.32}$$

where S is the surface of the waveguide cross-section.

We are going to study the propagation of electromagnetic waves along this waveguide using the coupled mode theory – the cross section method. According to the cross-section method, to describe the electromagnetic field in a nonuniform waveguide it is necessary to expand the field at each cross-section (z=constant) in a Fourier-like series of the modal fields of a reference waveguide. The reference waveguide will be a uniform waveguide where ε and μ are the same functions of the transversal coordinates x and y as in the corresponding cross-section of the nonuniform waveguide. Obviously, the reference waveguides are different for different values of the longitudinal coordinate z. Let us denote the coordinate system in this reference waveguide as x, y and ζ. Obviously, the fields of the reference waveguide modes depend on ζ appearing in the exponential factor $e^{-j\cdot\beta_i\cdot\zeta}$, but they depend also on z, since simultaneously the functions $\varepsilon(x,y)$ and $\mu(x,y)$ depend on z.

We are going to formulate the theory for open waveguides that are essentially constituted by a ground plane with perturbations (i.e. they are formed by a ground plane and customarily include a single dielectric and other conductors, and are surrounded by air). This case includes the microstrip line, the slotline, the coplanar waveguide... , and the structures produced by etching the ground plane in these planar technologies. Therefore, it includes all our cases of interest. For this kind of open waveguides the modal expansion of the fields has the following form in uniform waveguides and hence in a reference waveguide (see eqn. (2.22)):

$$\begin{aligned}\hat{E}(x,y,\zeta) &= \sum_{i=-M}^{M} A_i \cdot \vec{E}^i(x,y) \cdot e^{-j\cdot\beta_i\cdot\zeta} + \sum_{i=-Q}^{Q} \int_0^{\infty} A_i(k_t) \cdot \vec{E}^i(x,y,k_t) \cdot e^{-j\cdot\beta_i(k_t)\cdot\zeta} \cdot dk_t = \\ &= \sum_{i=-M}^{M} a_i \cdot \vec{E}^i(x,y) + \sum_{i=-Q}^{Q} \int_0^{\infty} a_i(k_t) \cdot \vec{E}^i(x,y,k_t) \cdot dk_t\end{aligned}$$

$$\begin{aligned}\hat{H}(x,y,\zeta) &= \sum_{i=-M}^{M} A_i \cdot \vec{H}^i(x,y) \cdot e^{-j\cdot\beta_i\cdot\zeta} + \sum_{i=-Q}^{Q} \int_0^{\infty} A_i(k_t) \cdot \vec{H}^i(x,y,k_t) \cdot e^{-j\cdot\beta_i(k_t)\cdot\zeta} \cdot dk_t = \\ &= \sum_{i=-M}^{M} a_i \cdot \vec{H}^i(x,y) + \sum_{i=-Q}^{Q} \int_0^{\infty} a_i(k_t) \cdot \vec{H}^i(x,y,k_t) \cdot dk_t\end{aligned}$$

where

$$k_t^2 = k_0^2 - \beta_i^2(k_t) \quad , \quad \text{with} \quad \beta_i(k_t) = +\sqrt{k_0^2 - k_t^2} \quad \text{for } i > 0$$

$$\beta_i(k_t) = -\sqrt{k_0^2 - k_t^2} \quad \text{for } i < 0$$

$$k_0 = \omega \cdot \sqrt{\mu_0 \cdot \varepsilon_0}$$

If we were interested in other types of open waveguides (like for example the dielectric rib waveguide or the optical fiber) the expansion corresponding to the continuous spectrum would have slightly different forms, although it would always include the integral of the mode fields over a continuous parameter (see section 2.2.2.1). If we were interested, on the other hand, in closed waveguides then the expansion of the fields would only include the modes of the discrete spectrum, resulting in a significantly simplified expression (see eqn. (2.15) and section 2.2.1.1). The modes will be orthogonal between them satisfying the orthogonality relations given by eqns. (2.23), and will be normalized following eqns. (2.25). Therefore they will satisfy also eqns. (2.27):

$$\iint_S \left(\left(\vec{E}^i \times \vec{H}^m \right) + \left(\vec{E}^m \times \vec{H}^i \right) \right) \cdot \hat{z} \cdot dS = \delta_{im} \cdot 2 \cdot N_i$$

$$\iint_S \left(\left(\vec{E}^i \times \vec{H}^m(k_t)\right) + \left(\vec{E}^m(k_t) \times \vec{H}^i\right)\right) \cdot \hat{z} \cdot dS = 0$$

$$\iint_S \left(\left(\vec{E}^i(k_t) \times \vec{H}^m(\widetilde{k}_t)\right) + \left(\vec{E}^m(\widetilde{k}_t) \times \vec{H}^i(k_t)\right)\right) \cdot \hat{z} \cdot dS = \delta_{im} \cdot \delta(k_t - \widetilde{k}_t) \cdot 2 \cdot N_i(k_t)$$

Let us represent the transversal components (components in the *x* and *y* directions) of the electromagnetic fields present in an arbitrary cross-section (fixed by *z*) of a straight nonuniform waveguide, as a linear combination of the transversal field components of the modes of an auxiliary uniform waveguide (reference waveguide) that has the same cross-section and identical distribution of ε and μ as the cross-section of interest. In this expansion only the modes propagating in the forward direction are needed.

$$\hat{E}_x(x,y,z) = \sum_{i=1}^{M} Q_i(z) \cdot E_x^i(x,y,z) + \sum_{i=1}^{Q} \int_0^\infty Q_i(k_t,z) \cdot E_x^i(x,y,k_t,z) \cdot dk_t$$

$$\hat{E}_y(x,y,z) = \sum_{i=1}^{M} Q_i(z) \cdot E_y^i(x,y,z) + \sum_{i=1}^{Q} \int_0^\infty Q_i(k_t,z) \cdot E_y^i(x,y,k_t,z) \cdot dk_t \qquad \text{(2.33a)}$$

$$\hat{H}_x(x,y,z) = \sum_{i=1}^{M} R_i(z) \cdot H_x^i(x,y,z) + \sum_{i=1}^{Q} \int_0^\infty R_i(k_t,z) \cdot H_x^i(x,y,k_t,z) \cdot dk_t$$

$$\hat{H}_y(x,y,z) = \sum_{i=1}^{M} R_i(z) \cdot H_y^i(x,y,z) + \sum_{i=1}^{Q} \int_0^\infty R_i(k_t,z) \cdot H_y^i(x,y,k_t,z) \cdot dk_t \qquad \text{(2.33b)}$$

Let's recall that in our notation $\hat{\vec{E}} = \hat{E}_x \cdot \vec{x} + \hat{E}_y \cdot \vec{y} + \hat{E}_z \cdot \vec{z}$ is the total field present, and $\vec{E}^i = E_x^i \cdot \vec{x} + E_y^i \cdot \vec{y} + E_z^i \cdot \vec{z}$ is the (*x,y*) dependent part of the field of the *i* mode.

Since the cross-section (and hence the reference waveguide) varies with *z*, the values for Q_i , $Q_i(k_t)$, R_i , $R_i(k_t)$, $E_x^i(x,y)$, $E_y^i(x,y)$, $E_x^i(x,y,k_t)$, $E_y^i(x,y,k_t)$, $H_x^i(x,y)$, $H_y^i(x,y)$, $H_x^i(x,y,k_t)$, $H_y^i(x,y,k_t)$ depend also on *z*. The expansion that we have done is possible since the fields in a cross-section of a nonuniform waveguide where $\varepsilon(x,y,z)$ and $\mu(x,y,z)$ are functions continuous with *z,* and the fields in the reference waveguide (that is uniform and has the same cross-section with identical distribution of ε and μ) see the same medium and satisfy the same boundary conditions. Consequently, the modal fields of the reference waveguide can be used as a base to expand the fields present in the cross-section of the nonuniform waveguide.

Let us introduce new coefficients for the expansion, related to the previous ones in the following way:

$$\begin{aligned} Q_i &= a_i - a_{-i} \quad ; \quad Q_i(k_t) = a_i(k_t) - a_{-i}(k_t) \\ R_i &= a_i + a_{-i} \quad ; \quad R_i(k_t) = a_i(k_t) + a_{-i}(k_t) \end{aligned} \tag{2.34}$$

Using the new coefficients and taking into account the relation between the fields of the forward and backward travelling waves associated to the same *i* mode and given by eqn. (2.14), the expansions of eqns. (2.33) can be rewritten as:

$$\begin{aligned} \hat{E}_x(x,y,z) &= \sum_{i=-M}^{M} a_i(z) \cdot E_x^i(x,y,z) + \sum_{i=-Q}^{Q} \int_0^{\infty} a_i(k_t,z) \cdot E_x^i(x,y,k_t,z) \cdot dk_t \\ \hat{E}_y(x,y,z) &= \sum_{i=-M}^{M} a_i(z) \cdot E_y^i(x,y,z) + \sum_{i=-Q}^{Q} \int_0^{\infty} a_i(k_t,z) \cdot E_y^i(x,y,k_t,z) \cdot dk_t \end{aligned} \tag{2.35a}$$

$$\begin{aligned} \hat{H}_x(x,y,z) &= \sum_{i=-M}^{M} a_i(z) \cdot H_x^i(x,y,z) + \sum_{i=-Q}^{Q} \int_0^{\infty} a_i(k_t,z) \cdot H_x^i(x,y,k_t,z) \cdot dk_t \\ \hat{H}_y(x,y,z) &= \sum_{i=-M}^{M} a_i(z) \cdot H_y^i(x,y,z) + \sum_{i=-Q}^{Q} \int_0^{\infty} a_i(k_t,z) \cdot H_y^i(x,y,k_t,z) \cdot dk_t \end{aligned} \tag{2.35b}$$

As it can be seen the last equations, unlike eqns. (2.33), contain forward and backward travelling waves. Moreover, all of them have the same expansion coefficients, including the expressions for the electric and magnetic fields.

The functions employed in the expansion in eqns. (2.35) (mode fields of the reference waveguide) satisfy in the cross-section the same boundary conditions as the fields of the nonuniform waveguide that they represent, and therefore the series will converge to the field that it represents in all the points of the cross-section. As a result, the term by term differentiation of the series can be done without problems.

Let us develop the third and forth Maxwell equations, eqns. (2.4), into their components:

$$\frac{\partial E_z}{\partial y} - \frac{\partial E_y}{\partial z} = -j \cdot \omega \cdot \mu \cdot H_x \tag{2.36a}$$

$$\frac{\partial E_x}{\partial z} - \frac{\partial E_z}{\partial x} = -j \cdot \omega \cdot \mu \cdot H_y \tag{2.36b}$$

$$\frac{\partial E_y}{\partial x} - \frac{\partial E_x}{\partial y} = -j \cdot \omega \cdot \mu \cdot H_z \tag{2.36c}$$

$$\frac{\partial H_z}{\partial y} - \frac{\partial H_y}{\partial z} = j \cdot \omega \cdot \varepsilon \cdot E_x \tag{2.36d}$$

$$\frac{\partial H_x}{\partial z}-\frac{\partial H_z}{\partial x}=j\cdot\omega\cdot\varepsilon\cdot E_y \tag{2.36e}$$

$$\frac{\partial H_y}{\partial x}-\frac{\partial H_x}{\partial y}=j\cdot\omega\cdot\varepsilon\cdot E_z \tag{2.36f}$$

Substituting eqns. (2.35a) into the third component of the third Maxwell equation, eqn. (2.36c), differentiating the series term by term, commuting the spatial derivatives with the integration in k_t and comparing the result with the third expression of eqns. (2.9) it is obtained that:

$$\hat{H}_z(x,y,z)=\sum_{i=-M}^{M}a_i(z)\cdot H_z^i(x,y,z)+\sum_{i=-Q}^{Q}\int_0^\infty a_i(k_t,z)\cdot H_z^i(x,y,k_t,z)\cdot dk_t \tag{2.37a}$$

In the same way, substituting eqns. (2.35b) into the third component of the fourth Maxwell equation, eqn. (2.36f), differentiating the series term by term, commuting the spatial derivatives with the integration in k_t and comparing the result with the third expression of eqns. (2.10) it is obtained:

$$\hat{E}_z(x,y,z)=\sum_{i=-M}^{M}a_i(z)\cdot E_z^i(x,y,z)+\sum_{i=-Q}^{Q}\int_0^\infty a_i(k_t,z)\cdot E_z^i(x,y,k_t,z)\cdot dk_t \tag{2.37b}$$

The last two equations, eqns. (2.37), are the expansions for the longitudinal field components which are similar to the expansions for the transversal field components previously calculated, eqns. (2.35), and have the same expansion coefficients, $a_i(z)$, $a_i(k_t,z)$. In this way, we can consider $a_i(z)$, $a_i(k_t,z)$ as the complex amplitudes of the modes in the given nonuniform waveguide.

2.3.1.1. Coupled mode equations and coupling coefficients

Let's continue our study deducing the coupled mode equations, i.e. the equations for the complex amplitudes $a_i(z)$, $a_i(k_t,z)$ in the nonuniform waveguide. In first place we are going to substitute eqns. (2.35) and (2.37) into eqn. (2.36a). Differentiating the series term by term, and commuting the spatial derivatives with the integration in k_t, it is obtained:

$$\begin{aligned}
&\sum_{i=-M}^{M} a_i \cdot \frac{\partial E_z^i}{\partial y} + \sum_{i=-Q}^{Q}\int_0^\infty a_i(k_t)\cdot\frac{\partial E_z^i(k_t)}{\partial y}\cdot dk_t - \sum_{i=-M}^{M}\left(\frac{da_i}{dz}\cdot E_y^i + a_i\cdot\frac{\partial E_y^i}{\partial z}\right) - \\
&\qquad - \sum_{i=-Q}^{Q}\int_0^\infty\left(\frac{da_i(k_t)}{dz}\cdot E_y^i(k_t)+a_i(k_t)\cdot\frac{\partial E_y^i(k_t)}{\partial z}\right)\cdot dk_t = \\
&\qquad = -j\cdot\omega\cdot\mu\cdot\left(\sum_{i=-M}^{M} a_i\cdot H_x^i + \sum_{i=-Q}^{Q}\int_0^\infty a_i(k_t)\cdot H_x^i(k_t)\cdot dk_t\right)
\end{aligned}$$

Using the first formula of eqns. (2.9), the term to the right of the equality sign becomes:

$$\sum_{i=-M}^{M} a_i\cdot\left(\frac{\partial E_z^i}{\partial y}+j\cdot\beta_i\cdot E_y^i\right)+\sum_{i=-Q}^{Q}\int_0^\infty a_i(k_t)\cdot\left(\frac{\partial E_z^i(k_t)}{\partial y}+j\cdot\beta_i(k_t)\cdot E_y^i(k_t)\right)\cdot dk_t$$

and reorganizing the terms of the equality it can be finally rewritten as:

$$\begin{aligned}
&-\sum_{i=-M}^{M}\left(\frac{da_i}{dz}+j\cdot\beta_i\cdot a_i\right)\cdot E_y^i-\sum_{i=-Q}^{Q}\int_0^\infty\left(\frac{da_i(k_t)}{dz}+j\cdot\beta_i(k_t)\cdot a_i(k_t)\right)\cdot E_y^i(k_t)\cdot dk_t = \\
&\qquad = \sum_{i=-M}^{M} a_i\cdot\frac{\partial E_y^i}{\partial z}+\sum_{i=-Q}^{Q}\int_0^\infty a_i(k_t)\cdot\frac{\partial E_y^i(k_t)}{\partial z}\cdot dk_t
\end{aligned} \tag{2.38}$$

In the same way, substituting eqns. (2.35) and (2.37) into eqn. (2.36b), differentiating the series term by term, commuting the spatial derivatives with the integration in k_t, and using the second formula of eqns. (2.9), it is obtained:

$$\begin{aligned}
&-\sum_{i=-M}^{M}\left(\frac{da_i}{dz}+j\cdot\beta_i\cdot a_i\right)\cdot E_x^i-\sum_{i=-Q}^{Q}\int_0^\infty\left(\frac{da_i(k_t)}{dz}+j\cdot\beta_i(k_t)\cdot a_i(k_t)\right)\cdot E_x^i(k_t)\cdot dk_t = \\
&\qquad = \sum_{i=-M}^{M} a_i\cdot\frac{\partial E_x^i}{\partial z}+\sum_{i=-Q}^{Q}\int_0^\infty a_i(k_t)\cdot\frac{\partial E_x^i(k_t)}{\partial z}\cdot dk_t
\end{aligned} \tag{2.39}$$

Analogously, substituting eqns. (2.35) and (2.37) into eqn. (2.36d), differentiating the series term by term, commuting the spatial derivatives with the integration in k_t, and using the first formula of eqns. (2.10), it is obtained:

$$-\sum_{i=-M}^{M}\left(\frac{da_i}{dz}+j\cdot\beta_i\cdot a_i\right)\cdot H_y^i-\sum_{i=-Q}^{Q}\int_0^{\infty}\left(\frac{da_i(k_t)}{dz}+j\cdot\beta_i(k_t)\cdot a_i(k_t)\right)\cdot H_y^i(k_t)\cdot dk_t = \\ =\sum_{i=-M}^{M}a_i\cdot\frac{\partial H_y^i}{\partial z}+\sum_{i=-Q}^{Q}\int_0^{\infty}a_i(k_t)\cdot\frac{\partial H_y^i(k_t)}{\partial z}\cdot dk_t \tag{2.40}$$

And to finish, substituting eqns. (2.35) and (2.37) into eqn. (2.36e), differentiating the series term by term, commuting the spatial derivatives with the integration in k_t, and using the second formula of eqns. (2.10), it is obtained:

$$-\sum_{i=-M}^{M}\left(\frac{da_i}{dz}+j\cdot\beta_i\cdot a_i\right)\cdot H_x^i-\sum_{i=-Q}^{Q}\int_0^{\infty}\left(\frac{da_i(k_t)}{dz}+j\cdot\beta_i(k_t)\cdot a_i(k_t)\right)\cdot H_x^i(k_t)\cdot dk_t = \\ =\sum_{i=-M}^{M}a_i\cdot\frac{\partial H_x^i}{\partial z}+\sum_{i=-Q}^{Q}\int_0^{\infty}a_i(k_t)\cdot\frac{\partial H_x^i(k_t)}{\partial z}\cdot dk_t \tag{2.41}$$

To deduce the coupled mode equations let us multiply eqns. (2.38), (2.39), (2.40), (2.41) by $-H_x^m, H_y^m, E_x^m, -E_y^m$, respectively. The equations obtained are added, and the final result is integrated over the cross section obtaining:

$$-\iint_S\left[\sum_{i=-M}^{M}\left(\frac{da_i}{dz}+j\cdot\beta_i\cdot a_i\right)\cdot\left(-H_x^m\cdot E_y^i+H_y^m\cdot E_x^i+E_x^m\cdot H_y^i-E_y^m\cdot H_x^i\right)+\right. \\ +\sum_{i=-Q}^{Q}\int_0^{\infty}\left(\frac{da_i(k_t)}{dz}+j\cdot\beta_i(k_t)\cdot a_i(k_t)\right)\cdot\left(-H_x^m\cdot E_y^i(k_t)+H_y^m\cdot E_x^i(k_t)+\right. \\ \left.\left.+E_x^m\cdot H_y^i(k_t)-E_y^m\cdot H_x^i(k_t)\right)\cdot dk_t\right]\cdot dS =$$

$$=\iint_S\left[\sum_{i=-M}^{M}a_i\cdot\left(-H_x^m\cdot\frac{\partial E_y^i}{\partial z}+H_y^m\cdot\frac{\partial E_x^i}{\partial z}+E_x^m\cdot\frac{\partial H_y^i}{\partial z}-E_y^m\cdot\frac{\partial H_x^i}{\partial z}\right)+\right. \\ +\sum_{i=-Q}^{Q}\int_0^{\infty}a_i(k_t)\cdot\left(-H_x^m\cdot\frac{\partial E_y^i(k_t)}{\partial z}+H_y^m\cdot\frac{\partial E_x^i(k_t)}{\partial z}+\right. \\ \left.\left.+E_x^m\cdot\frac{\partial H_y^i(k_t)}{\partial z}-E_y^m\cdot\frac{\partial H_x^i(k_t)}{\partial z}\right)\cdot dk_t\right]\cdot dS$$

Taking into account the normalization and the orthogonality relations that are verified between the mode fields, eqns. (2.27), integrating the series term by term, and commuting the surface integral with the integral in k_t, the last equation can be rewritten as:

$$\begin{aligned}-\left(\frac{da_m}{dz}+j\cdot\beta_m\cdot a_m\right)\cdot 2\cdot N_m=\sum_{i=-M}^{M}a_i\cdot\left(-C_{mi}\cdot 2\cdot N_m\right)+&\\+\sum_{i=-Q}^{Q}\int_0^{\infty}a_i(k_t)\cdot\left(-C_{mi}(k_t)\cdot 2\cdot N_m\right)\cdot dk_t&\end{aligned}\tag{2.42}$$

where the new variables introduced C_{mi} , $C_{mi}(k_t)$, are known as the coupling coefficients, and have the following expressions:

$$C_{mi}=\frac{-1}{2\cdot N_m}\cdot\iint_S\left(-H_x^m\cdot\frac{\partial E_y^i}{\partial z}+H_y^m\cdot\frac{\partial E_x^i}{\partial z}+E_x^m\cdot\frac{\partial H_y^i}{\partial z}-E_y^m\cdot\frac{\partial H_x^i}{\partial z}\right)\cdot dS$$

$$C_{mi}(k_t)=\frac{-1}{2\cdot N_m}\cdot\iint_S\left(-H_x^m\cdot\frac{\partial E_y^i(k_t)}{\partial z}+H_y^m\cdot\frac{\partial E_x^i(k_t)}{\partial z}+E_x^m\cdot\frac{\partial H_y^i(k_t)}{\partial z}-E_y^m\cdot\frac{\partial H_x^i(k_t)}{\partial z}\right)\cdot dS$$

It is important to note that the surface integral of the orthogonality conditions is developed in the following way to be used here:

$$\iint_S\left(\left(\vec{E}^i\times\vec{H}^m\right)+\left(\vec{E}^m\times\vec{H}^i\right)\right)\cdot\hat{z}\cdot dS=\iint_S\left(-H_x^m\cdot E_y^i+H_y^m\cdot E_x^i+E_x^m\cdot H_y^i-E_y^m\cdot H_x^i\right)\cdot dS$$

Conversely, the surface integral of the coupling coefficients can be expressed as:

$$\begin{aligned}\iint_S\left(-H_x^m\cdot\frac{\partial E_y^i}{\partial z}+H_y^m\cdot\frac{\partial E_x^i}{\partial z}+E_x^m\cdot\frac{\partial H_y^i}{\partial z}-E_y^m\cdot\frac{\partial H_x^i}{\partial z}\right)\cdot dS=&\\=\iint_S\left(\frac{\partial\vec{E}^i}{\partial z}\times\vec{H}^m+\vec{E}^m\times\frac{\partial\vec{H}^i}{\partial z}\right)\cdot\hat{z}\cdot dS&\end{aligned}$$

Reorganizing the terms of eqn. (2.42), the following coupled mode equation is obtained:

$$\frac{da_m}{dz}+j\cdot\beta_m\cdot a_m=\sum_{i=-M}^{M}a_i\cdot C_{mi}+\sum_{i=-Q}^{Q}\int_0^{\infty}a_i(k_t)\cdot C_{mi}(k_t)\cdot dk_t\tag{2.43}$$

This expression is valid for any *m*, i.e. for any mode of the discrete spectrum, and therefore we will have a set of coupled mode equations like this for the modes of the discrete spectrum.

Let’s deduce now a similar expression for the modes of the continuous spectrum. To do it, we are going to proceed in the same way previously explained but multiplying eqns. (2.38), (2.39), (2.40), (2.41) by $-H_x^n(\tilde{k}_t), H_y^n(\tilde{k}_t), E_x^n(\tilde{k}_t), -E_y^n(\tilde{k}_t)$, respectively. Adding the equations obtained, integrating the result over the cross section, integrating the series term by term, commuting the surface integral with the integral in k_t , and taking into account the normalization and the orthogonality relations that are verified between the mode fields, eqns. (2.27), the following coupled mode equation is obtained:

$$\frac{da_n(\tilde{k}_t)}{dz} + j \cdot \beta_n(\tilde{k}_t) \cdot a_n(\tilde{k}_t) = \sum_{i=-M}^{M} a_i \cdot C_{ni}^c(\tilde{k}_t) + \sum_{i=-Q}^{Q} \int_0^\infty a_i(k_t) \cdot C_{ni}^c(\tilde{k}_t, k_t) \cdot dk_t \qquad (2.44)$$

where the new variables introduced $C_{ni}^c(\tilde{k}_t), C_{ni}^c(\tilde{k}_t, k_t)$, are the corresponding coupling coefficients. Their explicit expression are given in eqns. (2.45).

This expression is valid for any *n* and $\tilde{k}_t$, i.e. for any mode of the continuous spectrum, and therefore we will have a set of coupled mode equations like this for the modes of the continuous spectrum.

Summing up, an open straight waveguide that is nonuniform in the propagation direction can be characterized (using the coupled mode theory – the cross-section method) by a set of coupled mode equations that have the following form:

$$\frac{da_m}{dz} + j \cdot \beta_m \cdot a_m = \sum_{i=-M}^{M} a_i \cdot C_{mi} + \sum_{i=-Q}^{Q} \int_0^\infty a_i(k_t) \cdot C_{mi}(k_t) \cdot dk_t \qquad (2.43)$$

$$\frac{da_n(\tilde{k}_t)}{dz} + j \cdot \beta_n(\tilde{k}_t) \cdot a_n(\tilde{k}_t) = \sum_{i=-M}^{M} a_i \cdot C_{ni}^c(\tilde{k}_t) + \sum_{i=-Q}^{Q} \int_0^\infty a_i(k_t) \cdot C_{ni}^c(\tilde{k}_t, k_t) \cdot dk_t \qquad (2.44)$$

Eqn. (2.43) is valid for any *m*, i.e. for any mode of the discrete spectrum, and eqn. (2.44) is valid for any *n* and $\tilde{k}_t$, i.e. for any mode of the continuous spectrum. Therefore a set of coupled mode equations like these will exist for the modes of the open waveguide, constituting a system of integro-differential equations.

Regarding the coupling coefficients, they will have the following expressions:

$$C_{mi} = \frac{-1}{2 \cdot N_m} \cdot \iint_S \left(-H_x^m \cdot \frac{\partial E_y^i}{\partial z} + H_y^m \cdot \frac{\partial E_x^i}{\partial z} + E_x^m \cdot \frac{\partial H_y^i}{\partial z} - E_y^m \cdot \frac{\partial H_x^i}{\partial z} \right) \cdot dS \qquad (2.45)$$

$$C_{mi}(k_t) = \frac{-1}{2 \cdot N_m} \cdot \iint_S \left(-H_x^m \cdot \frac{\partial E_y^i(k_t)}{\partial z} + H_y^m \cdot \frac{\partial E_x^i(k_t)}{\partial z} + E_x^m \cdot \frac{\partial H_y^i(k_t)}{\partial z} - E_y^m \cdot \frac{\partial H_x^i(k_t)}{\partial z} \right) \cdot dS$$

$$C_{ni}^c(\tilde{k}_t) = \frac{-1}{2 \cdot N_n(\tilde{k}_t)} \cdot \iint_S \left(-H_x^n(\tilde{k}_t) \cdot \frac{\partial E_y^i}{\partial z} + H_y^n(\tilde{k}_t) \cdot \frac{\partial E_x^i}{\partial z} + E_x^n(\tilde{k}_t) \cdot \frac{\partial H_y^i}{\partial z} - E_y^n(\tilde{k}_t) \cdot \frac{\partial H_x^i}{\partial z} \right) \cdot dS$$

$$\begin{aligned} C_{ni}^c(\tilde{k}_t, k_t) = \frac{-1}{2 \cdot N_n(\tilde{k}_t)} \cdot \iint_S \Bigg(& -H_x^n(\tilde{k}_t) \cdot \frac{\partial E_y^i(k_t)}{\partial z} + H_y^n(\tilde{k}_t) \cdot \frac{\partial E_x^i(k_t)}{\partial z} + \\ & + E_x^n(\tilde{k}_t) \cdot \frac{\partial H_y^i(k_t)}{\partial z} - E_y^n(\tilde{k}_t) \cdot \frac{\partial H_x^i(k_t)}{\partial z} \Bigg) \cdot dS \end{aligned}$$

As it can be seen, the expressions for all the coupling coefficients have identical form. Actually all of them can be represented in a generic way as C_{mi} (eqn. 2.45), assuming that for a mode of the continuous spectrum its index (*m* or *i*) contains the information of the index and of the k_t parameter.

It is interesting to note that the expression for the coupling coefficients can be also rewritten as:

$$C_{mi} = \frac{-1}{2 \cdot N_m} \cdot \iint_S \left(\frac{\partial \vec{E}^i}{\partial z} \times \vec{H}^m + \vec{E}^m \times \frac{\partial \vec{H}^i}{\partial z} \right) \cdot \hat{z} \cdot dS \qquad (2.46)$$

As it was previously stated, the values for $a_i(z)$, $a_i(k_t,z)$, can be seen as the complex amplitudes of the *i* discrete spectrum mode, and of the (i , k_t) continuous spectrum mode, respectively, in the nonuniform waveguide. They replace the $e^{-j \cdot \beta_i \cdot z}$ (or $e^{-j \cdot \beta_i(k_t) \cdot z}$) factor in a straight waveguide. However, they vary along the waveguide in a more complicated way. Following eqns. (2.43) and (2.44), the variation of $a_i(z)$, $a_i(k_t,z)$ against the variation of *z* depends on the amplitudes of all the modes existing at the given value of *z*. The contribution of each mode amplitude to the variation of $a_i(z)$, $a_i(k_t,z)$ with *z*, increases with the increasing coefficient C_{mi} . For this reason the values C_{mi} are known as the coupling coefficients between the modes *i* and *m*.

In order to solve the system of coupled mode equations, boundary conditions must be imposed on the complex amplitudes of the modes, $a_i(z)$, $a_i(k_t,z)$. If the nonuniform waveguide under study of length *L* is connected between two uniform waveguides at $z=0$ and $z=L$, and there is an incident mode (of the discrete spectrum) with index *m* and unitary amplitude from the left-hand side uniform waveguide, then the boundary conditions will be the following:

$$\begin{aligned}
&a_m(z=0)=1\\
&a_i(z=0)=0 \quad \forall i>0 \text{ and } i\neq m\\
&a_i(z=0,k_t)=0 \quad \forall i>0\\
&a_i(z=L)=0 \quad \forall i<0\\
&a_i(z=L,k_t)=0 \quad \forall i<0
\end{aligned} \tag{2.47}$$

If the waveguide of interest were a closed waveguide, then only the modes of the discrete spectrum would exist. In that case, the coupled mode equations would be much simpler, and they would have the form of eqn. (2.43), but without the last term (the term related to the modes of the continuous spectrum).Thus the coupled mode equations would form a first-order ordinary differential equation system, with the coupling coefficients given by eqn. (2.45), [KAT 98].

2.3.1.2. Properties of the coupling coefficients

As it was seen in the previous section, the expressions for all the coupling coefficients have identical form. Actually all of them can be represented in a generic way as C_{mi} (eqn. 2.45), assuming that for a mode of the continuous spectrum its index (*m* or *i*) contains the information of the index and of the k_t parameter. Several simple properties can be deduced from the general expression for the coupling coefficients, eqn. (2.45).

In first place we are going to start from the normalization equation for the fields of the *m* mode, eqn. (2.25). Using the field components it can be rewritten as:

$$\iint_S \left(E_x^m \cdot H_y^m - E_y^m \cdot H_x^m\right) \cdot dS = N_m$$

Deriving the identity by *z* we obtain:

$$\iint_S \left(\frac{\partial E_x^m}{\partial z} \cdot H_y^m + E_x^m \cdot \frac{\partial H_y^m}{\partial z} - \frac{\partial E_y^m}{\partial z} \cdot H_x^m - E_y^m \cdot \frac{\partial H_x^m}{\partial z}\right) \cdot dS = \frac{dN_m}{dz} \tag{2.48}$$

This derivation has been performed for the integrand only, since the surface of integration is the same for all *z*: the infinite cross-section (excluding the metal areas). (Let’s recall that in this case only the dielectrics are nonuniform in the propagation direction. The metals have constant cross-section).

Introducing eqn. (2.48) in the coupling coefficient expression (2.45) it can be seen that:

$$C_{mm} = \frac{-1}{2 \cdot N_m} \cdot \frac{dN_m}{dz} \tag{2.49}$$

If the mode of interest is a mode of the continuous spectrum, the expression for the coupling coefficient will be slightly different this time. This happens because the normalization equation is slightly different for the modes of the continuous spectrum (eqn. (2.25)), and can be written using the field components as:

$$\iint_S \left(E_x^m(k_t) \cdot H_y^m(\tilde{k}_t) - E_y^m(k_t) \cdot H_x^m(\tilde{k}_t) \right) \cdot dS = N_m(k_t) \cdot \delta(k_t - \tilde{k}_t)$$

Consequently the coupling coefficient $C_{mm}^c\left(\tilde{k}_t, \tilde{k}_t\right)$ will have the value:

$$C_{mm}^c(\tilde{k}_t, \tilde{k}_t) = \frac{-1}{2 \cdot N_m(\tilde{k}_t)} \cdot \frac{dN_m(\tilde{k}_t)}{dz} \cdot \delta(0) \tag{2.50}$$

On the other hand, starting from the orthogonality expression for the mode fields, eqn. (2.23), and writing it using the field components we have:

$$\iint_S \left(-H_x^m \cdot E_y^i + H_y^m \cdot E_x^i + E_x^m \cdot H_y^i - E_y^m \cdot H_x^i \right) \cdot dS = 0 \qquad ; \quad m \neq i$$

Performing the derivation by z of the orthogonality expression and identifying the obtained integrals with those of the coupling coefficients, eqn. (2.45), we have:

$$C_{mi} \cdot 2 \cdot N_m + C_{im} \cdot 2 \cdot N_i = 0 \qquad ; \qquad m \neq i$$

and reorganizing:

$$C_{mi} \cdot N_m = -C_{im} \cdot N_i \qquad ; \qquad \mathrm{m} \neq \mathrm{i} \tag{2.51}$$

Finally, taking into account the relation between the fields of the forward and backward travelling waves associated to the same i mode, eqn. (2.14), and between their normalizations, eqn. (2.26), and introducing them into the coupling coefficient expression, eqn. (2.45), it can be seen that:

$$C_{mi} = C_{-m,-i} \tag{2.52}$$

It is interesting to note that eqns. (2.49) (and (2.50)) and (2.51) allow us to verify that the coupled mode equations, eqns. (2.43), (2.44), satisfy the requirements of energy conservation principle. This principle states that if ε and μ are real (i.e. if the waveguide has no dissipative losses), then for any electromagnetic field in a nonuniform waveguide the following expression has to be constant (with z):

$$P_{tot} = \sum_{i=-M}^{M} \frac{1}{2} \cdot |a_i|^2 \cdot N_i + \sum_{i=-Q}^{Q} \int_0^{k_0} \frac{1}{2} \cdot |a_i(k_t)|^2 \cdot N_i(k_t) \cdot dk_t$$

As it was seen in section (2.2.2.3), eqn. (2.30), this expression represents the total power carried by the open waveguide (in the increasing z direction), including the guided power and the radiated power, and must be constant if the waveguide has no dissipative losses.

2.3.1.3. Practical form of the coupling coefficients

As it was previously commented the expressions for all the coupling coefficients have identical form. Actually all of them can be represented in a generic way as C_{mi} (eqn. (2.45)), assuming that for a mode of the continuous spectrum its index (m or i) contains the information of the index and of the k_t parameter. However, the expression obtained for the coupling coefficients, eqn. (2.45), is not easy to employ in practical engineering problems. In this section we are going to deduce a more practical expression for the coupling coefficients, that will contain the z derivatives of ε and μ instead of the fields derivatives contained in eqn. (2.45).

Let us write the third and fourth Maxwell equations (eqns. (2.4)) for the $\hat{\vec{E}}^i$ and $\hat{\vec{H}}^i$ fields in the uniform reference waveguide, employing the variables x, y, ζ.

$$\nabla \times \hat{\vec{E}}^i = -j \cdot \omega \cdot \mu \cdot \hat{\vec{H}}^i$$
$$\nabla \times \hat{\vec{H}}^i = j \cdot \omega \cdot \varepsilon \cdot \hat{\vec{E}}^i$$

In these equations $\hat{\vec{E}}^i$, $\hat{\vec{H}}^i$, β_i, $\vec{E}^i$, $\vec{H}^i$, as well as ε and μ depend on z, since they depend on the uniform reference waveguide to which they correspond (let's recall that z is the longitudinal coordinate in the nonuniform waveguide under study). It is interesting to note that the unitary vectors $\hat{\zeta}$ and $\hat{z}$ will have identical value (unitary modulus and the same direction).

Let's calculate the derivatives by z of these equations:

$$\begin{aligned} \nabla \times \frac{\partial \hat{\vec{E}}^i}{\partial z} &= -j \cdot \omega \cdot \frac{\partial \mu}{\partial z} \cdot \hat{\vec{H}}^i - j \cdot \omega \cdot \mu \cdot \frac{\partial \hat{\vec{H}}^i}{\partial z} \\ \nabla \times \frac{\partial \hat{\vec{H}}^i}{\partial z} &= j \cdot \omega \cdot \frac{\partial \varepsilon}{\partial z} \cdot \hat{\vec{E}}^i + j \cdot \omega \cdot \varepsilon \cdot \frac{\partial \hat{\vec{E}}^i}{\partial z} \end{aligned} \tag{2.53}$$

Let's see now the value of the derivatives by z of the fields:

$$\begin{aligned}
&\hat{\vec{E}}^i = \vec{E}^i \cdot e^{-j\cdot\beta_i\cdot\zeta} \Rightarrow \frac{\partial\hat{\vec{E}}^i}{\partial z} = \left(\frac{\partial\vec{E}^i}{\partial z} - j\cdot\frac{\partial\beta_i}{\partial z}\cdot\zeta\cdot\vec{E}^i\right)\cdot e^{-j\cdot\beta_i\cdot\zeta}\\
&\hat{\vec{H}}^i = \vec{H}^i \cdot e^{-j\cdot\beta_i\cdot\zeta} \Rightarrow \frac{\partial\hat{\vec{H}}^i}{\partial z} = \left(\frac{\partial\vec{H}^i}{\partial z} - j\cdot\frac{\partial\beta_i}{\partial z}\cdot\zeta\cdot\vec{H}^i\right)\cdot e^{-j\cdot\beta_i\cdot\zeta}
\end{aligned} \tag{2.54}$$

We multiply eqns. (2.53) by $-\hat{\vec{H}}^{-m}$ and $-\hat{\vec{E}}^{-m}$, respectively. In the same way the third and fourth Maxwell equations (eqns. (2.4)) written for $\hat{\vec{E}}^{-m}$ and $\hat{\vec{H}}^{-m}$ are multiplied by $\partial\hat{\vec{H}}^i/\partial z$ and $\partial\hat{\vec{E}}^i/\partial z$, respectively. Adding the four resulting equations, the following equality is obtained:

$$\begin{array}{l}
\nabla\times\dfrac{\partial\hat{\vec{E}}^i}{\partial z}\cdot\left(-\hat{\vec{H}}^{-m}\right) = -j\cdot\omega\cdot\dfrac{\partial\mu}{\partial z}\cdot\hat{\vec{H}}^i\cdot\left(-\hat{\vec{H}}^{-m}\right) - j\cdot\omega\cdot\mu\cdot\dfrac{\partial\hat{\vec{H}}^i}{\partial z}\cdot\left(-\hat{\vec{H}}^{-m}\right)\\
\nabla\times\dfrac{\partial\hat{\vec{H}}^i}{\partial z}\cdot\left(-\hat{\vec{E}}^{-m}\right) = j\cdot\omega\cdot\dfrac{\partial\varepsilon}{\partial z}\cdot\hat{\vec{E}}^i\cdot\left(-\hat{\vec{E}}^{-m}\right) + j\cdot\omega\cdot\varepsilon\cdot\dfrac{\partial\hat{\vec{E}}^i}{\partial z}\cdot\left(-\hat{\vec{E}}^{-m}\right)\\
\nabla\times\hat{\vec{E}}^{-m}\cdot\left(\dfrac{\partial\hat{\vec{H}}^i}{\partial z}\right) = -j\cdot\omega\cdot\mu\cdot\hat{\vec{H}}^{-m}\cdot\left(\dfrac{\partial\hat{\vec{H}}^i}{\partial z}\right)\\
\nabla\times\hat{\vec{H}}^{-m}\cdot\left(\dfrac{\partial\hat{\vec{E}}^i}{\partial z}\right) = j\cdot\omega\cdot\varepsilon\cdot\hat{\vec{E}}^{-m}\cdot\left(\dfrac{\partial\hat{\vec{E}}^i}{\partial z}\right)\\
\hline
\end{array}$$

$$\begin{aligned}
&-\nabla\times\frac{\partial\hat{\vec{E}}^i}{\partial z}\cdot\left(\hat{\vec{H}}^{-m}\right) - \nabla\times\frac{\partial\hat{\vec{H}}^i}{\partial z}\cdot\left(\hat{\vec{E}}^{-m}\right) + \nabla\times\hat{\vec{E}}^{-m}\cdot\left(\frac{\partial\hat{\vec{H}}^i}{\partial z}\right) + \nabla\times\hat{\vec{H}}^{-m}\cdot\left(\frac{\partial\hat{\vec{E}}^i}{\partial z}\right) =\\
&\qquad = j\cdot\omega\cdot\frac{\partial\mu}{\partial z}\cdot\hat{\vec{H}}^i\cdot\left(\hat{\vec{H}}^{-m}\right) - j\cdot\omega\cdot\frac{\partial\varepsilon}{\partial z}\cdot\hat{\vec{E}}^i\cdot\left(\hat{\vec{E}}^{-m}\right)
\end{aligned}$$

Applying the vector identity:

$$\nabla\cdot\left(\vec{A}\times\vec{B}\right) = \vec{B}\cdot\left(\nabla\times\vec{A}\right) - \vec{A}\cdot\left(\nabla\times\vec{B}\right)$$

to the term placed to the left of the equality sign, and reorganizing the term to the right of the equality sign, the following expression is obtained:

$$\nabla\cdot\left(\hat{\vec{H}}^{-m}\times\frac{\partial\hat{\vec{E}}^i}{\partial z} - \frac{\partial\hat{\vec{H}}^i}{\partial z}\times\hat{\vec{E}}^{-m}\right) = j\cdot\omega\cdot\left(\frac{\partial\mu}{\partial z}\cdot\hat{\vec{H}}^i\cdot\hat{\vec{H}}^{-m} - \frac{\partial\varepsilon}{\partial z}\cdot\hat{\vec{E}}^i\cdot\hat{\vec{E}}^{-m}\right) \tag{2.55}$$

Now we are going to separate the derivative by ζ in the term to the left of the equality sign. To do it we have to recall that:

$$\nabla\cdot\vec{A}=\frac{\partial A_x}{\partial x}+\frac{\partial A_y}{\partial y}+\frac{\partial A_\zeta}{\partial \zeta}=\nabla_{x,y}\cdot\vec{A}_{x,y}+\frac{\partial A_\zeta}{\partial \zeta}$$

The resulting equation is integrated over the cross section, obtaining:

$$\iint_S \nabla_{x,y}\cdot\left(\hat{\vec{H}}^{-m}\times\frac{\partial\hat{\vec{E}}^{i}}{\partial z}-\frac{\partial\hat{\vec{H}}^{i}}{\partial z}\times\hat{\vec{E}}^{-m}\right)_{x,y}\cdot dS+\iint_S \frac{\partial}{\partial\zeta}\left(\hat{\vec{H}}^{-m}\times\frac{\partial\hat{\vec{E}}^{i}}{\partial z}-\frac{\partial\hat{\vec{H}}^{i}}{\partial z}\times\hat{\vec{E}}^{-m}\right)_{\zeta}\cdot dS=$$
$$=j\cdot\omega\cdot\iint_s\left(\frac{\partial\mu}{\partial z}\cdot\hat{\vec{H}}^{i}\cdot\hat{\vec{H}}^{-m}-\frac{\partial\varepsilon}{\partial z}\cdot\hat{\vec{E}}^{i}\cdot\hat{\vec{E}}^{-m}\right)\cdot dS$$

(2.56)

Let’s apply the two-dimensional Green theorem to the first term of the left hand side of the equation. The two-dimensional Green theorem states:
if we have a planar surface *S* with perimeter *l*, on which $\hat{\vec{n}}$ is the unit outward normal, perpendicular to the perimeter *l* and contained in the same plane (*x*,*y*), then the following identity will be verified:

$$\iint_S \nabla_{x,y}\cdot\vec{A}_{x,y}\cdot dS=\oint_l \vec{A}_{x,y}\cdot\hat{\vec{n}}\cdot dl$$

Applying it to the first term of the left hand side of eqn. (2.56), we have:

$$\iint_S \nabla_{x,y}\cdot\left(\hat{\vec{H}}^{-m}\times\frac{\partial\hat{\vec{E}}^{i}}{\partial z}-\frac{\partial\hat{\vec{H}}^{i}}{\partial z}\times\hat{\vec{E}}^{-m}\right)_{x,y}\cdot dS=\oint_l\left(\hat{\vec{H}}^{-m}\times\frac{\partial\hat{\vec{E}}^{i}}{\partial z}-\frac{\partial\hat{\vec{H}}^{i}}{\partial z}\times\hat{\vec{E}}^{-m}\right)_{x,y}\cdot\hat{\vec{n}}\cdot dl$$

(2.57)

Let’s see now the value of the line integral of the fields over the perimeter of the cross section surface, S.
The vector products can be developed as:

$$\hat{\vec{H}}^{-m}\times\frac{\partial\hat{\vec{E}}^{i}}{\partial z}=\begin{vmatrix}\hat{H}_t^{-m} & \hat{H}_n^{-m} & \hat{H}_\zeta^{-m}\\ \partial\hat{E}_t^{i}/\partial z & \partial\hat{E}_n^{i}/\partial z & \partial\hat{E}_\zeta^{i}/\partial z\\ \hat{t} & \hat{\vec{n}} & \hat{\zeta}\end{vmatrix}=\frac{\partial\hat{E}_t^{i}}{\partial z}\cdot\hat{H}_\zeta^{-m}\cdot\hat{\vec{n}}-\frac{\partial\hat{E}_\zeta^{i}}{\partial z}\cdot\hat{H}_t^{-m}\cdot\hat{\vec{n}}+\cdots$$

$$\frac{\partial \hat{H}^{i}}{\partial z} \times \hat{E}^{-m} = \begin{vmatrix} \partial \hat{H}_{t}^{i} / \partial z & \partial \hat{H}_{n}^{i} / \partial z & \partial \hat{H}_{\zeta}^{i} / \partial z \\ \hat{E}_{t}^{-m} & \hat{E}_{n}^{-m} & \hat{E}_{\zeta}^{-m} \\ \hat{t} & \hat{n} & \hat{\zeta} \end{vmatrix} = \hat{E}_{t}^{-m} \cdot \frac{\partial \hat{H}_{\zeta}^{i}}{\partial z} \cdot \hat{n} - \hat{E}_{\zeta}^{-m} \cdot \frac{\partial \hat{H}_{t}^{i}}{\partial z} \cdot \hat{n} + \cdots$$

where $\hat{t}$ is the unitary vector in the direction tangential to the perimeter of the cross section surface, S, and $\hat{n}$ is the unitary vector normal to the perimeter. On the other hand, as it was commented earlier, the unitary vector $\hat{\zeta}$ is equal to the unitary vector $\hat{z}$.

Thus, the line integral of the fields over the perimeter of the cross section surface, S, can be rewritten as:

$$\begin{aligned} &\oint_{l} \left(\hat{H}^{-m} \times \frac{\partial \hat{E}^{i}}{\partial z} - \frac{\partial \hat{H}^{i}}{\partial z} \times \hat{E}^{-m} \right)_{x,y} \cdot \hat{n} \cdot dl = \\ &\qquad = \oint_{l} \left(\frac{\partial \hat{E}_{t}^{i}}{\partial z} \cdot \hat{H}_{\zeta}^{-m} - \frac{\partial \hat{E}_{\zeta}^{i}}{\partial z} \cdot \hat{H}_{t}^{-m} - \hat{E}_{t}^{-m} \cdot \frac{\partial \hat{H}_{\zeta}^{i}}{\partial z} + \hat{E}_{\zeta}^{-m} \cdot \frac{\partial \hat{H}_{t}^{i}}{\partial z} \right) \cdot dl \end{aligned} \tag{2.58}$$

As it has been previously stated, the cross section, S, of an open waveguide extends to infinity, and hence its perimeter *l* will be placed at infinity. Therefore, if one (or both) of the implied modes (*i* and *m*) belongs to the discrete spectrum, then it will be a bounded mode and hence its fields and their *z* derivatives will vanish at the perimeter *l*, making the line integral of eqn. (2.58) vanish also.

If, on the other hand, both modes implied (*i* and *m*) belong to the continuous spectrum, then their fields will not vanish at infinity. However, as it was seen in section (2.2.2), each mode of an open waveguide can be seen as the limit of a mode of a closed waveguide (formed by surrounding the open waveguide with a metal clad) when the metal clad goes to infinity [SHE 71], [SNY 83], [ROZ 97]. So we can study the modes of the open waveguide as those of a waveguide closed at infinity. Using this property it can be seen that the components of the electric fields tangential to the virtual metal boundary placed at infinity (E_t and E_ζ), and their *z* derivatives, will vanish at infinity, and hence the line integral of eqn. (2.58) will vanish also. As a result, eqn. (2.58) will be equal to zero for any mode:

$$\oint_{l} \left(\hat{H}^{-m} \times \frac{\partial \hat{E}^{i}}{\partial z} - \frac{\partial \hat{H}^{i}}{\partial z} \times \hat{E}^{-m} \right)_{x,y} \cdot \hat{n} \cdot dl = 0 \tag{2.59}$$

A rigorous mathematical derivation of this result for a pair of continuous spectrum modes could be done using the limit point at infinity property of the transverse vector wave equation [FRI 56].

If the waveguide of interest were a closed waveguide, the cross section would be finite and it would be surrounded by a metallic cover of constant cross section. In that case, it is easy to demonstrate eqn. (2.59), because the electric field components tangential to the metal cover (E_t and E_ζ), and their *z* derivatives, will vanish over it, and as a result the line integral of eqn. (2.58) will vanish also.

Using this last result given by eqn. (2.59) together with the equality of eqn. (2.57), the expression of eqn. (2.56) becomes:

$$\iint_S \frac{\partial}{\partial \zeta}\left(\hat{\vec{H}}^{-m} \times \frac{\partial \hat{\vec{E}}^i}{\partial z} - \frac{\partial \hat{\vec{H}}^i}{\partial z} \times \hat{\vec{E}}^{-m} \right)_\zeta \cdot dS = j \cdot \omega \cdot \iint_S \left(\frac{\partial \mu}{\partial z} \cdot \hat{\vec{H}}^i \cdot \hat{\vec{H}}^{-m} - \frac{\partial \varepsilon}{\partial z} \cdot \hat{\vec{E}}^i \cdot \hat{\vec{E}}^{-m} \right) \cdot dS \tag{2.60}$$

To continue, we are going to develop the term on the left hand side of eqn. (2.60). It can be rewritten in a more comfortable form as:

$$\frac{\partial}{\partial \zeta} \iint_S \left(\hat{\vec{H}}^{-m} \times \frac{\partial \hat{\vec{E}}^i}{\partial z} - \frac{\partial \hat{\vec{H}}^i}{\partial z} \times \hat{\vec{E}}^{-m} \right) \cdot \hat{\zeta} \cdot dS \tag{2.61}$$

In first place we are going to substitute for the fields and for their *z* derivatives from eqns. (2.54):

$$\begin{aligned} \frac{\partial}{\partial \zeta} \iint_S \Bigg[\vec{H}^{-m} \cdot e^{-j \cdot \beta_{-m} \cdot \zeta} \times \left(\frac{\partial \vec{E}^i}{\partial z} - j \cdot \frac{\partial \beta_i}{\partial z} \cdot \zeta \cdot \vec{E}^i \right) \cdot e^{-j \cdot \beta_i \cdot \zeta} - \left(\frac{\partial \vec{H}^i}{\partial z} - j \cdot \frac{\partial \beta_i}{\partial z} \cdot \zeta \cdot \vec{H}^i \right) \cdot e^{-j \cdot \beta_i \cdot \zeta} \times \\ \times \vec{E}^{-m} \cdot e^{-j \cdot \beta_{-m} \cdot \zeta} \Bigg] \cdot \hat{\zeta} \cdot dS \end{aligned}$$

Reorganizing the term, taking into account the relation between the fields of the forward and backward travelling waves associated to the same *i* mode, eqn. (2.14), and using the unitary vector $\hat{z}$ instead of $\hat{\zeta}$ (recalling that they are identical) the term can be rewritten as:

$$\begin{aligned} \frac{\partial}{\partial \zeta} \Bigg[e^{-j \cdot \beta_{-m} \cdot \zeta} \cdot e^{-j \cdot \beta_i \cdot \zeta} \cdot \Bigg(\iint_S \left(\vec{H}^m \times \frac{\partial \vec{E}^i}{\partial z} + \frac{\partial \vec{H}^i}{\partial z} \times \vec{E}^m \right) \cdot \hat{z} \cdot dS - \\ - j \cdot \frac{\partial \beta_i}{\partial z} \cdot \zeta \cdot \iint_S \left(\vec{H}^m \times \vec{E}^i + \vec{H}^i \times \vec{E}^m \right) \cdot \hat{z} \cdot dS \Bigg) \Bigg] \end{aligned}$$

Taking into account the orthogonality relation satisfied between the mode fields, eqn. (2.23):

$$\iint_S \left(\left(\vec{E}^i \times \vec{H}^m \right) + \left(\vec{E}^m \times \vec{H}^i \right) \right) \cdot \hat{z} \cdot dS = 0 \quad , \quad m \neq i$$

the second surface integral of the term will vanish for $m \neq i$, and reorganizing the term it will become:

$$-\frac{\partial}{\partial \zeta} \left(e^{-j \cdot (\beta_{-m} + \beta_i) \cdot \zeta} \cdot \iint_S \left(\frac{\partial \vec{E}^i}{\partial z} \times \vec{H}^m + \vec{E}^m \times \frac{\partial \vec{H}^i}{\partial z} \right) \cdot \hat{z} \cdot dS \right) \quad , \quad m \neq i$$

Relating the surface integral with the value of the coupling coefficient, eqn. (2.46), the term is expressible as:

$$-\frac{\partial}{\partial \zeta} \left(e^{-j \cdot (\beta_{-m} + \beta_i) \cdot \zeta} \cdot \left(-2 \cdot N_m \cdot C_{mi} \right) \right) \quad , \quad m \neq i$$

and performing the differentiation by ζ it is finally obtained that the term on the left hand side of eqn. (2.60) can be expressed as:

$$-j \cdot \left(\beta_{-m} + \beta_i \right) \cdot e^{-j \cdot (\beta_{-m} + \beta_i) \cdot \zeta} \cdot 2 \cdot N_m \cdot C_{mi} \quad , \quad m \neq i \tag{2.62}$$

Now we are going to develop the term on the right hand side of eqn. (2.60). Its initial form is:

$$j \cdot \omega \cdot \iint_S \left(\frac{\partial \mu}{\partial z} \cdot \hat{\vec{H}}^i \cdot \hat{\vec{H}}^{-m} - \frac{\partial \varepsilon}{\partial z} \cdot \hat{\vec{E}}^i \cdot \hat{\vec{E}}^{-m} \right) \cdot dS \tag{2.63}$$

Substituting for the fields from eqns. (2.54) the term can be expressed as:

$$j \cdot \omega \cdot \iint_S \left(\frac{\partial \mu}{\partial z} \cdot \vec{H}^i \cdot e^{-j \cdot \beta_i \cdot \zeta} \cdot \vec{H}^{-m} \cdot e^{-j \cdot \beta_{-m} \cdot \zeta} - \frac{\partial \varepsilon}{\partial z} \cdot \vec{E}^i \cdot e^{-j \cdot \beta_i \cdot \zeta} \cdot \vec{E}^{-m} \cdot e^{-j \cdot \beta_{-m} \cdot \zeta} \right) \cdot dS$$

and reorganizing the expression we finally have that the term on the right hand side of eqn. (2.60) can be rewritten as:

$$j \cdot \omega \cdot e^{-j \cdot (\beta_i + \beta_{-m}) \cdot \zeta} \cdot \iint_S \left(\frac{\partial \mu}{\partial z} \cdot \vec{H}^i \cdot \vec{H}^{-m} - \frac{\partial \varepsilon}{\partial z} \cdot \vec{E}^i \cdot \vec{E}^{-m} \right) \cdot dS \tag{2.64}$$

Using the equivalent expressions obtained for the terms on the left hand side and on the right hand side of eqn. (2.60), (eqns. (2.62) and (2.64), respectively), eqn. (2.60) can be rewritten as:

$$
\begin{aligned}
&-j\cdot\left(\beta_{-m}+\beta_i\right)\cdot e^{-j\cdot\left(\beta_{-m}+\beta_i\right)\cdot\zeta}\cdot 2\cdot N_m\cdot C_{mi}= \\
&\qquad = j\cdot\omega\cdot e^{-j\cdot\left(\beta_i+\beta_{-m}\right)\cdot\zeta}\cdot\iint_S\left(\frac{\partial\mu}{\partial z}\cdot\vec{H}^i\cdot\vec{H}^{-m}-\frac{\partial\varepsilon}{\partial z}\cdot\vec{E}^i\cdot\vec{E}^{-m}\right)\cdot dS \quad , \; m\neq i
\end{aligned}
$$

Reorganizing this last equation, and taking into account the relation existent between the phase constants and the mode fields of the forward and backward travelling waves associated the same mode (eqns. (2.13), (2.14)), the following expression for the coupling coefficient is obtained:

$$
C_{mi}=\frac{-\omega}{2\cdot N_m\cdot\left(\beta_m-\beta_i\right)}\cdot\iint_S\left(\frac{\partial\varepsilon}{\partial z}\cdot\vec{E}^i\cdot\vec{E}^{-m}-\frac{\partial\mu}{\partial z}\cdot\vec{H}^i\cdot\vec{H}^{-m}\right)\cdot dS \quad , \; m\neq i \tag{2.65}
$$

or the equivalent expression:

$$
\begin{aligned}
C_{mi}=\frac{-\omega}{2\cdot N_m\cdot\left(\beta_i-\beta_m\right)}\cdot\iint_S\Bigg(&\frac{\partial\varepsilon}{\partial z}\cdot\left(E_x^i\cdot E_x^m+E_y^i\cdot E_y^m-E_z^i\cdot E_z^m\right)+ \\
&+\frac{\partial\mu}{\partial z}\cdot\left(H_x^i\cdot H_x^m+H_y^i\cdot H_y^m-H_z^i\cdot H_z^m\right)\Bigg)\cdot dS
\end{aligned}
\quad , \; m\neq i \tag{2.66}
$$

The last formulae obtained (eqns. (2.65) and (2.66)) are known as the practical form of the coupling coefficients, and they contain the derivative by *z* of ε and μ, instead of the derivative by *z* of the mode fields present in the original expression, eqn. (2.45).
The difference between the phase constants $\left(\beta_m-\beta_i\right)$ appearing in the denominator of the obtained formula does not imply that the coupling coefficient of these two modes could be very large when their phase constants become nearly equal to each other. Indeed, the value of the integral in the nominator of eqns. (2.65), (2.66), becomes very small when the values of the phase constants are very close, and as a result the coupling coefficient C_{mi} remains finite.

To finish this section, the expression for $d\beta_m/dz$ will be obtained in a similar manner. To do it, we are going to start from the development done for the term on the left hand side of eqn. (2.60), but taking this time $m=i$. In this case it is straightforward to show (recalling the orthonormality relations satisfied by the mode fields, eqns. (2.27)) that the final expression for this term will be:

$$
j\cdot\frac{d\beta_m}{dz}\cdot 2\cdot N_m \tag{2.67}
$$

Regarding the term on the right hand side of eqn. (2.60), we can readily particularize for our case of $m = i$ the expression deduced for the term in eqn. (2.64), obtaining:

$$j \cdot \omega \cdot \iint_S \left(\frac{\partial \mu}{\partial z} \cdot \vec{H}^m \cdot \vec{H}^{-m} - \frac{\partial \varepsilon}{\partial z} \cdot \vec{E}^m \cdot \vec{E}^{-m} \right) \cdot dS \tag{2.68}$$

And finally, using these equivalent expressions obtained for the terms on the left hand side and on the right hand side of eqn. (2.60), (eqns. (2.67) and (2.68), respectively), eqn. (2.60) can be rewritten this time as:

$$j \cdot \frac{d\beta_m}{dz} \cdot 2 \cdot N_m = j \cdot \omega \cdot \iint_S \left(\frac{\partial \mu}{\partial z} \cdot \vec{H}^m \cdot \vec{H}^{-m} - \frac{\partial \varepsilon}{\partial z} \cdot \vec{E}^m \cdot \vec{E}^{-m} \right) \cdot dS$$

and reorganizing it, the sought expression for the z derivative of the phase constant follows:

$$\frac{d\beta_m}{dz} = \frac{-\omega}{2 \cdot N_m} \cdot \iint_S \left(\frac{\partial \varepsilon}{\partial z} \cdot \vec{E}^m \cdot \vec{E}^{-m} - \frac{\partial \mu}{\partial z} \cdot \vec{H}^m \cdot \vec{H}^{-m} \right) \cdot dS \tag{2.69}$$

2.3.1.4. Case of ε and μ piecewise constant functions

We have assumed from the beginning of section (2.3.1) that in the straight waveguide under study that is nonuniform in the propagation direction (the z direction), $\varepsilon(x,y,z)$ and $\mu(x,y,z)$ are continuous functions with z (eqn. (2.32)). This condition is necessary to guarantee that the fields present in a cross section of the nonuniform waveguide, and the modes of the uniform waveguide (reference waveguide) employed in their series expansion satisfy the same boundary conditions in the cross section of interest. If this requirement is fulfilled, the series expansions of eqns. (2.33) and (2.35) will be convergent to the field that they are meant to represent in all points of the cross section. Thanks to that condition the term by term differentiation of these series was possible, and the coupled mode equations, eqns. (2.43), (2.44), and the expressions for the coupling coefficients given by eqns. (2.45), were obtained [KAT 98].

If, on the other hand, $\varepsilon(x,y,z)$ and/or $\mu(x,y,z)$ are non continuous functions with z, then in the discontinuity surfaces there will be an interface between two different dielectric mediums (with different ε and/or μ), where the boundary conditions for the fields at a dielectric interface apply. As it is well known, these boundary conditions are the following for the interface between two lossless dielectric materials [POZ 98]:

$$\begin{aligned} &\varepsilon_1 \cdot E_{n1} = \varepsilon_2 \cdot E_{n2} \\ &\mu_1 \cdot H_{n1} = \mu_2 \cdot H_{n2} \\ &E_{t1} = E_{t2} \\ &H_{t1} = H_{t2} \end{aligned} \tag{2.70}$$

where the indices n and t refer to the directions normal and tangential to the interface, and the indices 1 and 2 refer to the side of the interface placed on the first and second medium. As it can be seen in Fig. 2.1, in this case the fields in the cross section of the nonuniform waveguide under study satisfy different boundary conditions than the mode fields of the uniform reference waveguide employed in their series expansion. As a result the series expansion will not converge towards the fields that it is meant to represent (the fields in the nonuniform waveguide) in the discontinuity (or boundary) contours (the zones at which the boundary conditions satisfied are different). The series will not be convergent in all points of the cross section. Consequently in the case of $\varepsilon(x,y,z)$ and/or $\mu(x,y,z)$ not continuous with z, the term by term differentiation of the series can not be taken and all the developments performed until now in section (2.3.1) are in principle not valid [KAT 98]. This important difficulty makes necessary

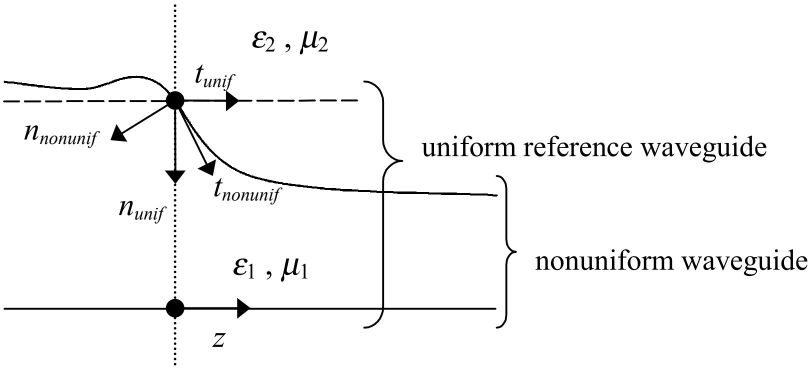

***Figure 2.1**: Sketch of a nonuniform waveguide with ε(x,y,z) and μ(x,y,z) not continuous with z. A cross section has been selected and its associated uniform reference waveguide is depicted using a dashed line. The unitary vectors normal and tangential to the discontinuity surface (boundary surface) are also depicted for the nonuniform waveguide ($n_{nonunif}$, $t_{nonunif}$) and for the uniform reference waveguide (n_{unif}, t_{unif}).*

to study this last case applying a mathematical trick that will allow us to solve the problem.

In this section we are going to demonstrate the validity of the coupled mode equations for the case of $\varepsilon(x,y,z)$ and/or $\mu(x,y,z)$ not continuous with z, and the value for the coupling coefficients will be calculated. Here the particular case of ε and μ piecewise constant functions will be studied, but it is straightforward to show that the general case is easily obtained as a combination of this one and the former studied case of $\varepsilon(x,y,z)$ and $\mu(x,y,z)$ continuous with z.

We are going to start our study of the nonuniform waveguide with ε and μ piecewise constant functions, substituting the separation border between areas with different ε and/or μ by a thin transition layer where ε and μ vary in a continuous way from the value that they have in one area, to the value that they have in the other area. In the thin transition layer ε and μ vary in a continuous way in the direction perpendicular to the interface between the two areas (at least at the limit when the thickness of the transition layer goes to zero). The resulting waveguide features $\varepsilon(x,y,z)$ and $\mu(x,y,z)$ that are continuous functions. Consequently the coupled mode equations (eqns. (2.43), (2.44)) and the expressions for the coupling coefficients (eqns. (2.45), (2.66)) that were previously obtained are still valid for this last waveguide.

2.3.1.4.1. Expression for the coupling coefficients

We are going to calculate the coupling coefficients for the case of a nonuniform waveguide with ε and μ piecewise constant functions, using the waveguide with continuous ε and μ that we have constructed. This last waveguide will have $\partial\varepsilon/\partial z$ and $\partial\mu/\partial z$ different form zero only in the thin transition layers introduced. Taking into account this fact, and to obtain a simpler result, the expression for the coupling coefficient that we are going to use here is the practical form of the coupling coefficient given by eqn. (2.66) (its surface integral will be different from zero only in the thin transition layers). For the sake of simplicity we are going to assume that there is only one separating border. Obviously, the result can be generalized for other cases when there are several of such borders.

Let us introduce a local coordinate system with axes t, n, z in the thin transition layer over which the integral of the coupling coefficient, eqn. (2.66), is calculated. The axes will satisfy that t is tangential to the contour where the separating border and the cross section intersect; n is normal to t and is placed in the cross section plane and is directed from the area with smaller ε and μ, towards the area with larger ε and μ ; z is in the direction of the waveguide axis. The unitary vectors $\hat{n}$, $\hat{t}$, $\hat{z}$ form a right hand side system of axes. Actually they satisfy that $\hat{n}\times\hat{t}=\hat{z}$. It is important to note that the vector $\hat{n}$ is not orthogonal to the separating border between areas with different ε and/or μ in the nonuniform waveguide (it will be orthogonal in the associated uniform reference waveguides). In Fig. 2.2 these vectors are shown for the simplest case in which $\hat{n}$, $\hat{z}$ and grad ε are coplanar.

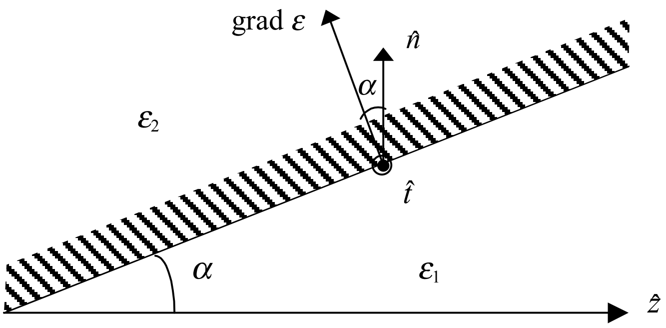

***Figure 2.2**: Sketch of the unitary vectors $\hat{n}$, $\hat{t}$, $\hat{z}$ together with the angle α and the gradient of ε, for the simplest case in which $\hat{n}$, $\hat{z}$ and grad ε are coplanar.*

According to the representation in Fig. 2.2, in this simple case it will be satisfied:

$$\begin{aligned} \frac{\partial \varepsilon}{\partial z} &= -\left|\operatorname{grad} \varepsilon\right| \cdot \sin(\alpha) \\ \frac{\partial \varepsilon}{\partial n} &= \left|\operatorname{grad} \varepsilon\right| \cdot \cos(\alpha) \end{aligned} \tag{2.71}$$

and from these equations it can be seen that:

$$\frac{\partial \varepsilon}{\partial z} = -\tan(\alpha) \cdot \frac{\partial \varepsilon}{\partial n} \quad \Rightarrow \quad \frac{\partial \varepsilon}{\partial z} = -v \cdot \frac{\partial \varepsilon}{\partial n}$$

where $v = \tan(\alpha)$, is the tangent of the angle α defined between the *z* axis and the line tangential to the separating border and orthogonal to the contour of intersection between the separating border and the cross section.

Analogously it can be obtained that:

$$\frac{\partial \mu}{\partial z} = -v \cdot \frac{\partial \mu}{\partial n} \qquad ; \qquad v = \tan(\alpha)$$

In a more general case, the factors associated with grad ε in eqns. (2.71) will have a more complex form but their ratio will be equal to $-v$ in any case. Hence, in general, it will be always satisfied that [KAT 98]:

$$\frac{\partial \varepsilon}{\partial z} = -v \cdot \frac{\partial \varepsilon}{\partial n} \quad ; \quad \frac{\partial \mu}{\partial z} = -v \cdot \frac{\partial \mu}{\partial n} \quad ; \quad v = \tan(\alpha) \tag{2.72}$$

Strictly speaking eqns. (2.72) are only approximated when the thickness of the thin transition layer is finite. The approximation gets better as the transition layer gets thinner, and is exact in the limiting case when the thickness of the transition layer goes to zero. In this limiting case the transition layer is reduced to a surface (the separating border between the areas with different ε and μ) and grad ε and grad μ become exactly orthogonal to this surface, making the developed equations exact.

Substituting eqns. (2.72) in the practical form of the coupling coefficients, eqn. (2.66), and using the new local coordinate system with axis *n*, *t*, *z*, where $dS = dt \cdot dn$, we have:

$$\begin{aligned} C_{mi} = \frac{\omega}{2 \cdot N_m \cdot (\beta_i - \beta_m)} \cdot \oint v \cdot \Bigg\{ \int \Bigg[& \frac{\partial \varepsilon}{\partial n} \cdot \left(E_n^i \cdot E_n^m + E_t^i \cdot E_t^m - E_z^i \cdot E_z^m \right) + \\ & + \frac{\partial \mu}{\partial n} \cdot \left(H_n^i \cdot H_n^m + H_t^i \cdot H_t^m - H_z^i \cdot H_z^m \right) \Bigg] \cdot dn \Bigg\} . dt \end{aligned} \quad , \; m \neq i \tag{2.73}$$

It is important to recall that the electromagnetic fields that appear in this equation correspond to the uniform reference waveguide associated to the cross section of interest. The ν parameter is the only characteristic of the nonuniform waveguide.

The cross section of the uniform reference waveguide is composed of two areas where the parameters ε and μ have constant values, and of a thin transition layer where ε and μ vary with x and y. In this transition layer of the uniform reference waveguide the values of the fields $\vec{E}^m$ and $\vec{H}^m$ can be approximated in the following way [KAT 98]:

$$\begin{aligned} &\varepsilon(n)\cdot E_n^m(n)=\varepsilon_1\cdot E_n^m \quad ; \quad E_t^m(n)=E_t^m \quad ; \quad E_z^m(n)=E_z^m \\ &\mu(n)\cdot H_n^m(n)=\mu_1\cdot H_n^m \quad ; \quad H_t^m(n)=H_t^m \quad ; \quad H_z^m(n)=H_z^m \end{aligned} \tag{2.74}$$

where $E_n^m(n)$, $H_n^m(n)$, etc. are the components of the m mode fields existent in the thin transition layer, and E_n^m, H_n^m, etc. are the components of the m mode fields existent in the separating surface, in the side where $\varepsilon=\varepsilon_1$ and $\mu=\mu_1$.

The equalities of eqns. (2.74) have been deduced from the integral form of the Maxwell equations using the same reasoning customarily employed to deduce the boundary conditions for the fields at the interface between two lossless dielectrics.

It is important to note that the equalities obtained are only approximated when the thickness of the thin transition layer is finite; the approximation is better the thinner the transition layer is, and the approximation will be exact for the limiting case when the thickness of the transition layer goes to zero.

Obviously, the equalities obtained will be also valid for the *j* mode.

Substituting eqns. (2.74) into eqn. (2.73), the following expression is obtained:

$$\begin{aligned} C_{mi}=\frac{\omega}{2\cdot N_m\cdot(\beta_i-\beta_m)}\cdot\oint\nu\cdot\Bigg\{\int\Bigg[&\frac{\partial\varepsilon}{\partial n}\cdot\left(\frac{\varepsilon_1}{\varepsilon(n)}E_n^i\cdot\frac{\varepsilon_1}{\varepsilon(n)}E_n^m+E_t^i\cdot E_t^m-E_z^i\cdot E_z^m\right)+ \\ &+\frac{\partial\mu}{\partial n}\cdot\left(\frac{\mu_1}{\mu(n)}H_n^i\cdot\frac{\mu_1}{\mu(n)}H_n^m+H_t^i\cdot H_t^m-H_z^i\cdot H_z^m\right)\Bigg]\cdot dn\Bigg\}.dt \end{aligned}$$

valid for $m\neq i$. (2.75)

Let's see now the value of the first integral:

$$\int_0^{\Delta n}\frac{\partial\varepsilon}{\partial n}\cdot\left(\frac{(\varepsilon_1)^2}{(\varepsilon(n))^2}E_n^i\cdot E_n^m+E_t^i\cdot E_t^m-E_z^i\cdot E_z^m\right)\cdot dn$$

developing it we have:

$$(\varepsilon_1)^2 \cdot E_n^i \cdot E_n^m \cdot \int_0^{\Delta n} \frac{\partial \varepsilon}{\partial n} \cdot \frac{1}{\varepsilon^2} \cdot dn + \left(E_t^i \cdot E_t^m - E_z^i \cdot E_z^m\right) \cdot \int_0^{\Delta n} \frac{\partial \varepsilon}{\partial n} \cdot dn$$

and calculating the integrals we obtain:

$$E_n^i \cdot E_n^m \cdot \left(\varepsilon_1 - \frac{\varepsilon_1^{\,2}}{\varepsilon_2}\right) + \left(E_t^i \cdot E_t^m - E_z^i \cdot E_z^m\right) \cdot \left(\varepsilon_2 - \varepsilon_1\right)$$

It is important to note that in this calculation we have assumed that $\varepsilon_1 \le \varepsilon_2$, since the integration is realized in the direction of $\hat{n}$. ($\hat{n}$ is directed from the medium with smaller ε towards he medium with larger ε).

The integral with the magnetic fields of eqn. (2.75) can be calculated in a similar way and obtaining a similar result. Introducing these results in eqn. (2.75), the expression for the coupling coefficient becomes:

$$\begin{aligned} C_{mi} = \frac{-\omega}{2 \cdot N_m \cdot (\beta_m - \beta_i)} \cdot \oint \nu \cdot \Bigg[&\left(\varepsilon_2 - \varepsilon_1\right) \cdot \left(E_t^i \cdot E_t^m - E_z^i \cdot E_z^m\right) - \left(\frac{\varepsilon_1^{\,2}}{\varepsilon_2} - \varepsilon_1\right) \cdot E_n^i \cdot E_n^m + \\ &+ \left(\mu_2 - \mu_1\right) \cdot \left(H_t^i \cdot H_t^m - H_z^i \cdot H_z^m\right) - \left(\frac{\mu_1^{\,2}}{\mu_2} - \mu_1\right) \cdot H_n^i \cdot H_n^m \Bigg] \cdot dt \end{aligned} \tag{2.76}$$

valid for $m \neq i$ and for $\varepsilon_1 \le \varepsilon_2$ and $\mu_1 \le \mu_2$.

For the limiting case when the thickness of the transition layer goes to zero, the expression for the coupling coefficient will be exact. It is important to note that in this limiting case the transition layer is reduced to a surface (the separating border between the areas with different ε and μ), and the constructed waveguide with continuous ε and μ becomes the original waveguide of interest with ε and μ piecewise constant. Therefore, for a waveguide with ε and μ piecewise constant functions, the coupling coefficient can be calculated using eqn. (2.76), and the expression has no approximations involved, it is exact. It is important to note also that the coupled mode equations, eqns. (2.43), (2.44), initially obtained for waveguides with continuous ε and μ, do not depend on the smoothness of the functions ε and μ, and hence are valid at any stage when approaching the limit from continuous to discontinuous ε and μ. Actually, they will remain valid in the limit of discontinuous functions, and hence in the case of a waveguide with ε and μ piecewise constant functions.

Let's recall that in eqn. (2.76) $\nu = \tan(\alpha)$, is the tangent of the angle α defined between the z axis and the line tangential to the separating border and orthogonal to

the contour of intersection between the separating border and the cross section. The fields, on the other hand, are the fields existent in the side with ε_1 and μ_1. The definition for the unitary vectors $\hat{n}, \hat{t}, \hat{z}$ (system of axes) is given at the beginning of this section.
Therefore, to calculate the coupling coefficient of a waveguide with ε and μ piecewise constant using eqn. (2.76), it is sufficient to know the modal fields on the separating border between the two areas with different ε and/or μ, and the value of *v(t,z)*.

To finish this section an expression for $d\beta_m/dz$ when ε and μ are piecewise constant functions will be obtained in a similar manner. We start form the expression for $d\beta_m/dz$ calculated in the section (2.3.1.3), and given by eqn. (2.69). It is valid for ε and μ continuous with *z*:

$$\frac{d\beta_m}{dz} = \frac{-\omega}{2 \cdot N_m} \cdot \iint_S \left(\frac{\partial \varepsilon}{\partial z} \cdot \vec{E}^m \cdot \vec{E}^{-m} - \frac{\partial \mu}{\partial z} \cdot \vec{H}^m \cdot \vec{H}^{-m} \right) \cdot dS \tag{2.69}$$

We are going to follow the same development that we have used to obtain the coupling coefficients. In first place eqns. (2.72) will be substituted into eqn. (2.69), obtaining:

$$\frac{d\beta_m}{dz} = \frac{\omega}{2 \cdot N_m} \cdot \oint v \cdot \left\{ \int \left[\frac{\partial \varepsilon}{\partial n} \cdot \left(E_n^m \cdot E_n^{-m} + E_t^m \cdot E_t^{-m} + E_z^m \cdot E_z^{-m} \right) - \right.\right.$$
$$\left.\left. - \frac{\partial \mu}{\partial n} \cdot \left(H_n^m \cdot H_n^{-m} + H_t^m \cdot H_t^{-m} + H_z^m \cdot H_z^{-m} \right) \right] \cdot dn \right\} .dt$$

Now the equalities of eqns. (2.74) will be introduced, and the expression becomes:

$$\frac{d\beta_m}{dz} = \frac{\omega}{2 \cdot N_m} \oint v \left\{ \int \left[\frac{\partial \varepsilon}{\partial n} \left(\frac{\varepsilon_1}{\varepsilon(n)} E_n^m \cdot \frac{\varepsilon_1}{\varepsilon(n)} E_n^{-m} + E_t^m \cdot E_t^{-m} + E_z^m \cdot E_z^{-m} \right) - \right.\right.$$
$$\left.\left. - \frac{\partial \mu}{\partial n} \left(\frac{\mu_1}{\mu(n)} H_n^m \cdot \frac{\mu_1}{\mu(n)} H_n^{-m} + H_t^m \cdot H_t^{-m} + H_z^m \cdot H_z^{-m} \right) \right] \cdot dn \right\} .dt$$

Integrating in the direction of $\hat{n}$ (in the same way as we did to obtain the coupling coefficients) and using the relation between the fields of the forward and backward travelling waves associated to the same mode, eqns. (2.14), the expression can be finally rewritten as:

$$\frac{d\beta_m}{dz} = \frac{-\omega}{2\cdot N_m}\cdot\oint v\cdot\left[(\varepsilon_2-\varepsilon_1)\cdot\left(\left(E_t^m\right)^2-\left(E_z^m\right)^2\right)-\left(\frac{\varepsilon_1^{\,2}}{\varepsilon_2}-\varepsilon_1\right)\cdot\left(E_n^m\right)^2+\right.$$
$$\left.+(\mu_2-\mu_1)\cdot\left(\left(H_t^m\right)^2-\left(H_z^m\right)^2\right)-\left(\frac{\mu_1^{\,2}}{\mu_2}-\mu_1\right)\cdot\left(H_n^m\right)^2\right]\cdot dt \qquad (2.77)$$

2.3.1.4.2. Other form for the coupling coefficients

In the previous section a simple expression for the coupling coefficients in the case of a nonuniform waveguide with ε and μ piecewise constant functions has been obtained. That expression was calculated starting from the practical form of the coupling coefficients, eqn. (2.66). Here, an alternative expression for the coupling coefficients for the same case will be obtained, starting this time from the initial form of the coupling coefficients, eqn. (2.45). As we did previously, we are going to start our study of the nonuniform waveguide with ε and μ piecewise constant functions, substituting the separation border between areas with different ε and/or μ by a thin transition layer where ε and μ vary in a continuous way from the value that they have in one area, to the value that they have in the other area. As it was commented earlier, the coupled mode equations (eqns. (2.43), (2.44)) and the expressions for the coupling coefficients (eqns. (2.45), (2.66)) that were previously obtained are still valid for this last waveguide.

The steps that we are going to follow are very similar to those employed in the previous section. In first place we are going to separate the surface integral of the coupling coefficient into two parts: the first one will contain the integral over the cross section surface corresponding to the thin transition layer, that we are going to name S_T, and the second one will contain the integral over the rest of the cross section surface, that will be named $S - S_T$:

$$C_{mi} = \frac{-1}{2\cdot N_m}\cdot\left[\iint_{S_T}\left(-H_x^m\cdot\frac{\partial E_y^i}{\partial z}+H_y^m\cdot\frac{\partial E_x^i}{\partial z}+E_x^m\cdot\frac{\partial H_y^i}{\partial z}-E_y^m\cdot\frac{\partial H_x^i}{\partial z}\right)\cdot dS+\right.$$
$$\left.+\iint_{S-S_T}\left(-H_x^m\cdot\frac{\partial E_y^i}{\partial z}+H_y^m\cdot\frac{\partial E_x^i}{\partial z}+E_x^m\cdot\frac{\partial H_y^i}{\partial z}-E_y^m\cdot\frac{\partial H_x^i}{\partial z}\right)\cdot dS\right] \qquad (2.78)$$

We are going to continue our deduction developing the integral over the surface

corresponding to the thin transition layer, S_T. In this surface, let's introduce a local coordinate system with axes *t*, *n*, *z* . The axes will satisfy, as in the previous section, that *t* is tangential to the contour where the separating border and the cross section intersect; *n* is normal to *t* and is placed in the cross section plane and is directed from the area with smaller ε and μ, towards the area with larger ε and μ ; *z* is in the direction of the waveguide axis. The unitary vectors $\hat{n}, \hat{t}, \hat{z}$ form a right hand side system of axes. A sketch of these vectors for the simplest case in which $\hat{n}, \hat{z}$ and grad ε are coplanar was shown in Fig. 2.2.
Using these new axes, the integral over the surface corresponding to the thin transition layer, S_T, can be rewritten as:

$$\iint_{S_T} \left(-H_n^m \cdot \frac{\partial E_t^i}{\partial z} + H_t^m \cdot \frac{\partial E_n^i}{\partial z} + E_n^m \cdot \frac{\partial H_t^i}{\partial z} - E_t^m \cdot \frac{\partial H_n^i}{\partial z} \right) \cdot dS \tag{2.79}$$

Let's see now the value of the derivative by *z* of the fields in the thin transition layer.
As it can be seen in [KOV 86], in the thin transition layer, the following relations between the fields will be satisfied:

$$\begin{aligned} \frac{\partial E_n^m}{\partial z} &= -\nu \cdot \frac{\partial E_n^m}{\partial n} + \frac{\partial \nu}{\partial t} \cdot E_t^m \\ \frac{\partial E_t^m}{\partial z} &= -\nu \cdot \frac{\partial E_t^m}{\partial n} - \frac{\partial \nu}{\partial t} \cdot E_n^m \\ \frac{\partial E_z^m}{\partial z} &= -\nu \cdot \frac{\partial E_z^m}{\partial n} \end{aligned} \tag{2.80a}$$

where, as in the previous section, $\nu = \tan(\alpha)$ is the tangent of the angle α defined between the *z* axis and the line tangential to the separating border and orthogonal to the contour of intersection between the separating border and the cross section.
In the same way, it can be obtained for the magnetic fields in the thin transition layer:

$$\begin{aligned} \frac{\partial H_n^m}{\partial z} &= -\nu \cdot \frac{\partial H_n^m}{\partial n} + \frac{\partial \nu}{\partial t} \cdot H_t^m \\ \frac{\partial H_t^m}{\partial z} &= -\nu \cdot \frac{\partial H_t^m}{\partial n} - \frac{\partial \nu}{\partial t} \cdot H_n^m \\ \frac{\partial H_z^m}{\partial z} &= -\nu \cdot \frac{\partial H_z^m}{\partial n} \end{aligned} \tag{2.80b}$$

Strictly speaking eqns. (2.80) are only approximated when the thickness of the thin transition layer is finite. The approximation gets better as the transition layer gets thinner, and is exact in the limiting case when the thickness of the transition layer goes to zero, and hence the transition layer is reduced to a surface (the separating border between the areas with different ε and μ).

Additionally, in this thin transition layer the values of the fields $\vec{E}^m$ and $\vec{H}^m$ can be approximated in the following way [KAT 98]:

$$\begin{array}{l} \varepsilon(n)\cdot E_n^m(n)=\varepsilon_1\cdot E_n^m \quad ; \quad E_t^m(n)=E_t^m \quad ; \quad E_z^m(n)=E_z^m \\ \mu(n)\cdot H_n^m(n)=\mu_1\cdot H_n^m \quad ; \quad H_t^m(n)=H_t^m \quad ; \quad H_z^m(n)=H_z^m \end{array} \tag{2.81}$$

where $E_n^m(n)$, $H_n^m(n)$, etc. are the components of the *m* mode fields existent in the thin transition layer, and E_n^m, H_n^m, etc. are the components of the *m* mode fields existent in the separating surface, in the side where $\varepsilon=\varepsilon_1$ and $\mu=\mu_1$.

The equalities of eqns. (2.81) have been deduced from the integral form of the Maxwell equations using the same reasoning customarily employed to deduce the boundary conditions for the fields at the interface between two lossless dielectrics.

It is important to note that the equalities obtained are only approximated when the thickness of the thin transition layer is finite; the approximation is better the thinner the transition layer is, and the approximation will be exact for the limiting case when the thickness of the transition layer goes to zero.

Combining eqns. (2.80) and (2.81) it can be seen that:

$$\frac{\partial E_t^i}{\partial z}=-\nu\cdot\frac{\partial E_t^i}{\partial n}-\frac{\partial \nu}{\partial t}\cdot E_n^i=-\nu\cdot 0-\frac{\partial \nu}{\partial t}\cdot\frac{\varepsilon_1}{\varepsilon}\cdot E_n^i \Rightarrow \frac{\partial E_t^i}{\partial z}=-\frac{\partial \nu}{\partial t}\cdot\frac{\varepsilon_1}{\varepsilon}\cdot E_n^i$$

$$\frac{\partial E_n^i}{\partial z}=-\nu\cdot\frac{\partial E_n^i}{\partial n}+\frac{\partial \nu}{\partial t}\cdot E_t^i=-\nu\cdot\left(-\varepsilon_1\cdot E_n^i\cdot\frac{\partial \varepsilon}{\partial n}\cdot\frac{1}{\varepsilon^2}\right)+\frac{\partial \nu}{\partial t}\cdot E_t^i \Rightarrow$$

$$\Rightarrow \frac{\partial E_n^i}{\partial z}=\nu\cdot\varepsilon_1\cdot E_n^i\cdot\frac{\partial \varepsilon}{\partial n}\cdot\frac{1}{\varepsilon^2}+\frac{\partial \nu}{\partial t}\cdot E_t^i$$

The same expressions are obtained for the magnetic fields:

$$\frac{\partial H_t^i}{\partial z}=-\frac{\partial \nu}{\partial t}\cdot\frac{\mu_1}{\mu}\cdot H_n^i$$

$$\frac{\partial H_n^i}{\partial z}=\nu\cdot\mu_1\cdot H_n^i\cdot\frac{\partial \mu}{\partial n}\cdot\frac{1}{\mu^2}+\frac{\partial \nu}{\partial t}\cdot H_t^i$$

Introducing these last expressions in the integral over the surface corresponding to the thin transition layer, S_T, eqn. (2.79), of the coupling coefficient formula, and using eqns. (2.81), the integral can be rewritten as:

$$\oint\left[\int\left\{H_n^m\cdot\frac{\mu_1}{\mu}\cdot\frac{\partial\nu}{\partial t}\cdot\frac{\varepsilon_1}{\varepsilon}\cdot E_n^i+H_t^m\cdot\left(\nu\cdot\varepsilon_1\cdot E_n^i\cdot\frac{\partial\varepsilon}{\partial n}\cdot\frac{1}{\varepsilon^2}+\frac{\partial\nu}{\partial t}\cdot E_t^i\right)+\right.\right.$$
$$\left.\left.+\frac{\varepsilon_1}{\varepsilon}\cdot E_n^m\cdot\left(-\frac{\partial\nu}{\partial t}\cdot\frac{\mu_1}{\mu}\cdot H_n^i\right)-E_t^m\cdot\left(\nu\cdot\mu_1\cdot H_n^i\cdot\frac{\partial\mu}{\partial n}\cdot\frac{1}{\mu^2}+\frac{\partial\nu}{\partial t}\cdot H_t^i\right)\right\}\cdot dn\right]\cdot dt$$

Let’s see the value of the different terms.

The value of the first term will be:

$$\int_0^{\Delta n}H_n^m\cdot\frac{\mu_1}{\mu}\cdot\frac{\partial\nu}{\partial t}\cdot\frac{\varepsilon_1}{\varepsilon}\cdot E_n^i\cdot dn=H_n^m\cdot\mu_1\cdot\frac{\partial\nu}{\partial t}\cdot\varepsilon_1\cdot E_n^i\cdot\int_0^{\Delta n}\frac{1}{\mu\cdot\varepsilon}\cdot dn$$

and in the limit when the thickness of the transition layer goes to zero,

$$\lim_{\Delta n\to 0}\left(\int_0^{\Delta n}H_n^m\cdot\frac{\mu_1}{\mu}\cdot\frac{\partial\nu}{\partial t}\cdot\frac{\varepsilon_1}{\varepsilon}\cdot E_n^i\cdot dn\right)=0$$

The value of the second term will be:

$$\int_0^{\Delta n}H_t^m\cdot\nu\cdot\varepsilon_1\cdot E_n^i\frac{\partial\varepsilon}{\partial n}\frac{1}{\varepsilon^2}\cdot dn+\int_0^{\Delta n}H_t^m\frac{\partial\nu}{\partial t}E_t^i\cdot dn=H_t^m\cdot\nu\cdot E_n^i\left(1-\frac{\varepsilon_1}{\varepsilon_2}\right)+H_t^m\frac{\partial\nu}{\partial t}E_t^i\cdot\int_0^{\Delta n}dn$$

and in the limit when the thickness of the transition layer goes to zero,

$$\lim_{\Delta n\to 0}\left(\int_0^{\Delta n}H_t^m\cdot\nu\cdot\varepsilon_1\cdot E_n^i\cdot\frac{\partial\varepsilon}{\partial n}\cdot\frac{1}{\varepsilon^2}\cdot dn+\int_0^{\Delta n}H_t^m\cdot\frac{\partial\nu}{\partial t}\cdot E_t^i\cdot dn\right)=H_t^m\cdot\nu\cdot E_n^i\left(1-\frac{\varepsilon_1}{\varepsilon_2}\right)$$

The third term has a form parallel to that of the first one, and its value in the limit when the thickness of the transition layer goes to zero will be the same:

$$\lim_{\Delta n\to 0}\left(\int_0^{\Delta n}\frac{\varepsilon_1}{\varepsilon}\cdot E_n^m\cdot\left(-\frac{\partial\nu}{\partial t}\cdot\frac{\mu_1}{\mu}\cdot H_n^i\right)\cdot dn\right)=0$$

The fourth term, on the other hand, has a form parallel to that of the second one, and its value in the limit when the thickness of the transition layer goes to zero will be also parallel:

$$\lim_{\Delta n\to 0}\left(\int_0^{\Delta n}-E_t^m\cdot\nu\cdot\mu_1\cdot H_n^i\cdot\frac{\partial\mu}{\partial n}\cdot\frac{1}{\mu^2}\cdot dn+\int_0^{\Delta n}-E_t^m\cdot\frac{\partial\nu}{\partial t}\cdot H_t^i\cdot dn\right)=-E_t^m\cdot\nu\cdot H_n^i\cdot\left(1-\frac{\mu_1}{\mu_2}\right)$$

Therefore, in the limiting case when the thickness of the transition layer goes to zero, the integral over the cross section surface corresponding to the thin transition layer, S_T, eqn. (2.79), will have the value:

$$\lim_{\Delta n \to 0} \iint_{S_T} \left(-H_n^m \cdot \frac{\partial E_t^i}{\partial z} + H_t^m \cdot \frac{\partial E_n^i}{\partial z} + E_n^m \cdot \frac{\partial H_t^i}{\partial z} - E_t^m \cdot \frac{\partial H_n^i}{\partial z} \right) \cdot dS = \\ = \oint \nu \cdot \left(H_t^m \cdot E_n^i \cdot \left(1 - \frac{\varepsilon_1}{\varepsilon_2} \right) - E_t^m \cdot H_n^i \cdot \left(1 - \frac{\mu_1}{\mu_2} \right) \right) \cdot dt \tag{2.82}$$

Returning to the coupling coefficient expression, eqn. (2.78), if we take the limit when the thickness of the transition layer goes to zero, then the transition layer is reduced to a surface (the separating border between the areas with different ε and μ), and the constructed waveguide with continuous ε and μ becomes the original waveguide of interest with ε and μ piecewise constant functions. In that case, using eqn. (2.82), the coupling coefficient expression becomes:

$$C_{mi} = \frac{-1}{2 \cdot N_m} \cdot \left[\iint_S \left(-H_x^m \cdot \frac{\partial E_y^i}{\partial z} + H_y^m \cdot \frac{\partial E_x^i}{\partial z} + E_x^m \cdot \frac{\partial H_y^i}{\partial z} - E_y^m \cdot \frac{\partial H_x^i}{\partial z} \right) \cdot dS + \\ + \oint \nu \cdot \left(H_t^m \cdot E_n^i \cdot \left(1 - \frac{\varepsilon_1}{\varepsilon_2} \right) - E_t^m \cdot H_n^i \cdot \left(1 - \frac{\mu_1}{\mu_2} \right) \right) \cdot dt \right] \tag{2.83}$$

where S covers all the cross section surface except the contour of intersection between the separating border between areas with different ε and/or μ, and the cross section. On the other hand, the line integral is performed over this last contour.

It is important to note that in eqn. (2.83) it is assumed that $\varepsilon_2 \geq \varepsilon_1$, $\mu_2 \geq \mu_1$. In the same way, $\nu = \tan(\alpha)$ is the tangent of the angle α defined between the z axis and the line tangential to the separating border and orthogonal to the contour of intersection between the separating border and the cross section. The definition for the unitary vectors $\hat{n}, \hat{t}, \hat{z}$ (system of axes) is given at the beginning of section (2.3.1.4.1). To finish it is important to recall that the fields that appear in the line integral are those existent in the separating surface, in the side where $\varepsilon = \varepsilon_1$ and $\mu = \mu_1$.

2.3.1.4.3. Abrupt discontinuity in the propagation direction

Until now in section (2.3.1.4) we have studied nonuniform waveguides with ε and μ piecewise constant functions, where the intersection between the separating border between areas with different ε and/or μ, and the cross section, is a line or contour. Actually, the coupling coefficients obtained, eqns. (2.76), (2.83), are valid under that assumption. If, on the other hand, the intersection between the separating border and the cross section is an area, then the last expressions for the coupling coefficients are not valid. In this case we say that we have an abrupt discontinuity in the propagation direction, and to solve the problem the following technique will be applied.

We start from a nonuniform waveguide, with ε and μ piecewise constant functions, where the intersection between the separating border between areas with different ε and/or μ, and the cross section, is a surface. For the sake of simplicity it will be assumed that there is only one surface of intersection between the separating border and the cross section, placed at $z=z_0$. In order to calculate the coupling coefficient we have substituted the cross section surface placed at $z=z_0$ by a thin transition layer where in the zone corresponding to the intersection surface, ε and μ vary in a continuous way and in the z direction, from the value that they have in one area, towards the value that they have in the other area. In the rest of the layer (that corresponds to the rest of the cross section surface) ε and μ remain constant.

The resulting waveguide features ε and μ that are continuous with z. Consequently the coupled mode equations (eqns. (2.43), (2.44)) and the expressions for the coupling coefficients (eqns. (2.45), (2.66)) obtained in section (2.3.1.1) and (2.3.1.3), are still valid for this last waveguide.

We are going to designate the coupling coefficient formulated for the constructed waveguide (that includes the thin transition layer, and has ε and μ that are continuous with z) as $C_{mi}^{aux}(z)$. Integrating it over the thin transition layer, taking the limit when the thickness of the transition layer goes to zero, and taking advantage of the properties of the Dirac's delta function, $\delta(t)$, the coupling coefficient of the original waveguide (with ε and μ piecewise constant functions, where the intersection between the separating border between areas with different ε and/or μ, and the cross section, is a surface placed at $z=z_0$) is obtained:

$$C_{mi}(z=z_0)=\lim_{\Delta z\to 0}\left(\int_{z_0}^{z_0+\Delta z} C_{mi}^{aux}(z)\cdot dz\right)\cdot\delta(z-z_0) \qquad (2.84)$$

It is important to note that to calculate the required integral we can take the variation of ε and μ in the thin transition layer as needed, provided that the variation is verified in the z direction and in a continuous way, and that the values of ε and μ go from the value that they have in one area, towards the value that they have in the other area. (or remain constant outside the zone corresponding to the intersection surface).

2.3.2. Waveguides that include metals with variable cross-section

Until now, in this chapter we have applied the cross section method to nonuniform waveguides with dielectrics that have ε and μ variable in the propagation direction. We have assumed implicitly that the metals present in the waveguide (if any) do not vary in the propagation direction, i.e. that they have a constant cross section. Here we are going to study the case of nonuniform waveguides that include metals with variable cross section.

As it is well known, at the interface between a dielectric and a perfect conductor the fields must satisfy several boundary conditions [POZ 98]:

$$\begin{aligned} E_t &= 0 \\ H_n &= 0 \end{aligned} \tag{2.85}$$

where the indices n and t refer to the directions normal and tangential to the interface, and the fields are placed at the side of the dielectric (the value of all the fields in a perfect conductor is zero).

A direct application of the cross section method to a waveguide that includes metals with variable cross section encounters difficulties since, as it can be seen in Fig. 2.3, the fields in the cross section of the nonuniform waveguide under study, and the mode fields of the uniform reference waveguide employed in their series expansion, satisfy

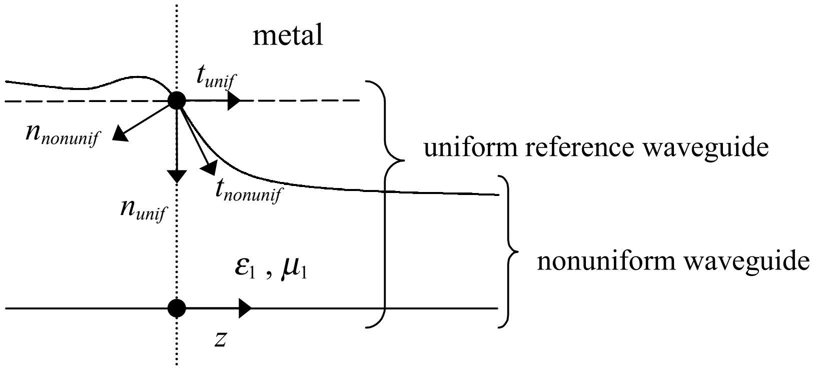

***Figure 2.3**: Sketch of a nonuniform waveguide that includes metals with variable cross section. A cross section of the nonuniform waveguide has been selected and its associated uniform reference waveguide is depicted using a dashed line. The unitary vectors normal and tangential to the metal-dielectric interface are also depicted for the nonuniform waveguide ($n_{nonunif}$, $t_{nonunif}$) and for the uniform reference waveguide (n_{unif}, t_{unif}).*

different boundary conditions. As a result the series expansion, eqns. (2.33), (2.35), will not converge towards the fields that it is meant to represent (the fields in the nonuniform waveguide) at the dielectric-metal interfaces (the zones at which the boundary conditions satisfied are different). The series will not be convergent in all points of the cross section. Consequently, in the case of a waveguide that includes metals with variable cross section, the term by term differentiation of the series can not be taken and all the developments performed in sections (2.3.1.1), (2.3.1.2), (2.3.1.3) are not directly applicable [KAT 98], [SHE 71]. From the physical point of view the reason for the difficulty is the following: the field representation as a series expansion can not be applied in the neighborhood of a metal with variable cross section, i.e. at the place where the different boundary conditions apply.

To avoid this problem we are going to proceed in a similar way as we did in the previous section for the case of ε and μ piecewise constant functions.

In first place, we are going to substitute the metals by a dielectric medium with dielectric constant $\varepsilon_2 = \text{const} \neq \varepsilon_0$, and permeability $\mu_2 = \text{const}$. The resulting waveguide will be a dielectric waveguide with ε and μ piecewise constant functions. Hence, as it was seen in section (2.3.1.4), the series expansions of eqns. (2.35), (2.37), the coupled mode equations (eqns. (2.43), (2.44)) and the expressions for the coupling coefficients (eqns. (2.76), (2.83)) that were previously obtained are also valid for this last waveguide. Actually, these results are valid for any values of ε_2 and μ_2.

As it was seen in section (2.2), eqn. (2.5), the existence of a medium with conductivity σ can be taken into account defining a complex ε with value:

$$\varepsilon_{comp} = \varepsilon - j \cdot \frac{\sigma}{\omega}$$

and therefore the dielectric can be turned into a perfect conductor ($\sigma \to \infty$) by taking the limit when the modulus of the complex ε goes to infinity, in our case taking the limit when $|\varepsilon_2| \to \infty$. Obviously, taking this limit, the constructed waveguide becomes the original waveguide of interest that contains metals with variable cross section.

2.3.2.1. Expression for the coupling coefficients

We are going to calculate the coupling coefficients valid for a nonuniform waveguide that contains metals with variable cross section, using the waveguide with piecewise constant ε and μ that we have constructed. We will start from the coupling coefficient expression given by eqn. (2.76).

$$C_{mi}=\frac{-\omega}{2\cdot N_m\cdot(\beta_m-\beta_i)}\cdot\oint\nu\cdot\left[(\varepsilon_2-\varepsilon_1)\cdot\left(E_t^i\cdot E_t^m-E_z^i\cdot E_z^m\right)-\left(\frac{\varepsilon_1^{\ 2}}{\varepsilon_2}-\varepsilon_1\right)\cdot E_n^i\cdot E_n^m+\right.$$
$$\left.+(\mu_2-\mu_1)\cdot\left(H_t^i\cdot H_t^m-H_z^i\cdot H_z^m\right)-\left(\frac{\mu_1^{\ 2}}{\mu_2}-\mu_1\right)\cdot H_n^i\cdot H_n^m\right]\cdot dt$$

(valid for $m\neq i$ and for $\varepsilon_1\leq\varepsilon_2$ and $\mu_1\leq\mu_2$. $\nu=\tan(\alpha)$, is the tangent of the angle α defined between the *z* axis and the line tangential to the separating border and orthogonal to the contour of intersection between the separating border and the cross section. The fields, on the other hand, are the fields existent in the side with ε_1 and μ_1. The definition for the unitary vectors $\hat{n},\hat{t},\hat{z}$ (system of axes) is: *t* is tangential to the contour where the separating border and the cross section intersect; *n* is normal to *t* and is placed in the cross section plane and is directed from the area with smaller ε and μ, towards the area with larger ε and μ ; *z* is in the direction of the waveguide axis). (It is important to note that since $\varepsilon_1\leq\varepsilon_2$, the dielectric medium that substitutes the conductors must be medium 2).

Now we increase the dielectric constant of the dielectric medium that substitutes the conductors, ε_2, and assume that it is complex. All the equations mentioned earlier are still valid, moreover, they are also valid when the limit $|\varepsilon_2|\to\infty$ is reached. As it was mentioned previously, at this limit the constructed waveguide becomes the original waveguide that includes metals with variable cross section. Therefore, the series expansions of eqns. (2.35), (2.37), the coupled mode equations, eqns. (2.43), (2.44), and the properties of the coupling coefficients, eqns. (2.49), (2.50), (2.51), (2.52), derived for waveguides with ε and μ variable in the propagation direction, are also valid for waveguides that include metals with variable cross section [KAT 98], [SHE 71].

An indetermination of the kind $0\cdot\infty$ will appear in eqn. (2.76), the coupling coefficient expression, when we take the limit when $|\varepsilon_2|\to\infty$, since the components E_t^m, E_z^m at the metal-dielectric interface of the uniform reference waveguide (tangential components) will tend to zero. To solve this indetermination we are going to use the Leontovich boundary condition, also known as the surface impedance condition of a good conductor [KAT 98], [NIK 76], that allows us to relate the tangential electric fields and the tangential magnetic fields at the surface of a good conductor, obtaining in our case:

$$E_t^m = \sqrt{\frac{\mu_2}{\varepsilon_2}} \cdot H_z^m \quad ; \quad E_z^m = -\sqrt{\frac{\mu_2}{\varepsilon_2}} \cdot H_t^m$$
$$E_t^i = \sqrt{\frac{\mu_2}{\varepsilon_2}} \cdot H_z^i \quad ; \quad E_z^i = -\sqrt{\frac{\mu_2}{\varepsilon_2}} \cdot H_t^i \qquad (2.86)$$

The Leontovich boundary condition constitutes an approximation valid for good conductors, that will be exact for the limiting case when the conductivity $\sigma \rightarrow \infty$ (perfect conductor), or equivalently when $|\varepsilon_2| \rightarrow \infty$.

Let's recall that the fields in eqns. (2.86) correspond to the uniform reference waveguide associated to the cross section of interest, and that $\hat{t}$ and $\hat{z}$ are always tangential to the metal-dielectric interface in the uniform reference waveguide.

Introducing eqns. (2.86) in the expression for the coupling coefficients, eqn. (2.76), and assuming that the dielectric medium is not magnetic ($\mu_1 = \mu_0$), it is obtained:

$$C_{mi} = \frac{-\omega}{2 \cdot N_m(\beta_m - \beta_i)} \oint \nu \left[(\varepsilon_2 - \varepsilon_1) \cdot \left(\frac{\mu_2}{\varepsilon_2} H_z^i H_z^m - \frac{\mu_2}{\varepsilon_2} H_t^i H_t^m \right) - \left(\frac{\varepsilon_1^{\,2}}{\varepsilon_2} - \varepsilon_1 \right) E_n^i E_n^m + \right.$$
$$\left. + (\mu_2 - \mu_0) \cdot \left(H_t^i H_t^m - H_z^i H_z^m \right) - \left(\frac{\mu_0^{\,2}}{\mu_2} - \mu_0 \right) H_n^i H_n^m \right] \cdot dt$$

and reorganizing the expression:

$$C_{mi} = \frac{-\omega}{2 \cdot N_m(\beta_m - \beta_i)} \oint \nu \cdot \left[-\frac{\varepsilon_1 \cdot \mu_2}{\varepsilon_2} \cdot \left(H_z^i H_z^m - H_t^i H_t^m \right) - \left(\frac{\varepsilon_1^{\,2}}{\varepsilon_2} - \varepsilon_1 \right) E_n^i E_n^m - \right.$$
$$\left. - \mu_0 \cdot \left(H_t^i H_t^m - H_z^i H_z^m \right) - \left(\frac{\mu_0^{\,2}}{\mu_2} - \mu_0 \right) H_n^i H_n^m \right] \cdot dt$$

Taking the limit when $|\varepsilon_2| \rightarrow \infty$, the constructed waveguide will become the original waveguide that includes metals with variable cross section, and hence the field components E_t^m, E_z^m and H_n^m will tend to zero at the metal-dielectric interface of the uniform reference waveguide (tangential electric field components and normal magnetic field component, respectively). Therefore, taking the limit when $|\varepsilon_2| \rightarrow \infty$ the coupling coefficient for the nonuniform waveguide that contains metals with variable cross section is obtained as:

$$C_{mi} = \frac{-\omega}{2 \cdot N_m \cdot (\beta_m - \beta_i)} \cdot \oint \nu \cdot \left(\mu_0 \cdot H_z^i \cdot H_z^m - \mu_0 \cdot H_t^i \cdot H_t^m + \varepsilon_1 \cdot E_n^i \cdot E_n^m \right) \cdot dt \tag{2.87}$$

where the electric and magnetic fields that appear in the equation are the mode fields of the uniform reference waveguide, present at the metal-dielectric interface, in the side of the dielectric (the value of all the fields in a perfect conductor is zero).

Regarding the system of axes, *n, t, z*, its definition can be found at the beginning of this section. Finally, $\nu = \tan(\alpha)$, is the tangent of the angle α defined between the *z* axis and the line tangential to the metal-dielectric interface, and orthogonal to the contour of intersection between the separating border and the cross section.

It is interesting to note that eqn. (2.87) expresses the coupling coefficient through the surface currents and the surface charges excited by the propagating modes with superscripts *i* and *m* on the surfaces of the metals of the reference waveguide.

Let's see now the value of $d\beta_m / dz$ in the nonuniform waveguide that contains metals with variable cross section. To calculate it we are going to start from the expression valid for the constructed waveguide with ε and μ piecewise constant functions, obtained in section (2.3.1.4.1), eqn. (2.77):

$$\frac{d\beta_m}{dz} = \frac{-\omega}{2 \cdot N_m} \cdot \oint \nu \cdot \left[(\varepsilon_2 - \varepsilon_1) \cdot \left(\left(E_t^m\right)^2 - \left(E_z^m\right)^2 \right) - \left(\frac{\varepsilon_1^{\ 2}}{\varepsilon_2} - \varepsilon_1 \right) \cdot \left(E_n^m\right)^2 + \right.$$
$$\left. + (\mu_2 - \mu_1) \cdot \left(\left(H_t^m\right)^2 - \left(H_z^m\right)^2 \right) - \left(\frac{\mu_1^{\ 2}}{\mu_2} - \mu_1 \right) \cdot \left(H_n^m\right)^2 \right] \cdot dt$$

We are going to realize the same development previously used to obtain the coupling coefficient: we take the limit when $|\varepsilon_2| \to \infty$, in this case the constructed waveguide becomes the original waveguide that includes metals with variable cross section, and hence the field components E_t^m, E_z^m and H_n^m tend to zero at the metal-dielectric interface of the uniform reference waveguide. To solve the indetermination that appears in eqn. (2.77) the Leontovich boundary condition is used obtaining eqns. (2.86). Finally, it is assumed that the dielectric medium is not magnetic ($\mu_1 = \mu_0$). With all of this, eqn. (2.77) becomes:

$$\frac{d\beta_m}{dz} = \frac{-\omega}{2 \cdot N_m} \cdot \oint \nu \cdot \left(\mu_0 \cdot \left(H_z^m\right)^2 - \mu_0 \cdot \left(H_t^m\right)^2 + \varepsilon_1 \cdot \left(E_n^m\right)^2 \right) \cdot dt \tag{2.88}$$

valid for a nonuniform waveguide that contains metals with variable cross section.
To finish this section we are going to calculate the value of the particular coupling coefficient $C_{m,-m}$. Starting from eqn. (2.87) we obtain:

$$C_{m,-m} = \frac{-\omega}{2 \cdot N_m \cdot (\beta_m - \beta_{-m})} \cdot \oint \nu \cdot \left(\mu_0 \cdot H_z^{-m} \cdot H_z^m - \mu_0 \cdot H_t^{-m} \cdot H_t^m + \varepsilon_1 \cdot E_n^{-m} \cdot E_n^m \right) \cdot dt$$

Taking into account the relation existent between the fields of the forward and backward travelling waves associated to the same mode, eqns. (2.14), and the relation between their phase constants, eqn. (2.13), the expression can be rewritten as:

$$C_{m,-m} = \frac{-\omega}{4 \cdot N_m \cdot \beta_m} \cdot \oint \nu \cdot \left(-\mu_0 \cdot \left(H_z^m\right)^2 - \mu_0 \cdot \left(H_t^m\right)^2 - \varepsilon_1 \cdot \left(E_n^m\right)^2 \right) \cdot dt$$

Reorganizing the expression and identifying part of it with the recently obtained formula for $d\beta_m / dz$, eqn. (2.88), it can be finally seen that:

$$C_{m,-m} = \frac{-1}{2 \cdot \beta_m} \cdot \frac{d\beta_m}{dz} + \frac{\omega}{2 \cdot N_m \cdot \beta_m} \cdot \oint \nu \cdot \mu_0 \cdot \left(H_t^m\right)^2 \cdot dt \qquad (2.89)$$

valid for a nonuniform waveguide that contains metals with variable cross section.

2.3.2.1.1. Microstrip line with patterned ground plane

In this section we are going to study a particular case of special interest in the framework of this thesis: a microstrip line with a pattern etched in the ground plane. Obviously, all the equations and considerations exposed until now in section (2.3.2) for nonuniform waveguides that include metals with variable cross section, will be applicable to this particular case. Here the specific application of the coupling coefficient expression, eqn. (2.87), to the case will be studied.
In Fig. 2.4 a front view and a top view of the waveguide is shown, including the unitary vectors $\hat{n}, \hat{t}, \hat{z}$. It is assumed that the thickness of the metals is negligible. Following Fig. 2.4 we have:

$$W_+ = W_+(z)$$
$$W_- = W_-(z)$$

where W_+ , W_- are the distances between the waveguide axis, *z*, and the edge of the right and left conductor, respectively.

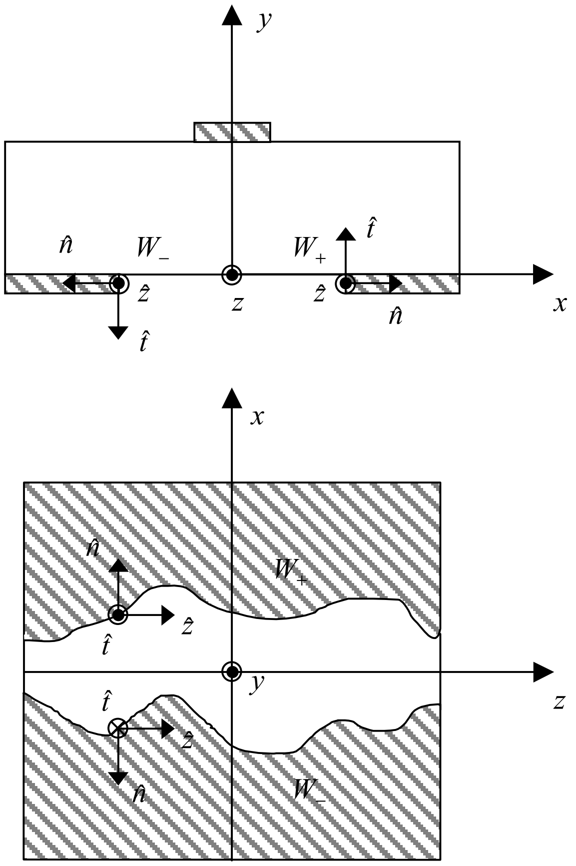

Figure 2.4: Front view and top view of a microstrip line with a pattern etched in the ground plane. For the sake of clarity in the top view only the ground plane is shown. The unitary vectors $\hat{n}$, $\hat{t}$, $\hat{z}$ are also depicted.

The generic coupling coefficient expression for a waveguide that includes metals with variable cross section , eqn. (2.87), has the following form:

$$C_{mi} = \frac{-\omega}{2 \cdot N_m \cdot (\beta_m - \beta_i)} \cdot \oint v \cdot \left(\mu_0 \cdot H_z^i \cdot H_z^m - \mu_0 \cdot H_t^i \cdot H_t^m + \varepsilon_1 \cdot E_n^i \cdot E_n^m \right) \cdot dt$$

where the line integral is to be taken over the metal-dielectric interfaces. In our case of a microstrip line with a pattern etched in the ground plane, the integration paths are depicted in Fig. 2.5, where the limit when Δ tends to zero has to be taken due to the negligible thickness assumed for the metals [SHE 00].

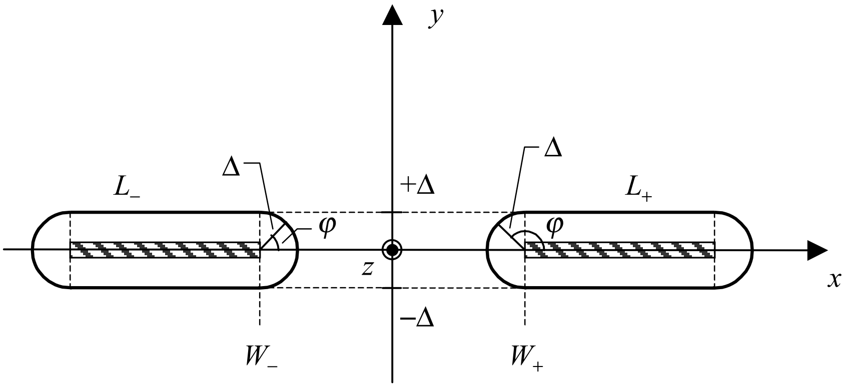

Figure 2.5: *Front view of a microstrip line with a pattern etched in the ground plane, showing the integration paths,* L_+ *,* L_- *, for the coupling coefficient expression. For the sake of clarity only the ground plane is shown.*

Following Fig. 2.5 the coupling coefficient expression can be rewritten as:

$$C_{mi} = \frac{-\omega}{2 \cdot N_m \cdot (\beta_m - \beta_i)} \cdot \lim_{\Delta \to 0} \left[\oint_{L_+} \nu \cdot F_{mi}(x,y,z) \cdot dt + \oint_{L_-} \nu \cdot F_{mi}(x,y,z) \cdot dt \right]$$

where

$$F_{mi}(x,y,z) = \mu_0 \cdot H_z^i \cdot H_z^m - \mu_0 \cdot H_t^i \cdot H_t^m + \varepsilon_1 \cdot E_n^i \cdot E_n^m$$

Finally, developing the coupling coefficient expression, we obtain for a microstrip line with a pattern etched in the ground plane:

$$C_{mi} = \frac{-\omega}{2 \cdot N_m \cdot (\beta_m - \beta_i)} \cdot \left[\frac{dW_+}{dz} \cdot \lim_{\Delta \to 0} \int_{3\pi/2}^{\pi/2} F_{mi}(W_+ + \Delta \cdot \cos(\varphi), \Delta \cdot \sin(\varphi), z) \cdot \Delta \cdot d\varphi + \right.$$
$$\left. + \frac{dW_-}{dz} \cdot \lim_{\Delta \to 0} \int_{\pi/2}^{-\pi/2} F_{mi}(W_- + \Delta \cdot \cos(\varphi), \Delta \cdot \sin(\varphi), z) \cdot \Delta \cdot d\varphi \right] \tag{2.90}$$

where

$$F_{mi}(x,y,z) = \mu_0 \cdot H_z^i \cdot H_z^m - \mu_0 \cdot H_t^i \cdot H_t^m + \varepsilon_1 \cdot E_n^i \cdot E_n^m \tag{2.91}$$

The integration over the rest of the path L_+ and L_- is equal to zero since the value of ν will be null, and hence it is omitted in the final expression.

2.3.2.2. Other form for the coupling coefficients

In this section we are going to obtain an alternative form for the coupling coefficients valid for a nonuniform waveguide that contains metals with variable cross section, using again the waveguide with piecewise constant ε and μ that we constructed in section (2.3.2). This time we are going to start from the coupling coefficient expression given by eqn. (2.83):

$$C_{mi} = \frac{-1}{2\cdot N_m}\cdot\left[\iint_S\left(-H_x^m\cdot\frac{\partial E_y^i}{\partial z}+H_y^m\cdot\frac{\partial E_x^i}{\partial z}+E_x^m\cdot\frac{\partial H_y^i}{\partial z}-E_y^m\cdot\frac{\partial H_x^i}{\partial z}\right)\cdot dS + \right.$$
$$\left. + \oint \nu\cdot\left(H_t^m\cdot E_n^i\cdot\left(1-\frac{\varepsilon_1}{\varepsilon_2}\right)-E_t^m\cdot H_n^i\cdot\left(1-\frac{\mu_1}{\mu_2}\right)\right)\cdot dt\right]$$

where *S* covers all the cross section surface except the contour of intersection between the separating border between areas with different ε and/or μ (metal-dielectric interface in the original waveguide) and the cross section, and the line integral is performed over this last contour. It is important to note that in eqn. (2.83) it is assumed that $\varepsilon_2 \geq \varepsilon_1$, $\mu_2 \geq \mu_1$ (therefore, the dielectric medium that substitutes the conductors must be medium 2). In the same way, $\nu = \tan(\alpha)$ is the tangent of the angle α defined between the *z* axis and the line tangential to the separating border and orthogonal to the contour of intersection between the separating border and the cross section. The definition for the unitary vectors $\hat{n}, \hat{t}, \hat{z}$ (system of axes) is: *t* is tangential to the contour where the separating border and the cross section intersect; *n* is normal to *t* and is placed in the cross section plane and is directed from the area with smaller ε and μ, towards the area with larger ε and μ ; *z* is in the direction of the waveguide axis. To finish it is important to recall that the fields that appear in the line integral are those existent in the separating surface, in the side where $\varepsilon = \varepsilon_1$ and $\mu = \mu_1$.

We are going to proceed in a similar way as we did in section (2.3.2.1): we increase the dielectric constant of the dielectric medium that substitutes the conductors, ε_2, and assume that it is complex. All the equations obtained earlier in section (2.3.1.4) for waveguides with ε and μ piecewise constant functions are still valid, moreover, they are also valid when the limit $|\varepsilon_2| \to \infty$ is reached. At the same time, taking the limit when $|\varepsilon_2| \to \infty$, the constructed waveguide will become the original waveguide that includes metals with variable cross section, and hence the field components E_t^m, E_z^m and H_n^m will tend to zero at the metal-dielectric interface of the uniform reference waveguide (tangential electric field components and normal magnetic field component, respectively). Therefore, taking the limit when $|\varepsilon_2| \to \infty$ the coupling coefficient for the nonuniform waveguide that contains metals with variable cross section is obtained form eqn. (2.83) as:

$$C_{mi} = \frac{-1}{2\cdot N_m}\cdot\left[\iint_S\left(-H_x^m\cdot\frac{\partial E_y^i}{\partial z}+H_y^m\cdot\frac{\partial E_x^i}{\partial z}+E_x^m\cdot\frac{\partial H_y^i}{\partial z}-E_y^m\cdot\frac{\partial H_x^i}{\partial z}\right)\cdot dS + \right. \\ \left. + \oint \nu\cdot H_t^m\cdot E_n^i\cdot dt\right] \tag{2.92}$$

This last result can be expressed in a more compact form. Let's see.

As it was seen in section (2.3.1.1), the surface integral of the coupling coefficient expression, eqn. (2.92), can be rewritten using vector notation as:

$$\iint_S\left(-H_x^m\cdot\frac{\partial E_y^i}{\partial z}+H_y^m\cdot\frac{\partial E_x^i}{\partial z}+E_x^m\cdot\frac{\partial H_y^i}{\partial z}-E_y^m\cdot\frac{\partial H_x^i}{\partial z}\right)\cdot dS = \\ = \iint_S\left(\frac{\partial \vec{E}^i}{\partial z}\times\vec{H}^m+\vec{E}^m\times\frac{\partial \vec{H}^i}{\partial z}\right)\cdot\hat{z}\cdot dS \tag{2.93}$$

On the other hand, the line integral of the coupling coefficient expression, eqn. (2.92), satisfies that:

$$\oint \nu\cdot H_t^m\cdot E_n^i\cdot dt = -\oint \nu\cdot(\vec{H}^m\times\vec{E}^i)\cdot\hat{z}\cdot dt \tag{2.94}$$

since

$$(\vec{H}^m\times\vec{E}^i)\cdot\hat{z} = \begin{vmatrix} H_n^m & H_t^m & H_z^m \\ E_n^i & E_t^i & E_t^i \\ \hat{n} & \hat{t} & \hat{z} \end{vmatrix}\cdot\hat{z} = H_n^m\cdot E_t^i - E_n^i\cdot H_t^m$$

and $E_t^m = 0,\ E_z^m = 0,\ H_n^m = 0$, at the metal-dielectric interface. (Let's recall that they are the modal fields of the uniform reference waveguide, and therefore they are tangential and normal, respectively, to the metal-dielectric interface).

Using the last two equalities, eqns. (2.93) and (2.94), the coupling coefficient expression of eqn. (2.92) can be rewritten as:

$$C_{mi} = \frac{-1}{2 \cdot N_m} \cdot \left[\iint_S \left(\frac{\partial \vec{E}^i}{\partial z} \times \vec{H}^m + \vec{E}^m \times \frac{\partial \vec{H}^i}{\partial z} \right) \cdot \hat{z} \cdot dS - \oint v \cdot (\vec{H}^m \times \vec{E}^i) \cdot \hat{z} \cdot dt \right] \qquad (2.95)$$

This expression can be simplified realizing several mathematical manipulations.
Let's recall the normalization relations satisfied by the fields of the discrete spectrum modes, and by the fields of the continuous spectrum modes, eqns. (2.25)

$$\iint_S \left(\vec{E}^i \times \vec{H}^i \right) \cdot \hat{z} \cdot dS = N_i$$

$$\iint_S \left(\vec{E}^i(k_t) \times \vec{H}^i(\tilde{k}_t) \right) \cdot \hat{z} \cdot dS = N_i(k_t) \cdot \delta(k_t - \tilde{k}_t)$$

Using at the same time the orthogonality relations satisfied by the fields of the modes, eqns. (2.24), and taking into account the relations existent between the fields of the forward and backward travelling waves associated to the same mode, eqns. (2.14), the preceeding equations can be rewritten as:

$$\iint_S \left(\vec{E}^i \times \vec{H}^m \right) \cdot \hat{z} \cdot dS = (\delta_{im} + \delta_{i,-m}) \cdot N_i$$

$$\iint_S \left(\vec{E}^i(k_t) \times \vec{H}^m(\tilde{k}_t) \right) \cdot \hat{z} \cdot dS = (\delta_{im} + \delta_{i,-m}) \cdot N_i(k_t) \cdot \delta(k_t - \tilde{k}_t)$$

where the first equation applies when the *i* mode belongs to the discrete spectrum modes, and the second equation applies when the *i* mode belongs to the continuous spectrum modes.
We are going to continue our deduction with the first equation, valid when the *i* mode is a discrete spectrum mode. (a similar result would be obtained for the second equation). Taking the derivative by *z* of the equality it follows:

$$\frac{d}{dz} \iint_S \left(\vec{E}^i \times \vec{H}^m \right) \cdot \hat{z} \cdot dS = (\delta_{im} + \delta_{i,-m}) \cdot \frac{dN_i}{dz}$$

and reorganizing the terms we have:

$$\frac{d}{dz} \iint_S \left(\vec{H}^m \times \vec{E}^i \right) \cdot \hat{z} \cdot dS = -(\delta_{im} + \delta_{i,-m}) \cdot \frac{dN_i}{dz} \qquad (2.96)$$

The term to the left of the equality sign can be developed, following [SPO 79], in the following way:

$$\frac{d}{dz}\iint_S \left(\vec{H}^m \times \vec{E}^i\right)\cdot \hat{z}\cdot dS = \oint v\cdot \left(\vec{H}^m \times \vec{E}^i\right)\cdot \hat{z}\cdot dt + \iint_S \left(\frac{\partial \vec{H}^m}{\partial z}\times \vec{E}^i + \vec{H}^m \times \frac{\partial \vec{E}^i}{\partial z}\right)\cdot \hat{z}\cdot dS \tag{2.97}$$

where S covers all the cross section surface except the metals and the contour of intersection between the metal-dielectric interfaces and the cross section, and the line integral is performed over this last contour. On the other hand, $v = \tan(\alpha)$ has the same definition previously seen at the beginning of this section: it is the tangent of the angle α defined between the z axis and the line tangential to the metal-dielectric interface, and orthogonal to the contour of intersection between the metal-dielectric interface and the cross section.

It is important to note that the surface integral:

$$\iint_S \left(\vec{H}^m \times \vec{E}^i\right)\cdot \hat{z}\cdot dS$$

has the same value when S covers all the cross section surface, and when S covers all the cross section surface except the metals and the contour of intersection between the metal-dielectric interfaces and the cross section, since the value of the fields in the perfect conductors will be null, and the value of a surface integral is not affected by the value of its integrand in a line, provided that the integrand remains finite in the mentioned line.

Combining eqns. (2.96) and (2.97), the following equality is obtained:

$$\oint v\cdot \left(\vec{H}^m \times \vec{E}^i\right)\cdot \hat{z}\cdot dt = -\iint_S \left(\frac{\partial \vec{H}^m}{\partial z}\times \vec{E}^i + \vec{H}^m \times \frac{\partial \vec{E}^i}{\partial z}\right)\cdot \hat{z}\cdot dS - (\delta_{im} + \delta_{i,-m})\cdot \frac{dN_i}{dz}$$

and introducing it in eqn. (2.95), the coupling coefficient expression for a nonuniform waveguide that contains metals with variable cross section can be finally rewritten as:

$$C_{mi} = \frac{-1}{2\cdot N_m}\cdot \iint_S \left(\vec{E}^m \times \frac{\partial \vec{H}^i}{\partial z} + \frac{\partial \vec{H}^m}{\partial z}\times \vec{E}^i\right)\cdot \hat{z}\cdot dS - (\delta_{im} + \delta_{i,-m})\cdot \frac{1}{2\cdot N_m}\cdot \frac{dN_i}{dz} \tag{2.98}$$

where S covers all the cross section surface except the metals and the contour of intersection between the metal-dielectric interfaces and the cross section, and δ_{im} is the Kronecker symbol.

An expression similar to eqn. (2.98) was also obtained in [SPO 79], but using a different way to deduce it.

To finish this section it is important to note that this time the coupling coefficient expression will have a slightly different form in the case of two modes of the continuous spectrum. It will be:

$$C_{mi}^{c}(\tilde{k}_t,k_t)=\frac{-1}{2\cdot N_m(\tilde{k}_t)}\cdot\iint_S\left(\vec{E}^m(\tilde{k}_t)\times\frac{\partial\vec{H}^i(k_t)}{\partial z}+\frac{\partial\vec{H}^m(\tilde{k}_t)}{\partial z}\times\vec{E}^i(k_t)\right)\cdot\hat{z}\cdot dS$$
$$-(\delta_{im}+\delta_{i,-m})\cdot\frac{1}{2\cdot N_m(\tilde{k}_t)}\cdot\frac{dN_i(k_t)}{dz}\cdot\delta(k_t-\tilde{k}_t) \tag{2.99}$$

2.3.2.3. Coupling coefficient $C_{m,-m}$ as a function of the characteristic impedance of the mode, Z_{0m}

As it will be seen in the next chapter, the coupling coefficient $C_{m,-m}$ will be of primary importance if single mode operation can be assumed for the nonuniform waveguide under analysis and for the frequency range of interest. Here, to make easier its calculation, we are going to obtain an expression for it as a function of the characteristic impedance of the mode, Z_{0m}.

In order to obtain the sought expression for $C_{m,-m}$, we are going to start from the coupling coefficient expressions calculated in the previous section, eqns. (2.98) (2.99), valid for nonuniform waveguides that include metals with variable cross section, and dielectrics that can feature ε and μ variable with z, but continuous with z. To simplify the expressions, we are going to assume that the normalization of the modes, N_m, is constant with z. In that case, both eqns. (2.98) and (2.99) will have the same form:

$$C_{mi}=\frac{-1}{2\cdot N_m}\cdot\iint_S\left(\vec{E}^m\times\frac{\partial\vec{H}^i}{\partial z}+\frac{\partial\vec{H}^m}{\partial z}\times\vec{E}^i\right)\cdot\hat{z}\cdot dS \tag{2.100}$$

Particularizing it for our case of interest, $C_{m,-m}$, it follows:

$$C_{m,-m}=\frac{-1}{2\cdot N_m}\cdot\iint_S\left(\vec{E}^m\times\frac{\partial\vec{H}^{-m}}{\partial z}+\frac{\partial\vec{H}^m}{\partial z}\times\vec{E}^{-m}\right)\cdot\hat{z}\cdot dS$$

and taking advantage of the relation existent between the fields of the forward and backward travelling waves associated to the same mode, eqns. (2.14), the expression can be rewritten as:

$$C_{m,-m}=\frac{-1}{2\cdot N_m}\cdot\iint_S\left(\vec{E}^m\times\frac{\partial\vec{H}^m}{\partial z}-\frac{\partial\vec{H}^m}{\partial z}\times\vec{E}^m\right)\cdot\hat{z}\cdot dS=-\frac{1}{N_m}\cdot\iint_S\left(\vec{E}^m\times\frac{\partial\vec{H}^m}{\partial z}\right)\cdot\hat{z}\cdot dS \tag{2.101}$$

Let's introduce the characteristic impedance of the mode, Z_{0m} , expressing the mode fields as a function of it and of other fields:

$$\vec{E}^m = \sqrt{Z_{0m}} \cdot \vec{e}^m$$
$$\vec{H}^m = \frac{1}{\sqrt{Z_{0m}}} \cdot \vec{h}^m \tag{2.102}$$

The characteristic impedance of the m mode, Z_{0m} , is the characteristic impedance that the m mode has in the uniform reference waveguide associated to the cross section of interest (it varies with z). Therefore, Z_{0m} will be variable with z in the nonuniform waveguide under study.

Taking into account eqns. (2.102), the derivative by z of $\vec{H}^m$ will have the form:

$$\frac{\partial \vec{H}^m}{\partial z} = -\frac{1}{2} \cdot (Z_{0m})^{-3/2} \cdot \frac{dZ_{0m}}{dz} \cdot \vec{h}^m + \frac{1}{\sqrt{Z_{0m}}} \cdot \frac{\partial \vec{h}^m}{\partial z} \tag{2.103}$$

On the other hand, from eqns. (2.25), the normalization factor N_m will satisfy for a mode of the discrete spectrum:

$$\iint_S \left(\vec{E}^m \times \vec{H}^m\right) \cdot \hat{z} \cdot dS = N_m \Rightarrow \iint_S \left(\sqrt{Z_{0m}} \cdot \vec{e}^m \times \frac{1}{\sqrt{Z_{0m}}} \cdot \vec{h}^m \right) \cdot \hat{z} \cdot dS = N_m \Rightarrow$$
$$\Rightarrow \iint_S \left(\vec{e}^m \times \vec{h}^m\right) \cdot \hat{z} \cdot dS = N_m \tag{2.104}$$

and similarly for a mode of the continuous spectrum:

$$\iint_S \left(\vec{e}^m(k_t) \times \vec{h}^m(\tilde{k}_t)\right) \cdot \hat{z} \cdot dS = N_m(k_t) \cdot \delta(k_t - \tilde{k}_t) \tag{2.105}$$

Introducing eqns. (2.102) and (2.103) in the coupling coefficient expression, eqn. (2.101), it is obtained:

$$C_{m,-m} = -\frac{1}{N_m} \cdot \iint_S \left(\sqrt{Z_{0m}} \cdot \vec{e}^m \times \left(-\frac{1}{2} \cdot (Z_{0m})^{-3/2} \cdot \frac{dZ_{0m}}{dz} \cdot \vec{h}^m + \frac{1}{\sqrt{Z_{0m}}} \cdot \frac{\partial \vec{h}^m}{\partial z} \right) \right) \cdot \hat{z} \cdot dS$$

and reorganizing the expression, we have:

$$C_{m,-m} = -\frac{1}{N_m} \cdot \left(-\frac{1}{2} \cdot \frac{1}{Z_{0m}} \cdot \frac{dZ_{0m}}{dz} \cdot \iint_S \left(\vec{e}^m \times \vec{h}^m\right) \cdot \hat{z} \cdot dS + \iint_S \left(\vec{e}^m \times \frac{\partial \vec{h}^m}{\partial z} \right) \cdot \hat{z} \cdot dS \right)$$

Now, using eqn. (2.104) it is obtained that the expression for the coupling coefficient $C_{m,-m}$ as a function of the characteristic impedance of the mode, has the following form when the *m* mode is a discrete spectrum mode:

$$C_{m,-m} = \frac{1}{2} \cdot \frac{1}{Z_{0m}} \cdot \frac{dZ_{0m}}{dz} - \frac{1}{N_m} \cdot \iint_S \left(\vec{e}^{\,m} \times \frac{\partial \vec{h}^m}{\partial z} \right) \cdot \hat{z} \cdot dS \tag{2.106}$$

In the same way, using eqn. (2.105), the expression for the coupling coefficient $C_{m,-m}$ when the *m* mode is a continuous spectrum mode, will be:

$$C^c_{m,-m}(k_t,k_t) = \frac{1}{2} \cdot \frac{1}{Z_{0m}(k_t)} \cdot \frac{dZ_{0m}(k_t)}{dz} \cdot \delta(0) - \frac{1}{N_m(k_t)} \cdot \iint_S \left(\vec{e}^{\,m}(k_t) \times \frac{\partial \vec{h}^m(k_t)}{\partial z} \right) \cdot \hat{z} \cdot dS \tag{2.107}$$

It is important to recall that the last expressions (eqns. (2.106) and (2.107)) have been obtained assuming that the normalization of the mode, N_m , does not vary with *z*.

The fields that appear in the resulting equations, $\vec{e}^{\,m}$, $\vec{h}^m$, are related to the mode fields, $\vec{E}^m$, $\vec{H}^m$ as indicated by eqns. (2.102).

To finish this section we are going to discuss the concept of characteristic impedance of the *m* mode, Z_{0m}.

As it is well known, if a mode is TEM, its associated voltage *V* and current *I* can be defined in a unique way. In that case the definition of the characteristic impedance of the mode is also unique and can be calculated as [POZ 98]:

$$Z_{0m} = \frac{V^+}{I^+} = -\frac{V^-}{I^-}$$

where the +, − indices refer to the forward and backward travelling waves, respectively.

If a mode is not pure TEM, then the definition of its characteristic impedance is no longer unique. In that case, which is the most interesting definition of characteristic impedance of a mode, for our problem?

The most interesting definition of Z_{0m} for the calculation of the coupling coefficient $C_{m,-m}$ is the one that achieves the best characterization of the propagation of the mode along the nonuniform waveguide, in terms of reflection produced by the variations of cross section present in the waveguide.

If the characteristic impedance of the mode, Z_{0m} , characterizes adequately the variations of cross section present in the waveguide in terms of reflection coefficient of the incident mode over the reflected one, the part corresponding to the fields of the coupling coefficient $C_{m,-m}$ expressions (eqns. (2.106), (2.107)) will be negligible, and the coupling coefficient could be approximated as:

$$C_{m,-m} \approx \frac{1}{2} \cdot \frac{1}{Z_{0m}} \cdot \frac{dZ_{0m}}{dz} \tag{2.108}$$

for the discrete spectrum modes, and as:

$$C^{c}_{m,-m}(k_t,k_t) \approx \frac{1}{2} \cdot \frac{1}{Z_{0m}(k_t)} \cdot \frac{dZ_{0m}(k_t)}{dz} \cdot \delta(0) \tag{2.109}$$

for the continuous spectrum modes.
An explanation for this fact can be found in appendix A. There, the equivalent voltage and current model is obtained for a waveguide mode, and from it, the coupling coefficient $C_{m,-m}$ is calculated. The expression obtained for this coupling coefficient is identical to eqn. (2.108), revealing that if the nonuniform waveguide is adequately characterized by the characteristic impedance of the mode employed, then the part of the fields in the coupling coefficient $C_{m,-m}$ expressions (eqns. (2.106), (2.107)) is negligible.

For the case of a fundamental microstrip or quasi-microstrip mode, the definition of characteristic impedance that best characterizes the variation of cross section in the microstrip line is the following [GET 83]:

$$Z_0 = 2 \cdot \frac{P^+}{\left|I^+\right|^2} \tag{2.110}$$

i.e. the expression that uses the power and the current associated to the mode. Therefore, in a microstrip line with a pattern etched in the ground plane, the coupling coefficient $C_{m,-m}$ for the fundamental microstrip or quasi-microstrip mode can be successfully approximated using eqn. (2.108), provided that the characteristic impedance of the mode is calculated using eqn. (2.110).

2.3.2.4. Abrupt discontinuity in the propagation direction

Until now in section (2.3.2) we have studied nonuniform waveguides that include metals with variable cross section, where the intersection between the metal-dielectric interface and the waveguide cross section, is a line or contour. Actually, the coupling coefficients obtained are valid under that assumption. If, on the other hand, the intersection between the metal-dielectric interface and the cross section is an area, then the last expressions for the coupling coefficients are not valid. The problem is similar to the one seen in section (2.3.1.4.3), and as in that section it is produced by the presence of an abrupt discontinuity in the propagation direction. To solve it, a similar technique to the one proposed in the mentioned section will be applied.

Here we are going to obtain an expression for the coupling coefficient $C_{m,-m}$ valid for a nonuniform waveguide that features an abrupt discontinuity in the propagation direction. The discontinuity can be produced by an abrupt variation of the cross section of a metal contained in the waveguide, or by an abrupt variation, in the z direction, of the dielectric ε and/or μ, of the kind described in section (2.3.1.4.3).

We will start from the approximated expression for the coupling coefficient $C_{m,-m}$ given by eqn. (2.108) (valid for discrete spectrum modes), obtained in the previous section:

$$C_{m,-m} = \frac{1}{2} \cdot \frac{1}{Z_{0m}} \cdot \frac{dZ_{0m}}{dz}$$

As it was seen in section (2.3.1.4.3), the coupling coefficient produced by the presence of an abrupt discontinuity at $z=z_0$ can be calculated, following eqn. (2.84), as:

$$C_{m,-m}(z=z_0) = \lim_{\Delta z \to 0} \left(\int_{z_0}^{z_0+\Delta z} C_{m,-m}^{aux}(z) \cdot dz \right) \cdot \delta(z-z_0) \tag{2.111}$$

where $C_{m,-m}^{aux}(z)$ is the coupling coefficient formulated for an auxiliary waveguide that includes a thin transition layer (of thickness Δz), and has ε and μ, as well as the cross section variation of the metals, that are continuous with z.

Using eqn. (2.108) as the expression to calculate $C_{m,-m}^{aux}(z)$, and introducing it in eqn. (2.111), it follows:

$$C_{m,-m}(z=z_0) = \lim_{\Delta z \to 0} \left(\int_{z_0}^{z_0+\Delta z} \frac{1}{2} \cdot \frac{1}{Z_{0m}} \cdot \frac{dZ_{0m}}{dz} \cdot dz \right) \cdot \delta(z-z_0)$$

and calculating the integral we obtain:

$$C_{m,-m}(z=z_0) = \lim_{\Delta z \to 0} \left(\frac{1}{2} \cdot \left(\ln\left(Z_{0m,2}\right) - \ln\left(Z_{0m,1}\right) \right) \right) \cdot \delta(z-z_0)$$

where $Z_{0m,1}$, $Z_{0m,2}$ are the characteristic impedance of the *m* mode to the left and to the right of the abrupt discontinuity, respectively.

Finally, reorganizing the expression and taking the limit it is obtained:

$$C_{m,-m}(z=z_0)=\frac{1}{2}\cdot\ln\left(\frac{Z_{0m,2}}{Z_{0m,1}}\right)\cdot\delta(z-z_0) \qquad (2.112)$$

valid for discrete spectrum modes.

In the same way it can be deduced:

$$C^c_{m,-m}(k_t,k_t)(z=z_0)=\frac{1}{2}\cdot\ln\left(\frac{Z_{0m,2}(k_t)}{Z_{0m,1}(k_t)}\right)\cdot\delta(0)\cdot\delta(z-z_0) \qquad (2.113)$$

valid for continuous spectrum modes.

It is important to recall that the last equations obtained, valid for nonuniform waveguides that feature an abrupt discontinuity in the propagation direction placed at $z=z_0$, are only approximated since eqns. (2.108), (2.109) have been employed in their deduction.

CHAPTER 3

APPROXIMATE ANALYTICAL SOLUTIONS FOR PBG STRUCTURES IN MICROSTRIP TECHNOLOGY

The coupled mode theory presented in the previous chapter has allowed us to formulate the problem of electromagnetic wave propagation along PBG structures in microstrip technology in terms of a set of integro-differential equations that relate the complex amplitudes of the modes and the coupling coefficients. There was no approximation involved in this approach. However, the problem can be notably simplified by realizing several reasonable approximations that will eventually lead to a simplified system of coupled mode equations with analytical solutions. In this chapter the approximations needed and the analytical solutions obtained will be presented and discussed. Using them, a comprehensive set of analytical expressions for the most important design parameters of the PBG microstrip devices will be furnished. The set of analytical expressions available cover a wide scope, ranging from the S parameters to the Bloch wave analysis, and constitutes a very useful and unique set of tools for the analysis and design of these devices.

3.1. Introduction

The organization of this chapter will be the following: we will start from the general system of coupled mode integro-differential equations that characterize a PBG structure in microstrip technology, obtained in the previous chapter. There was no approximation involved to obtain this system. From it, and introducing several reasonable approximations that will lead us to assume single mode operation in the PBG microstrip structure, a simplified system of 2 coupled mode differential equations will be obtained in section (3.2). A way to numerically solve the simplified system will be also presented. To continue, in section (3.3), additional reasonable approximations will be introduced and the system will be simplified to a from that features analytical solutions. Using them, a set of analytical expressions for the main design parameters of the PBG device (including the S parameters and the transmission matrix) will be developed throughout the section. The chapter will continue dealing with the Bloch wave analysis of the PBG microstrip structures in section (3.4), and again, using the approximate analytical solutions previously calculated, analytical expressions will be obtained for the main parameters (including the dispersion diagram and the Bloch wave characteristic impedance). In section (3.5) the interesting and fruitful relation between the coupling coefficient and the S_{11} (reflection) parameter of the PBG device will be presented. A very simple and approximate expression will be given together with the more complicated and exact relation. To finish the chapter, in section (3.6), this approximate theory and expressions will be applied to several PBG microstrip devices to study their performance and behavior, and to have a further insight into their operation. It will also allow us to check the accuracy of the theory and of the analytical expressions developed. To this end, the studied prototypes will be also fabricated and the measured results will be included in the section.

3.2. Simplified system of coupled mode equations

As it has been seen in the previous chapter, an open waveguide non-uniform in the propagation direction (*z* direction) will be characterized by the following system of integro-differential coupled mode equations:

$$\frac{da_m}{dz} + j \cdot \beta_m \cdot a_m = \sum_i a_i \cdot C_{mi} + \sum_i \int_0^\infty a_i(k_t) \cdot C_{mi}(k_t) \cdot dk_t \qquad (3.1)$$

$$\frac{da_n(\tilde{k}_t)}{dz} + j \cdot \beta_n(\tilde{k}_t) \cdot a_n(\tilde{k}_t) = \sum_i a_i \cdot C_{ni}^c(\tilde{k}_t) + \sum_i \int_0^\infty a_i(k_t) \cdot C_{ni}^c(\tilde{k}_t, k_t) \cdot dk_t \qquad (3.2)$$

with one equation for each possible value of *m* and *n*, including the negative values. The coupling coefficients and phase constants will satisfy the following properties:

$$C_{mi} \cdot N_m = -C_{im} \cdot N_i \quad ; \; m \neq i \tag{3.3}$$

$$C_{mi} = C_{-m-i} \tag{3.4}$$

$$N_m = -N_{-m} \tag{3.5}$$

$$\beta_m = -\beta_{-m} \tag{3.6}$$

being N_m the normalization of the fields; $\vec{E}^m, \vec{H}^m$ the (x,y) dependent part of the electric and magnetic fields of the *m* mode corresponding to the auxiliary uniform waveguide associated to the cross-section of interest (it varies with *z*), and β_m the phase constant of this *m* mode.

The total electric and magnetic fields present in the non-uniform open waveguide will be given by:

$$\hat{E} = \sum_i a_i \cdot \vec{E}^i + \sum_i \int_0^\infty a_i(k_t) \cdot \vec{E}^i(k_t) \cdot dk_t \tag{3.7}$$

$$\hat{H} = \sum_i a_i \cdot \vec{H}^i + \sum_i \int_0^\infty a_i(k_t) \cdot \vec{H}^i(k_t) \cdot dk_t \tag{3.8}$$

In this way we can consider a_i as the complex amplitude of the *i* mode along the non-uniform waveguide, and it will be only function of *z* and frequency.

3.2.1. Obtaining the simplified system

Focusing our study on PBG structures for microstrip lines, the system of coupled mode equations can be notably simplified by realizing several very reasonable approximations:

- In first place, we are going to neglect the coupling of energy to the modes of the continuous spectrum. This can be done because the energy of these modes is primarily radiated, and since the devices that we are going to study (filters, resonators, ..) have very little radiation losses in the frequency bands of interest, the error involved in the approximation will be small. It is important to notice that if our aim were to design devices to radiate (antennas), then the coupling of energy to the modes of the continuous spectrum couldn't be neglected.

- Regarding the modes of the discrete part of the spectrum, for the frequency band of interest we will only have the quasi-TEM mode for the sections of pure

> microstrip line, and a quasi-microstrip mode together with a quasi-slot mode for the sections of microstrip with slot in the ground plane that appear due to the introduction of the PBG structure. There will be no higher order modes due to the frequency band of interest and to the thickness of the substrate employed, in the same way as it would happen for a pure microstrip line [GUP 96] [AIK 89]. Since the excitation of the devices under study will be done through a pure microstrip line, the excitation mode will be always the quasi-TEM mode of the microstrip line (fundamental microstrip mode). This mode has very high correlation with the quasi-microstrip mode (actually it can be seen as the same mode), and very low correlation with the quasi-slot mode, so we can approximate neglecting the excitation of the quasi-slot mode and assuming that only the quasi-microstrip mode is excited.

These approximations lead us to assume single mode operation in our PBG structure for microstrip lines, and in this way they significantly simplify the coupled mode equations. With them, we have to take into account only one mode (the fundamental microstrip or quasi-microstrip mode), with two associated waves: the forward and backward travelling waves, and the system of coupled equations simplifies to:

$$\frac{da^+}{dz} + j \cdot \beta^+ \cdot a^+ = a^+ \cdot C^{++} + a^- \cdot C^{+-} \tag{3.9}$$

$$\frac{da^-}{dz} + j \cdot \beta^- \cdot a^- = a^- \cdot C^{--} + a^+ \cdot C^{-+} \tag{3.10}$$

with the (+) index designating the forward travelling wave associated to the fundamental microstrip or quasi-microstrip mode (actually they are the same mode), and the (–) index designating the backward travelling wave associated to the same mode.

These equations can be further simplified taking advantage of some properties of the involved variables:

from eqn. (3.6), $\beta_m = -\beta_{-m} \Rightarrow \beta^+ = -\beta^- = \beta$ (3.11)

from eqn. (3.4), $C_{mi} = C_{-m-i} \Rightarrow C^{++} = C^{--} = C^{auto}$ (3.12)

$$\left.\begin{array}{ll} \text{from eqn. (3.3),} & C_{mi} \cdot N_m = -C_{im} \cdot N_i \Rightarrow C^{+-} \cdot N^+ = -C^{-+} \cdot N^- \\ \text{from eqn. (3.5),} & N_m = -N_{-m} \Rightarrow N^+ = -N^- \end{array}\right\} \Rightarrow C^{+-} = C^{-+} = K \tag{3.13}$$

Taking all of this into account, the coupled mode equations can be rewritten as:

$$\frac{da^+}{dz} + j \cdot \beta \cdot a^+ = a^+ \cdot C^{auto} + a^- \cdot K \tag{3.14}$$

$$\frac{da^-}{dz} - j \cdot \beta \cdot a^- = a^- \cdot C^{auto} + a^+ \cdot K \tag{3.15}$$

This system of equations can be simplified once more. It can be seen that it is equivalent (it has the same solution) to the following simplified version:

$$\frac{da^+}{dz} + j \cdot \beta \cdot a^+ = a^- \cdot K \tag{3.16}$$

$$\frac{da^-}{dz} - j \cdot \beta \cdot a^- = a^+ \cdot K \tag{3.17}$$

To finish, it is worth noticing that the resulting system of coupled equations can be rewritten in the following normalized form:

$$\frac{d}{dz}\begin{bmatrix} a^+ \\ a^- \end{bmatrix} = \begin{bmatrix} -j \cdot \beta & K \\ K & j \cdot \beta \end{bmatrix} \cdot \begin{bmatrix} a^+ \\ a^- \end{bmatrix} \tag{3.18}$$

with a^+, a^-, the amplitudes of the forward and backward travelling waves associated to the fundamental microstrip or quasi-microstrip mode, β the phase constant of the mode, and K the coupling coefficient between both waves.

It is important also to stress that the only approximation introduced to obtain this simplified system of coupled mode equations is to assume single mode operation.

Another important point to highlight is that although the PBG structure employed can be two dimensional, due to the high confinement of the fields around the conductor strip of the microstrip line, we only take advantage of the periodicity along the conductor strip direction (*z*), and as a result the operation and modeling of the device is 1-D effective.

3.2.2. Numerical solution

As it has been shown, a PBG structure in microstrip technology can be characterized by the simplified system of coupled equations given in eqn. (3.18). The input variables of the problem are $\beta(z,f)$ and $K(z,f)$, being z the direction of propagation and f the frequency of operation.

- The β variable is the phase constant of the operation mode (in our case the fundamental microstrip or quasi-microstrip mode) in the auxiliary uniform waveguide associated to the cross section of interest (it varies with z). It can be expressed as:

$$\beta(z,f) = \frac{2 \cdot \pi \cdot f}{c} \cdot \sqrt{\varepsilon_{eff}(z,f)} \tag{3.19}$$

and it can be calculated by using a numerical method able to calculate the modes of a waveguide. Specifically, for our case, the method must be able to calculate the modes of the discrete spectrum of an open waveguide with a two dimensional and non-separable cross section. In principle this calculation can be done by applying the transverse resonance in the spectral [ITO 80] or in the space domain [ROZ 87] or in the equivalent network form [KOS 86]. The implementation of these numerical methods is beyond the scope of this work, and a commercial software (*Agilent HFSS*) has been used here to calculate the phase constant β.

- The K variable is the coupling coefficient. It depends on the position along the propagation axis, z, and on the operation frequency, f. Several expressions have been obtained in chapter 2 to calculate its value, being each one valid for a different kind of perturbation. All the exact expressions involve the calculation of the fields of the modes in the auxiliary uniform waveguide associated to the cross section of interest (it varies with z). However, we also have an approximate expression given by eqn. (2.108) that requires only the calculation of the characteristic impedance, Z_0, of the mode and that will be employed in our case:

$$K(z,f) = \frac{1}{2} \cdot \frac{1}{Z_0} \cdot \frac{dZ_0}{dz} \tag{3.20}$$

As it was explained earlier, this expression is accurate if the Z_0 of the mode characterizes adequately the propagation of the mode along the waveguide in terms of reflection produced by the variations of cross section present in the waveguide. This can be achieved for our case of fundamental microstrip or quasi-microstrip mode calculating the Z_0 by using the power and the current carried by the mode [GET 83]:

$$Z_0(z,f) = 2 \cdot \frac{P^+}{\left|I^+\right|^2} \tag{3.21}$$

The expression (3.20) for the coupling coefficient assumes also that the normalization of the fields employed is constant along the z direction (i.e. it does not vary with the variation of cross section).

As it has been said above, the implementation of a numerical method to calculate the modes of a waveguide is beyond the scope of this work, and to obtain the Z_0 values needed the commercial software *Agilent HFSS* has been used, selecting the power and current method as the one to be employed in the calculations.

The problem that we have to solve (eqn. (3.18)) is a system of first order linear ordinary differential equations. We have to solve it for the *z* interval that goes from $z =$ 0 to $z = L$, being *L* the length of the device under study. To complete the definition of the problem the boundary conditions must be fixed. In order to study the propagation of the modes along the microstrip PBG when the output port is matched, and to obtain the S parameters of the device, we are interested in solving our problem for the following boundary values:

$$a^+(z=0) = a_{in}^+ = 1 \tag{3.22}$$

$$a^-(z=L) = a_{out}^- = 0 \tag{3.23}$$

With eqn. (3.22) a unitary excitation is set at the input of the device, and with eqn. (3.23) matching conditions are assumed at the output port.

With these boundary conditions our problem becomes a two-point boundary value problem, and to solve it we will use a numerical method implemented in *Matlab*, based on a collocation method for the solution of boundary value problems [SHA 00]. The name of the *Matlab* function employed is *bvp4c*. The phase constant β (and hence ε_{eff}), and the characteristic impedance Z_0 of the auxiliary uniform waveguides are calculated for a set of them (microstrip lines with slots of different widths in the ground plane) and the exact values needed to solve the coupled mode equations with the numerical method are obtained by interpolation.

3.2.3. Calculation of the S-parameters of the device

The S-parameters are widely employed to characterize linear microwave circuits. In their generalized form, they relate the power and the phase of the forward and backward travelling waves at the input and output ports of a circuit, in terms of wave amplitudes [POZ 98]. Here we are going to define them for a single mode of the discrete spectrum that is in propagation at the input and output ports.

The device under study is characterized in the following way by using the complex amplitudes of the mode of interest and its equivalent voltage:

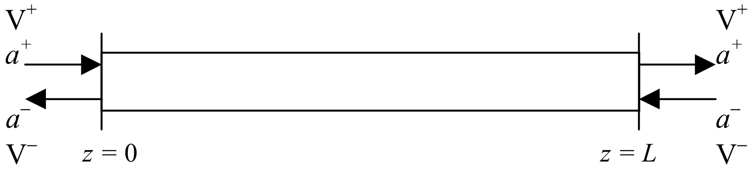

On the other hand a two port device is represented in the following generic form for the calculation of its S-parameters :

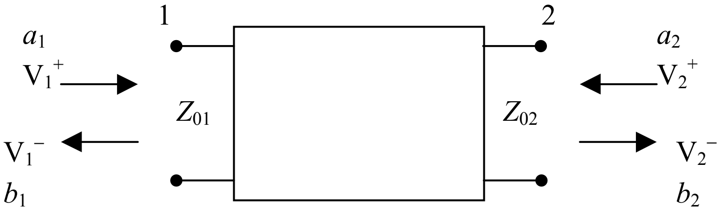

being Z_{0n} the characteristic impedance of the *n* port and

$$a_n = \frac{V_n^+}{\sqrt{Z_{0n}}} \quad ; \quad b_n = \frac{V_n^-}{\sqrt{Z_{0n}}} \tag{3.24}$$

As it can be seen from the graphical representations, the relation between both notations is the following:

$$\begin{aligned} V_1^+ &= V^+(z=0) \\ V_1^- &= V^-(z=0) \\ V_2^+ &= V^-(z=L) \\ V_2^- &= V^+(z=L) \end{aligned} \tag{3.25}$$

and using the expressions for the equivalent voltages obtained in Appendix A, section (A.1), and given by eqn. (A.9) (valid for a discrete spectrum mode in propagation) the following relations hold also:

$$\begin{aligned}
a_1 &= \frac{V_1^+}{\sqrt{Z_{01}}} = \frac{V^+(z=0)}{\sqrt{Z_{01}}} = \frac{\sqrt{Z_{01}}\cdot\sqrt{N_1}\cdot a^+(z=0)}{\sqrt{Z_{01}}} = \sqrt{N_1}\cdot a^+(z=0) \\
b_1 &= \frac{V_1^-}{\sqrt{Z_{01}}} = \frac{V^-(z=0)}{\sqrt{Z_{01}}} = \frac{-\sqrt{Z_{01}}\cdot\sqrt{N_1}\cdot a^-(z=0)}{\sqrt{Z_{01}}} = -\sqrt{N_1}\cdot a^-(z=0) \\
a_2 &= \frac{V_2^+}{\sqrt{Z_{02}}} = \frac{V^-(z=L)}{\sqrt{Z_{02}}} = \frac{-\sqrt{Z_{02}}\cdot\sqrt{N_2}\cdot a^-(z=L)}{\sqrt{Z_{02}}} = -\sqrt{N_2}\cdot a^-(z=L) \\
b_2 &= \frac{V_2^-}{\sqrt{Z_{02}}} = \frac{V^+(z=L)}{\sqrt{Z_{02}}} = \frac{\sqrt{Z_{02}}\cdot\sqrt{N_2}\cdot a^+(z=L)}{\sqrt{Z_{02}}} = \sqrt{N_2}\cdot a^+(z=L)
\end{aligned} \tag{3.26}$$

being $N_n = \left|N_n^{\,+}\right| = \left|N_n^{\,-}\right|$, the normalization of the mode of interest at the *n* port. Taking into account the expression for the power carried by a propagating mode of the discrete spectrum that was deduced in section (2.2.2.3), eqn. (2.28), the power carried by the waves with complex amplitudes a^+, a^- will be:

$$\begin{aligned}
P^+ &= \frac{1}{2}\cdot\left|a^+\right|^2\cdot N \\
P^- &= -\frac{1}{2}\cdot\left|a^-\right|^2\cdot N
\end{aligned} \tag{3.27}$$

As it can be seen from the last equations, the wave amplitudes a_n , b_n are valid to establish physically meaningful power relations, because the power flow is proportional to the square of their modulus.

The S-parameters of a two port network relate the incident and reflected power wave amplitudes a_n , b_n in the following way:

$$\begin{bmatrix} b_1 \\ b_2 \end{bmatrix} = \begin{bmatrix} S_{11} & S_{12} \\ S_{21} & S_{22} \end{bmatrix}\cdot\begin{bmatrix} a_1 \\ a_2 \end{bmatrix} \tag{3.28}$$

From these equations it can be readily seen that:

$$S_{11} = \left.\frac{b_1}{a_1}\right|_{a_2=0} = \left.\frac{-\sqrt{N_1}\cdot a^-(z=0)}{\sqrt{N_1}\cdot a^+(z=0)}\right|_{a^-(z=L)=0} = \left.\frac{-a^-(z=0)}{a^+(z=0)}\right|_{a^-(z=L)=0} \tag{3.29}$$

$$S_{21} = \left.\frac{b_2}{a_1}\right|_{a_2=0} = \left.\frac{\sqrt{N_2}\cdot a^+(z=L)}{\sqrt{N_1}\cdot a^+(z=0)}\right|_{a^-(z=L)=0} \tag{3.30}$$

It is worth noting that if the normalization of the fields is the same at the input and output port of the device (because both ports are identical, or because the normalization doesn't vary with *z*), the expression for the S_{21} parameter is simplified becoming:

$$S_{21} = \left. \frac{a^+(z=L)}{a^+(z=0)} \right|_{a^-(z=L)=0} \tag{3.31}$$

This always happens in our simplified system of coupled mode equations, because the equation taken for the coupling coefficient (3.20) assumes that the normalization of the fields does not vary in the direction of propagation, *z*.

Regarding the S_{11} parameter, it is interesting to note that if the relation between the fields of the forward and backward travelling waves associated to the same *i* mode were:

$$\begin{array}{lll} E_x^{-i} = E_x^{\,i} & ; \; E_y^{-i} = E_y^{\,i} & ; \; E_z^{-i} = -E_z^{\,i} \\ H_x^{-i} = -H_x^{\,i} & ; \; H_y^{-i} = -H_y^{\,i} & ; \; H_z^{-i} = H_z^{\,i} \end{array} \tag{3.32}$$

then the relation between the complex amplitudes of the mode a^+, a^-, and the equivalent voltage and current would be the one calculated in Appendix A, section (A.1), and given by eqn. (A.12), and the S_{11} parameter would have the value:

$$S_{11} = \left. \frac{a^-(z=0)}{a^+(z=0)} \right|_{a^-(z=L)=0} \tag{3.33}$$

It is important to note that this change in the relation between the fields of the forward and backward travelling waves would imply also a change in the sign of the coupling coefficient $K = C^{+-} = C^{-+}$ in such a way that:

$$K_{\substack{new \\ relation}} = -K_{\substack{this \\ work}} \tag{3.34}$$

As it can be seen, fixing the boundary conditions as stated by eqn. (3.22) and (3.23), and solving the simplified system of coupled mode equations, the S parameters are easily obtained by using eqn. (3.29) and (3.31).

3.3. Approximate analytical solutions

In this section, the approximate analytical solution for the simplified system of coupled mode equations that characterizes a PBG structure in microstrip technology is obtained and studied. From this solution, analytical expressions for the parameters that characterize the operation of the PBG (S_{11}, S_{21}, BW, frequency of maximum attenuation, value of the maximum attenuation ..) are deduced, constituting an excellent set of tools for the analysis and design of these devices.

3.3.1 Approximations realized and system with analytical solution

We start from the simplified system of coupled mode equations obtained in section 3.2, eqn. (3.16), (3.17), for a PBG structure in microstrip technology:

$$\begin{aligned} &\frac{da^+}{dz} + j \cdot \beta \cdot a^+ = a^- \cdot K \\ &\frac{da^-}{dz} - j \cdot \beta \cdot a^- = a^+ \cdot K \end{aligned} \tag{3.35}$$

This system has no analytical solution and must be solved by using a numerical method (see section 3.2.2.), but if we introduce two reasonable approximations it will give rise to a system that features the desired analytical solution. The approximations needed are the following:

In first place, we approximate the phase constant β (and hence the effective dielectric constant ε_{eff}) as a variable constant with z. This approximation involves the election of an “averaged” β (and ε_{eff}) for the device under study. As it will be shown later in section 3.3.4, the most adequate value for it is:

$$\varepsilon_{eff} = \left(\frac{1}{\Lambda} \cdot \int_0^{\Lambda} \sqrt{\varepsilon_{eff}(z)} \cdot dz \right)^2 \tag{3.36}$$

being Λ the period of the PBG pattern.

In second place, due to the fact that the PBG structure for microstrip lines will be periodic along the z direction with period Λ, the coupling coefficient, $K(z)$, will be periodic with the same period, and hence it will be amenable to be expanded in a Fourier series [CAR 86]. A similar treatment is presented in [VAS 85], where the periodic coupling is transformed into a constant coupling for the relevant term of the Fourier expansion, allowing an analytical solution for the problem. In our case:

$$K(z)=\sum_{n=-\infty}^{n=\infty} K_n \cdot e^{j\cdot\frac{2\pi}{\Lambda}\cdot n\cdot z} \tag{3.37}$$

with

$$K_n=\frac{1}{\Lambda}\cdot\int_{\Lambda} K(z)\cdot e^{-j\cdot\frac{2\pi}{\Lambda}\cdot n\cdot z}\cdot dz \tag{3.38}$$

From the Fourier theory we know that since *K(z)* is a real function, the following relations will hold:

$$K_{-n}=K_n^{\ *}=\left|K_n\right|\cdot e^{-j\cdot\arg(K_n)} \tag{3.39}$$

$$K(z)=K_0+\sum_{n=1}^{\infty}\left|2\cdot K_n\right|\cdot\cos\left(\frac{2\cdot\pi}{\Lambda}\cdot n\cdot z+\arg(K_n)\right) \tag{3.40}$$

where K_0 will be null, since the mean value of the coupling coefficient of a periodic structure is always zero.

Introducing this expansion of the coupling coefficient *K(z)* in a Fourier series, we will be able to simplify the coupled mode equations. Let's see.

First, we are going to realize a change in the notation:

$$\begin{aligned} a^+(z)&=A^+(z)\cdot e^{-j\cdot\beta\cdot z}\\ a^-(z)&=A^-(z)\cdot e^{+j\cdot\beta\cdot z} \end{aligned} \tag{3.41}$$

Using these new variables the simplified system of coupled mode equations can be rewritten as:

$$\begin{aligned} \frac{dA^+}{dz}&=K(z)\cdot A^-\cdot e^{j\cdot 2\cdot\beta\cdot z}\\ \frac{dA^-}{dz}&=K(z)\cdot A^+\cdot e^{-j\cdot 2\cdot\beta\cdot z} \end{aligned} \tag{3.42}$$

Introducing the expansion in Fourier series of *K(z)*, we obtain:

$$\begin{aligned} \frac{dA^+}{dz}=\Bigg(&K_1\cdot e^{j\cdot 2\cdot\left(\beta+\frac{\pi}{\Lambda}\right)\cdot z}+K_{-1}\cdot e^{j\cdot 2\left(\beta-\frac{\pi}{\Lambda}\right)\cdot z}+K_2\cdot e^{j\cdot 2\cdot\left(\beta+\frac{2\cdot\pi}{\Lambda}\right)\cdot z}+\\ &+K_{-2}\cdot e^{j\cdot 2\cdot\left(\beta-\frac{2\cdot\pi}{\Lambda}\right)\cdot z}+K_3\cdot e^{j\cdot 2\cdot\left(\beta+\frac{3\cdot\pi}{\Lambda}\right)\cdot z}+K_{-3}\cdot e^{j\cdot 2\cdot\left(\beta-\frac{3\cdot\pi}{\Lambda}\right)\cdot z}+\cdots\cdots\Bigg)\cdot A^- \end{aligned} \tag{3.43}$$

$$\frac{dA^-}{dz} = \left(K_1 \cdot e^{-j \cdot 2 \cdot \left(\beta - \frac{\pi}{\Lambda}\right) \cdot z} + K_{-1} \cdot e^{-j \cdot 2 \cdot \left(\beta + \frac{\pi}{\Lambda}\right) \cdot z} + K_2 \cdot e^{-j \cdot 2 \cdot \left(\beta - \frac{2 \cdot \pi}{\Lambda}\right) \cdot z} + \right.$$

$$\left. + K_{-2} \cdot e^{-j \cdot 2 \cdot \left(\beta + \frac{2 \cdot \pi}{\Lambda}\right) \cdot z} + K_3 \cdot e^{-j \cdot 2 \cdot \left(\beta - \frac{3 \cdot \pi}{\Lambda}\right) \cdot z} + K_{-3} \cdot e^{-j \cdot 2 \cdot \left(\beta + \frac{3 \cdot \pi}{\Lambda}\right) \cdot z} + \cdots\cdots \right) \cdot A^+ \quad (3.44)$$

If we have a finite perturbation in the waveguide, $A^+(z)$ and $A^-(z)$ will be function of the position along the waveguide axis, z, and they will vary slowly with z. (It happens because $\left|A^+(z)\right|^2$ and $\left|A^-(z)\right|^2$ are proportional to the power carried by the forward and backward travelling waves, respectively).

To continue our reasoning, we are going to introduce the condition of resonant coupling. By resonant coupling we mean a mode coupling when the following condition is satisfied:

$$\beta_m - \beta_i - n \cdot \frac{2 \cdot \pi}{\Lambda} = 0 \quad (3.45)$$

being n an integer. This condition is of fundamental importance and it is known in the literature as longitudinal phase matching or just phase matching. It can be seen also as conservation of momentum [YAR 84]. When this condition holds, an important transfer of energy can exist between the two modes involved. The condition of resonant coupling has the following form in our case of mode coupling between the forward and backward travelling waves associated to the same mode:

$$\beta^+ - \beta^- - n \cdot \frac{2 \cdot \pi}{\Lambda} = 0 \Rightarrow \beta - (-\beta) - n \cdot \frac{2 \cdot \pi}{\Lambda} = 0 \Rightarrow 2 \cdot \beta - n \cdot \frac{2 \cdot \pi}{\Lambda} = 0 \quad (3.46)$$

and is customarily formulated as:

$$\beta - n \cdot \frac{\pi}{\Lambda} = 0 \Rightarrow \beta = n \cdot \frac{\pi}{\Lambda} \quad (3.47)$$

When this last condition is satisfied, the forward and backward travelling waves are strongly coupled by the perturbation, and an important amount of the power carried by the forward wave is transferred to the backward wave, giving rise to a large reflection. Actually, as it will be seen later, the n-th rejected frequency band of a PBG structure in microstrip technology will be placed around the exact frequency at which the resonant coupling happens, and the frequency of maximum reflectivity of this n-th rejected band will be the frequency of resonant coupling.

So, if our frequency band of interest is placed around the *n*-th rejected frequency band, then the variable $\Delta\beta$ defined as:

$$\Delta\beta = \beta - n \cdot \frac{\pi}{\Lambda} \tag{3.48}$$

will have a very little value, because we will be placed around the condition of resonant coupling given by eqn. (3.47). In this case, all the complex exponentials that appear in eqn. (3.43), excluding the one that multiplies the coefficient K_{-n}, will be complex exponentials of the form $e^{j \cdot func(\beta) \cdot z}$ that vary very quickly with *z*. The complex exponential that multiplies K_{-n} will have the form $e^{j \cdot 2 \cdot \Delta\beta \cdot z}$ and therefore it will vary very slowly with *z* (all of this will happen for the frequency band of interest: i.e. the frequency range around the *n*-th rejected frequency band).

When we multiply the function $A^{-}(z)$, a function that varies slowly with *z*, by a complex exponential that oscillates very quickly with *z*, and we integrate the product in *z*, over a distance which is much larger than the period of oscillation, we obtain a result that tends to vanish. (It will be a contribution close to zero). On the other hand, when we multiply the function $A^{-}(z)$, a function that varies slowly with *z*, by the term $K_{-n} \cdot e^{j \cdot 2 \cdot \Delta\beta \cdot z}$, a term that also varies slowly with *z*, and we integrate in *z*, a relevant contribution will be obtained in such a way that the contributions of the other terms of equation (3.43) will be negligible when compared to it. As it can be seen this statement will be valid for the range of frequencies placed around the *n*-th rejected frequency band, in which the conditions of quick oscillation and slow oscillation of the complex exponentials involved will hold. Moreover, in order to have a negligible contribution from the terms with exponentials that oscillate very quickly with *z* it will be necessary to perform the integration in *z* over a distance much larger than the period of oscillation, and hence the length of the PBG under study must be "large enough". It is important to notice, however, that a length around two PBG periods is usually enough.

By using the same reasoning in eqn. (3.44), the only relevant contribution once the integration has been done will be contribution of the term $K_{n} \cdot e^{-j \cdot 2 \cdot \Delta\beta \cdot z}$.

This phenomenon that makes that only the contribution of certain terms of the coupled mode equations is relevant, for a certain frequency band, is known in the literature as phase matching [YAR 84].

Consequently, for the frequency range around the *n*-th rejected frequency band, and for a PBG "large enough", the coupled mode equations can be approximated and simplified in the following way:

$$
\begin{aligned}
\frac{dA^+}{dz} &= K_n^{\,*} \cdot e^{j \cdot 2 \cdot \Delta\beta \cdot z} \cdot A^- \\
\frac{dA^-}{dz} &= K_n \cdot e^{-j \cdot 2 \cdot \Delta\beta \cdot z} \cdot A^+
\end{aligned}
\tag{3.49}
$$

after having taken advantage of eqn. (3.39), and of the definition of $\Delta\beta$, eqn. (3.48).

It is interesting to note that an identical system of coupled mode equations is also obtained when a uniform Fiber Bragg Grating or a uniform optical periodic dielectric waveguide is studied by using the coupled mode theory [PAS 96, YAR 97, YAR 84]. However, the starting point to obtain the equations is different from the one that we have used for PBG structures in microstrip technology.

In the case of Fiber Bragg Gratings, the longitudinal perturbation introduced in the refraction index is very small, and therefore we can approximate assuming that the longitudinal perturbation doesn't alter the (x,y) dependent part of the fields of the mode, nor its phase constant, and it only affects the amplitude of the associated wave and hence the power carried.

The approach taken assumes that the fields in a cross section of the perturbed optical fiber can be represented as a superposition of the modes of the unperturbed optical fiber. The amplitude of the waves associated to these modes will be variable with z though. This approach is referred to in [MAR 91] as "expansion in terms of ideal modes", while the approach that we use to model PBG structures for microstrip lines (the cross section method) is referred to as "expansion in terms of local normal modes".

It is worth noting that the expansion in terms of ideal modes is very good for the case of Fiber Bragg Gratings because the perturbation present in the optical fiber is very small, but it wouldn't be suitable for PBG´s in microstrip technology. In the PBG case, the perturbation introduced is so strong that the modes of the unperturbed structure can no longer be taken as a base to expand the fields in all the perturbed structure, but different modes must be taken for different cross sections.

However, the fact that the simplified equations that govern the behavior of both kind of devices are the same suggests that a lot of ideas and techniques employed in the developed and mature field of Fiber Bragg Gratings [KAS 99, OTH 99] could be easily and successfully translated to the novel and emerging field of PBG structures for planar microwave and millimeter wave circuits.

3.3.2. Obtaining the analytical solution

Let's see now the analytical solution of the approximate simplified system of coupled mode equations that characterizes a PBG structure for microstrip lines, given in the previous section by eqn. (3.49):

$$\frac{dA^+}{dz} = K_n^{\ *} \cdot e^{j \cdot 2 \cdot \Delta\beta \cdot z} \cdot A^-$$

$$\frac{dA^-}{dz} = K_n \cdot e^{-j \cdot 2 \cdot \Delta\beta \cdot z} \cdot A^+$$

and (3.48):

$$\Delta\beta = \beta - n \cdot \frac{\pi}{\Lambda}$$

The expression for the coupling coefficient that we are going to use is, as we have stated in section (3.2.2.), the one given by eqn. (3.20):

$$K(z) = \frac{1}{2} \cdot \frac{1}{Z_0} \cdot \frac{dZ_0}{dz}$$

and for our case of PBG´s in microstrip technology, if the perturbation introduced in the ground plane to form the PBG pattern starts with a slot width equal to zero, and evolves increasing and decreasing the slot width in a continuos manner, without abrupt discontinuities, then the coupling coefficient will satisfy:

$$K(z) = \sum_{n=1}^{\infty} |2 \cdot K_n| \cdot \mathrm{sen}\left(\frac{2 \cdot \pi}{\Lambda} \cdot n \cdot z\right) = \sum_{n=1}^{\infty} |2 \cdot K_n| \cdot \cos\left(\frac{2 \cdot \pi}{\Lambda} \cdot n \cdot z + \arg(K_n)\right) \tag{3.50}$$

and therefore the value for the argument of K_n will be $\arg(K_n) = -90°$, and hence:

$$K_n = -j \cdot |K_n| \tag{3.51}$$

Due to the form of eqn. (3.51), it seems convenient to redefine the coupling coefficient parameter, introducing the k parameter, in such a way that:

$$k = j \cdot K_n \tag{3.52}$$

With this definition the novel k parameter will be always a real number for our case of PBG´s printed in the ground plane of a microstrip line, provided that the conditions about the slot width starting from zero, and evolving without abrupt discontinuities are satisfied.

Using the novel coupling coefficient parameter, *k*, the approximate coupled mode equations can be rewritten as:

$$\begin{aligned} \frac{dA^+}{dz} &= j \cdot k^* \cdot e^{j \cdot 2 \cdot \Delta\beta \cdot z} \cdot A^- \\ \frac{dA^-}{dz} &= -j \cdot k \cdot e^{-j \cdot 2 \cdot \Delta\beta \cdot z} \cdot A^+ \end{aligned} \tag{3.53}$$

with Δβ given by eqn. (3.48)

$$\Delta\beta = \beta - n \cdot \frac{\pi}{\Lambda}$$

In order to obtain the analytical solution of eqn. (3.53) in a simpler way, we are going to perform a change in the notation. A pair of new variables will be introduced following the notation of Kogelnik [KOG 72, PAS 96]:

$$\begin{aligned} R(z) &= A^+(z) \cdot e^{-j \cdot \Delta\beta \cdot z} = A^+(z) \cdot e^{-j \cdot \left(\beta - n \cdot \frac{\pi}{\Lambda}\right) \cdot z} = a^+(z) \cdot e^{j \cdot n \cdot \frac{\pi}{\Lambda} \cdot z} \\ S(z) &= -A^-(z) \cdot e^{j \cdot \Delta\beta \cdot z} = -A^-(z) \cdot e^{j \cdot \left(\beta - n \cdot \frac{\pi}{\Lambda}\right) \cdot z} = -a^-(z) \cdot e^{-j \cdot n \cdot \frac{\pi}{\Lambda} \cdot z} \end{aligned} \tag{3.54}$$

Using the new variables the approximate coupled mode equations can be rewritten as:

$$\begin{aligned} \frac{dR}{dz} &= -j \cdot \Delta\beta \cdot R - j \cdot k^* \cdot S \\ \frac{dS}{dz} &= j \cdot \Delta\beta \cdot S + j \cdot k \cdot R \end{aligned} \tag{3.55}$$

The general solution of these equations (3.55) is of the form [KOG 72, PAS 96]:

$$\begin{aligned} R(z) &= R^+ \cdot e^{-\gamma \cdot z} + R^- \cdot e^{\gamma \cdot z} \\ S(z) &= S^+ \cdot e^{-\gamma \cdot z} + S^- \cdot e^{\gamma \cdot z} \end{aligned} \tag{3.56}$$

where

$$\gamma = +\sqrt{|k|^2 - (\Delta\beta)^2} \tag{3.57}$$

To obtain the analytical solution for our particular problem we have to fix the boundary conditions. To do it we will assume that the perturbed waveguide with length *L* extends from *z*=-*L* to *z*=0. We will suppose also that the output port at *z*=0 is matched, and hence the reflected wave at this point will be equal to zero, that is:

$$a^{-}(z=0)=0 \Rightarrow S(z=0)=0 \tag{3.58}$$

From this last condition (3.58), and applying the solution (3.56) we obtain that $S^{+}=-S^{-}$, and therefore, again form eqn. (3.56), the following partial result for *S(z)* is obtained:

$$S(z)=-2\cdot S^{+}\cdot\sinh(\gamma\cdot z) \tag{3.59}$$

Introducing the result (3.59) in the coupled mode equations (3.55) the corresponding partial solution for *R(z)* is also obtained:

$$R(z)=-2\cdot S^{+}\cdot\left(\frac{\gamma}{j\cdot k}\cdot\cosh(\gamma\cdot z)-j\cdot\frac{\Delta\beta}{j\cdot k}\cdot\sinh(\gamma\cdot z)\right) \tag{3.60}$$

Assuming an incident wave at the input port $R(z=-L)=R_0$, we can eliminate the constant S^{+} from eqn. (3.60) and (3.59), giving rise to the following expressions for *R(z)* and *S(z)*:

$$\begin{aligned} R(z)&=\frac{R_0\cdot\left(\Delta\beta\cdot\sinh(\gamma\cdot z)+j\cdot\gamma\cdot\cosh(\gamma\cdot z)\right)}{-\Delta\beta\cdot\sinh(\gamma\cdot L)+j\cdot\gamma\cdot\cosh(\gamma\cdot L)}\\ S(z)&=\frac{-R_0\cdot k\cdot\sinh(\gamma\cdot z)}{-\Delta\beta\cdot\sinh(\gamma\cdot L)+j\cdot\gamma\cdot\cosh(\gamma\cdot L)} \end{aligned} \tag{3.61}$$

Performing the following change of variable:

$$z'=z+L \tag{3.62}$$

to have the perturbed waveguide of length L placed between $z'=0$ and $z'=L$, and using again the variable z for simplicity, we will have that the analytical solution for the approximate coupled mode equations (3.55) that characterize a PBG structure in microstrip technology with length L placed between z=0 and $z = L$, with an incident wave $R(z=0)=R_0$ and with the output port matched, will be:

$$R(z)=\frac{R_0\cdot\left(\Delta\beta\cdot\sinh(\gamma\cdot(z-L))+j\cdot\gamma\cdot\cosh(\gamma\cdot(z-L))\right)}{-\Delta\beta\cdot\sinh(\gamma\cdot L)+j\cdot\gamma\cdot\cosh(\gamma\cdot L)}$$

$$S(z)=\frac{-R_0\cdot k\cdot\sinh(\gamma\cdot(z-L))}{-\Delta\beta\cdot\sinh(\gamma\cdot L)+j\cdot\gamma\cdot\cosh(\gamma\cdot L)} \tag{3.63}$$

To finish, we are going to change the variables *R(z)* , *S(z)* that we have used to solve the approximate coupled mode equations, for the complex amplitudes $a^+(z)$, $a^-(z)$ of the forward and backward travelling waves associated to the mode of interest using the relations of eqn. (3.54). By means of this change of variable we obtain that the analytic solution of the approximate system of coupled mode equations:

$$\begin{aligned}&\frac{da^+}{dz}+j\cdot\beta\cdot a^+=K^*(z)\cdot a^-\\&\frac{da^-}{dz}-j\cdot\beta\cdot a^-=K(z)\cdot a^+\end{aligned} \tag{3.64}$$

with

$$K(z)=-j\cdot k\cdot e^{j\cdot\frac{2\cdot\pi}{\Lambda}\cdot n\cdot z}=K_n\cdot e^{j\cdot\frac{2\cdot\pi}{\Lambda}\cdot n\cdot z} \tag{3.65}$$

that characterize a PBG structure in microstrip technology with length L placed between $z=0$ and $z=L$, excited by an incident wave $a^+(z=0)=a^+(0)$ and with the output port matched, (i.e. $a^-(z=L)=0$) will be:

$$a^+(z)=\frac{\Delta\beta\cdot\sinh(\gamma\cdot(z-L))+j\cdot\gamma\cdot\cosh(\gamma\cdot(z-L))}{-\Delta\beta\cdot\sinh(\gamma\cdot L)+j\cdot\gamma\cdot\cosh(\gamma\cdot L)}\cdot a^+(0)\cdot e^{-j\cdot\frac{\pi}{\Lambda}\cdot n\cdot z}$$

$$a^-(z)=\frac{k\cdot\sinh(\gamma\cdot(z-L))}{-\Delta\beta\cdot\sinh(\gamma\cdot L)+j\cdot\gamma\cdot\cosh(\gamma\cdot L)}\cdot a^+(0)\cdot e^{j\cdot\frac{\pi}{\Lambda}\cdot n\cdot z} \tag{3.66}$$

with

$$\begin{aligned}&\Delta\beta=\beta-n\cdot\frac{\pi}{\Lambda}\\&\gamma=+\sqrt{|k|^2-(\Delta\beta)^2}\end{aligned}$$

$\Delta\beta$ is given by eqn. (3.48) and γ by eqn. (3.57).

Equivalent analytical expressions to those of eqn. (3.66) are obtained in [YAR 73, YAR 84, PAS 96] in the optical domain, for uniform periodic dielectric waveguides and for Fiber Bragg Gratings. It should be noted, however, that the theory of coupled modes was originated in the microwave area, driven by the research for the waveguide telecommunication projects [MIL 54]. Several approaches to the theory can be traced since then. In [MIL 54a], an analytical solution for the constant coupling case is presented, and the periodic coupling case is addressed in [MIL 68]. Moreover, this theory has been applied to the case of mode conversion in oversized circular waveguides, using periodic wall perturbations, for high-power millimeter wave applications, see [THU 84]. There, by using an averaging of the rapidly oscillating terms, the periodic coupling coefficient is transformed into an uniform effective coupling coefficient in order to apply the theory of tight coupling of Miller, [MIL 54a]. Nevertheless, the coupled mode theory has experienced a remarkable development due to contributions from the integrated optics area, where it is today a very mature tool for the analysis and design of advanced devices, see [HAU 91]. Now, we experience a backward wave from the optical community that returns to the microwave researchers the seminal work, forward wave, initiated during the fifties. This fact is an example of fruitful interaction between two research fields sharing a same theory, the coupled mode method.

Continuing with eqns. (3.66), the relation between the complex amplitudes $a^+(z)$, $a^-(z)$ and the total field present in the waveguide was given for the general case in section (3.2) by eqn. (3.7) and (3.8), and for the simplified system of coupled mode equations it has the form:

$$\begin{aligned} \hat{\vec{E}} &= a^+ \cdot \vec{E}^+ + a^- \cdot \vec{E}^- \\ \hat{\vec{H}} &= a^+ \cdot \vec{H}^+ + a^- \cdot \vec{H}^- \end{aligned} \tag{3.67}$$

being $\vec{E}^+, \vec{H}^+, \vec{E}^-, \vec{H}^-$ the (x,y) dependent part of the electric and magnetic fields of the forward (+) and backward (–) travelling waves corresponding to the fundamental microstrip (or quasi-microstrip) mode of the auxiliary uniform waveguide associated to the cross-section of interest (it varies with z). The details about the normalization and relations between these fields were studied in chapter 2, section (2.2).

As we have seen previously in section (3.3.1), to go from the simplified system of coupled mode equations, eqn. (3.35), that characterizes a PBG structure in microstrip technology, to the approximate system (3.64) that has analytical solution, we have realized two reasonable approximations:

- We approximate the phase constant β as a variable constant with z. This approximation involves the election of an "averaged" β that is assumed to remain constant along the device.
- We neglect the terms that include complex exponentials that oscillate very quickly with z, keeping the terms with complex exponentials that vary slowly with z. This can be done for the range of frequencies placed around the maximum reflection frequency of the rejected band (bandgap) of interest, and for a PBG device "large enough". As it can be seen this approximation involves the election of a rejected band of interest around which the analytical solution will be valid. Each K_n of the coupling coefficient Fourier series, eqn. (3.37), will correspond to the rejected band of index n, being the index of the first rejected band $n=1$. The approximation will get worse as the frequency of calculation moves away from the rejected band of interest and if the length of the device is short. It is important to notice, however, that regarding the length around two PBG periods is usually enough.

Taking into account all of this we can say that the analytical solutions given by eqn. (3.66) are also approximate analytical solutions for the equations that characterize the operation of a PBG in microstrip technology, eqn. (3.35), and it will happen that the better the two approximations that we have just detailed are satisfied, the more accurate the prediction given by the approximate analytical solutions will be.

3.3.3. Analytical expressions for several Important parameters

Using the analytical solutions that we have just calculated in the previous section for the complex amplitudes $a^+(z)$, $a^-(z)$ in a PBG in microstrip technology with length L, and with the output port matched (eqn. (3.66)), we can also obtain analytical solutions for several important parameters that characterize its operation: S_{11} , S_{21} , frequency of maximum reflectivity, value of this maximum reflectivity, reflected bandwidth and transmission matrix. Similar deductions to those carried out along this section can be found in [YAR 84, YAM 87, KAS 99, OTH 99] for optical periodic dielectric waveguides and Fiber Bragg Gratings, giving rise to similar analytical expressions.

3.3.3.1. S$_{11}$ and S$_{21}$ parameters

The value for the S$_{11}$ and S$_{21}$ parameters will be, using eqn. (3.29) and (3.31):

$$S_{11} = \left.\frac{-a^-(z=0)}{a^+(z=0)}\right|_{a^-(z=L)=0} = \frac{k \cdot \sinh(\gamma \cdot L)}{-\Delta\beta \cdot \sinh(\gamma \cdot L) + j \cdot \gamma \cdot \cosh(\gamma \cdot L))} \tag{3.68}$$

$$S_{21} = \left.\frac{a^+(z=L)}{a^+(z=0)}\right|_{a^-(z=L)=0} = \frac{j \cdot \gamma \cdot e^{-j\cdot\frac{\pi}{\Lambda}\cdot n\cdot L}}{-\Delta\beta \cdot \sinh(\gamma \cdot L) + j \cdot \gamma \cdot \cosh(\gamma \cdot L)} \tag{3.69}$$

where k is the coupling coefficient parameter, eqn. (3.20), (3.38) and (3.52), $\Delta\beta$ is given by eqn. (3.48), γ is given by eqn. (3.57), n is the index of the rejected band of interest (n=1 for the first rejected band), and Λ and L are the period and length of the PBG structure, respectively.

$$\Delta\beta = \beta - n \cdot \frac{\pi}{\Lambda}$$
$$\gamma = +\sqrt{|k|^2 - (\Delta\beta)^2}$$

3.3.3.2. Frequency of maximum reflectivity, *f$_{max}$* , $|S_{11}|_{max}$ and $|S_{21}|_{min}$

With respect to the frequency of maximum reflectivity (and maximum attenuation), from eqn. (3.68) and (3.69) it can be seen that it corresponds to the frequency that satisfies $\Delta\beta = 0$, and therefore its value is

$$\begin{gathered} \Delta\beta = 0 \Rightarrow \beta_{max} = n \cdot \frac{\pi}{\Lambda} \Rightarrow \frac{2 \cdot \pi \cdot f_{max}}{c} \cdot \sqrt{\varepsilon_{eff}} = n \cdot \frac{\pi}{\Lambda} \Rightarrow \\ \Rightarrow f_{max} = n \cdot \frac{c}{2 \cdot \sqrt{\varepsilon_{eff}} \cdot \Lambda} \end{gathered} \tag{3.70}$$

where c is the speed of light in vacuum, $c = 3 \cdot 10^8$ m/s, and ε_{eff} is the effective dielectric constant of the PBG device.

The value of this maximum reflectivity is (from eqn. (3.68) with $\Delta\beta = 0$)

$$|S_{11}|_{max} = \tanh(|k| \cdot L) \tag{3.71}$$

and its phase

$$\arg(S_{11}(f_{max})) = -\frac{\pi}{2} + \arg(k) = \arg(K_n) \ \text{, rad} \tag{3.72}$$

and the corresponding value of maximum attenuation (minimum transmission), (from eqn. (3.69) with $\Delta\beta = 0$) is given by

$$|S_{21}|_{min} = \frac{1}{\cosh(|k| \cdot L)} = \mathrm{sech}(|k| \cdot L) \tag{3.73}$$

and its phase

$$\arg(S_{21}(f_{max})) = -\frac{\pi}{\Lambda} \cdot n \cdot L \ \text{, rad} \tag{3.74}$$

3.3.3.3. Reflected bandwidth, BW$_\infty$, and sidelobes

Regarding the reflected bandwidth around the frequency of maximum reflectivity, we are going to calculate it between the first minima or zeroes of reflection around the reflected band, BW$_\infty$.

From eqn. (3.68) it can be seen that the frequency of the first minimum of reflection will satisfy:

$$\gamma \cdot L = j \cdot \pi \tag{3.75}$$

and hence

$$\sqrt{|k|^2 - (\Delta\beta)^2} \cdot L = j \cdot \pi \Rightarrow \left(|k|^2 - (\Delta\beta)^2\right) \cdot L^2 = -\pi^2 \Rightarrow |k|^2 + \frac{\pi^2}{L^2} = (\Delta\beta)^2 \tag{3.76}$$

At the same time, if we assume ε_{eff} as constant with the frequency in the rejected bandwidth (i.e. if we neglect the dispersion):

$$\Delta\beta = \beta - n \cdot \frac{\pi}{\Lambda} = \beta - \beta_{max} = \frac{2 \cdot \pi}{c} \cdot \sqrt{\varepsilon_{eff}} \cdot (f - f_{max}) \tag{3.77}$$

On the other hand, if we take into account the dispersion:

$$\Delta\beta = \beta - n\cdot\frac{\pi}{\Lambda} = \beta - \beta_{max} \approx \frac{d\beta}{d\omega}\cdot(\omega-\omega_{max}) = \frac{1}{v_g}\cdot(\omega-\omega_{max}) = \\ = \frac{n_g}{c}\cdot(\omega-\omega_{max}) = \frac{2\cdot\pi}{c}\cdot n_g\cdot(f-f_{max}) \tag{3.78}$$

being v_g the group velocity, and n_g the group index.

As it can be seen, the expression for $\Delta\beta$ is the same in both cases (eqn. (3.77), (3.78)), if we replace $\sqrt{\varepsilon_{eff}} = n_{eff}$ (expression that neglects the dispersion) by n_g (expression that takes into account the dispersion).

Continuing our deduction with the expression that neglects the dispersion, eqn. (3.77), and introducing it in eqn. (3.76), the equation for the bandwidth of the reflected frequency band calculated between zeroes of reflection is obtained:

$$|k|^2 + \frac{\pi^2}{L^2} = \left(\frac{2\cdot\pi}{c}\sqrt{\varepsilon_{eff}}\right)^2 (f_{zero} - f_{max})^2 \Rightarrow |k|^2 + \frac{\pi^2}{L^2} = \left(\frac{2\cdot\pi}{c}\sqrt{\varepsilon_{eff}}\right)^2\left(\frac{BW_\infty}{2}\right)^2 \Rightarrow \\ \Rightarrow BW_\infty = \frac{c\cdot|k|}{\pi\cdot\sqrt{\varepsilon_{eff}}}\cdot\sqrt{1+\left(\frac{\pi}{|k|\cdot L}\right)^2} \tag{3.79}$$

As we have already discussed, to take into account the dispersion we have only to substitute the $\sqrt{\varepsilon_{eff}}$ by the group index, n_g , in the equation for the bandwidth, (3.79).

Let’s see now two extreme cases in the calculation of the rejected bandwidth:

- If $(|k|\cdot L)^2 << \pi^2$ (case of low reflectivity and low attenuation), then

$$BW_\infty = \frac{c\cdot|k|}{\pi\cdot\sqrt{\varepsilon_{eff}}}\cdot\frac{1}{|k|\cdot L}\sqrt{(|k|\cdot L)^2+\pi^2} \Rightarrow BW_\infty \approx \frac{c}{\sqrt{\varepsilon_{eff}}\cdot L} \tag{3.80}$$

- If $(|k|\cdot L)^2 >> \pi^2$ (case of high reflectivity and high attenuation), then

$$BW_\infty = \frac{c\cdot|k|}{\pi\cdot\sqrt{\varepsilon_{eff}}}\cdot\sqrt{1+\left(\frac{\pi}{|k|\cdot L}\right)^2} \Rightarrow BW_\infty \approx \frac{c\cdot|k|}{\pi\cdot\sqrt{\varepsilon_{eff}}} \tag{3.81}$$

Aside from the main rejected frequency band centered at the maximum reflection frequency f_{max} , and with a bandwidth BW_∞ , the reflectivity spectrum of the PBG structure in microstrip technology also consists of a series of sidelobes on both sides of the main rejected band. These sidelobes have their peak value approximately at:

$$\gamma \cdot L = j \cdot \left(p + \frac{1}{2}\right) \cdot \pi \quad ; \quad p=1, 2, 3, ... \tag{3.82}$$

which corresponds to:

$$\Delta\beta = \pm\sqrt{|k|^2 + \left(p + \frac{1}{2}\right)^2 \cdot \left(\frac{\pi}{L}\right)^2} = \frac{2 \cdot \pi}{c} \cdot \sqrt{\varepsilon_{eff}} \cdot (f_{peak} - f_{max}) \tag{3.83}$$

and the approximate value for their peak reflectivity is:

$$|S_{11}|_{peak} = \frac{|k \cdot L|}{\sqrt{|k \cdot L|^2 + (p + 1/2)^2 \cdot \pi^2}} \tag{3.84}$$

The sidelobes are separated by reflection zeroes that are placed exactly at:

$$\gamma \cdot L = j \cdot q \cdot \pi \quad ; \quad q=1, 2, 3, ... \tag{3.85}$$

which corresponds to

$$\Delta\beta = \pm\sqrt{|k|^2 + q^2 \cdot \left(\frac{\pi}{L}\right)^2} = \frac{2 \cdot \pi}{c} \cdot \sqrt{\varepsilon_{eff}} \cdot (f_{zero} - f_{max}) \tag{3.86}$$

3.3.3.4. Transmission matrix parameters

To complete our set of analytical expressions for PBG structures in microstrip technology, we are going to deduce the transmission matrix by using again the analytical expression obtained in the previous section for the complex amplitudes $a^+(z)$, $a^-(z)$ in a PBG of length L. The transmission matrix relates the complex amplitudes of the incident and reflected waves at the input (z=0) and output (z=L) ports of the PBG microstrip device in the following manner:

$$\begin{bmatrix} a^+(z=0) \\ a^-(z=0) \end{bmatrix} = \begin{bmatrix} A_{11} & A_{12} \\ A_{21} & A_{22} \end{bmatrix} \cdot \begin{bmatrix} a^+(z=L) \\ a^-(z=L) \end{bmatrix} \tag{3.87}$$

To make the calculation of the transmission matrix easier, we are going to use an important property of this matrix shown in Appendix C, eqn. (C.6), and applicable to our PBG structures in microstrip technology. It states that the transmission matrix of a reciprocal (passive and without anisotropic elements) and lossless two port network, that has normalizations in both ports that are equal, or are real numbers or at least have a quotient that is a real number, satisfies that:

$$\begin{aligned} A_{12} &= A_{21}^{*} \\ A_{22} &= A_{11}^{*} \end{aligned} \tag{3.88}$$

and hence, using this property, it will be enough to calculate the value for the A_{11} and A_{21} parameters that are readily obtained from the equations for $a^{+}(z)$, $a^{-}(z)$ (3.66):

$$\begin{aligned} A_{11} &= \left.\frac{a^{+}(z=0)}{a^{+}(z=L)}\right|_{a^{-}(z=L)=0} = \left(\cosh(\gamma\cdot L)+\frac{j\cdot\Delta\beta\cdot L\cdot\sinh(\gamma\cdot L)}{\gamma\cdot L}\right)\cdot e^{j\cdot\frac{\pi}{\Lambda}\cdot n\cdot L} \\ A_{21} &= \left.\frac{a^{-}(z=0)}{a^{+}(z=L)}\right|_{a^{-}(z=L)=0} = \frac{j\cdot k\cdot L\cdot\sinh(\gamma\cdot L)}{\gamma\cdot L}\cdot e^{j\cdot\frac{\pi}{\Lambda}\cdot n\cdot L} \end{aligned} \tag{3.89}$$

to finish we can calculate the rest of the values from eqn. (3.88).

The transmission matrices allow the analytical study of nonuniform PBG structures obtained by cascading uniform ones. The total transmission matrix can be calculated by multiplying the transmission matrices of the constituent structures:

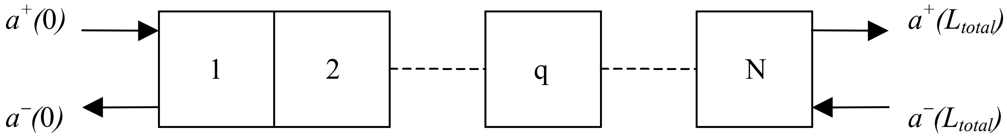

$$\begin{bmatrix} A_{11}^{\,total} & A_{12}^{\,total} \\ A_{21}^{\,total} & A_{22}^{\,total} \end{bmatrix} = \begin{bmatrix} A_{11}^{\,1} & A_{12}^{\,1} \\ A_{21}^{\,1} & A_{22}^{\,1} \end{bmatrix} \cdot \begin{bmatrix} A_{11}^{\,2} & A_{12}^{\,2} \\ A_{21}^{\,2} & A_{22}^{\,2} \end{bmatrix} \cdots \begin{bmatrix} A_{11}^{\,q} & A_{12}^{\,q} \\ A_{21}^{\,q} & A_{22}^{\,q} \end{bmatrix} \cdots \begin{bmatrix} A_{11}^{\,N} & A_{12}^{\,N} \\ A_{21}^{\,N} & A_{22}^{\,N} \end{bmatrix} \tag{3.90}$$

In particular the presence of defects (e.g. missing periods) can be modeled.

To make easier the study of phase shifts introduced in the PBG structure, the coupling coefficient, k, is expressed in the following form:

$$\begin{aligned} k &= |k|\cdot e^{j\cdot\phi} \\ \phi &= \arg(k) \end{aligned} \tag{3.91}$$

and with this notation the equations for the transmission matrix parameters become:

$$A_{11} = \left(\cosh(\gamma \cdot L) + \frac{j \cdot \Delta\beta \cdot L \cdot \sinh(\gamma \cdot L)}{\gamma \cdot L} \right) \cdot e^{j \cdot \frac{\pi}{\Lambda} \cdot n \cdot L}$$
$$A_{21} = \frac{j \cdot |k| \cdot L \cdot \sinh(\gamma \cdot L)}{\gamma \cdot L} \cdot e^{j \cdot \left(\frac{\pi}{\Lambda} \cdot n \cdot L + \phi \right)} \tag{3.92}$$

If the total PBG device is formed by cascading uniform PBG structures that can include phase shifts between them, $\Delta\phi$, the argument of the coupling coefficient of the q-th uniform PBG, ϕ^q, can be easily calculated by using the expression:

$$\phi^q = \phi^{q-1} + 2 \cdot \frac{\pi}{\Lambda} \cdot n \cdot L^{k-1} + \Delta\phi^q \tag{3.93}$$

The calculation of the S-parameters from the transmission matrix parameters is straightforward and can be done by using the following relations:

$$S_{11} = \left. \frac{-a^-(z=0)}{a^+(z=0)} \right|_{a^-(z=L)=0} = \frac{-A_{21}}{A_{11}} \quad \Rightarrow \quad S_{11} = \frac{-A_{21}}{A_{11}}$$
$$S_{21} = \left. \frac{a^+(z=L)}{a^+(z=0)} \right|_{a^-(z=L)=0} = \frac{1}{A_{11}} \quad \Rightarrow \quad S_{21} = \frac{1}{A_{11}} \tag{3.94}$$

with the general expression for the S_{11} and S_{21} parameters given by eqn. (3.29) and (3.31), respectively. It must be noted that in the deduction of the S_{21} parameter it has been assumed that the fields at the input and output port have the same normalization. If it weren't the case, the expression should be modified according to eqn. (3.30).

It is important to notice that the transmission matrix obtained characterizes the PBG structure in microstrip technology assuming continuity conditions for the forward and backward travelling waves at the interfaces of z=0 and z=L. That is, the transmission matrix calculated fully characterizes the device if the profile in the waveguide under analysis is continuous at the input and output port (i.e. it doesn't feature discontinuities at the ports).

It is important also to take into account that all the analytical expressions developed in this section have been obtained from the analytical solutions for the approximate system of coupled mode equations (3.64) that characterizes a PBG structure in microstrip technology. Therefore all the expressions are approximated, because as it was shown in section (3.3.1.) there are two reasonable approximations involved:

- The phase constant β is approximated as a variable constant with z. An "averaged" β is assigned to all the device.
- We neglect the terms with complex exponentials that vary very quickly with z and as a consequence the coupling coefficient *K(z)* is approximated by only one term of its Fourier series. This approximation is valid for the range of frequencies placed around the maximum reflection frequency, and for a PBG device large enough (several periods).

To finish, we are going to review the changes that the last expressions developed would suffer if the relation between the fields of the forward and backward travelling waves associated to the mode of interest were:

$$\begin{array}{lll} E_x^- = E_x^+ & ; \; E_y^- = E_y^+ & ; \; E_z^- = -E_z^+ \\ H_x^- = -H_x^+ & ; \; H_y^- = -H_y^+ & ; \; H_z^- = H_z^+ \end{array} \tag{3.95}$$

All the changes would consist on a change in the sign of the equation involved.
In first place, the coupling coefficient equation (3.20) would change its sign, becoming:

$$K(z) = -\frac{1}{2} \cdot \frac{1}{Z_0} \cdot \frac{dZ_0}{dz} \tag{3.96}$$

Consequently the coupling coefficient parameter would change the sign in its definition (3.52):

$$k = -j \cdot K_n \tag{3.97}$$

The relation between the complex amplitude of the backward travelling wave, *a^-(z)*, and the equivalent voltage (eqns. (A.9), Appendix A) would change also its sign:

$$V^- = \sqrt{Z_0} \cdot \sqrt{N} \cdot a^- \tag{3.98}$$

and consequently the definition of *S(z)* (3.54) would have positive sign:

$$S(z) = A^-(z) \cdot e^{j \cdot \left(\beta - n \cdot \frac{\pi}{\Lambda} \right) \cdot z} = a^-(z) \cdot e^{-j \cdot n \cdot \frac{\pi}{\Lambda} \cdot z} \tag{3.99}$$

Taking all this into account, the coupled mode equations for S and R (3.55) would remain unaltered .

The S_{11} definition (3.29) would have positive sign

$$S_{11} = \left. \frac{a^-(z=0)}{a^+(z=0)} \right|_{a^-(z=L)=0} \tag{3.100}$$

and the analytical solution for $a^-(z)$ (3.66) would change its sign, becoming:

$$a^-(z) = \frac{-k \cdot \sinh(\gamma \cdot (z-L))}{-\Delta\beta \cdot \sinh(\gamma \cdot L) + j \cdot \gamma \cdot \cosh(\gamma \cdot L)} \cdot a^+(0) \cdot e^{j \cdot \frac{\pi}{\Lambda} \cdot n \cdot z} \tag{3.101}$$

In this way, the analytical expression for S_{11} (3.68) would remain unaltered.
To finish, the A_{21} parameter of the transmission matrix (3.92) would have negative sign:

$$A_{21} = \frac{-j \cdot |k| \cdot L \cdot \sinh(\gamma \cdot L)}{\gamma \cdot L} \cdot e^{j \cdot \left(\frac{\pi}{\Lambda} \cdot n \cdot L + \phi \right)} \tag{3.102}$$

and consequently the relationship between the S_{11} and the A_{21} parameters (3.94) would change also its sign:

$$S_{11} = \frac{A_{21}}{A_{11}} \tag{3.103}$$

3.3.4. Introduction of the spatial variable “electrical position”

In this section we are going to introduce a novel spatial variable, χ , and we are going to name it “electrical position”. It is inspired in the electrical position variables proposed in [XIA 01, WOH 66], and is related to the physical position, z, in the following way:

$$\chi(z) = \int_0^z \sqrt{\varepsilon_{eff}(s)} \cdot ds \tag{3.104}$$

(in this definition it is assumed that the origin of the circuit is placed at z=0).

Applying the first fundamental theorem of calculus we obtain that:

$$\frac{d\chi}{dz} = \sqrt{\varepsilon_{eff}} \tag{3.105}$$

and from it, the inverse equation can be readily obtained:

$$\frac{dz}{d\chi} = \frac{1}{\sqrt{\varepsilon_{eff}}} \Rightarrow \int_0^{\chi} \frac{dz}{d\chi} \cdot d\chi = \int_0^{\chi} \frac{1}{\sqrt{\varepsilon_{eff}}} \cdot d\chi \Rightarrow z(\chi) - z(0) = \int_0^{\chi} \frac{1}{\sqrt{\varepsilon_{eff}}} \cdot d\chi \Rightarrow$$

$$\Rightarrow z(\chi) = \int_0^{\chi} \frac{1}{\sqrt{\varepsilon_{eff}(s)}} \cdot ds \tag{3.106}$$

The aim of the electrical position variable, χ, is to have a β constant with it along the PBG device. In this way, the first of the two approximations used in the previous sections to obtain the analytical solutions for the coupled mode equations can be avoided, achieving more accurate results.

Let's see the resulting system of coupled mode equations with the spatial variable electrical position, χ. The initial system, function of the physical position *z*, was given by eqn. (3.16) and (3.17):

$$\frac{da^+}{dz} = -j \cdot \beta \cdot a^+ + K \cdot a^-$$

$$\frac{da^-}{dz} = j \cdot \beta \cdot a^- + K \cdot a^+$$

We take the first of the equations, and we introduce in it the variable χ.

The first term of the equation can be rewritten as:

$$\frac{da^+}{dz} = \frac{da^+}{d\chi} \cdot \frac{d\chi}{dz} \tag{3.107}$$

On the other hand, the coupling coefficient *K(z)* has the form (eqn. (3.20)):

$$K(z) = \frac{1}{2} \cdot \frac{1}{Z_0} \cdot \frac{dZ_0}{dz}$$

and therefore it can be rewritten as:

$$K(z) = \frac{1}{2} \cdot \frac{1}{Z_0} \cdot \frac{dZ_0}{d\chi} \cdot \frac{d\chi}{dz} = K(\chi) \cdot \frac{d\chi}{dz} \tag{3.108}$$

where

$$K(\chi) = \frac{1}{2} \cdot \frac{1}{Z_0} \cdot \frac{dZ_0}{d\chi} \tag{3.109}$$

It is worth noting that in all the cases (including the general formulations given in chapter 2) the coupling coefficient will have the form of a derivative in the *z* direction, multiplied by other terms, plus a derivative in the *z* direction, multiplied by other terms, and so on. Consequently it will be always expressible in the following way:

$$K(z) = K(\chi) \cdot \frac{d\chi}{dz} \tag{3.110}$$

being $K(\chi)$ the coupling coefficient calculated using the spatial variable electrical position.

From eqn. (3.19) the phase constant β can be formulated as a function of ε_{eff} , and using eqn. (3.105) the following expression is obtained:

$$\beta = \frac{2 \cdot \pi \cdot f}{c} \cdot \sqrt{\varepsilon_{eff}} = \frac{2 \cdot \pi \cdot f}{c} \cdot \frac{d\chi}{dz} = \beta_0 \cdot \frac{d\chi}{dz} \tag{3.111}$$

where

$$\beta_0 = \frac{2 \cdot \pi \cdot f}{c} \tag{3.112}$$

With all of this, the first of the coupled mode equations can be rewritten as:

$$\frac{da^+}{d\chi} \cdot \frac{d\chi}{dz} = -j \cdot \beta_0 \cdot \frac{d\chi}{dz} \cdot a^+ + K(\chi) \cdot \frac{d\chi}{dz} \cdot a^- \tag{3.113}$$

and simplifying it becomes:

$$\frac{da^+}{d\chi} = -j \cdot \beta_0 \cdot a^+ + K(\chi) \cdot a^- \tag{3.114}$$

Taking the second of the coupled mode equations (eqn. (3.17)), and introducing in it the electrical position variable χ , we obtain in the same way:

$$\frac{da^-}{d\chi} = +j \cdot \beta_0 \cdot a^- + K(\chi) \cdot a^+ \tag{3.115}$$

So the system of coupled mode equations expressed as a function of the electrical position variable, χ , is given by eqn. (3.114) and (3.115). As it can be seen, it has identical form to the system expressed as a function of the physical position variable, *z*, (eqn. (3.16) and (3.17)), if we replace the physical position variable, *z*, by the electrical position variable, χ , the phase constant β (that can be function of *z*), by the

phase constant β_0 (that is constant with χ), and the coupling coefficient calculated using *z*, *K(z)*, by the coupling coefficient calculated using χ , *K(χ)*.
As a consequence, the analytical solutions found in the previous sections will be still valid for the new system expressed as a function of the electrical position variable, χ , provided that the three replacements described are introduced in the solutions. In fact, the analytical solutions will be more accurate for the new system because to obtain them it won't be necessary to approximate β_0 as constant with χ , since it will be actually constant with χ .

It is important to stress that the coupling coefficient *K(χ)* is not obtained by realizing a simple change of variable in *K(z)*, but it is obtained by calculating the coupling coefficient using the spatial variable electrical position, χ , as it can be seen in eqn. (3.109). Thus, for the calculation of the coupling coefficient *K(χ)*, all the elements of the coupling coefficient equation must be expressed as function of χ , and after it the derivatives must be taken in the direction of χ .

Using the electrical position variable, χ , an optimized value for the "averaged" β (and hence ε_{eff}) to be employed in the analytical solutions of the coupled mode equations expressed as function of *z* (eqn. (3.16) and (3.17)), can be obtained. We are going to calculate it by adjusting the expression for the frequency of maximum reflectivity.
As it was seen in eqn. (3.70) the frequency of maximum reflectivity will be the one that satisfies $\Delta\beta$=0, and therefore using the electrical position variable its value will be:

$$\Delta\beta = 0 \Rightarrow \beta_{0,max} = n \cdot \frac{\pi}{\chi(\Lambda)} \Rightarrow \frac{2 \cdot \pi \cdot f_{max}}{c} = n \cdot \frac{\pi}{\int_0^\Lambda \sqrt{\varepsilon_{eff}(z)} \cdot dz} \Rightarrow$$
$$\Rightarrow f_{max} = n \cdot \frac{c}{2 \cdot \int_0^\Lambda \sqrt{\varepsilon_{eff}(z)} \cdot dz} \qquad (3.116)$$

It is important to notice that to obtain this expression there is still one approximation involved: we neglect the terms with complex exponentials that vary very quickly with χ and as a consequence the coupling coefficient *K(χ)* is approximated by only one term of its Fourier series (the second of the two approximations used in the previous sections). This approximation is valid for the range of frequencies placed around the maximum reflection frequency, and for a PBG device large enough (several periods). So the approximation will be in general very good, and the results of the equation for the frequency of maximum reflectivity will be very accurate, but always approximated, not exact.

By comparing the equation for the frequency of maximum reflectivity obtained using the physical position variable, *z*, (eqn. (3.70)) , and this last equation obtained by using the electrical position variable, χ , (eqn. (3.116)), it can be readily deduced that the optimized value for the "averaged" ε_{eff} is given by:

$$\varepsilon_{eff} = \left(\frac{1}{\Lambda} \cdot \int_0^{\Lambda} \sqrt{\varepsilon_{eff}(z)} \cdot dz \right)^2 \tag{3.117}$$

where ε_{eff} is the "averaged" value, constant with z, that we are going to use in the analytical expressions to approximate the $\varepsilon_{eff}(z)$, variable with z, that is actually present in our PBG device.

3.3.5. Case of tapered PBG

In all the previous subsections of section 3.3 we have studied PBG structures in microstrip technology with constant parameters: constant period and constant amplitude of perturbation. As we have seen, for these purely periodic structures there are approximate analytical solutions and the analysis and design process can be quite simple. However, as it will be seen in chapter 4, the performance of a PBG structure in microstrip technology can be notably improved for certain applications by applying techniques that result in an optimized pattern that is almost periodic but not purely periodic. Unfortunately, in general, there are no analytical solutions for the non periodic patterns. However, an approximate analytical solution can be obtained for the frequency of maximum reflectivity and for the value of this maximum reflectivity when a tapering technique is applied. A tapered PBG will have an almost periodic pattern with constant period and tapered (variable) amplitude of perturbation. Its coupling coefficient will be expressible as:

$$K(z) = T(z) \cdot K^{\Lambda}(z) = T(z) \cdot \sum_{n=-\infty}^{n=\infty} K_n^{\Lambda} \cdot e^{j \cdot \frac{2\pi}{\Lambda} \cdot n \cdot z} \tag{3.118}$$

where *T(z)* is the tapering function applied (it is supposed to be a real function), and $K^{\Lambda}(z)$ the purely periodic part of the coupling coefficient that can be expanded in a Fourier series.

Applying the same reasoning employed in section (3.3.1), taking the same approximations:

- We approximate the phase constant β as a variable constant with z. An "averaged" β is assigned to all the device.
- We neglect the terms with complex exponentials that oscillate very quickly with z and as a consequence the coupling coefficient $K^{\Lambda}(z)$ is approximated by only one term of its Fourier series. This approximation is valid for the range of frequencies placed around the maximum reflection frequency, and for a PBG device large enough (several periods).

and defining the coupling coefficient parameter as:

$$k = j \cdot K_n^{\Lambda} \tag{3.119}$$

the coupled mode equations will take the form:

$$\begin{aligned} \frac{dA^+}{dz} &= j \cdot k^* \cdot T(z) \cdot e^{j \cdot 2 \cdot \Delta\beta \cdot z} \cdot A^- \\ \frac{dA^-}{dz} &= -j \cdot k \cdot T(z) \cdot e^{-j \cdot 2 \cdot \Delta\beta \cdot z} \cdot A^+ \end{aligned} \tag{3.120}$$

As we have done previously in section (3.3.2), we are going to introduce the *R(z)* and *S(z)* variables. They are defined as in eqn. (3.54). Using them and separating in the coupling coefficient parameter its modulus, $|k|$, and its argument, ϕ, the coupled mode equations (eqn. (3.120)) can be rewritten as:

$$\begin{aligned} \frac{dR}{dz} &= -j \cdot \Delta\beta \cdot R - j \cdot |k| \cdot e^{-j \cdot \phi} \cdot T(z) \cdot S \\ \frac{dS}{dz} &= j \cdot \Delta\beta \cdot S + j \cdot |k| \cdot e^{j \cdot \phi} \cdot T(z) \cdot R \end{aligned} \tag{3.121}$$

Following [KOG 76] we are going to define a modified reflection coefficient, Γ:

$$\Gamma = \frac{S}{R} \cdot e^{-j \cdot \phi} \tag{3.122}$$

and it will be related to the conventional reflection coefficient, ρ , in the following way:

$$\rho = \frac{-a^-}{a^+} = \frac{S \cdot e^{j \cdot \frac{\pi}{\Lambda} \cdot n \cdot z}}{R \cdot e^{-j \cdot \frac{\pi}{\Lambda} \cdot n \cdot z}} = \frac{S}{R} \cdot e^{j \cdot \frac{2 \cdot \pi}{\Lambda} \cdot n \cdot z} = \Gamma \cdot e^{j \cdot \left(\frac{2 \cdot \pi}{\Lambda} \cdot n \cdot z + \phi \right)} \tag{3.123}$$

Let's calculate now the Riccati equation for the modified reflection coefficient. By deriving eqn. (3.122), we have:

$$\frac{d\Gamma}{dz} = \frac{dS/dz \cdot R - dR/dz \cdot S}{R^2} \cdot e^{-j \cdot \phi} \tag{3.124}$$

and substituting for dS/dz and for dR/dz from eqns. (3.121), and simplifying, we obtain the so called Riccati equation:

$$\frac{d\Gamma}{dz} = j \cdot 2 \cdot \Delta\beta \cdot \Gamma + j \cdot |k| \cdot T(z) \cdot \left(1 + \Gamma^2\right) \tag{3.125}$$

The maximum reflectivity of the device will take place when *Δβ*=0, so the frequency of maximum reflectivity for the tapered PBG will be given by:

$$\begin{aligned} &\Delta\beta = 0 \Rightarrow \beta_{max} = n \cdot \frac{\pi}{\Lambda} \Rightarrow \frac{2 \cdot \pi \cdot f_{max}}{c} \cdot \sqrt{\varepsilon_{eff}} = n \cdot \frac{\pi}{\Lambda} \Rightarrow \\ &\Rightarrow f_{max} = n \cdot \frac{c}{2 \cdot \sqrt{\varepsilon_{eff}} \cdot \Lambda} \end{aligned} \tag{3.126}$$

and the value of maximum reflectivity will satisfy (introducing *Δβ*=0 in eqn. (3.125)):

$$\frac{d\Gamma}{dz} = j \cdot |k| \cdot T(z) \cdot \left(1 + \Gamma^2\right) \Rightarrow \frac{d\Gamma}{1 + \Gamma^2} = j \cdot |k| \cdot T(z) \cdot dz \tag{3.127}$$

Integrating both terms of the equation between *z*=0 and *z*=*L* (assuming that the device is placed between *z*=0 and *z*=*L*), and applying the boundary condition Γ(*L*)=0 (i.e. assuming that the output port is matched), it will be obtained:

$$\begin{aligned} &\operatorname{arctg}(\Gamma(L)) - \operatorname{arctg}(\Gamma(0)) = \int_0^L j \cdot |k| \cdot T(z) \cdot dz \Rightarrow 0 - \operatorname{arctg}(\Gamma(0)) = j \cdot |k| \cdot \int_0^L T(z) \cdot dz \Rightarrow \\ &\Rightarrow \Gamma(0) = -j \cdot \tanh\left(|k| \cdot \int_0^L T(z) \cdot dz \right) \Rightarrow \Gamma(0) = -j \cdot \tanh\left(|k| \cdot L_{eff} \right) \end{aligned} \tag{3.128}$$

defining the effective length, L_{eff}, of a tapered device as:

$$L_{eff} = \int_0^L T(z) \cdot dz \tag{3.129}$$

(we have to take into account that $\int \frac{dx}{1+x^2} = \mathrm{arctg}(x)$, and $\tan(-j\cdot x) = -j\cdot \tanh(x)$)

As we now there is a direct relationship between the S_{11} parameter and the reflection coefficient, and from eqn. (3.123) they are also related to the modified reflection coefficient in the following way:

$$S_{11} = \left.\frac{-a^-(z=0)}{a^+(z=0)}\right|_{a^-(z=L)=0} = \rho(z=0)\big|_{\rho(z=L)=0} = \Gamma(z=0)\big|_{\Gamma(z=L)=0}\cdot e^{j\cdot\phi} \qquad (3.130)$$

and therefore the value of maximum reflectivity for the tapered PBG will be:

$$S_{11,max} = -j\cdot e^{j\cdot\phi}\cdot \tanh\left(|k|\cdot L_{eff}\right) \qquad (3.131)$$

with modulus

$$|S_{11}|_{max} = \tanh\left(|k|\cdot L_{eff}\right) \qquad (3.132)$$

and with L_{eff} given by eqn. (3.129).

As it can be seen, the expression for the maximum reflectivity in the tapered PBG case (eqn. (3.132)) is identical to that in the uniform PBG case (eqn. (3.71)) provided that the physical length, L, is replaced by the effective length, L_{eff}.
Regarding the frequency of maximum reflectivity, the expression for it is identical in both cases (eqn. (3.126) and eqn. (3.70)).

3.4. Bloch wave analysis

In this section the Bloch wave formalism will be used to analyze PBG structures in microstrip technology. Concepts like the dispersion relation and the characteristic impedance of the Bloch wave will be introduced giving rise to a complementary and powerful point of view for the analysis and design of PBG structures in microstrip technology.

3.4.1. Floquet's theorem

Let us consider an infinite periodic structure, periodic along the direction of propagation z, with period Λ. In it, the permittivity and permeability will be periodic in such a way that:

$$\varepsilon(x,y,z)=\varepsilon(x,y,z+\Lambda) \quad ; \quad \mu(x,y,z)=\mu(x,y,z+\Lambda) \tag{3.133}$$

This equations indicate that the medium "looks" exactly the same to an observer placed at z as to an observer placed at $z+\Lambda$.

The propagation of electromagnetic waves in a medium is governed by Maxwell's equations. Assuming time-harmonic fields with an $e^{j\cdot\omega\cdot t}$ dependence, and assuming that the medium under study is source-free they can be written as:

$$\begin{aligned} \nabla\times\hat{E} &= -j\cdot\omega\cdot\mu\cdot\hat{H} \\ \nabla\times\hat{H} &= j\cdot\omega\cdot\varepsilon\cdot\hat{E} \end{aligned} \tag{3.134}$$

where $\hat{E}$ and $\hat{H}$ are the total electric and magnetic fields. These equations remain identical in our periodic structure after we have substituted z by $z+\Lambda$ in the operator ∇ and in ε and μ. The discrete translational symmetry of the structure allows us to take its modes in the following way [YAR 84, COL 92, JOA 95, BRI 53]:

$$\begin{aligned} \hat{E}(x,y,z) &= \vec{E}(x,y,z)\cdot e^{-j\cdot\beta'\cdot z} \\ \hat{H}(x,y,z) &= \vec{H}(x,y,z)\cdot e^{-j\cdot\beta'\cdot z} \end{aligned} \tag{3.135}$$

where $\vec{E}(x,y,z)$ and $\vec{H}(x,y,z)$ are periodic:

$$\begin{aligned} \vec{E}(x,y,z) &= \vec{E}(x,y,z+\Lambda) \\ \vec{H}(x,y,z) &= \vec{H}(x,y,z+\Lambda) \end{aligned} \tag{3.136}$$

The possibility of expressing the field in a periodic structure in the form given by eqns. (3.135) and (3.136) is known as Floquet's theorem [YAR 84, COL 92, JOA 95, BRI 53] (the generalization of this theorem for three dimensional periodicity is also known as Bloch's theorem). The modes resulting from the Floquet's theorem are the modes of the periodic structures, and they are known as Bloch waves. These equations state that the field behaviour in a periodic structure is describable in terms of a fundamental travelling wave, with phase constant β', and a standing wave $\vec{E}(x,y,z)$ (or $\vec{H}(x,y,z)$) which is the same in each period Λ, and which represents the local variations of the fields due to the existent periodicity.

This standing wave can alternatively be represented as a superposition of travelling waves. The representation is accomplished by expanding the periodic function $\vec{E}(x,y,z)$ in a Fourier series as:

$$\vec{E}(x,y,z) = \sum_{n=-\infty}^{\infty} \vec{E}_n(x,y) \cdot e^{-j \cdot \frac{2\cdot\pi}{\Lambda} \cdot n \cdot z} \tag{3.137}$$

where

$$\vec{E}_n(x,y) = \frac{1}{\Lambda} \cdot \int_{\Lambda} \vec{E}(x,y,z) \cdot e^{j \cdot \frac{2\cdot\pi}{\Lambda} \cdot n \cdot z} \cdot dz \tag{3.138}$$

Introducing eqn. (3.137) into eqn. (3.135) it can be seen that the field in the periodic structure is represented now as:

$$\hat{\vec{E}}(x,y,z) = \sum_{n=-\infty}^{\infty} \vec{E}_n(x,y) \cdot e^{-j \cdot \frac{2\cdot\pi}{\Lambda} \cdot n \cdot z} \cdot e^{-j \cdot \beta' \cdot z} = \sum_{n=-\infty}^{\infty} \vec{E}_n(x,y) \cdot e^{-j \cdot \left(\beta' + \frac{2\cdot\pi}{\Lambda} \cdot n \right) \cdot z} \tag{3.139}$$

and defining:

$$\beta'_n = \beta' + \frac{2\cdot\pi}{\Lambda} \cdot n \qquad ; \qquad n = 0, \pm 1, \pm 2, \ldots \tag{3.140}$$

we have:

$$\hat{\vec{E}}(x,y,z) = \sum_{n=-\infty}^{\infty} \vec{E}_n(x,y) \cdot e^{-j \cdot \beta'_n \cdot z} \tag{3.141}$$

As it can be seen the field present in the periodic structure is expressible as a sum of an infinite number of travelling waves. Each of these travelling waves is called spatial harmonic, in analogy to the familiar time harmonic expansion for an arbitrary function in time [COL 92, OLI 63].

It must be noted that although the Bloch wave can be expanded in an infinite set of spatial harmonics, these spatial harmonics can not exist independently and are not modal solutions by themselves, they are portions of a total solution and must exist simultaneously to have a total field that satisfies the boundary conditions.

The eigenvalue equation that allows the calculation of the phase constant β' for a periodic structure always yields solutions $\beta'_n = \beta' + 2n\pi/\Lambda$, in addition to the fundamental solution. These other possible solutions are clearly the propagation constants of the spatial harmonics. A complete k_0 - β' diagram is thus always periodic outside the range $-\pi \le \beta' \cdot \Lambda \le \pi$. Therefore, the dispersion curve is repeated every $\beta' \cdot \Lambda = 2 \cdot \pi$ and the range placed between $\beta' \cdot \Lambda = -\pi$ and $\beta' \cdot \Lambda = \pi$ contains all the information of the dispersion diagram and corresponds to the first Brillouin zone for these structures that are periodic in one dimension [JOA 95, BRI 53].

The use of the Bloch waves in the analysis of periodic structures is enough to permit the determination of all the macroscopic properties of the periodic structure. The alternative representation in terms of spatial harmonics allows us the exploration of certain microscopic properties and adds insight into many features of the behaviour of the periodic structures, for example the radiation in open periodic structures [OLI 63].

3.4.2. Dispersion diagram

In this section we are going to calculate the dispersion diagram or k_0 - β diagram for a PBG structure in microstrip technology. An approximate analytical expression will be obtained for it taking advantage of the approximate analytical solutions that we have for the coupled mode equations. To finish, a procedure to obtain a numerical solution for the dispersion diagram will be also presented.

3.4.2.1. Approximate analytical expression

Let's recall the approximate general solution of the coupled mode equations that characterize a PBG structure in microstrip technology, eqn. (3.56):

$$R(z) = R^+ \cdot e^{-\gamma\cdot z} + R^- \cdot e^{\gamma\cdot z}$$
$$S(z) = S^+ \cdot e^{-\gamma\cdot z} + S^- \cdot e^{\gamma\cdot z}$$

and thus the total electric field in the PBG device will be, from eqns. (3.54), (3.67):

$$\hat{\vec{E}}(x,y,z) = \vec{E}^+(x,y,z) \cdot \left(R^+ \cdot e^{-\gamma\cdot z} + R^- \cdot e^{\gamma\cdot z}\right) \cdot e^{-j\cdot\frac{\pi}{\Lambda}\cdot n\cdot z} +$$

$$-\vec{E}^{-}(x,y,z)\cdot\left(S^{+}\cdot e^{-\gamma\cdot z}+S^{-}\cdot e^{\gamma\cdot z}\right)\cdot e^{j\cdot\frac{\pi}{\Lambda}\cdot n\cdot z} \tag{3.142}$$

where $\vec{E}^{+}(x,y,z),\vec{E}^{-}(x,y,z)$ are the (*x,y*) dependent part of the electric field of the forward (+) and backward (−) travelling waves corresponding to the fundamental microstrip (or quasi-microstrip) mode of the auxiliary uniform waveguide associated to the cross-section of interest. The cross section varies with *z*, and hence the mode fields will vary with *z* also. Since the cross section variation is periodic, with period Λ, the mode fields $\vec{E}^{+}(x,y,z),\vec{E}^{-}(x,y,z)$ will be also periodic in *z* with the same period Λ, and therefore will satisfy:

$$\vec{E}^{+}(x,y,z)=\vec{E}^{+}(x,y,z+\Lambda)\quad ;\quad \vec{E}^{-}(x,y,z)=\vec{E}^{-}(x,y,z+\Lambda) \tag{3.143}$$

Comparing the general form for the Bloch waves given by eqn. (3.135) and the total electric field in our PBG device, eqn. (3.142), it can be deduced that in the general case in our PBG device there is a forward travelling Bloch wave and a backward travelling Bloch wave with phase constant [YAR 77, YAR 84]:

$$\beta'=\frac{\pi}{\Lambda}\cdot n\pm j\cdot\gamma \tag{3.144}$$

($\beta'=-\frac{\pi}{\Lambda}\cdot n\mp j\cdot\gamma$ for the backward travelling wave).

The ± sign appears due to the form of the expression for γ, given by eqn. (3.57):

$$\gamma=+\sqrt{|k|^{2}-(\Delta\beta)^{2}}$$

that makes necessary, in order to have a proper definition of the phase constant of the Bloch wave, to define it piecewise:

- forward travelling Bloch wave:

$$\beta'=\begin{cases}\frac{\pi}{\Lambda}\cdot n+j\cdot\gamma & ;\quad \Delta\beta\le-|k|\\ \frac{\pi}{\Lambda}\cdot n-j\cdot\gamma & ;\quad \Delta\beta>-|k|\end{cases} \tag{3.145}$$

- backward travelling Bloch wave:

$$\beta' = \begin{cases} -\dfrac{\pi}{\Lambda}\cdot n - j\cdot\gamma & ; \quad \Delta\beta \le -|k| \\ -\dfrac{\pi}{\Lambda}\cdot n + j\cdot\gamma & ; \quad \Delta\beta > -|k| \end{cases} \tag{3.146}$$

where $\Delta\beta$ is given by eqn. (3.48):

$$\Delta\beta = \beta - n\cdot\frac{\pi}{\Lambda}$$

n is the index of the rejected band of interest (*n*=1, 2, 3, ...) and *k* is the coupling coefficient parameter, eqn. (3.20), (3.38) and (3.52).

As it was previously shown, a complete k_0 - β' diagram (i.e. including the spatial harmonics) is always periodic outside the range $-\pi \le \beta'\cdot\Lambda \le \pi$, with the dispersion curve repeating itself every $\beta'\cdot\Lambda = 2\cdot\pi$. Therefore the dispersion (k_0 vs. β') diagram is customarily represented in the range $-0.5 \le \frac{\beta'\cdot\pi}{2\cdot\pi} \le 0.5$, (the first Brillouin zone) and in the form $\frac{k_0\cdot\Lambda}{2\cdot\pi}$ vs. $\frac{\beta'\cdot\Lambda}{2\cdot\pi}$, containing all the information about the dispersion [JOA 95].

Since k_0 is the phase constant of a plane wave in vacuum:

$$k_0 = \frac{2\cdot\pi\cdot f}{c} \tag{3.147}$$

the form customarily employed for the dispersion diagram can be rewritten as: $\frac{f\cdot\Lambda}{c}$ vs. $\frac{\beta'\cdot\Lambda}{2\cdot\pi}$.

In order to obtain the dispersion diagram (including the spatial harmonics) of a PBG in microstrip technology in the first Brillouin zone $\left(-0.5 \le \frac{\beta'\cdot\pi}{2\cdot\pi} \le 0.5\right)$ the following expressions must be represented :

$$\left.\begin{aligned} \beta' &= \frac{\pi}{\Lambda}\cdot n + j\cdot\gamma \\ \beta' &= -\frac{\pi}{\Lambda}\cdot n - j\cdot\gamma \end{aligned}\right\} \quad \forall\,\Delta\beta \tag{3.148}$$

in all the frequency range (without the necessity of defining them piecewise).

From the approximate analytical expression for the phase constant of the Bloch wave, eqn. (3.145), several important parameters of the rejected frequency band of the PBG device can be obtained. The rejected frequency band, forbidden band or Photonic Bandgap extends over the range of frequencies in which the phase constant β' has imaginary part, causing reactive attenuation in the Bloch waves that will have evanescent behaviour in the PBG device. This phenomenon is analogous to the energy gap in semiconductors where the periodic crystal potential causes the electron propagation constants to become complex [YAR 77, YAR 84].

The frequency of maximum attenuation will be that at which the imaginary part of the phase constant β' is maximum. This condition will be satisfied when $\Delta\beta=0$, and hence the frequency of maximum attenuation will have the value:

$$\begin{aligned}&\Delta\beta = 0 \Rightarrow \beta_{max} = n\cdot\frac{\pi}{\Lambda} \Rightarrow \frac{2\cdot\pi\cdot f_{max}}{c}\cdot\sqrt{\varepsilon_{eff}} = n\cdot\frac{\pi}{\Lambda} \Rightarrow \\ &\Rightarrow f_{max} = n\cdot\frac{c}{2\cdot\sqrt{\varepsilon_{eff}}\cdot\Lambda}\end{aligned} \tag{3.149}$$

and the value of this maximum attenuation obtained for the Bloch wave will be:

$$\alpha'_{max} = -\operatorname{Im}(\beta')\big|_{max} = |k| \quad \text{Np/m} \tag{3.150}$$

The bandwidth of the forbidden band or Photonic Bandgap will cover the frequency range in which the phase constant β' has imaginary part, i.e. when $|\Delta\beta| \le |k|$. So the maximum frequency of the Photonic Bandgap will satisfy:

$$\Delta\beta = |k| \tag{3.151}$$

At the same time, if we assume ε_{eff} as constant with the frequency in the Photonic Bandgap (i.e. if we neglect the dispersion):

$$\Delta\beta = \beta - n\cdot\frac{\pi}{\Lambda} = \beta - \beta_{max} = \frac{2\cdot\pi}{c}\cdot\sqrt{\varepsilon_{eff}}\cdot(f - f_{max}) \tag{3.152}$$

On the other hand, if we take into account the dispersion:

$$\begin{aligned}&\Delta\beta = \beta - n\cdot\frac{\pi}{\Lambda} = \beta - \beta_{max} \approx \frac{d\beta}{d\omega}\cdot(\omega - \omega_{max}) = \frac{1}{v_g}\cdot(\omega - \omega_{max}) = \\ &= \frac{n_g}{c}\cdot(\omega - \omega_{max}) = \frac{2\cdot\pi}{c}\cdot n_g\cdot(f - f_{max})\end{aligned} \tag{3.153}$$

where v_g is the group velocity, and n_g the group index.
As it can be seen, the expression for $\Delta\beta$ is the same in both cases (eqn. (3.152), (3.153)), if we replace $\sqrt{\varepsilon_{eff}} = n_{eff}$ (expression that neglects the dispersion) by n_g (expression that takes into account the dispersion).
Continuing our deduction with the expression that neglects the dispersion, eqn. (3.152), and introducing it in eqn. (3.151), the equation for the bandwidth of the Photonic Bandgap or forbidden band is obtained:

$$\begin{aligned} &\frac{2\cdot\pi}{c}\cdot\sqrt{\varepsilon_{eff}}\cdot(f-f_{max}) = |k| \Rightarrow \frac{2\cdot\pi}{c}\cdot\sqrt{\varepsilon_{eff}}\cdot\frac{BW_{gap}}{2} = |k| \Rightarrow \\ &\Rightarrow BW_{gap} = \frac{|k|\cdot c}{\pi\cdot\sqrt{\varepsilon_{eff}}} \end{aligned} \tag{3.154}$$

As we have already commented, to take into account the dispersion we have only to substitute the $\sqrt{\varepsilon_{eff}}$ by the group index, n_g , in the equation for the bandwidth, (3.154).

To finish this subsection it is important to stress that all the analytical expressions developed have been obtained from the general analytical solutions for the approximate system of coupled mode equations (3.55) that characterizes a PBG structure in microstrip technology. Therefore all the expressions are approximated, because as it was shown in section (3.3.1.) there are two reasonable approximations involved:

- The phase constant β is approximated as a variable constant with z. An "averaged" β is assigned to all the device.
- We neglect the terms with complex exponentials that vary very quickly with z and as a consequence the coupling coefficient $K(z)$ is approximated by only one term of its Fourier series. This approximation is valid for the range of frequencies placed around the maximum reflection frequency, and for a PBG device large enough. (this last condition is no problem in this case because the PBG is ideal (infinite)).

3.4.2.2. Calculation using numerical method

As we have seen previously the use of the cross section method to analyze PBG structures in microstrip technology has allowed us to express the field in the device, (after having simplified the problem assuming single mode operation, section (3.2)) as:

$$\hat{E}(x,y,z) = \vec{E}^{+}(x,y,z)\cdot a^{+}(z) + \vec{E}^{-}(x,y,z)\cdot a^{-}(z) \tag{3.155}$$

where $\vec{E}^{+}(x,y,z), \vec{E}^{-}(x,y,z)$ are the (x,y) dependent part of the electric field of the forward (+) and backward (–) travelling waves corresponding to the fundamental microstrip (or quasi-microstrip) mode of the auxiliary uniform waveguide associated to the cross-section of interest; and $a^{+}(z)$, $a^{-}(z)$ are the wave amplitudes of the mode along the nonuniform waveguide.

The cross section varies with z, and hence the mode fields will vary with z also. Since the cross section variation is periodic, with period Λ, the mode fields $\vec{E}^{+}(x,y,z), \vec{E}^{-}(x,y,z)$ will be also periodic in z with the same period Λ, and therefore will satisfy:

$$\vec{E}^{+}(x,y,z) = \vec{E}^{+}(x,y,z+\Lambda) \quad ; \quad \vec{E}^{-}(x,y,z) = \vec{E}^{-}(x,y,z+\Lambda) \tag{3.156}$$

Taking into account the relation between the fields of the forward and backward travelling waves associated to the same mode seen in chapter 2, eqn. (2.14):

$$E_x^{-} = -E_x^{+} \quad ; \quad E_y^{-} = -E_y^{+} \quad ; \quad E_z^{-} = +E_z^{+} \tag{3.157}$$

the eqn. (3.155) can be rewritten as:

$$\hat{E}(x,y,z) = \vec{E}^{+}_{x,y}(x,y,z)\cdot\left(a^{+}(z) - a^{-}(z)\right) + \vec{E}^{+}_{z}(x,y,z)\cdot\left(a^{+}(z) + a^{-}(z)\right) \tag{3.158}$$

Since our PBG microstrip device is a periodic structure with period Λ, it can be broken up in unitary cells, each of them equal to one period, in whose input and output terminals we are going to calculate the wave amplitudes $a^{+}(z)$, $a^{-}(z)$:

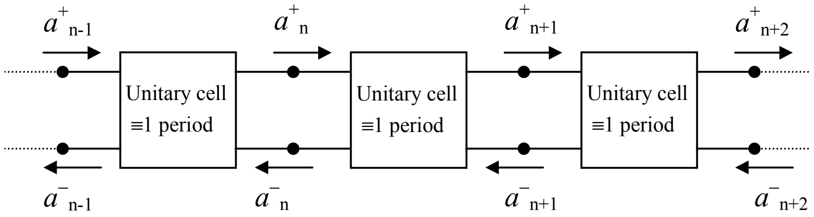

where:

$$\begin{aligned} a_n^{+} &= a^{+}(z = n\cdot\Lambda) \\ a_n^{-} &= a^{-}(z = n\cdot\Lambda) \end{aligned} \tag{3.159}$$

$$a_{n+1}^{+} = a^{+}(z = (n+1)\cdot\Lambda)$$
$$a_{n+1}^{-} = a^{-}(z = (n+1)\cdot\Lambda)$$

The values of eqn. (3.159) are related by the transmission matrix of the unitary cell in the following way:

$$\begin{bmatrix} a_n^{+} \\ a_n^{-} \end{bmatrix} = \begin{bmatrix} A_{11} & A_{12} \\ A_{21} & A_{22} \end{bmatrix} \cdot \begin{bmatrix} a_{n+1}^{+} \\ a_{n+1}^{-} \end{bmatrix} \tag{3.160}$$

On the other hand the total field present in the PBG device can be expressed using the Bloch waves in the following way:

$$\hat{E}(x,y,z) = \vec{E}^{FB}(x,y,z)\cdot e^{-j\cdot\beta'\cdot z} + \vec{E}^{BB}(x,y,z)\cdot e^{+j\cdot\beta'\cdot z} \tag{3.161}$$

where

$\vec{E}^{FB}(x,y,z), \vec{E}^{BB}(x,y,z)$ are the fields for the forward travelling Bloch wave (FB) and the backward travelling Bloch wave (BB), respectively, and satisfy:

$$\begin{aligned} \vec{E}^{FB}(x,y,z) &= \vec{E}^{FB}(x,y,z+\Lambda) \\ \vec{E}^{BB}(x,y,z) &= \vec{E}^{BB}(x,y,z+\Lambda) \end{aligned} \tag{3.162}$$

If there is only one forward travelling Bloch wave propagating in our periodic structure, then the expression for the total field simplifies, becoming:

$$\hat{E}(x,y,z) = \vec{E}^{FB}(x,y,z)\cdot e^{-j\cdot\beta'\cdot z} \tag{3.163}$$

Comparing this last expression for the field, with the one obtained in eqn. (3.158) as a function of the wave amplitudes $a^{+}(z)$, $a^{-}(z)$, it can be deduced that if in our PBG device there is only one forward travelling Bloch wave propagating, then it will be satisfied that [COL 92]:

$$a^{+}(z = (n+1)\cdot\Lambda) = a^{+}(z = n\cdot\Lambda)\cdot e^{-j\cdot\beta'\cdot\Lambda}$$
$$a^{-}(z = (n+1)\cdot\Lambda) = a^{-}(z = n\cdot\Lambda)\cdot e^{-j\cdot\beta'\cdot\Lambda}$$

and hence:

$$\begin{aligned} a_{n+1}^{+} = a_n^{+}\cdot e^{-j\cdot\beta'\cdot\Lambda} &\Rightarrow a_n^{+} = a_{n+1}^{+}\cdot e^{j\cdot\beta'\cdot\Lambda} \\ a_{n+1}^{-} = a_n^{-}\cdot e^{-j\cdot\beta'\cdot\Lambda} &\Rightarrow a_n^{-} = a_{n+1}^{-}\cdot e^{j\cdot\beta'\cdot\Lambda} \end{aligned} \tag{3.164}$$

Therefore the transmission matrix of the unitary cell will satisfy:

$$\begin{bmatrix} a_n^+ \\ a_n^- \end{bmatrix} = e^{j\cdot\beta'\cdot\Lambda}\cdot\begin{bmatrix} a_{n+1}^+ \\ a_{n+1}^- \end{bmatrix} = \begin{bmatrix} A_{11} & A_{12} \\ A_{21} & A_{22} \end{bmatrix}\cdot\begin{bmatrix} a_{n+1}^+ \\ a_{n+1}^- \end{bmatrix}$$

and reorganizing the equation:

$$\begin{bmatrix} A_{11} - e^{j\cdot\beta'\cdot\Lambda} & A_{12} \\ A_{21} & A_{22} - e^{j\cdot\beta'\cdot\Lambda} \end{bmatrix}\cdot\begin{bmatrix} a_{n+1}^+ \\ a_{n+1}^- \end{bmatrix} = 0 \tag{3.165}$$

A nontrivial solution for a^+_{n+1} , a^-_{n+1} , is obtained only if the determinant of the matrix is equal to zero. Consequently, the eigenvalue equation for γ is:

$$\left(A_{11} - e^{j\cdot\beta'\cdot\Lambda}\right)\cdot\left(A_{22} - e^{j\cdot\beta'\cdot\Lambda}\right) - A_{21}\cdot A_{12} = 0$$

and operating:

$$A_{11}\cdot A_{22} - A_{21}\cdot A_{12} + e^{2\cdot j\cdot\beta'\cdot\Lambda} - e^{j\cdot\beta'\cdot\Lambda}\cdot\left(A_{11} + A_{22}\right) = 0 \tag{3.166}$$

Since our PBG device in microstrip technology will be reciprocal (passive and without anisotropic elements), and since the two ports of the unitary cell are equal and hence will have the same normalization in any case (N_1=N_2), we can take advantage of the property for the transmission matrix given by eqn. (C.4) (the determinant of the transmission matrix will be equal to one), and simplify eqn. (3.166):

$$1 + e^{2\cdot j\cdot\beta'\cdot\Lambda} - e^{j\cdot\beta'\cdot\Lambda}\cdot\left(A_{11} + A_{22}\right) = 0 \Rightarrow e^{-j\cdot\beta'\cdot\Lambda} + e^{j\cdot\beta'\cdot\Lambda} - \left(A_{11} + A_{22}\right) = 0$$

and reorganizing

$$\cos(\beta'\cdot\Lambda) = \frac{A_{11} + A_{22}}{2} \tag{3.167}$$

Equation (3.167) can be further simplified for our PBG's in microstrip technology taking advantage of other important property of the transmission matrix. Since our PBG device will be reciprocal and lossless (it is assumed as lossless throughout all our study), and since the two ports of the unitary cell are equal and hence will have the same normalization in any case (N_1=N_2), the relation given by eqn. (C.6) will hold allowing us to rewrite eqn. (3.167) as:

$$\cos(\beta'\cdot\Lambda) = \frac{A_{11} + A_{11}^*}{2} \tag{3.168}$$

and using the relations with the S-parameters given by eqns. (C.3):

and using the relations with the S-parameters given by eqns. (C.3):

$$\cos(\beta' \cdot \Lambda) = \frac{1}{2} \cdot \left(\frac{1}{S_{21}} + \frac{1}{S_{21}^*} \right) \tag{3.169}$$

where A_{11} , S_{21} , are the parameters corresponding to the unitary cell (one period), Λ is the value of the period of the structure, and β' is the phase constant of the Bloch wave.

As it can be seen, the forward travelling Bloch wave which propagate in the PBG device is made up from a forward travelling wave and a backward travelling wave corresponding to the fundamental microstrip (or quasi-microstrip) mode of the auxiliary uniform waveguide associated to the cross section of interest.

3.4.3. Characteristic impedance of the Bloch wave

As it was shown in the previous section, if we assume that there is only one forward travelling Bloch wave propagating in our PBG microstrip circuit, then eqn. (3.165) will hold:

$$\begin{bmatrix} A_{11} - e^{j \cdot \beta' \cdot \Lambda} & A_{12} \\ A_{21} & A_{22} - e^{j \cdot \beta' \cdot \Lambda} \end{bmatrix} \cdot \begin{bmatrix} a_{n+1}^{+} \\ a_{n+1}^{-} \end{bmatrix} = 0$$

The ratio between the wave amplitudes in this situation (only one forward travelling Bloch wave propagating) is known as characteristic reflection coefficient, ρ_B , and its value at the $n+1$ terminal will be:

$$\rho_B = \frac{-a_{n+1}^{-}}{a_{n+1}^{+}} \tag{3.170}$$

The minus sign applied to the wave amplitude a^- arises due to the relation existent between the backward wave amplitude and its equivalent voltage, see eqn. (A.9), Appendix A.

From ρ_B it is easy to calculate the characteristic impedance of the Bloch wave, Z_B , through the well known relation:

$$\rho_B^{\pm} = \frac{Z_B^{\pm} - Z_0}{Z_B^{\pm} + Z_0}$$

and hence:

$$\frac{Z_B^{\pm}}{Z_0} = \frac{1+\rho_B^{\pm}}{1-\rho_B^{\pm}} \tag{3.171}$$

where the ± sign denotes the forward (+) or backward (−) travelling Bloch wave, respectively, and Z_0 is the characteristic impedance of the terminal for the fundamental microstrip mode (in our case) of the auxiliary uniform waveguide associated to the terminal.

3.4.3.1. Calculation using numerical method

From the initial matrix, eqn. (3.165), two equations can be extracted:

$$\left(A_{11} - e^{j\cdot\beta'\cdot\Lambda}\right)\cdot a_{n+1}^{+} + A_{12}\cdot a_{n+1}^{-} = 0 \tag{3.172}$$

$$A_{21}\cdot a_{n+1}^{+} + \left(A_{22} - e^{j\cdot\beta'\cdot\Lambda}\right)\cdot a_{n+1}^{-} = 0 \tag{3.173}$$

Calculating for $e^{j\cdot\beta'\cdot\Lambda}$ from eqn. (3.172) it follows that:

$$e^{j\cdot\beta'\cdot\Lambda} = A_{11} + A_{12}\cdot\frac{a_{n+1}^{-}}{a_{n+1}^{+}}$$

substituting it in eqn. (3.173) and reorganizing we obtain:

$$A_{21} + \left(A_{22} - A_{11} - A_{12}\cdot\frac{a_{n+1}^{-}}{a_{n+1}^{+}}\right)\cdot\frac{a_{n+1}^{-}}{a_{n+1}^{+}} = 0 \tag{3.174}$$

and taking into account the definition of ρ_B, eqn. (3.170), and reorganizing again:

$$-A_{12}\cdot{\rho_B}^2 - (A_{22} - A_{11})\cdot\rho_B + A_{21} = 0$$

and hence:

$$\rho_B = \frac{A_{22} - A_{11} \pm \sqrt{(A_{22} - A_{11})^2 - 4\cdot(-A_{12})\cdot A_{21}}}{-2\cdot A_{12}} \tag{3.175}$$

Thus, using eqn. (3.171), the characteristic impedance of the Bloch wave will be:

$$\frac{Z_B}{Z_0} = \frac{1+\rho_B}{1-\rho_B} = \frac{1 + \dfrac{A_{22} - A_{11} \pm \sqrt{(A_{22} - A_{11})^2 + 4 \cdot A_{12} \cdot A_{21}}}{-2 \cdot A_{12}}}{1 - \dfrac{A_{22} - A_{11} \pm \sqrt{(A_{22} - A_{11})^2 + 4 \cdot A_{12} \cdot A_{21}}}{-2 \cdot A_{12}}} \tag{3.176}$$

Since our PBG device in microstrip technology will be reciprocal (passive and without anisotropic elements), and since the two ports of the unitary cell are equal and hence will have the same normalization in any case (N_1=N_2), we can take advantage of the property for the transmission matrix given by eqn. (C.4) (the determinant of the transmission matrix will be equal to one), and simplify eqn. (3.176), obtaining:

$$\frac{Z_B}{Z_0} = \frac{-2 \cdot A_{12} + A_{22} - A_{11} \pm \sqrt{(A_{11} + A_{22})^2 - 4}}{-2 \cdot A_{12} - A_{22} + A_{11} \mp \sqrt{(A_{11} + A_{22})^2 - 4}} \tag{3.177}$$

This last equation is the final expression for the characteristic impedance of the Bloch wave [NAI 84] in the PBG device. Z_0 is the characteristic impedance of the fundamental microstrip mode (in our case) at the input/output port of the unitary cell. The transmission matrix parameters involved correspond to the unitary cell (one period). They can be easily calculated from the S-parameters since the network will be reciprocal and assumed as lossless, and the two ports of the unitary cell will be equal and hence will have the same normalization (N_1=N_2), giving rise from eqns. (C.3) and (C.6) to the following relations:

$$A_{11} = \frac{1}{S_{21}} \quad ; \quad A_{22} = \frac{1}{S_{21}^*} \quad ; \quad A_{12} = -\frac{S_{11}^*}{S_{21}^*} \tag{3.178}$$

The equation for the characteristic impedance of the Bloch wave has two results: one corresponds to the forward travelling Bloch wave (Z_B^+), and the other to the backward travelling Bloch wave (Z_B^-). If the unitary cell is symmetric then it will be satisfied that $Z_B^+ = -Z_B^-$, but if the unitary cell is asymmetric then there will be no relation between them. To avoid the ambiguity that we can have in the sign in eqn. (3.177), it is important to take into account that the Z_B^+ will be always real and positive in the propagation band.

Another way to avoid the previously commented ambiguity that can exist in eqn. (3.177) and to make sure that we are calculating the characteristic impedance of the forward or backward travelling Bloch wave in all the frequency range (including the forbidden band or Bandgap), we can use an alternative expression obtained as a function of β'. To do it, we start from eqn. (3.172) and reorganize it introducing ρ_B (eqn. (3.170)):

$$\frac{A_{11} - e^{j\cdot\beta'\cdot\Lambda}}{A_{12}} = -\frac{a_{n+1}^{-}}{a_{n+1}^{+}} = \rho_B$$

substituting the result in eqn. (3.171):

$$\frac{Z_B}{Z_0} = \frac{1+\rho_B}{1-\rho_B} = \frac{1 + \dfrac{A_{11} - e^{j\cdot\beta'\cdot\Lambda}}{A_{12}}}{1 - \dfrac{A_{11} - e^{j\cdot\beta'\cdot\Lambda}}{A_{12}}}$$

and reorganizing:

$$\frac{Z_B}{Z_0} = \frac{A_{12} + A_{11} - e^{j\cdot\beta'\cdot\Lambda}}{A_{12} - A_{11} + e^{j\cdot\beta'\cdot\Lambda}} \tag{3.179}$$

This last equation is also a valid expression for the calculation of the characteristic impedance of the Bloch wave in our PBG device in microstrip technology. If we use β' of the forward travelling Bloch wave, then Z_B^+ will be obtained, and if we employ β' of the backward travelling Bloch wave (= $-\beta'$ of the forward travelling Bloch wave), then Z_B^- will be obtained.

As in the expression previously calculated, Z_0 is the characteristic impedance of the fundamental microstrip mode (in our case) at the input/output port of the unitary cell (one period), and the transmission matrix parameters involved correspond to the unitary cell and can be easily calculated from the S-parameters using the relations of eqn. (3.178).

3.4.3.2. Approximate analytical expression

To finish this section a simple and approximate analytical expression for the characteristic impedance of the Bloch wave, Z_B , will be obtained. To do it, we are going to use a version of eqn. (3.179) calculated with the transmission matrix parameters of a PBG device with *N* periods. It can be readily seen that in this case the equation becomes:

$$\frac{Z_B}{Z_0} = \frac{A_{12} + A_{11} - e^{j\cdot\beta'\cdot N\cdot\Lambda}}{A_{12} - A_{11} + e^{j\cdot\beta'\cdot N\cdot\Lambda}} \tag{3.180}$$

We are interested in using the transmission matrix parameters of a PBG with N periods (and not with one period only), because we are going to employ the analytical expressions previously obtained for them (eqn. (3.89) and (3.88)) that are valid for PBG devices "large enough" (and for the range of frequencies placed around the rejected band).

We are going to calculate the expression for Z_B in the passbands placed at both sides of the forbidden band. In the passband placed to the left, the relation $-\Delta\beta \geq |k|$ will hold, and in the passband placed to the right $\Delta\beta \geq |k|$ will hold. Therefore, in the passbands it will be satisfied that:

$$\gamma = \sqrt{|k|^2 - (\Delta\beta)^2} = j\cdot\sqrt{(\Delta\beta)^2 - |k|^2} = j\cdot|\gamma| \quad ; \quad |\gamma| = \sqrt{(\Delta\beta)^2 - |k|^2} \tag{3.181}$$

where $\Delta\beta$ is given by eqn. (3.48):

$$\Delta\beta = \beta - n\cdot\frac{\pi}{\Lambda}$$

Taking advantage of eqn. (3.181), the approximate analytical expressions for the transmission matrix parameters of a PBG in microstrip technology with N periods (eqn. (3.89) and (3.88)) can be rewritten for the passbands as:

$$\begin{aligned} A_{11} &= \left(\cos(|\gamma|\cdot N\cdot\Lambda) + \frac{j\cdot\Delta\beta\cdot\sin(|\gamma|\cdot N\cdot\Lambda)}{|\gamma|}\right)\cdot e^{j\cdot\pi\cdot n\cdot N} \\ A_{12} &= A_{21}^* = \frac{-j\cdot k^*\cdot\sin(|\gamma|\cdot N\cdot\Lambda)}{|\gamma|}\cdot e^{-j\cdot\pi\cdot n\cdot N} \end{aligned} \tag{3.182}$$

(we have taken into account that $\cosh(j\theta) = \cos(\theta)$, $\sinh(j\theta) = j\cdot\sin(\theta)$)

In the same way, the $j\cdot\beta'$ term can be obtained from eqn. (3.145) and hence its approximate analytical expression will be:

$$j\cdot\beta' = j\cdot\frac{\pi}{\Lambda}\cdot n - \gamma = j\cdot\frac{\pi}{\Lambda}\cdot n - j\cdot|\gamma| \tag{3.183}$$

for the passband to the left of the forbidden band and

$$j\cdot\beta' = j\cdot\frac{\pi}{\Lambda}\cdot n+\gamma = j\cdot\frac{\pi}{\Lambda}\cdot n + j\cdot|\gamma| \tag{3.184}$$

for the passband to the right of the forbidden band, in both cases for the forward travelling Bloch wave.

Selecting in first place the passband to the left of the forbidden band, and introducing these expressions in eqn. (3.180), we have:

$$\frac{Z_B^+}{Z_0} = \frac{\left(\dfrac{-j\cdot k^*\cdot\sin(|\gamma|N\Lambda)}{|\gamma|} + \cos(|\gamma|N\Lambda) + \dfrac{j\cdot\Delta\beta\cdot\sin(|\gamma|N\Lambda)}{|\gamma|} - e^{-j\cdot|\gamma|\cdot N\cdot\Lambda}\right)\cdot e^{j\cdot\pi\cdot n\cdot N}}{\left(\dfrac{-j\cdot k^*\cdot\sin(|\gamma|N\Lambda)}{|\gamma|} - \cos(|\gamma|N\Lambda) - \dfrac{j\cdot\Delta\beta\cdot\sin(|\gamma|N\Lambda)}{|\gamma|} + e^{-j\cdot|\gamma|\cdot N\cdot\Lambda}\right)\cdot e^{j\cdot\pi\cdot n\cdot N}} \tag{3.185}$$

(taking into account that $e^{j\cdot\pi\cdot n\cdot N}$ has the same value as $e^{-j\cdot\pi\cdot n\cdot N}$, since *n* (number of the rejected band of interest) and *N* (number of periods taken) are integer numbers).

Reorganizing the equation and taking advantage of the definition of the sine and cosine functions in terms of exponentials ($\sin(\theta) = \dfrac{e^{j\theta}-e^{-j\theta}}{2j}$, $\cos(\theta) = \dfrac{e^{j\theta}+e^{-j\theta}}{2}$) it can be rewritten as:

$$\frac{Z_B^+}{Z_0} = \frac{\dfrac{-j\cdot\sin(|\gamma|\cdot N\cdot\Lambda)}{|\gamma|}\cdot\left(k^*-\Delta\beta\right) + j\cdot\sin(|\gamma|\cdot N\cdot\Lambda)}{\dfrac{-j\cdot\sin(|\gamma|\cdot N\cdot\Lambda)}{|\gamma|}\cdot\left(k^*+\Delta\beta\right) - j\cdot\sin(|\gamma|\cdot N\cdot\Lambda)}$$

and simplifying, the simple and approximate analytical expression for the characteristic impedance of the forward travelling Bloch wave is obtained:

$$\frac{Z_B^+}{Z_0} = \frac{k^*-\Delta\beta-|\gamma|}{k^*+\Delta\beta+|\gamma|} \tag{3.186}$$

valid for the passband to the left of the forbidden band. In the same way it can be easily obtained (using eqn. (3.184)) that for the passband to the right of the forbidden band the expression will be:

$$\frac{Z_B^+}{Z_0} = \frac{k^*-\Delta\beta+|\gamma|}{k^*+\Delta\beta-|\gamma|} \tag{3.187}$$

And finally, using the β' of the backward travelling Bloch wave (= -β' of the forward travelling Bloch wave), the expressions for the backward wave are calculated:

$$\frac{Z_B^-}{Z_0} = \frac{k^* - \Delta\beta + |\gamma|}{k^* + \Delta\beta - |\gamma|} \tag{3.188}$$

valid for the passband to the left of the forbidden band and:

$$\frac{Z_B^-}{Z_0} = \frac{k^* - \Delta\beta - |\gamma|}{k^* + \Delta\beta + |\gamma|} \tag{3.189}$$

valid for the passband to the right of the forbidden band.

In all of these equations Z_0 is the characteristic impedance of the fundamental microstrip mode (in our case) at the input/output port, $|\gamma|$ is given by eqn. (3.181), k is the coupling coefficient parameter given by eqns. (3.20), (3.38) and (3.52), and $\Delta\beta$ is given by eqn. (3.48).

To finish it is important to notice that these analytical expressions are approximate because they have been obtained using the approximate analytical expressions for the transmission matrix parameters and for the phase constant of the Bloch wave. Therefore they involve the two approximations detailed in section (3.3.1),

- The phase constant β is approximated as a variable constant with z. An "averaged" β is assigned to all the device.
- We neglect the terms with complex exponentials that vary very quickly with z and as a consequence the coupling coefficient $K(z)$ is approximated by only one term of its Fourier series. This approximation is valid for the range of frequencies placed around the maximum reflection frequency, and for a PBG device large enough. (this last condition is no problem in this case because the PBG taken has N periods and N can be as large as needed).

3.4.4. Analysis of terminated PBG structures

Let us consider a finite periodic structure (a PBG in microstrip technology in our case) with period Λ, and with an integer number of periods, N, excited at the input port by a source with a characteristic impedance Z_S , and terminated at the output port by a load impedance Z_L.

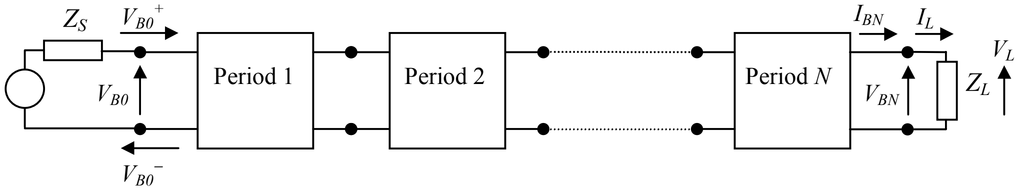

For the sake of simplicity, we are going to realize the study using the equivalent voltages and currents for the Bloch waves, V_B, I_B [COL 92]. The total voltage and current at the *n*-th terminal will be:

$$V_{Bn} = V_{B0}^+ \cdot e^{-j\cdot\beta'\cdot n\cdot\Lambda} + V_{B0}^- \cdot e^{j\cdot\beta'\cdot n\cdot\Lambda}$$
$$I_{Bn} = I_{B0}^+ \cdot e^{-j\cdot\beta'\cdot n\cdot\Lambda} + I_{B0}^- \cdot e^{j\cdot\beta'\cdot n\cdot\Lambda} = \frac{V_{B0}^+}{Z_B^+} \cdot e^{-j\cdot\beta'\cdot n\cdot\Lambda} + \frac{V_{B0}^-}{Z_B^-} \cdot e^{j\cdot\beta'\cdot n\cdot\Lambda} \tag{3.190}$$

On the other hand at the *N*-th terminal it will be satisfied:

$$V_L = V_{BN} = Z_L \cdot I_{BN} = Z_L \cdot I_L \tag{3.191}$$

and hence:

$$V_{BN} = V_{BN}^+ + V_{BN}^- = Z_L \cdot \left(\frac{V_{BN}^+}{Z_B^+} + \frac{V_{BN}^-}{Z_B^-} \right) \tag{3.192}$$

Calculating from eqn. (3.192) the reflection coefficient for the Bloch waves at the load impedance, $\rho_L = \rho_N = \dfrac{V_{BN}^-}{V_{BN}^+}$ we obtain:

$$V_{BN}^- \cdot \left(1 - \frac{Z_L}{Z_B^-} \right) = V_{BN}^+ \cdot \left(-1 + \frac{Z_L}{Z_B^+} \right) \Rightarrow$$
$$\Rightarrow \rho_L = \frac{V_{BN}^-}{V_{BN}^+} = \frac{-1 + Z_L / Z_B^+}{1 - Z_L / Z_B^-} \Rightarrow \rho_L = \frac{-Z_B^-}{Z_B^+} \cdot \frac{Z_L - Z_B^+}{Z_L - Z_B^-} \tag{3.193}$$

The reflection coefficient for the Bloch waves at the *n*-th terminal will be:

$$\rho_n = \frac{V_{Bn}^-}{V_{Bn}^+} = \frac{V_{BN}^- \cdot e^{-j\cdot\beta'\cdot(N-n)\cdot\Lambda}}{V_{BN}^+ \cdot e^{j\cdot\beta'\cdot(N-n)\cdot\Lambda}} = \rho_L \cdot e^{-2\cdot j\cdot\beta'\cdot(N-n)\cdot\Lambda} \tag{3.194}$$

and the input impedance at the *n*-th terminal will be given by the expression:

$$Z_{in,n} = \frac{V_{Bn}}{I_{Bn}} = \frac{V_{Bn}^{+} + V_{Bn}^{-}}{I_{Bn}^{+} + I_{Bn}^{-}} = \frac{V_{Bn}^{+} + V_{Bn}^{-}}{\dfrac{V_{Bn}^{+}}{Z_B^{+}} + \dfrac{V_{Bn}^{-}}{Z_B^{-}}} = \frac{V_{Bn}^{+} \cdot (1+\rho_n)}{V_{Bn}^{+} \cdot \left(\dfrac{1}{Z_B^{+}} + \dfrac{\rho_n}{Z_B^{-}} \right)} = \frac{Z_B^{+} \cdot Z_B^{-} \cdot (1+\rho_n)}{Z_B^{-} + Z_B^{+} \cdot \rho_n}$$

substituting for ρ_n from eqns. (3.194) and (3.193), and simplifying we obtain:

$$Z_{in,n} = \frac{Z_B^{+} \cdot Z_B^{-} \cdot \left(1 - \dfrac{Z_B^{-}}{Z_B^{+}} \cdot \dfrac{Z_L - Z_B^{+}}{Z_L - Z_B^{-}} \cdot e^{-2 \cdot j \cdot \beta' \cdot (N-n) \cdot \Lambda} \right)}{Z_B^{-} - Z_B^{-} \cdot \dfrac{Z_L - Z_B^{+}}{Z_L - Z_B^{-}} \cdot e^{-2 \cdot j \cdot \beta' \cdot (N-n) \cdot \Lambda}} \qquad (3.195)$$

and particularizing for the 0 terminal (input port), we have that the input impedance at the input port, Z_{in} , of the PBG microstrip device will be:

$$Z_{in} = \frac{Z_B^{+} \cdot Z_B^{-} \cdot \left(1 - \dfrac{Z_B^{-}}{Z_B^{+}} \cdot \dfrac{Z_L - Z_B^{+}}{Z_L - Z_B^{-}} \cdot e^{-2 \cdot j \cdot \beta' \cdot N \cdot \Lambda} \right)}{Z_B^{-} - Z_B^{-} \cdot \dfrac{Z_L - Z_B^{+}}{Z_L - Z_B^{-}} \cdot e^{-2 \cdot j \cdot \beta' \cdot N \cdot \Lambda}} \qquad (3.196)$$

An equation similar to eqn. (3.196) is presented in [NAI 84] for periodic structures in microstrip technology.

From the value for the input impedance Z_{in} , the reflection coefficient and the transmission coefficient of the device can be immediately calculated.
The reflection coefficient at the input port, calculated for the waves corresponding to the fundamental microstrip mode of the auxiliary uniform waveguide associated to the input port (whose characteristic impedance is Z_0) will have the value:

$$\rho_{in} = \frac{-a^{-}}{a^{+}} = \frac{V^{-}}{V^{+}} = \frac{Z_{in} - Z_0}{Z_{in} + Z_0} \qquad (3.197)$$

and it is equal to the S_{11} parameter if the output port is matched. The minus sign applied to the wave amplitude a^{-} arises due to the relation existent between the backward wave amplitude and its equivalent voltage, see eqn. (A.9), Appendix A.

The transmission coefficient at the input port will have the value:

$$\tau_{in} = \frac{a_{in}}{a^+} = \frac{V_{in}}{V^+} = \frac{2 \cdot Z_{in}}{Z_{in} + Z_0} \tag{3.198}$$

where $V_{in} = V^+ + V^-$ is the total equivalent voltage at the input port, and $a_{in} = a^+ - a^-$ is proportional to the total transversal electric field at the input port.

The ratio between the power given to the circuit (the loaded PBG device in our case) and the incident power at the input port will be $T_{in} = \frac{P_{in}}{P^+}$ and hence:

$$P = \frac{1}{2} \cdot \mathrm{Re}\left(V \cdot I^*\right) = \frac{1}{2} \cdot \mathrm{Re}\left(V \cdot \frac{V^*}{Z^*}\right) = \frac{1}{2} \cdot \mathrm{Re}\left(\frac{|V|^2}{Z^*}\right)$$

$$P_{in} = \frac{1}{2} \cdot \mathrm{Re}\left(\frac{|V_{in}|^2}{Z_{in}^*}\right) \quad ; \quad P^+ = \frac{1}{2} \cdot \mathrm{Re}\left(\frac{|V^+|^2}{Z_0^*}\right)$$

$$T_{in} = \frac{P_{in}}{P^+} = \frac{|V_{in}|^2}{|V^+|^2} \cdot \frac{\mathrm{Re}\left(1/Z_{in}^*\right)}{\mathrm{Re}\left(1/Z_0^*\right)} \Rightarrow T_{in} = |\tau_{in}|^2 \cdot Z_0 \cdot \mathrm{Re}\left(1/Z_{in}^*\right) \tag{3.199}$$

(taking into account that the characteristic impedance of the input port, Z_0 , will be a real number).

The power transmission coefficient, T_{in} , will satisfy $T_{in} = |S_{21}|^2$ if the PBG device is lossless and if the output port is matched.

To finish this section it is important to note that if the unitary cell (or period) of the PBG microstrip structure under analysis is symmetrical, then the Bloch wave characteristic impedance will satisfy:

$$Z_B^+ = -Z_B^- = Z_B \tag{3.200}$$

and the resulting Z_B parameter will have the same function and properties as the characteristic impedance in the uniform transmission lines. Let's see.

From eqn. (3.193), the reflection coefficient for the Bloch waves at the load impedance (*N*-th terminal) has the form:

$$\rho_L = \frac{V_{BN}^-}{V_{BN}^+} = \frac{Z_L - Z_B}{Z_L + Z_B} \tag{3.201}$$

and at the *n*-th terminal (from eqn. (3.194)):

$$\rho_n = \rho_L \cdot e^{-2\cdot j\cdot\beta'\cdot(N-n)\cdot\Lambda} \tag{3.202}$$

The input impedance at the *n*-th terminal will be (from eqn. (3.195)):

$$Z_{in,n} = \frac{V_{Bn}}{I_{Bn}} = Z_B \cdot \frac{(1+\rho_n)}{(1-\rho_n)} \tag{3.203}$$

or from eqn. (3.195) also:

$$Z_{in,n} = \frac{V_{Bn}}{I_{Bn}} = Z_B \cdot \frac{\left(1 + \dfrac{Z_L - Z_B}{Z_L + Z_B} \cdot e^{-2\cdot j\cdot\beta'\cdot(N-n)\cdot\Lambda}\right)}{\left(1 - \dfrac{Z_L - Z_B}{Z_L + Z_B} \cdot e^{-2\cdot j\cdot\beta'\cdot(N-n)\cdot\Lambda}\right)}$$

and simplifying we obtain the classical form:

$$Z_{in,n} = Z_B \cdot \frac{Z_L + j \cdot Z_B \cdot \tan(\beta' \cdot (N-n) \cdot \Lambda)}{Z_B + j \cdot Z_L \cdot \tan(\beta' \cdot (N-n) \cdot \Lambda)} \tag{3.204}$$

Particularizing for the 0 terminal (input port), we have that the input impedance at the input port, Z_{in} , of the PBG microstrip device has also the classical form:

$$Z_{in} = Z_B \cdot \frac{Z_L + j \cdot Z_B \cdot \tan(\beta' \cdot N \cdot \Lambda)}{Z_B + j \cdot Z_L \cdot \tan(\beta' \cdot N \cdot \Lambda)} \tag{3.205}$$

As a conclusion it is important to stress that to have the forward travelling Bloch wave matched (i.e. to avoid the appearance of a reflected wave due to the load) it is necessary to have a load impedance equal to the forward Bloch wave characteristic impedance ($Z_L = Z_B^+$). In the same way, to have the backward travelling Bloch wave matched it is necessary that the characteristic impedance of the source satisfies $Z_S = -Z_B^-$ (to make the backward travelling Bloch wave not to have reflection when it arrives to the source). Moreover, if the unitary cell is symmetric the PBG structure in microstrip technology will behave as a uniform transmission line with characteristic impedance Z_B and phase constant β', and hence it will be matched when the source impedance, load impedance and Bloch wave characteristic impedance satisfy:

$$Z_S = Z_L = Z_B \tag{3.206}$$

3.5. Relation between *K(z)* and *S*11*(f)* in terms of Fourier Transforms

In this section several expressions that relate the coupling coefficient, *K(z)*, of a nonuniform waveguide (a PBG structure in microstrip technology in our case) and its reflection parameter $S_{11}(f)$, will be obtained. The relation will be given through the Fourier Transform, resulting in a straightforward expression for the simplified case of low reflectivity and in a series type solution for the general case.

3.5.1. Approximate expression for structures with low reflectivity

We start from the simplified system of coupled mode equations valid for PBG structures in microstrip technology, eqns. (3.16), (3.17) (the only approximation involved is to assume single mode operation, see section (3.2.1)).

$$\frac{da^+}{dz} = -j \cdot \beta \cdot a^+ + K \cdot a^-$$

$$\frac{da^-}{dz} = j \cdot \beta \cdot a^- + K \cdot a^+$$

We introduce the reflection coefficient parameter, $\rho = V^- / V^+ = -a^- / a^+$ (the minus sign applied to the wave amplitude a^- arises due to the relation existent between the backward wave amplitude and its equivalent voltage, see eqn. (A.9), Appendix A), and taking its derivative it follows:

$$\frac{d\rho}{dz} = -\frac{\left(\frac{da^-}{dz} \cdot a^+ - \frac{da^+}{dz} \cdot a^-\right)}{\left(a^+\right)^2} = -\frac{\left(j \cdot \beta \cdot a^- + K \cdot a^+\right) \cdot a^+ - \left(-j \cdot \beta \cdot a^+ + K \cdot a^-\right) \cdot a^-}{\left(a^+\right)^2}$$

and reorganizing the equation:

$$\frac{d\rho}{dz} = -j \cdot \beta \cdot \frac{a^-}{a^+} - K - j \cdot \beta \cdot \frac{a^-}{a^+} + K \cdot \frac{(a^-)^2}{(a^+)^2}$$

reorganizing again and introducing ρ again:

$$\frac{d\rho}{dz} = 2 \cdot j \cdot \beta \cdot \rho - K \cdot \left(1 - \rho^2\right) \tag{3.207}$$

Equation (3.207) is called a Riccati equation [COL 92]. It is a nonlinear equation because of the term ρ^2 and does not have a known general solution.

To solve it, we are going to realize the following approximations:

- We assume that the phase constant β (and hence ε_{eff}) is a variable constant with z. An "averaged" β (and hence ε_{eff}) is assigned to all the device.
- We assume that $|\rho(z)|^2 << 1$, i.e. we assume that the reflectivity is low along all the device.

With these approximations eqn. (3.207) can be simplified as:

$$\frac{d\rho}{dz} = 2 \cdot j \cdot \beta \cdot \rho - K \tag{3.208}$$

We are going to integrate this last equation between z=0 and z=L (being L the length of the device). To do it, we multiply both members of the equation by $e^{-j \cdot 2 \cdot \beta \cdot z}$:

$$\frac{d\rho}{dz} \cdot e^{-j \cdot 2 \cdot \beta \cdot z} = 2 \cdot j \cdot \beta \cdot \rho \cdot e^{-j \cdot 2 \cdot \beta \cdot z} - K \cdot e^{-j \cdot 2 \cdot \beta \cdot z}$$

and using the equality:

$$\frac{d}{dz}\left(\rho \cdot e^{-j \cdot 2 \cdot \beta \cdot z}\right) = \frac{d\rho}{dz} \cdot e^{-j \cdot 2 \cdot \beta \cdot z} - 2 \cdot j \cdot \beta \cdot \rho \cdot e^{-j \cdot 2 \cdot \beta \cdot z}$$

(since β is assumed as constant with z)

the equation can be rewritten as:

$$\frac{d}{dz}\left(\rho \cdot e^{-j \cdot 2 \cdot \beta \cdot z}\right) = -K \cdot e^{-j \cdot 2 \cdot \beta \cdot z} \tag{3.209}$$

Integrating both sides of eqn. (3.209) between z=0 and z=L (assuming that the device has a length L and is placed between z=0 and z=L) we have:

$$\rho \cdot e^{-j \cdot 2 \cdot \beta \cdot z}\Big|_{z=0}^{z=L} = -\int_0^L K \cdot e^{-j \cdot 2 \cdot \beta \cdot z} \cdot dz \Rightarrow \rho(L) \cdot e^{-j \cdot 2 \cdot \beta \cdot z} - \rho(0) = -\int_0^L K \cdot e^{-j \cdot 2 \cdot \beta \cdot z} \cdot dz$$

and assuming that the output port of the device is matched ($\rho(L) = 0$):

$$\rho(0)\Big|_{\rho(L)=0} = \int_0^L K \cdot e^{-j \cdot 2 \cdot \beta \cdot z} \cdot dz$$

and hence:

$$S_{11} = \int_0^L K(z) \cdot e^{-j \cdot 2 \cdot \beta \cdot z} \cdot dz \tag{3.210}$$

As it can be seen, eqn. (3.210) gives the relation between the coupling coefficient of a device *K(z)*, and its reflection parameter $S_{11}(f)$. From the form of the equation a Fourier Transform relation can be envisaged between both parameters. Let's see now how is exactly this Fourier Transform relation.

Expressing the phase constant β as a function of the effective dielectric constant (eqn. (3.19)), (where ε_{eff} is allowed to be a function of the frequency, f):

$$\beta = \frac{2 \cdot \pi \cdot f}{c} \cdot \sqrt{\varepsilon_{eff}}$$

the relation given by eqn. (3.210) becomes:

$$S_{11} = \int_0^L K(z) \cdot e^{-j \cdot 2 \cdot \frac{2 \cdot \pi \cdot f}{c} \cdot \sqrt{\varepsilon_{eff}} \cdot z} \cdot dz$$

and if we assume that the coupling coefficient *K(z)*=0 , $\forall z \notin [0, L]$ it can be rewritten as:

$$S_{11} = \int_{-\infty}^{\infty} K(z) \cdot e^{-j \cdot 2 \cdot \pi \cdot \left(\frac{2 \cdot \sqrt{\varepsilon_{eff}}}{c} \cdot f \right) \cdot z} \cdot dz \tag{3.211}$$

Taking the following definition for the Fourier Transform pair:

$$\begin{gathered} V(f) = F(v(t)) = \int_{-\infty}^{\infty} v(t) \cdot e^{-j \cdot 2 \cdot \pi \cdot f \cdot t} \cdot dt \\ v(t) = F^{-1}(V(f)) = \int_{-\infty}^{\infty} V(f) \cdot e^{j \cdot 2 \cdot \pi \cdot f \cdot t} \cdot df \\ v(t) \xleftrightarrow{FT} V(f) \end{gathered} \tag{3.212}$$

then eqn. (3.211) can be rewritten as:

$$K(z) \xleftrightarrow{FT} S_{11}\left(f \cdot 2 \cdot \sqrt{\varepsilon_{eff}} / c\right) \tag{3.213}$$

giving rise to the sought Fourier Transform pair, where c is the speed of light in vacuum, $c = 3 \cdot 10^8$ m/s

Moreover, from eqns. (3.212) and (3.213) it can be deduced that:

$$K(z)=\int_{-\infty}^{\infty} S_{11}\left(f\cdot 2\cdot\sqrt{\varepsilon_{eff}}/c\right)\cdot e^{j\cdot 2\cdot\pi\cdot\left(\frac{2\cdot\sqrt{\varepsilon_{eff}}}{c}\cdot f\right)\cdot z}\cdot d\left(f\cdot 2\cdot\sqrt{\varepsilon_{eff}}/c\right) \qquad (3.214)$$

The approximations used to obtain equation (3.211) (besides single mode operation) are the two previously detailed in this section: β (and hence ε_{eff}) is assumed to be constant with *z*, and we assume that $|\rho(z)|^2 << 1$, (i.e. the reflectivity is low along all the device). To obtain eqn. (3.214), (and the Fourier Transform relation in full sense, eqn. (3.213)) it is assumed also that *K(z)* is not a function of the frequency, *f*.

On the other hand, if we take the following definition for the Fourier Transform pair:

$$\begin{aligned} V(\omega)&=F(v(t))=\int_{-\infty}^{\infty} v(t)\cdot e^{-j\cdot\omega\cdot t}\cdot dt \\ v(t)&=F^{-1}(V(\omega))=\frac{1}{2\cdot\pi}\int_{-\infty}^{\infty} V(\omega)\cdot e^{j\cdot\omega\cdot t}\cdot d\omega \\ &v(t)\xleftrightarrow{FT}V(\omega) \end{aligned} \qquad (3.215)$$

then eqn. (3.211) can be rewritten as:

$$K(z)\xleftrightarrow{FT}S_{11}(2\cdot\beta) \qquad (3.216)$$

and, of course, the approximations involved are the same as those previously detailed.

The fundamentals that have inspired the development of this section can be found in [BOL 50, BOL 56, COL 92].

3.5.1.1. Use of the spatial variable “electrical position”

The electrical position variable χ was introduced in section (3.3.4), and is obtained form the physical position *z* by using eqn. (3.104):

$$\chi(z)=\int_0^z\sqrt{\varepsilon_{eff}(s)}\cdot ds$$

(in this definition it is assumed that the origin of the circuit is placed at $z=0$).
With it, and following the same reasoning as in section (3.3.4) for the coupled mode equations, the Riccati equation (eqn. (3.207)) can be rewritten as:

$$\frac{d\rho}{d\chi}=2\cdot j\cdot\beta_0\cdot\rho-K(\chi)\cdot\left(1-\rho^2\right) \qquad (3.217)$$

where:

$$\beta_0 = \frac{2 \cdot \pi \cdot f}{c} \tag{3.218}$$

and is constant with the electrical position variable χ , and *K(χ)* is the coupling coefficient calculated using the electrical position variable χ, as shown in eqn. (3.109). The aim of the electrical position variable, χ , is to obtain a β constant with it along the PBG device. In this way, the first of the two approximations used in the previous section to obtain the Fourier Transform relation can be avoided, achieving more accurate results. Thus, in this case, we have to make only one approximation:

- We assume that $|\rho(\chi)|^2 << 1$, i.e. we assume that the reflectivity is low along all the device.

We are going to define also L_χ :

$$L_\chi = \chi(L) = \int_0^L \sqrt{\varepsilon_{eff}(s)} \cdot ds \tag{3.219}$$

From eqn. (3.217) and with the approximation introduced we obtain, following the same reasoning detailed in the previous section:

$$S_{11} = \int_0^{L_\chi} K(\chi) \cdot e^{-j \cdot 2 \cdot \beta_0 \cdot \chi} \cdot d\chi \tag{3.220}$$

Let's see how is exactly the Fourier Transform relation.

Assuming that the coupling coefficient *K(χ)*=0 , $\forall \chi \notin \lfloor 0, L_\chi \rfloor$, and using eqn. (3.218) the last expression can be rewritten as:

$$S_{11} = \int_{-\infty}^{\infty} K(\chi) \cdot e^{-j \cdot 2 \cdot \pi \cdot (f \cdot 2/c) \cdot \chi} \cdot d\chi \tag{3.221}$$

If we take the definition for the Fourier Transform pair given by eqn. (3.212), then eqn. (3.221) can be rewritten as:

$$K(\chi) \xleftrightarrow{FT} S_{11}(f \cdot 2/c) \tag{3.222}$$

and consequently we will have also:

$$K(\chi) = \int_{-\infty}^{\infty} S_{11}(f \cdot 2/c) \cdot e^{j \cdot 2 \cdot \pi \cdot (f \cdot 2/c) \cdot \chi} \cdot d(f \cdot 2/c) \tag{3.223}$$

The approximation used to obtain equation (3.221) (besides single mode operation) is the one previously detailed in this section: we assume that $|\rho(\chi)|^2 << 1$, (i.e. the reflectivity is low along all the device). To obtain eqn. (3.223), (and the Fourier Transform relation in full sense, eqn. (3.222)) it is assumed also that *K(χ)* and *χ(z)* ($\Rightarrow \varepsilon_{eff}(z)$) are not functions of the frequency, *f*.

To finish, if we take the definition for the Fourier Transform pair given in eqn. (3.215), then eqn. (3.221) can be rewritten as:

$$K(\chi) \xleftrightarrow{FT} S_{11}(2 \cdot \beta_0) \tag{3.224}$$

3.5.1.2. Use of the "echo time" variable

In this section we are going to introduce a new variable calculated from the physical position variable, *z*. It will be called "echo time" and its definition is [KOB 92]:

$$\tau(z) = 2 \cdot \int_0^z \frac{\sqrt{\varepsilon_{eff}(s)}}{c} \cdot ds \tag{3.225}$$

where τ is the "echo time" variable and *c* is the speed of light in vacuum.
It is interesting to note that τ is equal to the time employed by a signal of frequency *f* transmitted at *z*=0 to travel along the waveguide, reflect at position *z* and return to the sending point at *z*=0. (let's recall that $v_p = c/\sqrt{\varepsilon_{eff}}$). That's why it is called "echo time".
Using the τ variable, the Riccati equation (eqn. (3.207)) will become:

$$\frac{d\rho}{d\tau} = 2 \cdot j \cdot \pi \cdot f \cdot \rho - K(\tau) \cdot \left(1 - \rho^2\right) \tag{3.226}$$

(since applying the first fundamental theorem of calculus: $\frac{d\tau}{dz} = 2 \cdot \frac{\sqrt{\varepsilon_{eff}}}{c}$)
where *K(τ)* is the coupling coefficient calculated using the echo time variable, in the same sense as *K(χ)* was the coupling coefficient calculated using the electrical position variable χ, as shown in eqn. (3.109).
We are going to take the following approximation:

- We assume that $|\rho(\tau)|^2 << 1$, i.e. we assume that the reflectivity is low along all the device.

with it, eqn. (3.226) can be rewritten as:

$$\frac{d\rho}{d\tau} = 2 \cdot j \cdot \pi \cdot f \cdot \rho - K(\tau) \tag{3.227}$$

Integrating eqn. (3.227) between τ=0 and τ=τ_L , where *L* is the length of the device under analysis that is placed between *z*=0 and *z*=*L*, and:

$$\tau_L = \tau(L) = 2 \cdot \int_0^L \frac{\sqrt{\varepsilon_{eff}(z)}}{c} \cdot dz \tag{3.228}$$

and following the same reasoning detailed in section (3.5.1), we obtain:

$$S_{11} = \int_0^{\tau_L} K(\tau) \cdot e^{-j \cdot 2 \cdot \pi \cdot f \cdot \tau} \cdot d\tau \tag{3.229}$$

Let's see how is exactly the Fourier Transform relation with the echo time variable. Assuming that the coupling coefficient *K(τ)*=0 , $\forall \tau \notin [0, \tau_L]$, the last expression can be rewritten as:

$$S_{11} = \int_{-\infty}^{\infty} K(\tau) \cdot e^{-j \cdot 2 \cdot \pi \cdot f \cdot \tau} \cdot d\tau \tag{3.230}$$

Taking the definition for the Fourier Transform pair given by eqn. (3.212), then eqn. (3.230) can be rewritten as:

$$K(\tau) \xleftrightarrow{FT} S_{11}(f) \tag{3.231}$$

and consequently we will have also:

$$K(\tau) = \int_{-\infty}^{\infty} S_{11}(f) \cdot e^{j \cdot 2 \cdot \pi \cdot f \cdot \tau} \cdot df \tag{3.232}$$

The approximation used to obtain equation (3.230) (besides single mode operation) is the one previously detailed in this section: we assume that $|\rho(\tau)|^2 << 1$, (i.e. the reflectivity is low along all the device). To obtain eqn. (3.232), (and the Fourier Transform relation in full sense, eqn. (3.231)) it is assumed also that *K(τ)* and *τ(z)* ($\Rightarrow \varepsilon_{eff}(z)$) are not functions of the frequency, *f*.

To finish, if we take the definition for the Fourier Transform pair given in eqn. (3.215), then eqn. (3.230) can be rewritten as:

$$K(\tau) \xleftrightarrow{FT} S_{11}(\omega) \tag{3.224}$$

where $\omega = 2 \cdot \pi \cdot f$

3.5.2. General expressions

The simple expressions calculated in the previous section have been obtained for devices with low reflectivity. In this section general more complicated expressions without this restriction will be obtained, and it will be shown that the simple expressions can be seen also as a first approximation to the general more complicated expressions.

3.5.2.1. Exact expression for *S*₁₁*(f)* from *K(z)*

We start from the simplified system of coupled mode equations valid for PBG structures in microstrip technology, eqns. (3.16), (3.17) (the only approximation involved is to assume single mode operation, see section (3.2.1)).

$$\frac{da^+}{dz} = -j \cdot \beta \cdot a^+ + K \cdot a^-$$
$$\frac{da^-}{dz} = j \cdot \beta \cdot a^- + K \cdot a^+$$

We introduce the variables $A^+(z)$, $A^-(z)$:

$$\begin{aligned} a^+(z) &= A^+(z) \cdot e^{-j \cdot \beta \cdot z} \\ a^-(z) &= A^-(z) \cdot e^{j \cdot \beta \cdot z} \end{aligned} \tag{3.225}$$

The coupled mode equations then become:

$$\begin{aligned} \frac{dA^+}{dz} &= K(z) \cdot A^-(z) \cdot e^{j \cdot 2 \cdot \beta \cdot z} \\ \frac{dA^-}{dz} &= K(z) \cdot A^+(z) \cdot e^{-j \cdot 2 \cdot \beta \cdot z} \end{aligned} \tag{3.226}$$

assuming that β is constant in z.

The boundary conditions that we are going to use are the following:

$$A^+(z=0, \beta) = 1 \tag{3.227}$$

$$A^{-}(z=L,\beta)=0 \tag{3.228}$$

and hence we are assuming unitary excitation at the input, and matching conditions at the output of the device.

Applying them, and taking into account the expression for the S_{11} parameter as a function of the complex amplitudes of the mode, a^{+}, a^{-} (eqn. (3.29), section (3.2.3)):

$$S_{11}(\beta)=\left.\frac{-a^{-}(z=0,\beta)}{a^{+}(z=0,\beta)}\right|_{a^{-}(z=L,\beta)=0}=\frac{-A^{-}(z=0,\beta)}{A^{+}(z=0,\beta)}=-A^{-}(z=0,\beta)$$

and therefore:

$$S_{11}(\beta)=-A^{-}(z=0,\beta) \tag{3.229}$$

Integrating the second coupled mode equation of eqns. (3.226):

$$\int_{z_1=z}^{z_1=L}\frac{dA^{-}}{dz_1}\cdot dz_1=\int_{z_1=z}^{z_1=L}K(z_1)\cdot A^{+}\cdot e^{-j\cdot 2\cdot\beta\cdot z_1}\cdot dz_1$$

$$A^{-}(L,\beta)-A^{-}(z,\beta)=\int_{z_1=z}^{z_1=L}K(z_1)\cdot A^{+}(z_1,\beta)\cdot e^{-j\cdot 2\cdot\beta\cdot z_1}\cdot dz_1$$

and taking into account that from eqn. (3.228), $A^{-}(L,\beta)=0$, we have:

$$A^{-}(z,\beta)=-\int_{z_1=z}^{z_1=L}K(z_1)\cdot A^{+}(z_1,\beta)\cdot e^{-j\cdot 2\cdot\beta\cdot z_1}\cdot dz_1 \tag{3.230}$$

Integrating now the first coupled mode equation of eqns. (3.226):

$$\int_{z_2=0}^{z_2=z}\frac{dA^{+}}{dz_2}\cdot dz_2=\int_{z_2=0}^{z_2=z}K(z_2)\cdot A^{-}(z_2,\beta)\cdot e^{+j\cdot 2\cdot\beta\cdot z_2}\cdot dz_2$$

$$A^{+}(z,\beta)-A^{+}(0,\beta)=\int_{z_2=0}^{z_2=z}K(z_2)\cdot A^{-}(z_2,\beta)e^{+j\cdot 2\cdot\beta\cdot z_2}\cdot dz_2$$

and taking into account that from eqn. (3.227), $A^{+}(0,\beta)=0$, we have:

$$A^{+}(z,\beta)=1+\int_{z_2=0}^{z_2=z}K(z_2)\cdot A^{-}(z_2,\beta)e^{+j\cdot 2\cdot\beta\cdot z_2}\cdot dz_2 \tag{3.231}$$

Substituting the expression of eqn. (3.231), in that of eqn. (3.230), we obtain:

$$A^{-}(z,\beta) = -\int_{z_1=z}^{L} K(z_1)\cdot e^{-j\cdot 2\cdot \beta\cdot z_1}\cdot dz_1 -$$

$$-\int_{z_1=z}^{z_1=L} dz_1 \int_{z_2=0}^{z_2=z_1} dz_2 \cdot K(z_1)\cdot K(z_2)\cdot e^{-j\cdot 2\cdot \beta\cdot z_1}\cdot e^{-j\cdot 2\cdot \beta\cdot z_2}\cdot A^{-}(z_2,\beta)$$

Proceeding in an iterative manner (i.e., substituting the expression of eqn. (3.230) in the last result, and then the expression of eqn. (3.231) in what remains, and again substituting expression of eqn. (3.230), and so on) we obtain the following infinite series:

$$A^{-}(z,\beta) = -\int_{z_1=z}^{L} K(z_1)\cdot e^{-j\cdot 2\cdot \beta\cdot z_1}\cdot dz_1 +$$

$$+\int_{z_1=z}^{L} dz_1 \int_{z_2=0}^{z_1} dz_2 \int_{z_3=z_2}^{L} dz_3 \cdot K(z_1)\cdot K(z_2)\cdot K(z_3)\cdot e^{-j\cdot 2\cdot \beta\cdot (z_1-z_2+z_3)}$$

$$+.............+$$

$$+(-1)^{n}\cdot \int_{z_1=z}^{L} dz_1 \int_{z_2=0}^{z_1} dz_2 \int_{z_3=z_2}^{L} dz_3 .... \int_{z_{2n-2}=0}^{z_{2n-3}} dz_{2n-2} \int_{z_{2n-1}=z_{2n-2}}^{L} dz_{2n-1}\cdot$$

$$\cdot K(z_1)\cdot K(z_2).K(z_3)...K(z_{2n-1})\cdot e^{-j\cdot 2\cdot \beta\cdot (z_1-z_2+z_3-...-z_{2n-2}+z_{2n-1})}$$

So, since $S_{11}(\beta) = -A^{-}(z=0,\beta)$ (see eqn. (3.229)), we will finally have:

$$S_{11}(\beta) = +\int_{z_1=0}^{L} K(z_1)\cdot e^{-j\cdot 2\cdot \beta\cdot z_1}\cdot dz_1 -$$

$$-\int_{z_1=0}^{L} dz_1 \int_{z_2=0}^{z_1} dz_2 \int_{z_3=z_2}^{L} dz_3 \cdot K(z_1)\cdot K(z_2)\cdot K(z_3)\cdot e^{-j\cdot 2\cdot \beta\cdot (z_1-z_2+z_3)}$$

$$+.........+$$

$$+(-1)^{n+1}\cdot \int_{z_1=0}^{L} dz_1 \int_{z_2=0}^{z_1} dz_2 \int_{z_3=z_2}^{L} dz_3 .... \int_{z_{2n-2}=0}^{z_{2n-3}} dz_{2n-2} \int_{z_{2n-1}=z_{2n-2}}^{L} dz_{2n-1}\cdot$$

$$\cdot K(z_1)\cdot K(z_2).K(z_3)....K(z_{2n-1})\cdot e^{-j\cdot 2\cdot \beta\cdot (z_1-z_2+z_3-...-z_{2n-2}+z_{2n-1})} \quad (3.232)$$

It is important to note that the only approximation introduced to obtain this expression (besides single mode operation) is to assume β constant with z. (Particularly, it will keep being valid if *K(z)* is function of the frequency).

It is also interesting to note that each one of the terms in the series is an integral that extends to all the propagation paths with a given number of scattering events.

An expression similar to eqn. (3.232) was obtained in [FEC 99] for Fiber Bragg Gratings in the optical regime.

3.5.2.2. Exact expression for *K(z)* from $S_{11}(f)$

As usually, we start from the simplified system of coupled mode equations valid for PBG structures in microstrip technology, eqns. (3.16), (3.17) (the only approximation involved is to assume single mode operation, see section (3.2.1)).

$$\frac{da^{+}}{dz} = -j \cdot \beta \cdot a^{+} + K \cdot a^{-}$$

$$\frac{da^{-}}{dz} = j \cdot \beta \cdot a^{-} + K \cdot a^{+}$$

Reorganizing the equations in order to express them in the form of the Zakharov-Shabat (ZS) system of quantum mechanics, we obtain:

$$j \cdot \begin{pmatrix} \frac{d}{dz} & -K \\ K^{*} & \frac{-d}{dz} \end{pmatrix} \cdot \begin{pmatrix} a^{+} \\ a^{-} \end{pmatrix} = \beta \cdot \begin{pmatrix} a^{+} \\ a^{-} \end{pmatrix} \tag{3.233}$$

To do this we have taken advantage of the fact that *K(z)* is a real function in our system (and hence *K(z)* = $K^{*}(z)$). Additionally, we are going to approximate β as a constant function with z (it will only be a function of the frequency, *f*).

We are going to introduce four vectorial functions, which are known as the Jost functions, $\phi, \bar{\phi}, \psi, \bar{\psi}$, that are solution of the ZS system. Their asymptotic behavior is described by:

$$z \rightarrow \infty \qquad \begin{cases} \psi \rightarrow \begin{pmatrix} 0 \\ 1 \end{pmatrix} \cdot e^{j \cdot \beta \cdot z} \\ \bar{\psi} \rightarrow \begin{pmatrix} 1 \\ 0 \end{pmatrix} \cdot e^{-j \cdot \beta \cdot z} \end{cases}$$

$$z \rightarrow -\infty \qquad \begin{cases} \bar{\phi} \rightarrow \begin{pmatrix} 0 \\ 1 \end{pmatrix} \cdot e^{j \cdot \beta \cdot z} \\ \phi \rightarrow \begin{pmatrix} 1 \\ 0 \end{pmatrix} \cdot e^{-j \cdot \beta \cdot z} \end{cases}$$

In the following lines a couple of properties of the Jost functions that are derived directly of the particular form of the ZS system, will be shown:

- If the Jost function $\phi = \begin{bmatrix} \phi_1(z,\beta) \\ \phi_2(z,\beta) \end{bmatrix}$ is a solution of the ZS system, then it is possible to obtain another solution that is linearly independent of this one by simply applying the complex conjugate operator to the ZS system. The resulting function will be the Jost function $\bar{\phi}$, and it will be related to the previous one in the following manner:

$$\bar{\phi} = \begin{bmatrix} \bar{\phi}_1(z,\beta) \\ \bar{\phi}_2(z,\beta) \end{bmatrix} = \begin{bmatrix} \phi_2^*(z,\beta^*) \\ \phi_1^*(z,\beta^*) \end{bmatrix} \tag{3.234}$$

- Each Jost function can be represented as a linear combination of two linearly independent functions which are solution of the ZS system. As an example, for the case of ψ it can be written as:

$$\psi(z,\beta) = a(\beta)\cdot\phi(z,\beta) + b(\beta)\cdot\bar{\phi}(z,\beta) \tag{3.235}$$

If we divide this last solution (both components of the equation) by $a(\beta)$, we continue having a solution of the ZS system that will have the form:

$$\frac{1}{a(\beta)}\cdot\psi(z,\beta) = \phi(z,\beta) + \frac{b(\beta)}{a(\beta)}\cdot\bar{\phi}(z,\beta) \tag{3.236}$$

Let's assume now that the solution $\phi(z,\beta)$ can be expressed as:

$$\phi(z,\beta) = \begin{pmatrix} 1 \\ 0 \end{pmatrix}\cdot e^{-j\cdot\beta\cdot z} + \int_{-\infty}^{\infty} A(z,\tau)\cdot e^{-j\cdot\beta\cdot z}\cdot d\tau \tag{3.237}$$

where

$$A(z,\tau) = \begin{bmatrix} A_1(z,\tau) \\ A_2(z,\tau) \end{bmatrix}$$

To solve the problem we are going to assume that the coupling region begins at z = 0 and therefore:

$$K(z) = 0 \quad , \quad z < 0 \tag{3.238}$$

From this condition, causality restrictions that will be applied later to solve the problem, are derived.

We are going to reformulate the problem in the time domain, using the following inverse Fourier transform:

$$\begin{aligned} V^{+}(z,\tau) &= \frac{1}{2\pi}\int_{-\infty}^{\infty} a^{+}(z,\beta)\cdot e^{j\cdot\beta\cdot\tau}\cdot d\beta \\ V^{-}(z,\tau) &= \frac{1}{2\pi}\int_{-\infty}^{\infty} a^{-}(z,\beta)\cdot e^{j\cdot\beta\cdot\tau}\cdot d\beta \end{aligned} \tag{3.239}$$

The reformulation in the time domain is made since the solution is going to be obtained by deduction applying causality requirements, so the study will be simpler in the time domain.
The variable τ is related to the real time by means of the phase velocity v_p. In fact, if v_p is constant with frequency in the full bandwidth of the signal, it follows that $\tau = v_p \cdot t$, where t is the real time.

(This is so since $v(\alpha\cdot t) \xleftrightarrow{FT} \frac{1}{|\alpha|}\cdot V\left(\frac{\omega}{\alpha}\right)$, and therefore in our case:

$$v(v_p\cdot t) \xleftrightarrow{FT} \frac{1}{v_p}\cdot V\left(\frac{\omega}{v_p}\right)).$$

Now we perform the inverse Fourier transform of the coupled mode equations. We are going to approximate the coupling coefficient *K(z)* by allowing it not to be a function of frequency and only of *z*. Taking this into account, the inverse Fourier transform of the coupled mode equations become:

$$\begin{aligned} \frac{\partial V^{+}(z,\tau)}{\partial z} + \frac{\partial V^{+}(z,\tau)}{\partial \tau} &= K(z)\cdot V^{-}(z,\tau) \\ \frac{\partial V^{-}(z,\tau)}{\partial z} - \frac{\partial V^{-}(z,\tau)}{\partial \tau} &= K(z)\cdot V^{+}(z,\tau) \end{aligned} \tag{3.240}$$

Let's consider now two solutions of the ZS system (and therefore of the coupled mode equations) in the time domain, $\Phi(z,\tau)$ and $U(z,\tau)$, that are respectively the inverse Fourier transform of $\phi(z,\beta)$ and $\frac{\psi(z,\beta)}{a(\beta)}$.

Applying the inverse Fourier transformation to eqns. (3.237) and (3.236), and using eqn. (3.234), a new expression will be obtained. Let's see:

$$\Phi(z,\tau)=\begin{pmatrix}\delta(\tau-z)\\0\end{pmatrix}+A(z,\tau)$$, applying the inverse transform to eqn. (3.237).

and

$$U(z,\tau)=\begin{pmatrix}\delta(\tau-z)\\0\end{pmatrix}+\begin{pmatrix}A_1(z,\tau)\\A_2(z,\tau)\end{pmatrix}+\begin{pmatrix}0\\1\end{pmatrix}\cdot F(z+\tau)+\int_{-\infty}^{+\infty}\begin{pmatrix}A_2^*(z,y)\\A_1^*(z,y)\end{pmatrix}\cdot F(y+\tau)\cdot dy \tag{3.241}$$

applying the inverse Fourier transform to eqn. (3.236), and using the relation of eqn. (3.234), knowing that β is real (let's recall that lossless waveguides are considered). The first and second terms to the right of the equality sign corresponds to $\Phi(z,\tau)$, and the third and fourth terms to the right of the equality sign are obtained by taking advantage of the generic relation:

$$\int_{-\infty}^{+\infty} v^*(\lambda)\cdot b(t+\lambda)\cdot d\lambda \xleftrightarrow{FT} V^*(\omega)\cdot B(\omega)$$

with the new function $F(\tau)$ defined as:

$$F(\tau)=\frac{1}{2\pi}\int_{-\infty}^{+\infty}\frac{b(\beta)}{a(\beta)}\cdot e^{j\cdot\beta\cdot\tau}\cdot d\beta$$

that is, as the inverse Fourier transform of $\dfrac{b(\beta)}{a(\beta)}$.

Let's see now the meaning of the quotient $\dfrac{b(\beta)}{a(\beta)}$.

For this purpose we part from eqn. (3.235), that was:

$$\psi(z,\beta)=a(\beta)\cdot\phi(z,\beta)+b(\beta)\cdot\bar{\phi}(z,\beta)$$

with $\psi(z,\beta)=\begin{bmatrix}a^+(z,\beta)\\a^-(z,\beta)\end{bmatrix}$, solution of the ZB system (and of the coupled mode equations).

As already indicated in eqn. (3.238), we assume that the coupling coefficient satisfies *K(z)*=0, $z<0$, so that coupling between modes will only occur for $z>0$ and therefore for $z \leq 0$ the modes will travel independently, satisfying:

$$\begin{array}{l} a^{+}(z,\beta) = a_{a}^{+}(\beta)\cdot e^{-j\cdot\beta\cdot z} \\ a^{-}(z,\beta) = a_{a}^{-}(\beta)\cdot e^{j\cdot\beta\cdot z} \end{array} \quad , \qquad z \leq 0$$

and the origin of the device is at $z = 0$.

We also know, from the definitions at the beginning of this section, that the solution $\psi(z,\beta)$ tends to $\begin{pmatrix}1\\0\end{pmatrix}\cdot e^{-j\cdot\beta\cdot z}$ when $z \to \infty$, i.e. that corresponds to $a^{+} = 1\cdot e^{-j\cdot\beta\cdot z}$, $a^{-} = 0$, which corresponds to only one forward propagating mode, with the backward propagating mode equal to zero. Therefore this solution corresponds to having the output of the device matched (without reflections).

The solution in $z \to -\infty$ will be (taking into account to what will tend ϕ and $\bar{\phi}$ when $z \to -\infty$):

$$a^{+} = a(\beta)\cdot 1\cdot e^{-j\cdot\beta\cdot z} + b(\beta).0 \Rightarrow a^{+} = a(\beta)\cdot e^{-j\cdot\beta\cdot z}$$

$$a^{-} = a(\beta)\cdot 0 + b(\beta)\cdot 1\cdot e^{j\cdot\beta\cdot z} \Rightarrow a^{-} = b(\beta)\cdot e^{j\cdot\beta\cdot z}$$

Since *K(z)*=0 , $z < 0$, and following the considerations made earlier, a^{+} and a^{-} will maintain this form $\forall\, z \leq 0$, and therefore at $z = 0$ their value will be:

$$\begin{array}{l} a^{+}(z=0,\beta) = a(\beta) \\ a^{-}(z=0,\beta) = b(\beta) \end{array}$$

and consequently:

$$\rho(z=0,\beta) = \frac{-a^{-}(z=0,\beta)}{a^{+}(z=0,\beta)} = -\frac{b(\beta)}{a(\beta)}$$

and hence

$$\frac{b(\beta)}{a(\beta)} = -\rho(z=0,\beta)$$

with this value of ρ calculated at the origin (z=0), and with the device output port matched. Therefore it will follow:

$$\frac{b(\beta)}{a(\beta)} = -\rho(z=0,\beta)\Big|_{\substack{output\\matched}} = -S_{11}(\beta) \quad \Rightarrow \quad \frac{b(\beta)}{a(\beta)} = -S_{11}(\beta)$$

taking into account the expression for the S_{11} parameter as a function of the complex amplitudes of the mode, a^+, a^- (eqn. (3.29), section (3.2.3)).
Therefore, the function $F(\tau)$ that appears in eqn. (3.241) will finally become:

$$F(\tau) = \frac{1}{2\pi}\int_{-\infty}^{\infty} -S_{11}(\beta)\cdot e^{j\cdot\beta\cdot\tau}\cdot d\beta \tag{3.242}$$

and will be the inverse Fourier transform of the $S_{11}(\beta)$ parameter (with the sign inverted), i.e. of the reflection coefficient calculated at $z = 0$ (origin of the device) when the output port is matched.
Due to causality considerations, the function $F(\tau)$ must satisfy the following relation:

$$F(\tau) = 0 \quad , \quad \tau < 0 \tag{3.243}$$

On the other hand, if we define the function:

$$Y(z,\tau) = U(z,\tau) - \begin{pmatrix} \delta(\tau - z) \\ 0 \end{pmatrix}$$

it will follow, applying again causality considerations that:

$$Y(z,\tau) = U(z,\tau) - \begin{pmatrix} \delta(\tau - z) \\ 0 \end{pmatrix} = 0 \quad , \quad |z| > \tau \tag{3.244}$$

Also, due once more to causality considerations, it will follow that:

$$A(z,\tau) = 0 \quad , \quad z < |\tau| \tag{3.245}$$

Applying eqns. (3.243) and (3.245), the integration range of equation (3.241) can be limited from $-\tau$ to z.

Also, by using eqn. (3.244), and introducing in it the value of $U(z,\tau)$ given in eqn. (3.241), we will obtain:

$$Y(z,\tau)=A(z,\tau)+\begin{pmatrix}0\\1\end{pmatrix}\cdot F(z+\tau)+\int_{-\tau}^{z}\begin{pmatrix}A_2^*(z,y)\\A_1^*(z,y)\end{pmatrix}\cdot F(y+\tau)\cdot dy=0 \tag{3.246}$$

$$\text{for}\quad \left.\begin{matrix}\tau<z\ ,\ z>0\\ \tau>z\ ,\ z<0\end{matrix}\right\}\Rightarrow\ |z|>\tau$$

which are the Gel'Fand-Levitan-Marchenko (GLM) coupled integral equations for the inverse scattering problem (also known as coupled GLM integral equations).
Let's recall that as it can be seen from eqn. (3.242), $F(\tau)$ will have the value:

$$F(\tau)=-\frac{1}{2\pi}\int_{-\infty}^{\infty}S_{11}(\beta)\cdot e^{j\cdot\beta\cdot\tau}\cdot d\beta$$

A rigorous demonstration for the equations obtained by using causality considerations (eqns. (3.243), (3.244) and (3.245)) can be found in [PER 96], [SON 85] and in the Doctoral Thesis of Eva Peral, presented at the Universidad Politécnica de Valencia, Spain.

We must continue by deducing the relation between the function $A(z,\tau)$ that appears in the coupled GLM integral equations, and the coupling coefficient *K(z)*. In order to do so, we part from the term of eqn. (3.244):

$$Y(z,\tau)=U(z,\tau)-\begin{pmatrix}\delta(\tau-z)\\0\end{pmatrix}$$

and we obtain $U(z,\tau)$, that is solution of the coupled mode equations in the time domain:

$$U(z,\tau)=Y(z,\tau)+\begin{pmatrix}\delta(\tau-z)\\0\end{pmatrix}=\begin{pmatrix}Y_1(z,\tau)+\delta(\tau-z)\\Y_2(z,\tau)\end{pmatrix}$$

$U(z,\tau)$ will verify the coupled mode equations in the time domain (eqns. (3.240)), and therefore it will follow that:

$$\frac{\partial Y_2(z,\tau)}{\partial z}-\frac{\partial Y_2(z,\tau)}{\partial\tau}=K(z)\cdot(Y_1(z,\tau)+\delta(\tau-z)) \tag{3.247}$$

By realizing the following coordinate change:

$$\mu = \frac{z+\tau}{2} \quad ; \quad \upsilon = \frac{\tau - z}{2} \qquad \text{(that leads to } \mu + \upsilon = \tau \quad ; \quad \mu - \upsilon = z \text{)}$$

it will be satisfied that:

$$\frac{\partial Y_2}{\partial z} - \frac{\partial Y_2}{\partial \tau} = \frac{\partial Y_2}{\partial \upsilon} \cdot \frac{\partial \upsilon}{\partial z} - \frac{\partial Y_2}{\partial \upsilon} \cdot \frac{\partial \upsilon}{\partial \tau} = \frac{\partial Y_2}{\partial \upsilon} \cdot \left(\frac{\partial \upsilon}{\partial z} - \frac{\partial \upsilon}{\partial \tau} \right) = \frac{\partial Y_2}{\partial \upsilon} \cdot \left(-\frac{1}{2} - \left(\frac{1}{2} \right) \right) = -\frac{\partial Y_2}{\partial \upsilon}$$

So that eqn. (3.247) can be rewritten as:

$$-\frac{\partial Y_2(\mu,\upsilon)}{\partial \upsilon} = K(\mu - \upsilon) \cdot (Y_1(\mu,\upsilon) + \delta(2\upsilon))$$

Applying integral: $\lim_{\varepsilon \to 0} \int_{-\varepsilon}^{+\varepsilon} d\upsilon$ at both sides of the previous equation, for $z > 0$, we will obtain:

$$\lim_{\varepsilon \to 0} \int_{-\varepsilon}^{+\varepsilon} -\frac{\partial Y_2(\mu,\upsilon)}{\partial \upsilon} \cdot d\upsilon = \lim_{\varepsilon \to 0} \int_{-\varepsilon}^{+\varepsilon} K(\mu - \upsilon) \cdot Y_1(\mu,\upsilon) \cdot d\upsilon + \lim_{\varepsilon \to 0} \int_{-\varepsilon}^{+\varepsilon} K(\mu - \upsilon) \cdot \delta(2\upsilon) \cdot d\upsilon \tag{3.248}$$

Let’s calculate first the term to the left of the equality sign. As we know from eqn. (3.244):

$$Y(z,\tau) = 0 \quad , \quad |z| > \tau$$

In our case $z > 0 \Rightarrow Y(z,\tau) = 0 \;\; , \;\; z > \tau$

Since:

$$\left. \begin{array}{l} \mu + \upsilon = \tau \\ \mu - \upsilon = z \end{array} \right\} \Rightarrow \upsilon < 0 \Rightarrow z > \tau \Rightarrow \upsilon = 0^- \Rightarrow Y(z,\tau) = 0 \Rightarrow Y_2(\mu,0^-) = 0$$

and therefore the term to the left of the equality sign of eqn. (3.248) can be rewritten as:

$$\lim_{\varepsilon \to 0} \left(-(Y_2(\mu,+\varepsilon) - Y_2(\mu,-\varepsilon)) \right) = -(Y_2(\mu,0^+) - Y_2(\mu,0^-)) = -Y_2(\mu,0^+)$$

On the other hand, the first term to the right of the equality sign of eqn. (3.248) will be null, since the value of the integrand is finite when $\upsilon = 0$.

Finally, we are going to calculate the value of the second term to the right of the equality sign of eqn. (3.248).

As it is well known:

$$\lim_{\Delta z \to 0} \int_{z_o - \Delta z}^{z_o + \Delta z} f(z) \cdot \delta(z - z_o) \cdot dz = f(z_o)$$

In the same way it will be satisfied that:

$$\lim_{\Delta z \to 0} \int_{-\Delta z}^{+\Delta z} f(z) \cdot \delta(2z) \cdot dz = \frac{1}{2} \cdot f(z = 0)$$

Therefore, the second term to the right of the equality sign of eqn. (3.248) will have the value:

$$\lim_{\varepsilon \to 0} \int_{-\varepsilon}^{+\varepsilon} K(\mu - \upsilon) \cdot \delta(2\upsilon) \cdot d\upsilon = \frac{1}{2} \cdot K(\mu)$$

So in the end, eqn. (3.248) can be rewritten as:

$$-Y_2(\mu, 0^+) = \frac{1}{2} \cdot K(\mu)$$

For a given $z > 0$, and going back to (z, τ) coordinates, we will have:

$$z = \mu - \upsilon \Rightarrow \mu = z + \upsilon \quad ; \quad \tau = \mu + \upsilon = (z + \upsilon) + \upsilon = z + 2\upsilon$$

Since $\upsilon = 0^+ \Rightarrow \tau = z^+$, and therefore:

$$-Y_2(z, z^+) = \frac{1}{2} \cdot K(z)$$

Substituting this last equation in eqn. (3.246) (taken as the definition of $Y(z, \tau)$), and applying eqn. (3.245), we will obtain:

$$-\frac{1}{2} \cdot K(z) = F(2z) + \int_{-z}^{z} A_1^*(z, y) \cdot F(y + z) \cdot dy \tag{3.249}$$

As it can be seen, this last equation gives the coupling coefficient *K(z)* from the solution of the GLM equations (that will be $A(z, \tau)$). If the second term to the right of the equality sign (the integral term) is neglected, the order zero approximation is obtained, which is also known as the first order Born approximation, and is valid for very weak coupling. The physical meaning of this approximation is that coupling is so weak that the amplitude of the incident mode is not affected by the perturbation. The neglected integral term corresponds to the cases when there are multiple reflections in intermediate points of the structure.

Therefore, the order zero approximation or the first order Born approximation will be:

$$K(z) \approx -2 \cdot F(2z)$$

and introducing the value of $F(\tau)$ (eqn. (3.242)), it becomes:

$$K(z) \approx \frac{1}{2\pi} \int_{-\infty}^{\infty} S_{11}(\beta) \cdot e^{j \cdot 2 \cdot \beta \cdot z} \cdot d(2\beta) \tag{3.250}$$

where eqn. (3.250) will be valid for weak coupling, with the amplitude of the incident mode not affected by the perturbation (i.e., it will be valid for low reflectivity along all the device). Actually, it is identical to the one that was obtained in section (3.5.1) assuming that $\rho(z) << 1$.

In order to solve eqn. (3.249), we need to know $A_1(z,\tau)$ in the region $|\tau| < z$ (since $z > 0$). In order to do so, we will solve the GLM coupling equations (eqn. (3.246)) using an iterative method. (GLM equations are valid particularly for $\tau < z,\ z > 0$, and this case includes the region of interest $|\tau| < z$, in which we need to know $A_1(z,\tau)$, since z will verify that $z > 0$). Let's see.

The zero order approximation (neglecting the integral) of the lower member of the GLM equations (eqns. (3.246)) is:

$$A_2(z,\tau) \cong -F(z+\tau)$$

Substituting this expression in the upper member of the GLM equations (eqns. (3.246)) we will be able to obtain an approximation for $A_1(z,\tau)$ that can be used to write the first order approximation to the coupling coefficient *K(z)* equation (obtained from eqn. (3.249)):

$$A_1(z,\tau) \cong \int_{-\tau}^{z} F^*(z+x_1) \cdot F(x_1+\tau) \cdot dx_1$$

$$-\frac{1}{2} \cdot K(z) = F(2z) + \int_{-z}^{z} dx_1 \cdot F(x_1+z) \cdot \int_{-x_1}^{z} dx_2 \cdot F(z+x_2) \cdot F^*(x_1+x_2)$$

If we continue with the iterative solution of the GLM equation (eqn. (3.246)), we introduce the expression obtained for $A_1(z,\tau)$ in the equation of *K(z)* (eqn. (3.249)), and by applying several variable changes, we will obtain the following expression in the form of chained convolutions for the order *N* approximation to the coupling coefficient, *K(z)*, equation:

$$\begin{aligned}
-\frac{1}{2}\cdot K(z) &= F(2z)+\int_0^{2z} dx_1\cdot F(x_1)\cdot\int_0^{x_1} dx_2'\cdot F^*(x_2')\cdot F(x_2'-x_1+2z)+\\
&+\int_0^{2z} dx_1\cdot F(x_1)\cdot\int_0^{x_1} dx_2'\cdot F^*(x_2')\cdot\int_0^{x_2} dx_3'\cdot F(x_3')\cdot\int_0^{x_3} dx_4'\cdot F^*(x_4')\cdot F(x_4'-x_3+2z)+\\
&+\cdots\cdots+\\
&+\int_0^{2z} dx_1\cdot F(x_1)\cdot\int_0^{x_1} dx_2'\cdot F^*(x_2')\cdot\int_0^{x_2}\cdots\cdots\int_0^{x_{2N-1}} dx_{2N}'\cdot F^*(x_{2N}')\cdot F(x_{2N}'-x_{2N-1}+2z)
\end{aligned}$$

where $x_i' = x_i + x_{i-1} - 2z$, for $i > 1$. The variables x_i are in the interval [0, 2*L*], where *L* is the length of the coupling region (length of the device).

Redefining $F(\tau)$ as the inverse Fourier transform of the reflection coefficient at z=0 (origin of the device) when the output port is matched (i.e., as the inverse Fourier transform of the S_{11} parameter), we will have:

$$F_{new}(\tau)=\frac{1}{2\pi}\int_{-\infty}^{\infty} S_{11}(\beta)\cdot e^{j\cdot\beta\cdot\tau}\cdot d\beta = -F_{old}(\tau)$$

and therefore, the expression for the coupling coefficient can be finally rewritten as:

$$\begin{aligned}
\frac{1}{2}\cdot K(z) &= F(2z)+\int_0^{2z} dx_1\cdot F(x_1)\cdot\int_0^{x_1} dx_2'\cdot F^*(x_2')\cdot F(x_2'-x_1+2z)+\\
&+\int_0^{2z} dx_1\cdot F(x_1)\cdot\int_0^{x_1} dx_2'\cdot F^*(x_2')\cdot\int_0^{x_2} dx_3'\cdot F(x_3')\cdot\int_0^{x_3} dx_4'\cdot F^*(x_4')\cdot F(x_4'-x_3+2z)+\\
&+\cdots\cdots+\\
&+\int_0^{2z} dx_1\cdot F(x_1)\cdot\int_0^{x_1} dx_2'\cdot F^*(x_2')\cdot\int_0^{x_2}\cdots\cdots\int_0^{x_{2N-1}} dx_{2N}'\cdot F^*(x_{2N}')\cdot F(x_{2N}'-x_{2N-1}+2z)
\end{aligned} \tag{3.251}$$

where $x_i' = x_i + x_{i-1} - 2z$, for $i > 1$. The variables x_i are in the interval [0, 2*L*], where *L* is the length of the coupling region (length of the device).

And the function $F(\tau)$ is defined as:

$$F(\tau) = \frac{1}{2\pi} \int_{-\infty}^{\infty} S_{11}(\beta) \cdot e^{j \cdot \beta \cdot \tau} \cdot d\beta \tag{3.252}$$

The expression obtained (eqn. (3.251)) corresponds to the order *N* approximation to the coupling coefficient, *K(z)*, equation.

It is important to note that the only approximations introduced to obtain this expression (besides single mode operation) are to assume that β is constant with z, and to assume also that *K(z)* is not a function of the frequency, *f*, (or equivalently of *β*).

The value of $F(\tau)$ can be efficiently calculated with the aid of an inverse Fast Fourier Transform (iFFT). In the same way, the integrals present in eqn. (3.251) can be solved efficiently in a recursive manner, since they are related in the following way:

$$I_i(x_i) = \int_0^{x_i} dx_{i+1} \cdot F(x_{i+1}) \cdot I_{i+1}(x_{i+1} - x_i + 2z)$$

Moreover, since the devices we are going to work with will be real, the inverse Fourier Transform of their reflection coefficient (i.e., the impulsional response in reflection of the device) is going to be real, and therefore $F(\tau) \in \Re$, satisfying:

$$F(\tau) = F^*(\tau)$$

allowing the algorithm for the calculation of *K(z)* from the desired value of $S_{11}(\beta)$ to be very compact (see the algorithm proposed in the next page).

By means of the proposed algorithm, it is assured that the same factor is not calculated repeatedly, therefore minimizing calculation time. The expression obtained relates the necessary coupling coefficient, *K(z)*, with the desired reflection coefficient, $S_{11}(\beta)$.

The determination of the coupling coefficient can be done with further degrees of accuracy, increasing the order of the approximation and therefore the number of necessary iterations.

An expression similar to eqn. (3.251) was obtained in [PER 96] for Fiber Bragg Gratings in the optical regime.

- Algorithm for the efficient calculation of the coupling coefficient *K(z)* from the desired $S_{11}(\beta)$ ($\Rightarrow F(\tau)$)

```
Input: $F(\tau)$ , $\forall\tau \in [0, 2L]$
       $NGLM \equiv$ Order of the approximation

Output: $KGLM \equiv K(z)$

For $z_n \in [0, L]$
    $V = F$
    $KGLM_n = F(2z_n)$
    For $i = 0$ to $2 \cdot (NGLM - 1)$
        Calculate $U(u) = \int_0^u dt \cdot F(t) \cdot V(t - u + 2z_n)$ , $\forall u \in [0, 2L]$
        $V = U$
        If $i$ is even $\Rightarrow$ $KGLM_n = KGLM_n + \int_0^{2z_n} dt \cdot F(t) \cdot U(t)$
    $KGLM_n = 2 \cdot KGLM_n$
```

3.6. Application to several PBG microstrip devices: Examples

Throughout this chapter several expressions and numerical techniques developed for PBG structures in microstrip technology have been presented. Their aim is to provide a simple and effective way to analyze and design these novel PBG devices, and to give a better insight into their operation. However all the work presented until now has been theoretical. In this section the expressions and numerical techniques are applied to real PBG devices and the results are compared between them and checked against measurements showing their high accuracy.

3.6.1. PBG featuring a discrete pattern of circles

The first PBG device in microstrip technology that we are going to analyze is the structure proposed by Professor T. Itoh’s group at UCLA in 1998 [RAD 98]. It is obtained by etching a periodic pattern of circles, following a square lattice, in the ground plane of a microstrip line. In the upper plane, the strip conductor width is kept constant to have an also constant nominal characteristic impedance equal to 50 Ω. The prototype that we are going to analyze is a scaled version of the one presented in [RAD 98] in order to be measured with our *HP* 8753D vector network analyzer (up to 6 GHz). The substrate employed is a Rogers RT/Duroid 6010, with dielectric constant ε_r=10.2 and substrate thickness h=1.27 mm. The period of the PBG structure will have a value Λ=14.1 mm, and the radius of the circle to period ratio will be r/Λ=0.25. The strip conductor width will be constant, w=1.2 mm. A photograph of the upper plane and of the ground plane of the PBG microstrip prototype is given in Fig. 3.1.

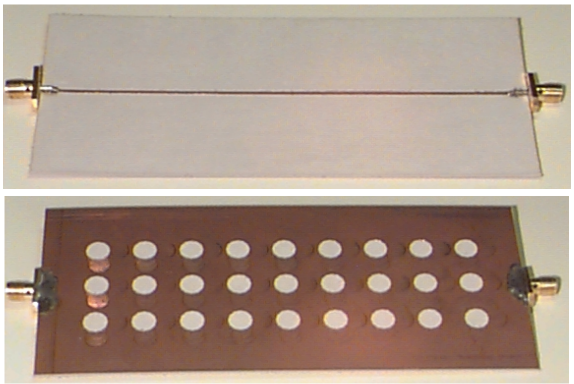

***Figure 3.1**: Photograph of the upper plane and of the ground plane of the PBG microstrip prototype featuring a discrete pattern of circles.*

3.6.1.1. Perturbation profile and coupling coefficient

To begin the analysis of the proposed PBG prototype we are going to calculate its coupling coefficient, and we are going to depict it together with the profile of the perturbation (width of the slot in the ground plane) and with the characteristic impedance variation produced by the perturbation. They can be seen for one period of the PBG structure in Fig. 3.2. The characteristic impedance variation is calculated from the perturbation profile by interpolating the characteristic impedance values previously calculated (by using *Agilent HFSS* in our case) for a set of uniform auxiliary waveguides (microstrip lines with slots of different widths in the ground plane), as explained in section 3.2.2. The coupling coefficient is immediately obtained from the characteristic impedance by using eqn. (3.20).

It is important to notice that although the PBG pattern employed is two dimensional, due to the high confinement of the fields around the conductor strip only the central row of circles (placed behind the conductor strip) is relevant, and consequently the behavior and modeling of the device is 1-D effective [FAL 99].

In Fig. 3.3 the conventional coupling coefficient (calculated using the physical position variable) and the coupling coefficient calculated using the electrical position variable (as explained in section 3.3.4) are compared showing the deformation introduced in it by the variation of phase constant, β, present along the PBG device.

Finally, the values for the coupling coefficient parameters calculated using the physical position variable (eqns. (3.38), (3.52)) and the electrical position variable are given in Table 3.1, for the first (n=1) and second (n=2) rejected bands. The results obtained using the electrical position variable are more accurate because they take into account the deformation introduced in the coupling coefficient by the variation of β along the PBG device. The value of the "averaged" $\varepsilon_{\mathrm{eff}}$ for the PBG device (calculated through eqn. 3.117) is also included.

Band index, *n*	$k_{(z)}$	$k_{(\chi)}$	$k_{(\chi)} \cdot \sqrt{\varepsilon_{eff}}$	ε_{eff}
1	42.89	17.20	40.56	5.563
2	-20.62	-13.24	-31.23	

Table 3.1: *Values for the coupling coefficient parameters calculated using the physical position variable ($k_{(z)}$) and the electrical position variable ($k_{(\chi)}$), for the first (n=1) and second (n=2) forbidden bands. $k_{(\chi)} \cdot \sqrt{\varepsilon_{eff}}$ is also included for comparison purposes, as well as the "averaged" ε_{eff} for the PBG device.*

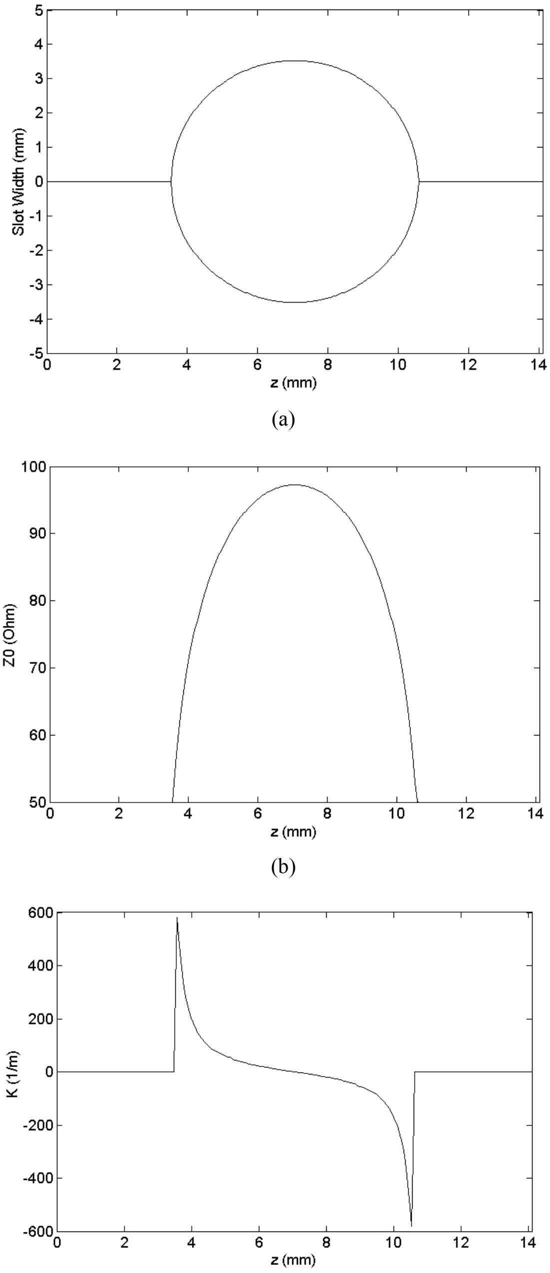

(a)

(b)

(c)

Figure 3.2: *(a) Profile of the PBG perturbation (width of the slot in the ground plane), (b) variation of characteristic impedance produced by the perturbation,* $Z_0(z)$ *and (c) resulting coupling coefficient,* $K(z)$.

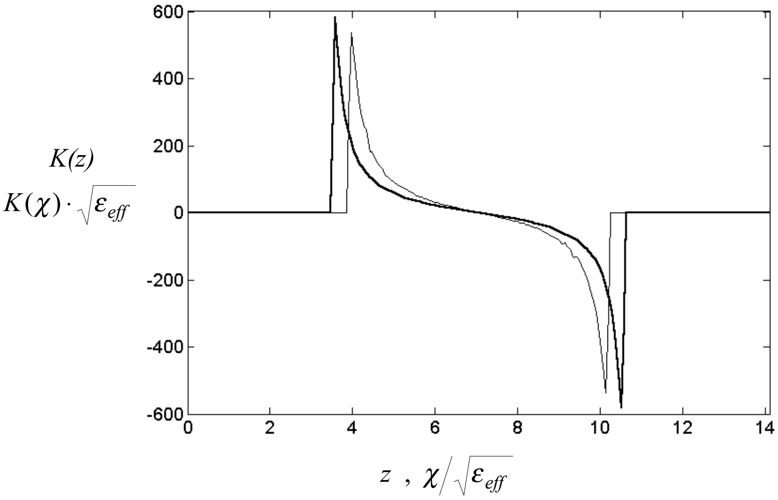

Figure 3.3: *Coupling coefficient produced by the PBG perturbation calculated using the physical position variable, K(z) (thick line), and using the electrical position variable, K(χ) (thin line). The later is represented with χ divided by $\sqrt{\varepsilon_{eff}}$ in the horizontal axis, and with K multiplied by $\sqrt{\varepsilon_{eff}}$ in the vertical axis for comparison purposes. ε_{eff} is the "averaged" value for the PBG device calculated using eqn. (3.117) and given in Table 3.1.*

3.6.1.2. S_{11} and S_{21} parameters

To continue, we are going to focus our study on a PBG microstrip prototype of finite length, designed as stated in section (3.6.1) and with 9 periods. Firstly, its S_{11} (reflection) and S_{21} (transmission) parameters will be calculated through numerical solution of the coupled mode equations (section (3.2.2)), using the approximate analytical solutions obtained in section (3.3.3.1) (eqns. (3.68), (3.69)), and using the analytical solutions with the electrical position variable (section (3.3.4)). The prototype will be also fabricated employing a *LPKF* numerical milling machine, and its S parameters measured with our *HP* 8753D vector network analyzer. The S_{11} and S_{21} parameters obtained are depicted in Fig. 3.4 for the first rejected band (n=1), and in Fig. 3.5 for the second rejected band (n=2).

Secondly, the value for the frequency of maximum attenuation (or reflectivity), the value of this maximum attenuation, and the bandwidth (between zeroes) of the rejected band are obtained from the measurements, from the numerical solution for the coupled mode equations, using the approximate analytical expressions given for them in sections (3.3.3.2) and (3.3.3.3) (eqns. (3.70), (3.73), (3.79)), and using the analytical

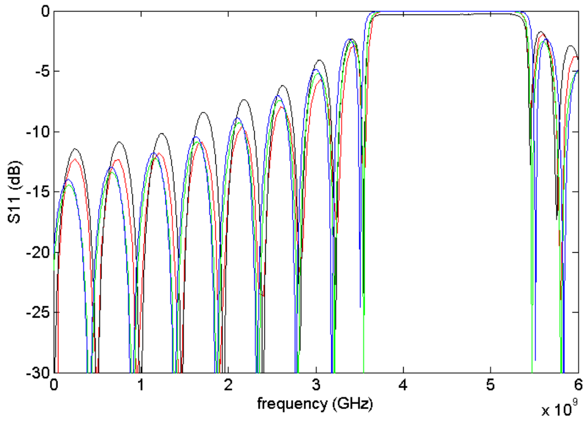

(a)

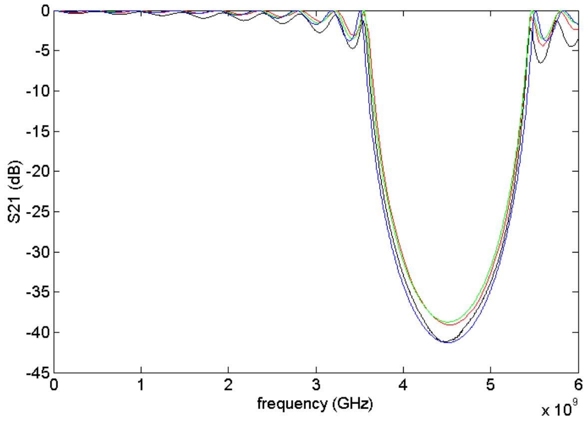

(b)

Figure 3.4: *(a) S_{11} and (b) S_{21} parameters for the PBG microstrip prototype of 9 periods designed as stated in section (3.6.1). They have been calculated through numerical solution of the coupled mode equations (red line), using the approximate analytical solutions (blue line), and using the analytical solutions with the electrical position variable (green line). The measurement results are also included for comparison (black line).*

	Numerical solution of coupled mode eqns.	Analytical solutions (z)	Analytical solutions (χ)	Measurements
f_{max} (GHz)	4.54	4.51	4.51	4.45
$\lvert S_{21}\rvert_{min}$ (dB)	-39.06	-41.28	-38.72	-41.20
BW_∞ (GHz)	1.90	2.00	1.92	1.91

Table 3.2: *Values for the frequency of maximum attenuation, f_{max} , the value of this maximum attenuation, $\lvert S_{21}\rvert_{min}$, and the bandwidth (between zeroes), BW_∞ , for the first (n=1) forbidden band, calculated through the same methods as Fig. 3.4.*

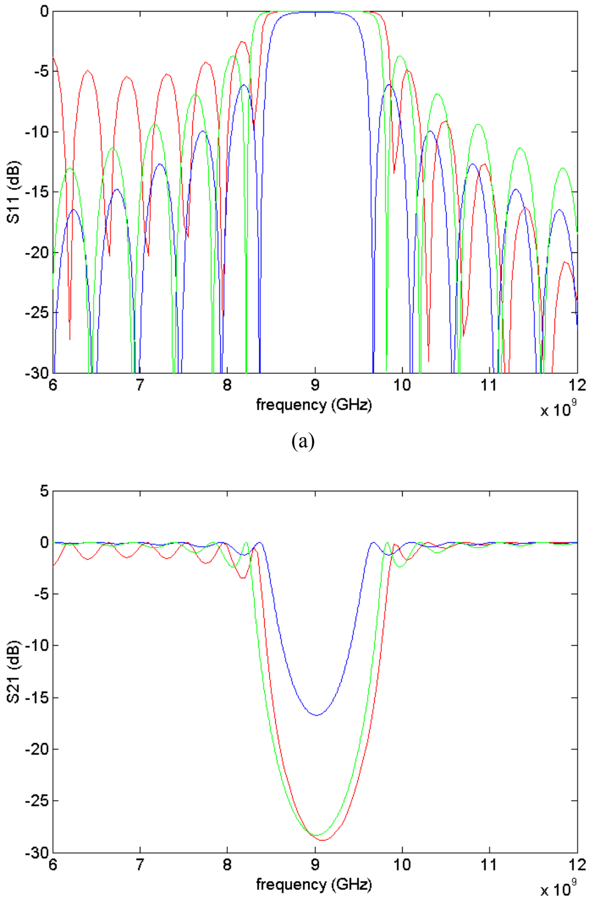

(a)

(b)

Figure 3.5: *(a) S_{11} and (b) S_{21} parameters for the PBG microstrip prototype of 9 periods designed as stated in section (3.6.1). They have been calculated through numerical solution of the coupled mode equations (red line), using the approximate analytical solutions (blue line), and using the analytical solutions with the electrical position variable (green line). This time they are depicted for the second (n=2) forbidden band.*

	Numerical solution of coupled mode eqns.	Analytical solutions (z)	Analytical solutions (χ)
f_{max} (GHz)	9.10	9.02	9.02
$\lvert S_{21}\rvert_{min}$ (dB)	-28.83	-16.72	-28.32
BW_∞ (GHz)	1.60	1.30	1.61

Table 3.3: *Values for the frequency of maximum attenuation, f_{max} , the value of this maximum attenuation, $\lvert S_{21}\rvert_{min}$, and the bandwidth (between zeroes), BW_∞ , for the second (n=2) forbidden band, calculated through the same methods as Fig. 3.5.*

expressions with the electrical position variable. All of them are given in Table 3.2 for the first rejected band (n=1), and in Table 3.3 for the second rejected band (n=2).

As it can be seen in Fig. 3.4 and in Table 3.2, the agreement between the numerical solution of the coupled mode equations and the approximate analytical solutions is very good in the first rejected band. The agreement with the measurements is very good also. The small discrepancies found (mainly in the matching of the passband) are due to the discontinuities introduced by the connectors unions in the constructed prototype. Regarding the second rejected band (n=2), Fig. 3.5 and Table 3.3 show that to have an accurate prediction using the approximate analytical solutions it is necessary to employ the electrical position variable. However, using it, a very good agreement is again obtained between the numerical solution of the coupled mode equations and the approximate analytical solutions. In general, the discrepancies found between the numerical and the approximate analytical solutions are more important as we go away from the central frequency of the rejected band due to the approximation involved to obtain the analytical solutions. However the predictions for the fundamental parameters of the PBG device given in Tables 3.2 and 3.3 are very good, and they confirm that the approximate analytical solutions can be successfully used for analysis and synthesis of PBG microstrip circuits. The presence of an important second rejected band for this PBG microstrip structure is confirmed in measurement by the downscaled prototype designed and presented in chapter 4, section (4.6) in order to measure its first and second rejected bands with our *HP* 8753D vector network analyzer (up to 6 GHz).

To finish this section we are going to check the accuracy of the approximate analytical solutions for the proposed PBG microstrip structure as the number of periods of the PBG device diminish. As it was stated in section (3.3.2) the approximation used to obtain the analytical solutions required the length of the PBG circuit to be “large enough”. In Fig. 3.6 the S_{21} parameter of three PBG microstrip circuits with 4, 3 and 2 periods respectively are depicted comparing the results obtained through numerical solution of the coupled mode equations with the approximate analytical solutions that employ the conventional physical position variable z, and the electrical position variable χ. The figures show that the analytical solution that employs the electrical position variable, χ , is always more accurate, and although the discrepancies found between the analytical and the numerical solutions increase as the number of periods decreases, the agreement is good even for the 2 periods device. On the other hand, Fig. 3.7 shows the same representation for a PBG device with only 1 period. It can be seen that this time the form of the curves is different and the discrepancies found are more

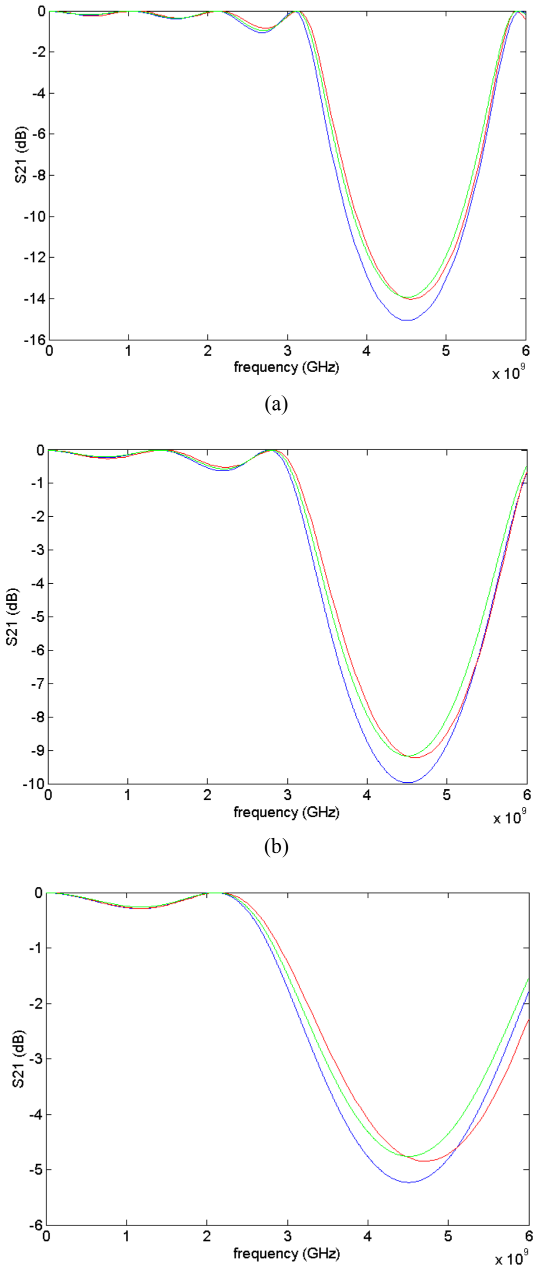

(a)

(b)

(c)

Figure 3.6: *S_{21} parameter for the PBG microstrip prototype designed as stated in section (3.6.1), having (a) 4 periods, (b) 3 periods, (c) 2 periods. They have been calculated through numerical solution of the coupled mode equations (red line), using the approximate analytical solutions (blue line), and using the analytical solutions with the electrical position variable (green line).*

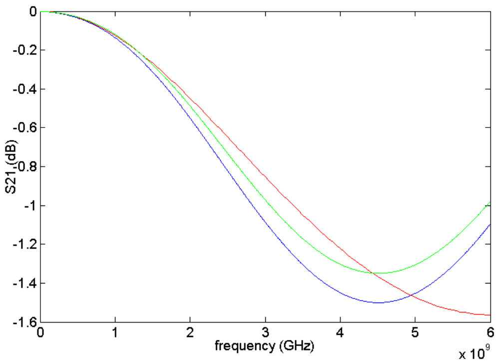

Figure 3.7: *S_{21} parameter for the PBG microstrip prototype designed as stated in section (3.6.1), having 1 period. It has been calculated through numerical solution of the coupled mode equations (red line), using the approximate analytical solutions (blue line), and using the analytical solutions with the electrical position variable (green line).*

important. Therefore from the data shown it can be concluded that for this PBG structure with fairly complicated coupling coefficient (it has harmonics of considerable value) a length of 2 periods can be considered "large enough" for the successful use of the approximate analytical solutions.

3.6.1.3. Complex amplitudes of the mode, $a^+(z)$, $a^-(z)$

In this section the complex amplitudes $a^+(z)$, $a^-(z)$ of the propagating mode (the microstrip or quasi-microstrip mode in our case), in our PBG microstrip prototype designed as stated in section (3.6.1) and with 9 periods, will be given for a frequency placed in the forbidden band (f=4.5 GHz), Fig. 3.8, and for a frequency placed in the passband (f=1.9 GHz), Fig. 3.9. The excitation taken has been the conventional one: a forward travelling wave of unitary amplitude at the input port ($a^+(z=0)=1$) and matching conditions at the output port ($a^-(z=L)=0$). The complex amplitudes have been calculated through numerical solution of the coupled mode equations (section (3.2.2)), using the approximate analytical expressions (section (3.3.2), eqns. (3.66)) and using the approximate analytical expressions with the electrical position variable (section (3.3.4)). The agreement between the numerical solutions and the approximate analytical expressions is good, although it can be seen that the details about the exact variation of the complex amplitudes along the PBG device are lost in the analytical results.

The modulus of the complex amplitudes of the mode follow the expected evolution along the PBG circuit: the forward travelling wave attenuates along the PBG in the forbidden band exciting strongly the backward travelling wave and giving rise to almost no transmission. The electromagnetic energy penetrates only partially into the PBG in this case. On the other hand, in the passband, the forward travelling wave propagates along the PBG almost without attenuation and exciting the backward travelling wave only partially and in localized areas of the circuit. The electromagnetic energy can go freely through the PBG.

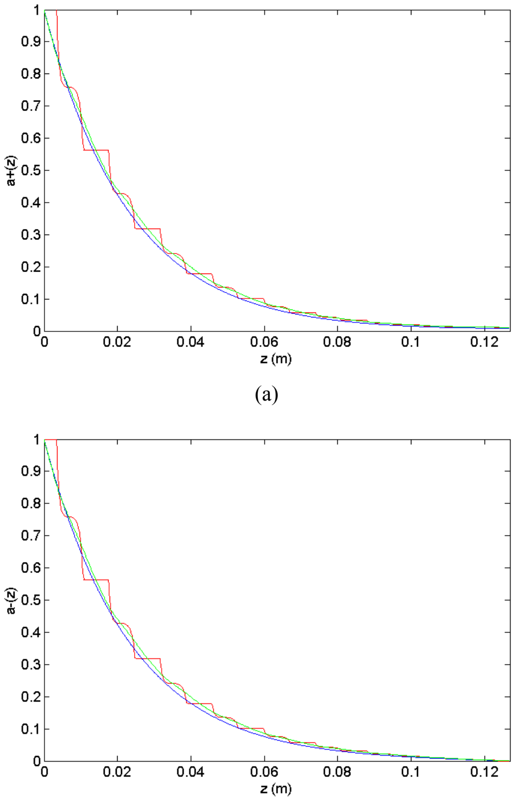

(a)

(b)

Figure 3.8: *Evolution of the modulus of the complex amplitudes of the mode, (a)* $a^+(z)$*, and (b)* $a^-(z)$*, along the PBG microstrip prototype designed as stated in section (3.6.1) and having 9 periods, for a frequency placed in the forbidden band (f=4.5 GHz). They have been calculated through numerical solution of the coupled mode equations (red line), using the approximate analytical solutions (blue line), and using the analytical solutions with the electrical position variable (green line).*

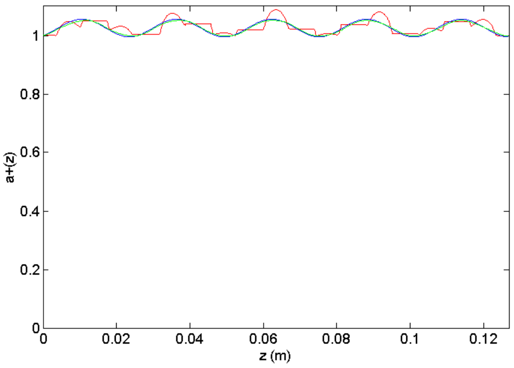

(a)

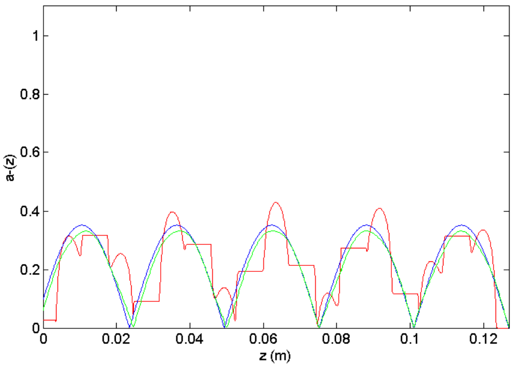

(b)

Figure 3.9: *Evolution of the modulus of the complex amplitudes of the mode, (a)* $a^+(z)$*, and (b)* $a^-(z)$*, along the PBG microstrip prototype designed as stated in section (3.6.1) and having 9 periods, for a frequency placed in passband (f=2 GHz). They have been calculated through numerical solution of the coupled mode equations (red line), using the approximate analytical solutions (blue line), and using the analytical solutions with the electrical position variable (green line).*

3.6.1.4. Dispersion diagram

To continue our study the dispersion diagram of the PBG microstrip structure proposed in section (3.6.1) will be presented. It will be given in the first Brillouin zone, and around the first rejected band. The dispersion diagram has been calculated using the numerical method described in section (3.4.2.2), eqn. (3.169), using the approximate analytical expression given in section (3.4.2.1), eqn. (3.148), and using the approximate analytical expression with the electrical position variable (see section (3.3.4)). The results are depicted in Fig. 3.10, giving the real part and the imaginary

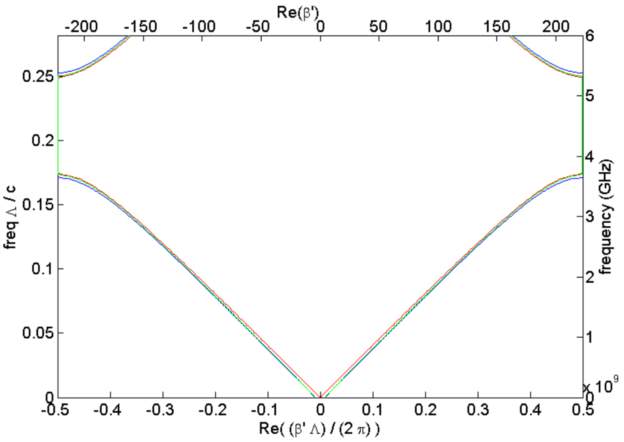

(a)

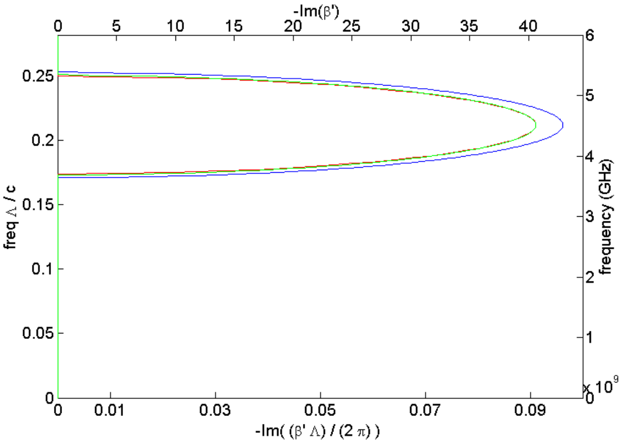

(b)

Figure 3.10: *(a) Dispersion diagram for the PBG microstrip prototype designed as stated in section (3.6.1). The first Brillouin zone is represented for the range of frequencies placed around the first rejected band. The imaginary part of the phase constant β' is also represented (b). The phase constant has been calculated using the numerical method (red line), using the approximate analytical expression (blue line), and using the approximate analytical expression with the electrical position variable (green line).*

part of the phase constant β'. The agreement between the numerical and the analytical results is very good, although as expected the analytical expression using the electrical position variable is more accurate. From the figures it can be clearly seen that for the range of frequencies placed around 4 – 5 GHz the phase constant has imaginary part, giving rise to reactive attenuation for the Bloch waves that attempt to propagate along the PBG structure. This frequency region in which the phase constant β' has imaginary part will produce evanescent behavior in the Bloch waves preventing their propagation along the PBG structure, and will be referred to as the forbidden band or Photonic Bandgap of the PBG structure.

The frequency at which the Bloch waves suffer maximum attenuation, the value of this maximum attenuation and the bandwidth of the Photonic Bandgap have been also calculated from the numerical method, using the approximate analytical expressions given for them in section (3.4.2.1) (eqns. (3.149), (3.150), (3.154)), and using the analytical expressions with the electrical position variable. The results are presented in Table 3.4. The agreement between the numerical and the analytical results is very good, being again more accurate the approximate analytical expressions with the electrical position variable.

	Numerical method	Analytical expression (z)	Analytical expression (χ)
f_{max} (GHz)	4.51	4.51	4.51
$\alpha'_{max} = -\mathrm{Im}(\beta')_{max}$ (Np/m)	40.58	42.89	40.56
BW_{gap} (GHz)	1.59	1.73	1.64

Table 3.4: *Values for the frequency of maximum attenuation of the Bloch waves,* f_{max} *, the value of this maximum attenuation,* α'_{max} *, and the bandwidth of the Photonic Bandgap,* BW_{gap} *, calculated from the numerical method, using the approximate analytical expressions, and using the approximate analytical expressions with the electrical position variable,* χ.

3.6.1.5. Characteristic impedance of the Bloch wave, Z_B

The characteristic impedance of the Bloch wave, Z_B , in the PBG microstrip structure proposed in section (3.6.1) has been studied in this section. In first place it is worth noting that since the unitary cell of the PBG microstrip structure under study is symmetrical, the following relation will be satisfied between the characteristic impedances corresponding to the forward and the backward travelling Bloch waves:

$$Z_B^{\,+} = -Z_B^{\,-} = Z_B$$

and hence, here, we will be concerned only with the "characteristic impedance of the Bloch waves", Z_B . The evolution of its value with the frequency has been calculated using the numerical method proposed in section (3.4.3.1), and specifically eqn. (3.179), it has been calculated also using the approximate analytical expressions developed in section (3.4.3.2), eqns. (3.186), (3.187), and using the approximate analytical expressions with the electrical position variable, χ , (see section (3.3.4)). The results are depicted in Fig. 3.11, giving the real part and the imaginary part of the characteristic impedance. The agreement between the numerical and the analytical results is very good, although the analytical results obtained using the electrical position variable are more accurate. As it can be seen, the characteristic impedance of the Bloch wave is real in the passbands and purely imaginary in the forbidden band or

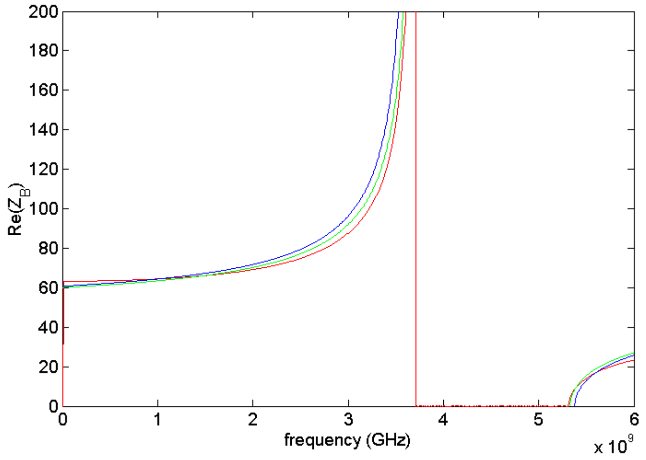

(a)

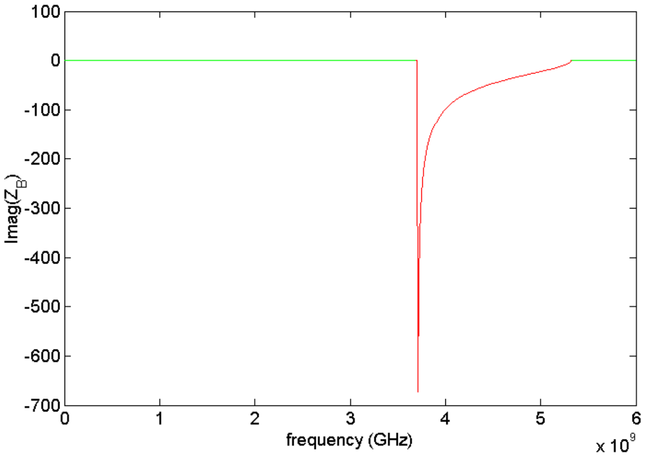

(b)

Figure 3.11: *Real part (a), and imaginary part (b), of the characteristic impedance of the Bloch wave,* Z_B*, in the PBG microstrip prototype designed as stated in section (3.6.1). It has been calculated using the numerical method (red line), using the approximate analytical expressions (blue line), and using the approximate analytical expressions with the electrical position variable (green line). The calculation using the analytical expressions is done only for the passbands, and not for the forbidden band.*

Photonic Bandgap. Its value clearly differs from the characteristic impedance of the ports (Z_0=50 Ω in our case), and is quite stable in the first part of the passband, but grows very quickly in the part close to the forbidden band. The difference between the characteristic impedance of the ports and the characteristic impedance of the Bloch waves produces the ripple (or sidelobes) that appears in the passband of the transmission (S_{21}) and reflection coefficients (S_{11}) of the PBG device.

3.6.1.5.1. “Matched” PBG microstrip circuit

As we have just commented, the ripple that appears in the passband of the transmission and reflection coefficients of our PBG microstrip circuit is due to the difference between the characteristic impedance of the ports, Z_0 , and the characteristic impedance of the Bloch waves in the PBG circuit, Z_B. Since the Z_B parameter is not constant in the passband (as it has been seen in Fig 3.11), we can not find a value for Z_0 such that all the passband is simultaneously matched (without ripple), but we can try to match the part of interest of the passband for the intended application, using a characteristic impedance for the ports, Z_0, equal to the value of Z_B in the part of interest of the passband. To probe the validity of this approach, the transmission, T, and reflection, R, coefficients of the PBG microstrip circuit under study (with 9 periods) have been calculated for several interesting cases using the technique detailed in section (3.4.4): they have been calculated for the conventional case (Z_0=50 Ω), where R=S_{11} and T=S_{21}, for the case in which we try to match the frequency range around 1 GHz, (Z_0=65 Ω), and for the case in which we try to match the frequency range around 2 GHz (Z_0=70 Ω). The results are depicted in Fig. 3.12. From them it can be clearly seen that the matching of the ports achieves an almost perfect matching around the target frequency, and reduces notably the ripple in almost all the passband. On the other hand, the rejected band remains almost unaltered.

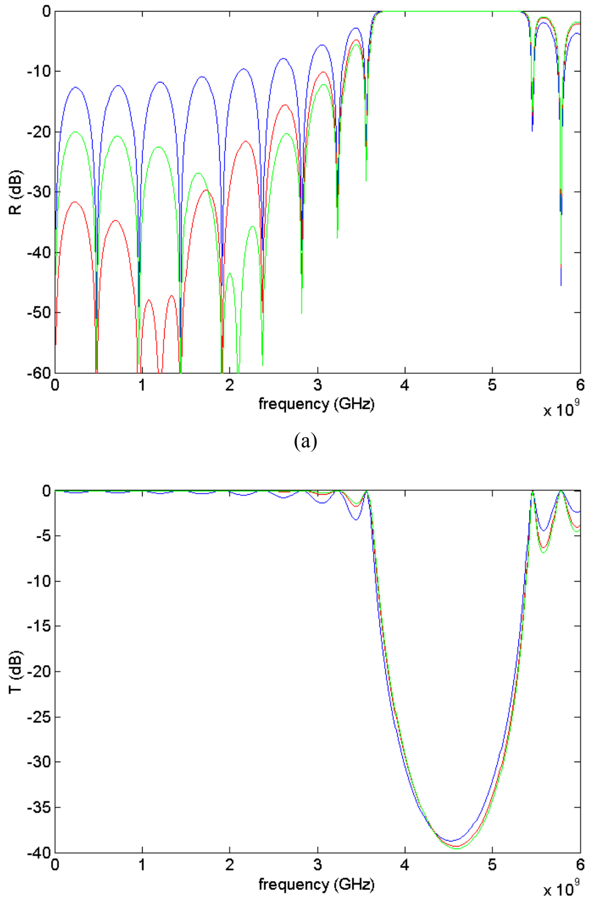

(a)

(b)

Figure 3.12: *(a) Reflection, R (b) and Transmission, T, parameters for the PBG microstrip prototype of 9 periods designed as stated in section (3.6.1), and for different characteristic impedances of the ports,* Z_0*. The conventional case (*$Z_0=50\ \Omega$*), where* $R=S_{11}$ *and* $T=S_{21}$ *is given (blue line), together with the case where* $Z_0=65\ \Omega$ *(red line), and* $Z_0=70\ \Omega$ *(green line).*

3.6.1.6. Fourier transform of the coupling coefficient

To finish the study of the PBG microstrip circuit with a pattern of circles, the Fourier transform of its coupling coefficient will be compared with its S_{11} (reflection) parameter. The relation between them is studied in section (3.5), and is given for the simplified case of structures with low reflectivity by eqn. (3.213). In Fig. 3.13 the evolution with the frequency of the S_{11} (reflection) parameter for the PBG microstrip device designed as stated in section (3.6.1) is given for a prototype with 9 periods and for a prototype with 4 periods, calculated through the numerical solution of the coupled mode equations, section (3.2.2). Together with it, the estimate of the S_{11} parameter through a plain Fourier transform of the coupling coefficient (eqn. (3.213)), and through a plain Fourier transform of the coupling coefficient using the electrical position variable (eqn. (3.222)) are also represented. It is important to stress that these simple expressions that use a plain Fourier transform of the coupling coefficient give

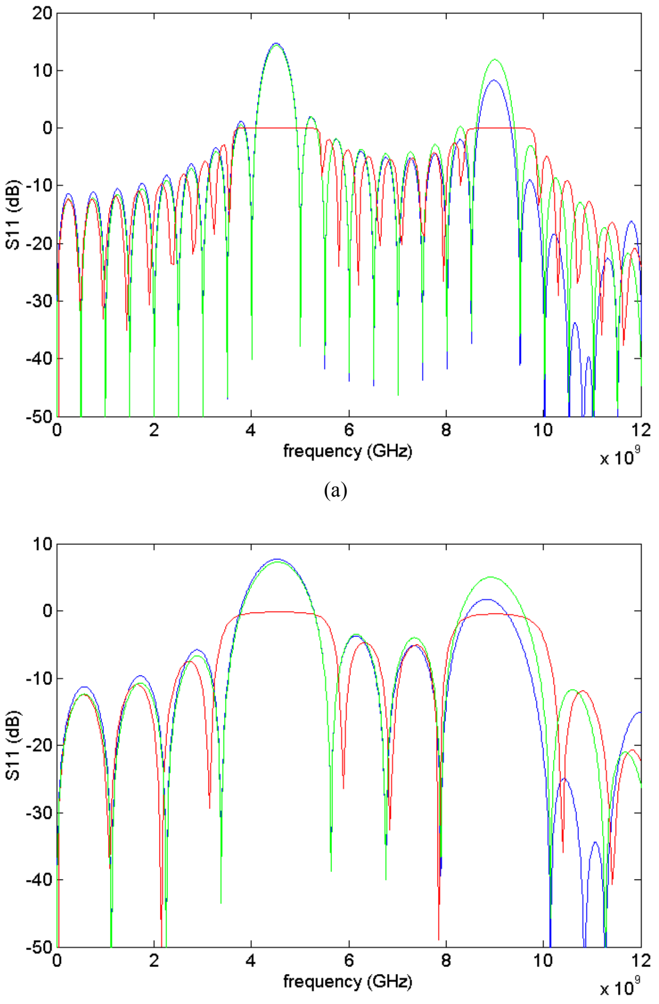

(a)

(b)

Figure 3.13: *S_{11} parameter for the PBG microstrip prototype designed as stated in section (3.6.1), with 9 periods (a), and with 4 periods (b). It has been calculated through numerical solution of the coupled mode equations (red line) and is compared to the estimates obtained realizing a plain Fourier transform of the coupling coefficient (blue line), and realizing a plain Fourier transform of the coupling coefficient using the electrical position variable (green line).*

an approximation to the reflection (S_{11}) parameter accurate for structures with low reflectivity, but that still constitutes a first approach to the response of general structures. This fact can be seen in the results presented in Fig. 3.13, where the Fourier transform of the coupling coefficient gives a reasonable estimate for the reflection response, although when the reflectivity of the device is very high the estimated value can not be taken into account. It is also interesting to note that the estimate for the device with lower reflectivity (the PBG circuit with 4 periods) is better than the estimate obtained for the largest one. It can be also seen that, as usually, the calculation using the electrical position variable provides more accurate results.

3.6.2. PBG featuring a continuous pattern with sinusoidal profile

The second PBG device in microstrip technology that we are going to analyze was proposed by our group in 2000 [LOP 00], and can be seen as an evolution of the previous structure to have a better control in its frequency response. The details about the motivation and reasoning that led to it, as well as its performance, advantages and applications will be presented in the next chapters. Here we will be concerned only with an analysis of the structure similar to that carried in the previous section.

The PBG device under analysis is obtained by etching a periodic pattern following continuous raised sine function in the ground plane of a microstrip line. In the upper plane, the strip conductor width is kept constant to have an also constant nominal characteristic impedance equal to 50 Ω. The prototype that we are going to analyze has the same design parameters as the previous one, in order to be measured with our *HP* 8753D vector network analyzer (up to 6 GHz) and to be easily compared with it. The substrate employed is a Rogers RT/Duroid 6010, with dielectric constant ε_r=10.2 and substrate thickness h=1.27 mm. The period of the PBG structure will have a value Λ=14.1 mm, and the maximum semi-width of the perturbation to period ratio will be r/Λ=0.25. The strip conductor width will be constant, w=1.2 mm. A photograph of the ground plane of the PBG microstrip prototype is given in Fig. 3.1.

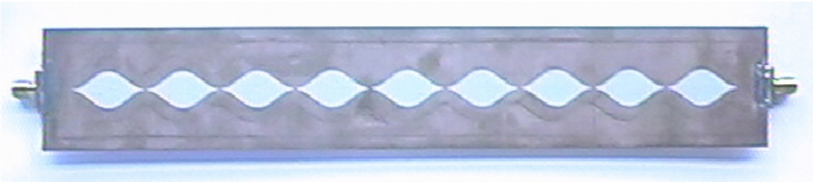

Figure 3.14: *Photograph of the ground plane of the PBG microstrip prototype featuring a continuous pattern with sinusoidal profile*

3.6.2.1. Perturbation profile and coupling coefficient

To begin the analysis of the proposed PBG prototype we are going to calculate its coupling coefficient, and we are going to depict it together with the profile of the perturbation (width of the slot in the ground plane) and with the characteristic impedance variation produced by the perturbation. They can be seen for one period of the PBG structure in Fig. 3.15. The characteristic impedance variation is calculated from the perturbation profile by interpolating the characteristic impedance values previously calculated (by using *Agilent HFSS* in our case) for a set of uniform auxiliary waveguides (microstrip lines with slots of different widths in the ground plane), as explained in section 3.2.2. The coupling coefficient is immediately obtained from the characteristic impedance by using eqn. (3.20).

It is important to notice that this time the PBG pattern employed is one dimensional. We have done it because, as explained previously for the 2-D pattern of circles, due to the high confinement of the fields around the conductor strip only the central row of the perturbation (placed behind the conductor strip) is relevant, and consequently the behavior is 1-D effective in any case [FAL 99].

In Fig. 3.16 the conventional coupling coefficient (calculated using the physical position variable) and the coupling coefficient calculated using the electrical position variable (as explained in section 3.3.4) are compared showing the deformation introduced in it by the variation of phase constant, β, present along the PBG device. Finally, the values for the coupling coefficient parameters calculated using the physical position variable (eqns. (3.38), (3.52)) and the electrical position variable are given in Table 3.5, for the first (n=1) and second (n=2) rejected bands. The results obtained using the electrical position variable are more accurate because they take into account the deformation introduced in the coupling coefficient by the variation of β along the PBG device. The differences found are very small for the first rejected band,

Band index, n	$k_{(z)}$	$k_{(\chi)}$	$k_{(\chi)} \cdot \sqrt{\varepsilon_{eff}}$	ε_{eff}
1	39.83	17.35	39.73	5.244
2	1.97	-2.22	-5.08	

Table 3.5: *Values for the coupling coefficient parameters calculated using the physical position variable ($k_{(z)}$) and the electrical position variable ($k_{(\chi)}$), for the first (n=1) and second (n=2) forbidden bands. $k_{(\chi)} \cdot \sqrt{\varepsilon_{eff}}$ is also included for comparison purposes, as well as the "averaged" ε_{eff} for the PBG device.*

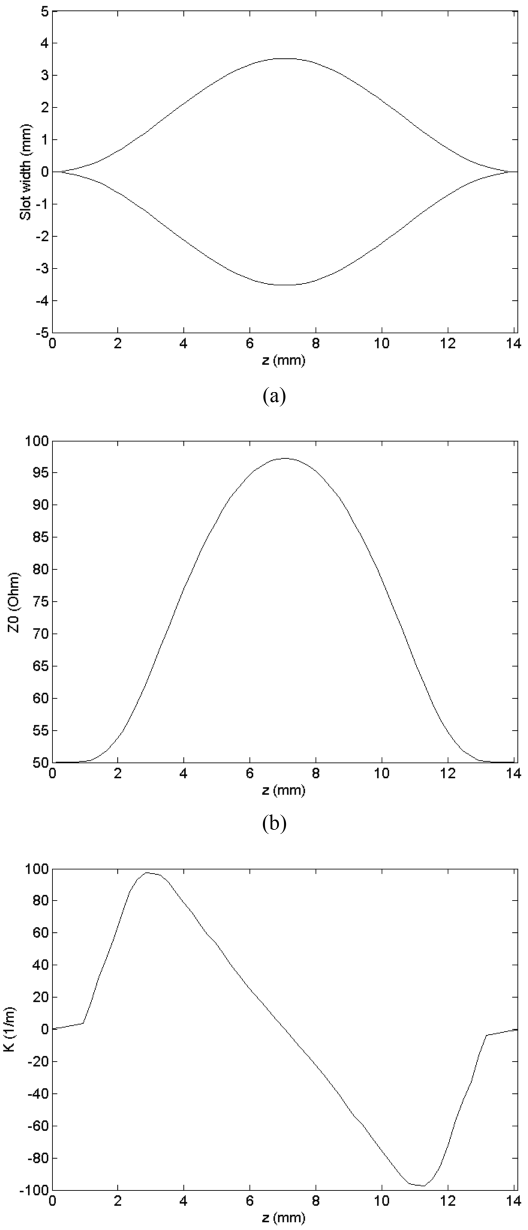

(a)

(b)

(c)

Figure 3.15: *(a) Profile of the PBG perturbation (width of the slot in the ground plane), (b) variation of characteristic impedance produced by the perturbation,* $Z_0(z)$ *and (c) resulting coupling coefficient, K(z).*

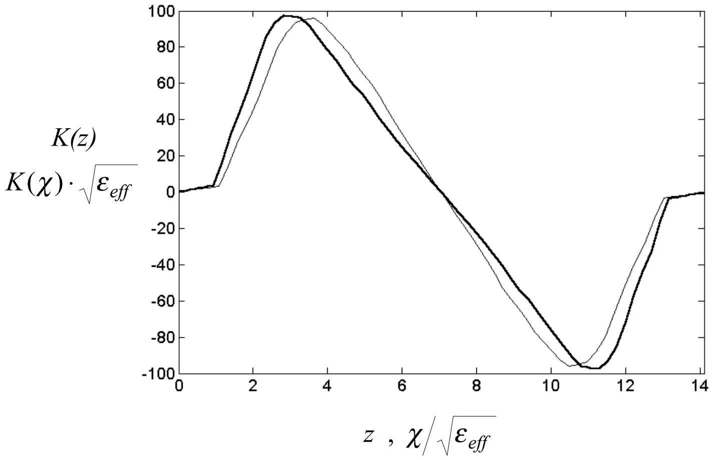

Figure 3.16: *Coupling coefficient produced by the PBG perturbation calculated using the physical position variable, K(z) (thick line), and using the electrical position variable, K(χ) (thin line). The later is represented with χ divided by $\sqrt{\varepsilon_{eff}}$ in the horizontal axis, and with K multiplied by $\sqrt{\varepsilon_{eff}}$ in the vertical axis for comparison purposes. ε_{eff} is the "averaged" value for the PBG device calculated using eqn. (3.117) and given in Table 3.5.*

in this case, but are significant for the second rejected band. The value of the "averaged" ε_{eff} for the PBG device (calculated through eqn. 3.117) is also included. It is interesting to note that this PBG perturbation with sinusoidal profile produces a coupling coefficient with almost sinusoidal variation, and hence the coupling coefficient parameter calculated for the second rejected band has a very small value. On the other hand, the coupling coefficient for the first rejected band has a value similar to that obtained for the PBG prototype with a discrete pattern of circles.

3.6.2.2. S_{11} and S_{21} parameters

To continue, we are going to focus our study on a PBG microstrip prototype of finite length, designed as stated in section (3.6.2) and with 9 periods. Firstly, its S_{11} (reflection) and S_{21} (transmission) parameters will be calculated through numerical solution of the coupled mode equations (section (3.2.2)), using the approximate analytical solutions obtained in section (3.3.3.1) (eqns. (3.68), (3.69)), and using the analytical solutions with the electrical position variable (section (3.3.4)). The prototype will be also fabricated employing a *LPKF* numerical milling machine, and its S parameters measured with our *HP* 8753D vector network analyzer. The S_{11} and S_{21} parameters obtained are depicted in Fig. 3.17 for the first rejected band (n=1), and

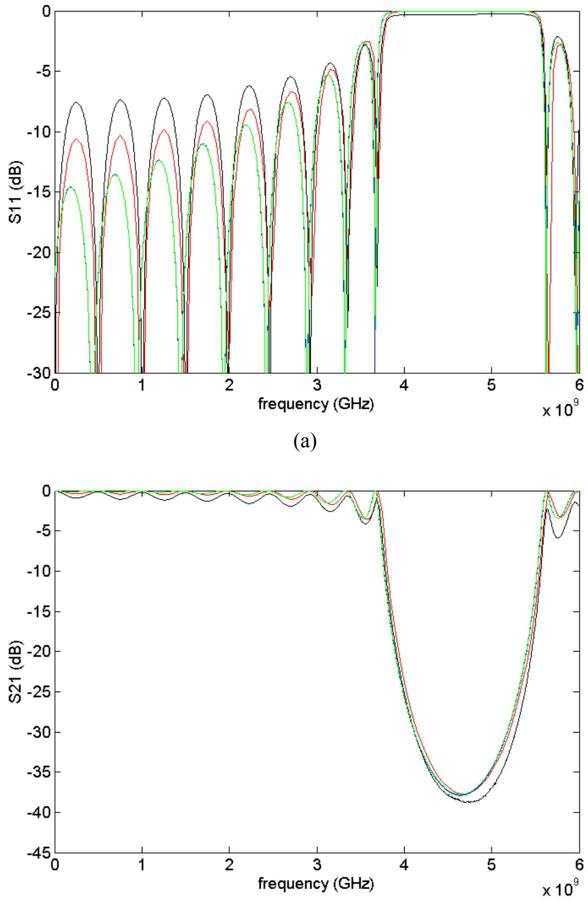

(a)

(b)

Figure 3.17: *(a) S_{11} and (b) S_{21} parameters for the PBG microstrip prototype of 9 periods designed as stated in section (3.6.2). They have been calculated through numerical solution of the coupled mode equations (red line), using the approximate analytical solutions (blue line), and using the analytical solutions with the electrical position variable (green line). The measurement results are also included for comparison (black line).*

	Numerical solution of coupled mode eqns.	Analytical solutions (z)	Analytical solutions (χ)	Measurements
f_{max} (GHz)	4.67	4.64	4.64	4.75
$\left\|S_{21}\right\|_{min}$ (dB)	-37.7	-37.88	-37.77	-38.70
BW_∞ (GHz)	1.95	1.95	1.95	1.94

Table 3.6: *Values for the frequency of maximum attenuation, f_{max} , the value of this maximum attenuation, $\left|S_{21}\right|_{min}$, and the bandwidth (between zeroes), BW_∞ , for the first (n=1) forbidden band, calculated through the same methods as Fig. 3.17.*

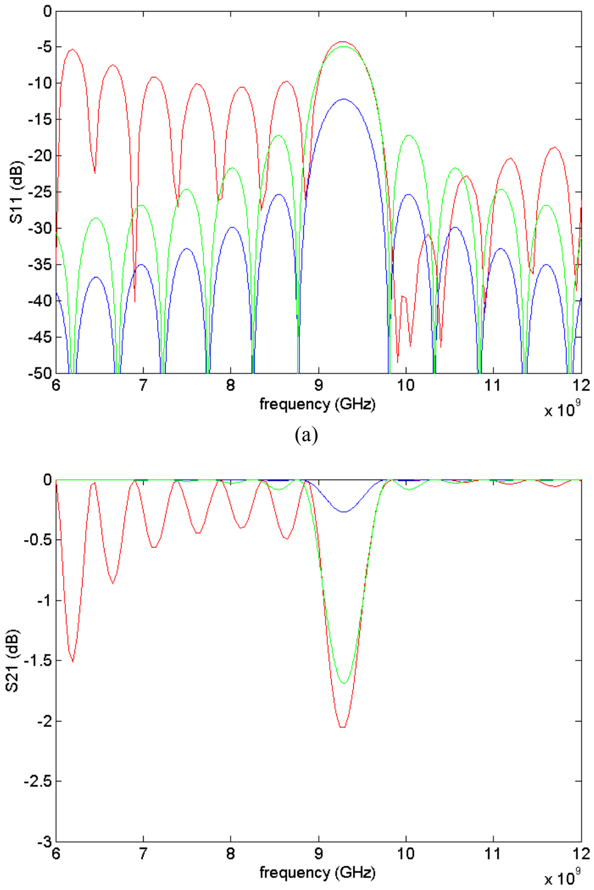

(a)

(b)

Figure 3.18: *(a) S_{11} and (b) S_{21} parameters for the PBG microstrip prototype of 9 periods designed as stated in section (3.6.2). They have been calculated through numerical solution of the coupled mode equations (red line), using the approximate analytical solutions (blue line), and using the analytical solutions with the electrical position variable (green line). This time they are depicted for the second (n=2) forbidden band.*

	Numerical solution of coupled mode eqns.	Analytical solutions (z)	Analytical solutions (χ)
f_{max} (GHz)	9.28	9.29	9.29
$\left\|S_{21}\right\|_{min}$ (dB)	-2.07	-0.27	-1.69
BW_∞ (GHz)	1.05	1.03	1.05

Table 3.7: *Values for the frequency of maximum attenuation, f_{max} , the value of this maximum attenuation, $\left|S_{21}\right|_{min}$, and the bandwidth (between zeroes), BW_∞ , for the second (n=2) forbidden band, calculated through the same methods as Fig. 3.18.*

in Fig. 3.18 for the second rejected band (n=2).

Secondly, the value for the frequency of maximum attenuation (or reflectivity), the value of this maximum attenuation, and the bandwidth (between zeroes) of the rejected band are obtained from the measurements, from the numerical solution for the coupled mode equations, using the approximate analytical expressions given for them in sections (3.3.3.2) and (3.3.3.3) (eqns. (3.70), (3.73), (3.79)), and using the analytical expressions with the electrical position variable. All of them are given in Table 3.6 for the first rejected band (n=1), and in Table 3.7 for the second rejected band (n=2).

As it can be seen in Fig. 3.17 and in Table 3.6, the agreement between the numerical solution of the coupled mode equations and the approximate analytical solutions is very good in the first rejected band. The agreement with the measurements is very good also. The small discrepancies found (mainly in the matching of the passband) are due to the discontinuities introduced by the connector unions in the constructed prototype. Regarding the second rejected band (n=2), Fig. 3.18 and Table 3.7 show that to have an accurate prediction using the approximate analytical solutions it is necessary to employ the electrical position variable. However, using it, a very good agreement is again obtained between the numerical solution of the coupled mode equations and the approximate analytical solutions. In general, the discrepancies found between the numerical and the approximate analytical solutions are more important as we go away from the central frequency of the rejected band due to the approximation involved to obtain the analytical solutions. However the predictions for the fundamental parameters of the PBG device given in Tables 3.6 and 3.7 are very good, and they confirm that the approximate analytical solutions can be successfully used for analysis and synthesis of PBG microstrip circuits. The fact that the second rejected band is almost non-existent for this PBG microstrip structure is confirmed in measurement by the downscaled prototype designed and presented in chapter 4, section (4.6) in order to measure its first and second rejected bands with our *HP* 8753D vector network analyzer (up to 6 GHz). The virtual absence of second rejected band can be predicted from the low value that the coupling coefficient parameter has for this band, as it was previously seen in section (3.6.2.1).

To finish this section we are going to check the accuracy of the approximate analytical solutions for the proposed PBG microstrip structure as the number of periods of the PBG device diminish. As it was stated in section (3.3.2) the approximation used to obtain the analytical solutions required the length of the PBG circuit to be “large enough”. In Fig. 3.19 the S_{21} parameter of three PBG microstrip circuits with 4, 3 and 2 periods respectively are depicted comparing the results obtained through numerical solution of the coupled mode equations with the approximate analytical solutions that

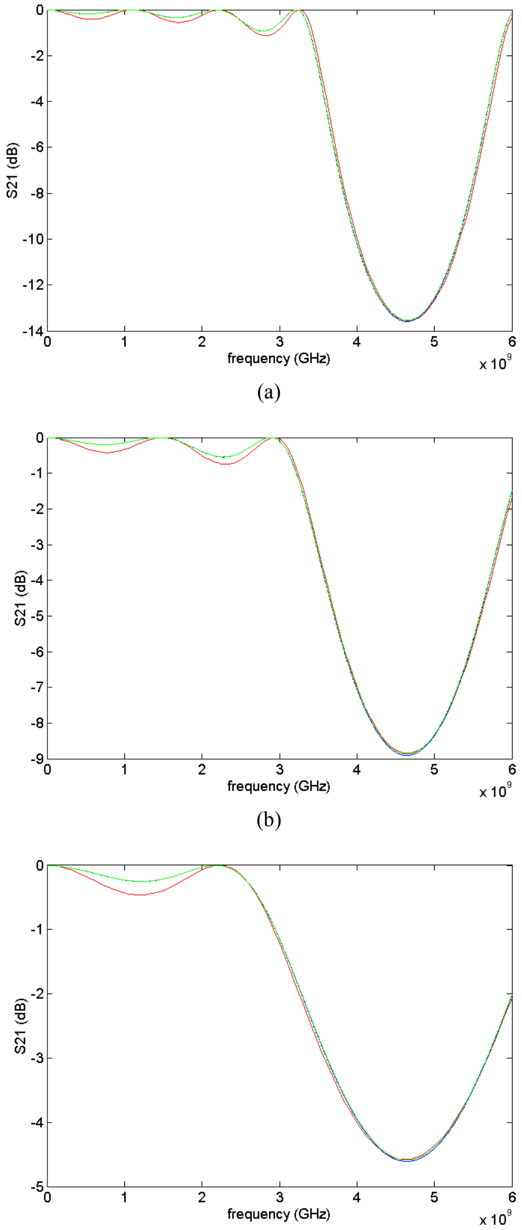

(a)

(b)

(c)

Figure 3.19: *S_{21} parameter for the PBG microstrip prototype designed as stated in section (3.6.2), having (a) 4 periods, (b) 3 periods, (c) 2 periods. They have been calculated through numerical solution of the coupled mode equations (red line), using the approximate analytical solutions (blue line), and using the analytical solutions with the electrical position variable (green line).*

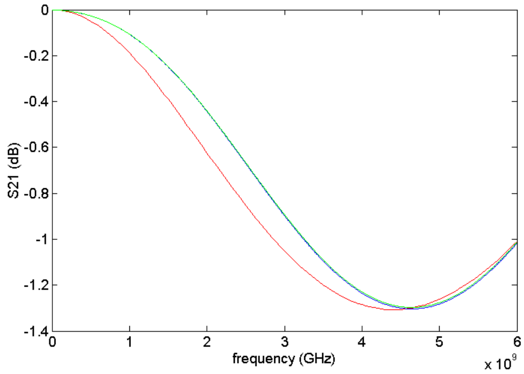

Figure 3.20: *S_{21} parameter for the PBG microstrip prototype designed as stated in section (3.6.2), having 1 period. It has been calculated through numerical solution of the coupled mode equations (red line), using the approximate analytical solutions (blue line), and using the analytical solutions with the electrical position variable (green line).*

employ the conventional physical position variable z, and the electrical position variable χ. The figures show that this time (and for the first rejected band) the analytical solutions give almost the same result, and the discrepancies found between the analytical and the numerical solutions increase very slightly (and only in the passband) as the number of periods decreases, with a good agreement even for the 2 periods device. On the other hand, Fig. 3.20 shows the same representation for a PBG device with only 1 period. It can be seen that this time the discrepancies found are more important. Therefore from the data shown it can be concluded that for this PBG structure with quite simple coupling coefficient (it has almost no harmonics) a length of 2 periods can be considered "large enough" for the successful use of the approximate analytical solutions, and in all the cases the predictions for the rejected band are very accurate.

3.6.2.3. Complex amplitudes of the mode, $a^+(z)$, $a^-(z)$

In this section the complex amplitudes $a^+(z)$, $a^-(z)$ of the propagating mode (the microstrip or quasi-microstrip mode in our case), in our PBG microstrip prototype designed as stated in section (3.6.2) and with 9 periods, will be given for a frequency placed in the forbidden band (f=4.65 GHz), Fig. 3.21, and for a frequency placed in the passband (f=2 GHz), Fig. 3.22. The excitation taken has been the conventional one: a forward travelling wave of unitary amplitude at the input port ($a^+(z=0)=1$) and matching conditions at the output port ($a^-(z=L)=0$). The complex amplitudes have been calculated through numerical solution of the coupled mode equations (section

(3.2.2)), using the approximate analytical expressions (section (3.3.2), eqns. (3.66)) and using the approximate analytical expressions with the electrical position variable (section (3.3.4)). The agreement between the numerical solutions and the approximate analytical expressions is good, although it can be seen that the details about the exact variation of the complex amplitudes along the PBG device are lost in the analytical results.

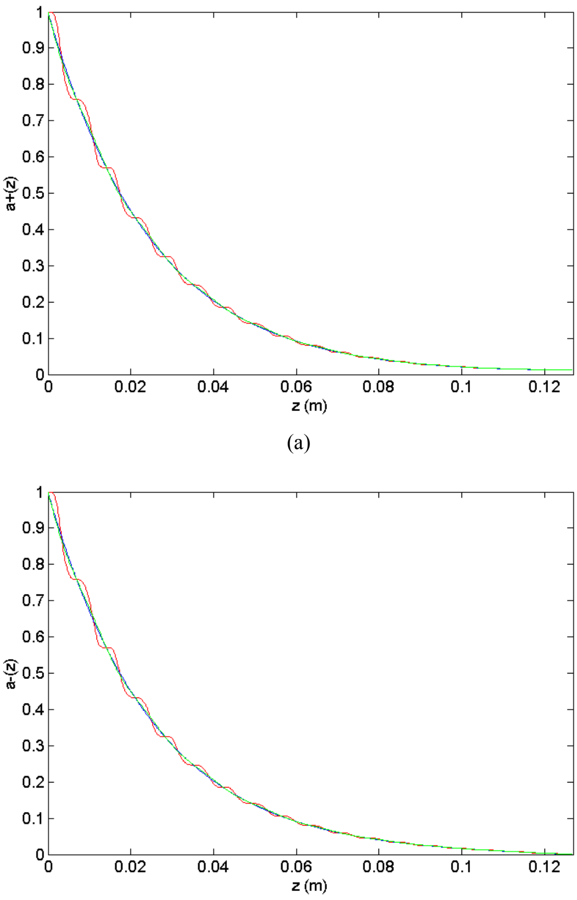

(a)

(b)

Figure 3.21: *Evolution of the modulus of the complex amplitudes of the mode, (a)* $a^{+}(z)$*, and (b)* $a^{-}(z)$*, along the PBG microstrip prototype designed as stated in section (3.6.2) and having 9 periods, for a frequency placed in the forbidden band (f=4.65 GHz). They have been calculated through numerical solution of the coupled mode equations (red line), using the approximate analytical solutions (blue line), and using the analytical solutions with the electrical position variable (green line).*

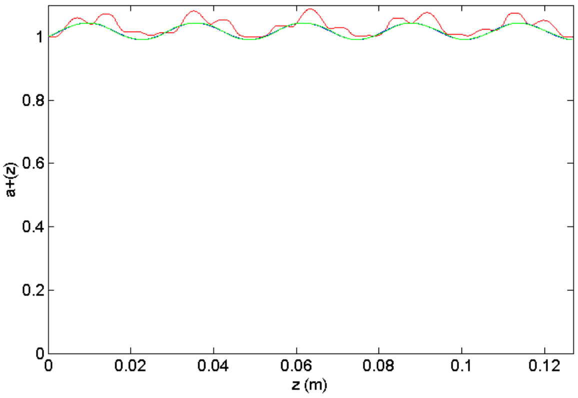

(a)

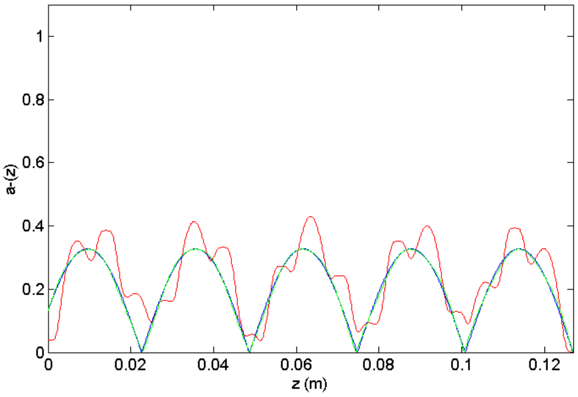

(b)

Figure 3.22: *Evolution of the modulus of complex amplitudes of the mode, (a)* $a^{+}(z)$*, and (b)* $a^{-}(z)$*, along the PBG microstrip prototype designed as stated in section (3.6.2) and having 9 periods, for a frequency placed in passband (f=2 GHz). They have been calculated through numerical solution of the coupled mode equations (red line), using the approximate analytical solutions (blue line), and using the analytical solutions with the electrical position variable (green line).*

The modulus of the complex amplitudes of the mode follow the expected evolution along the PBG circuit: the forward travelling wave attenuates along the PBG in the forbidden band exciting strongly the backward travelling wave and giving rise to almost no transmission. The electromagnetic energy penetrates only partially into the PBG in this case. On the other hand, in the passband, the forward travelling wave propagates along the PBG almost without attenuation and exciting the backward travelling wave only partially and in localized areas of the circuit. The electromagnetic energy can go freely through the PBG.

3.6.2.4. Dispersion diagram

To continue our study the dispersion diagram of the PBG microstrip structure proposed in section (3.6.2) will be presented. It will be given in the first Brillouin zone, and around the first rejected band. The dispersion diagram has been calculated using the numerical method described in section (3.4.2.2), eqn. (3.169), using the approximate analytical expression given in section (3.4.2.1), eqn. (3.148), and using the approximate analytical expression with the electrical position variable (see section (3.3.4)). The results are depicted in Fig. 3.23, giving the real part and the imaginary part of the phase constant β'. The agreement between the numerical and the analytical results is very good, and in this case both analytical expressions give almost the same result.

From the figures it can be clearly seen that for the range of frequencies placed around 4 – 5 GHz the phase constant has imaginary part, giving rise to reactive attenuation for the Bloch waves that attempt to propagate along the PBG structure. This frequency region in which the phase constant β' has imaginary part will produce evanescent behavior in the Bloch waves preventing their propagation along the PBG structure, and will be referred to as the forbidden band or Photonic Bandgap of the PBG structure.

The frequency at which the Bloch waves suffer maximum attenuation, the value of this maximum attenuation and the bandwidth of the Photonic Bandgap have been also calculated from the numerical method, using the approximate analytical expressions given for them in section (3.4.2.1) (eqns. (3.149), (3.150), (3.154)), and using the analytical expressions with the electrical position variable. The results are presented in Table 3.8. The agreement between the numerical and the analytical results is again remarkably good.

	Numerical method	Analytical expression (z)	Analytical expression (χ)
f_{max} (GHz)	4.68	4.64	4.64
$\alpha'_{max} = -\mathrm{Im}(\beta')_{max}$ (Np/m)	39.70	39.83	39.73
BW_{gap} (GHz)	1.66	1.66	1.65

Table 3.8: *Values for the frequency of maximum attenuation of the Bloch waves,* f_{max} *, the value of this maximum attenuation,* α'_{max} *, and the bandwidth of the Photonic Bandgap,* BW_{gap} *, calculated from the numerical method, using the approximate analytical expressions, and using the approximate analytical expressions with the electrical position variable,* χ.

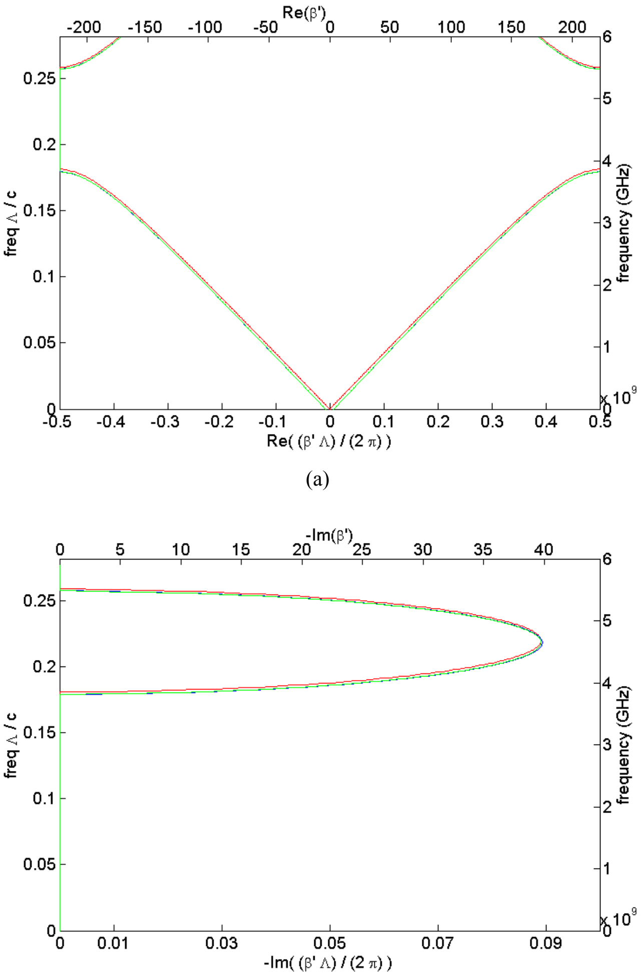

(a)

(b)

Figure 3.23: *(a) Dispersion diagram for the PBG microstrip prototype designed as stated in section (3.6.2). The first Brillouin zone is represented for the range of frequencies placed around the first rejected band. The imaginary part of the phase constant β' is also represented (b). The phase constant has been calculated using the numerical method (red line), using the approximate analytical expression (blue line), and using the approximate analytical expression with the electrical position variable (green line).*

3.6.2.5. Characteristic impedance of the Bloch wave, Z_B

The characteristic impedance of the Bloch wave, Z_B , in the PBG microstrip structure proposed in section (3.6.2) has been studied in this section. In first place it is worth noting that since the unitary cell of the PBG microstrip structure under study is symmetrical, the following relation will be satisfied between the characteristic impedances corresponding to the forward and the backward travelling Bloch waves:

$$Z_B^{\ +} = -Z_B^{\ -} = Z_B$$

and hence, here, we will be concerned only with the "characteristic impedance of the Bloch waves", Z_B . The evolution of its value with the frequency has been calculated using the numerical method proposed in section (3.4.3.1), and specifically eqn. (3.179), it has been calculated also using the approximate analytical expressions developed in section (3.4.3.2), eqns. (3.186), (3.187), and using the approximate analytical expressions with the electrical position variable, χ , (see section (3.3.4)). The results are depicted in Fig. 3.24, giving the real part and the imaginary part of the characteristic impedance. Again, both analytical expressions give almost the same results. On the other hand, the agreement between the numerical and the analytical results is very good, although the difference between them increases for the low frequencies of the passband.

As it can be seen, the characteristic impedance of the Bloch wave is real in the passbands and purely imaginary in the forbidden band or Photonic Bandgap. Its value clearly differs from the characteristic impedance of the ports (Z_0=50 Ω in our case), and is quite stable in the first part of the passband, but grows very quickly in the part close to the forbidden band. The difference between the characteristic impedance of the ports and the characteristic impedance of the Bloch waves produces the ripple (or sidelobes) that appears in the passband of the transmission (S_{21}) and reflection coefficients (S_{11}) of the PBG device.

3.6.2.5.1. "Matched" PBG microstrip circuit

As we have just mentioned, the ripple that appears in the passband of the transmission and reflection coefficients of our PBG microstrip circuit is due to the difference between the characteristic impedance of the ports, Z_0 , and the characteristic impedance of the Bloch waves in the PBG circuit, Z_B. Since the Z_B parameter is not constant in the passband (as it has been seen in Fig 3.24), we can not find a value for Z_0 such that all the passband is simultaneously matched (without ripple), but we can

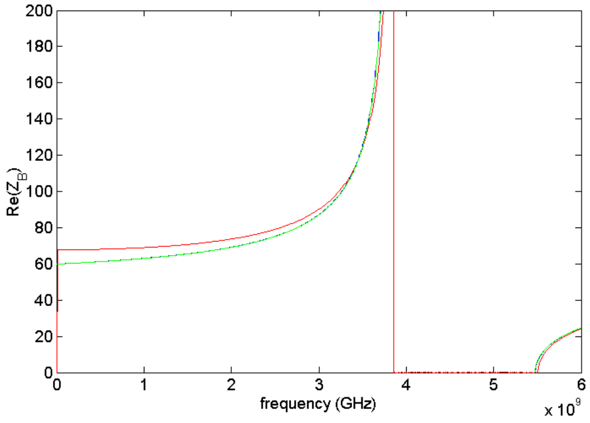

(a)

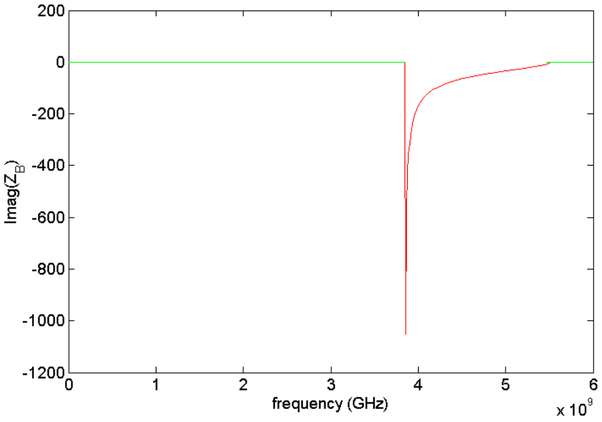

(b)

Figure 3.24: *Real part (a), and imaginary part (b), of the characteristic impedance of the Bloch wave, Z_B, in the PBG microstrip prototype designed as stated in section (3.6.2). It has been calculated using the numerical method (red line), using the approximate analytical expressions (blue line), and using the approximate analytical expressions with the electrical position variable (green line). The calculation using the analytical expressions is done only for the passbands, and not for the forbidden band.*

try to match the part of interest of the passband for the intended application, using a characteristic impedance for the ports, Z_0, equal to the value of Z_B in the part of interest of the passband. To probe the validity of this approach, the transmission, T, and reflection, R, coefficients of the PBG microstrip circuit under study (with 9 periods) have been calculated for several interesting cases using the technique detailed in section (3.4.4): they have been calculated for the conventional case (Z_0=50 Ω), where R=S_{11} and T=S_{21}, for the case in which we try to match the frequency range around 1 GHz, (Z_0=69 Ω), and for the case in which we try to match the frequency range around 2 GHz (Z_0=73 Ω). The results are depicted in Fig. 3.25. From them it can be clearly seen that the matching of the ports achieves an almost perfect matching around the target frequency, and reduces notably the ripple in almost all the passband. On the other hand, the rejected band remains almost unaltered.

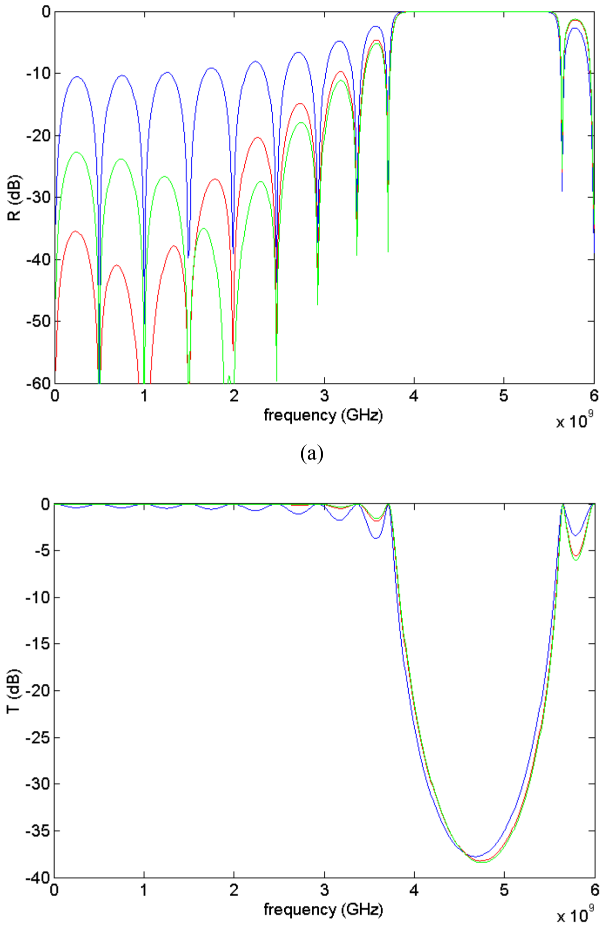

(a)

(b)

Figure 3.25: *(a) Reflection, R (b) and Transmission, T, parameters for the PBG microstrip prototype of 9 periods designed as stated in section (3.6.2), and for different characteristic impedances of the ports, Z_0. The conventional case (Z_0=50 Ω), where $R=S_{11}$ and $T=S_{21}$ is given (blue line), together with the case where Z_0=69 Ω (red line), and Z_0=73 Ω (green line).*

3.6.2.6. Fourier transform of the coupling coefficient

To finish the study of the PBG microstrip circuit with a sinusoidal pattern, the Fourier transform of its coupling coefficient will be compared with its S_{11} (reflection) parameter. The relation between them is studied in section (3.5), and is given for the simplified case of structures with low reflectivity by eqn. (3.213). In Fig. 3.26 the evolution with the frequency of the S_{11} (reflection) parameter for the PBG microstrip device designed as stated in section (3.6.2) is given for a prototype with 9 periods and for a prototype with 4 periods, calculated through the numerical solution of the

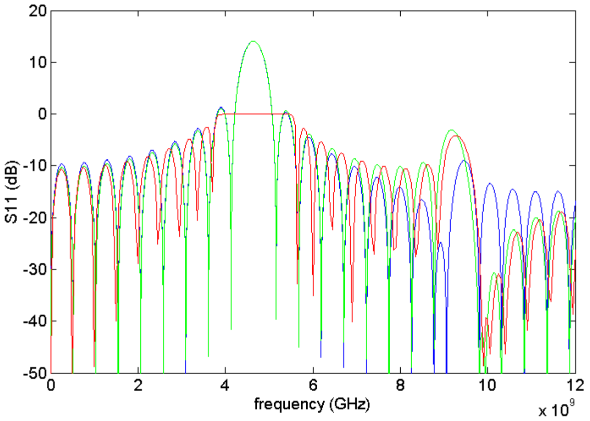

(a)

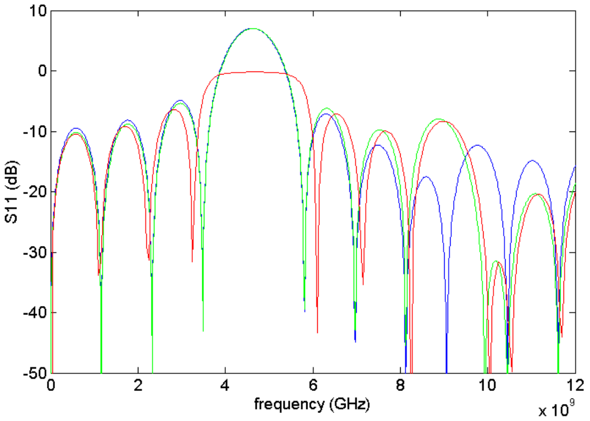

(b)

Figure 3.26: *S_{11} parameter for the PBG microstrip prototype designed as stated in section (3.6.2), with 9 periods (a), and with 4 periods (b). It has been calculated through numerical solution of the coupled mode equations (red line) and is compared to the estimates obtained realizing a plain Fourier transform of the coupling coefficient (blue line), and realizing a plain Fourier transform of the coupling coefficient using the electrical position variable (green line).*

coupled mode equations, section (3.2.2). Together with it, the estimate of the S_{11} parameter through a plain Fourier transform of the coupling coefficient (eqn. (3.213)), and through a plain Fourier transform of the coupling coefficient using the electrical position variable (eqn. (3.222)) are also represented. It is important to stress that these simple expressions that use a plain Fourier transform of the coupling coefficient give an approximation to the reflection (S_{11}) parameter accurate for structures with low reflectivity, but that still constitutes a first approach to the response of general structures. This fact can be seen in the results presented in Fig. 3.26, where the Fourier transform of the coupling coefficient gives a reasonable estimate for the reflection response, although when the reflectivity of the device is very high the estimated value can not be taken into account. It is also interesting to note that the estimate for the device with lower reflectivity (the PBG circuit with 4 periods) is better than the estimate obtained for the largest one. However it is important to stress that in any case the virtual absence of second rejected band is successfully predicted by the Fourier transform of the coupling coefficient, and even the specific value for the maximum reflectivity obtained in it is very accurately predicted using the Fourier transform with the electrical position variable. It can be also seen that, in general, the calculation using the electrical position variable provides more accurate results.

3.6.3. Defected PBG with a pattern of circles

To finish this section of examples, a prototype of defected PBG with a pattern of circles is studied. It is obtained by removing the central period of the PBG device featuring a discrete pattern of circles designed in section (3.6.1), and leaving a defect length equal to L_{def}=6.25 mm. In this way, the PBG resonator proposed in [LOP 99] is reproduced. The details about the design technique, the operation, performance and potential applications of this resonator structure will be presented in the next chapters. Here we will be concerned only with an analysis of the structure similar to that carried in the previous sections.

The device is obtained by etching a periodic pattern of circles, following a square lattice, in the ground plane of a microstrip line, whose central period is removed. The resulting defect would have a length equal to a period, but to obtain a better performance it is optimized giving rise to a defect length equal to L_{def}=6.25 mm. In the upper plane, the strip conductor width is kept constant to have an also constant nominal characteristic impedance equal to 50 Ω. The prototype that we are going to analyze has the same design parameters as the previous ones, in order to be measured with our *HP* 8753D vector network analyzer (up to 6 GHz) and to be easily compared

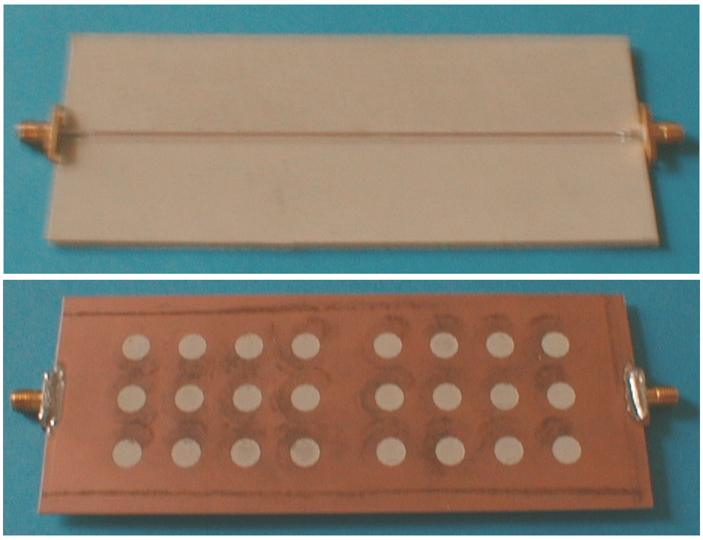

Figure 3.27*: Photograph of the upper plane and of the ground plane of the defected PBG microstrip prototype featuring a discrete pattern of circles.*

with them. The substrate employed is a Rogers RT/Duroid 6010, with dielectric constant ε_r=10.2 and substrate thickness h=1.27 mm. The period of the PBG structure will have a value Λ=14.1 mm, and the radius of the circle to period ratio will be r/Λ=0.25. The number of periods of the device will be 8. The strip conductor width will be constant, w=1.2 mm. A photograph of the upper plane and of the ground plane of the defected PBG microstrip prototype is given in Fig. 3.27.

3.6.3.1. S_{11} and S_{21} parameters

To begin the analysis of the defected PBG prototype we are going to calculate its S_{11} (reflection) and S_{21} (transmission) parameters. They will be obtained through numerical solution of the coupled mode equations (section (3.2.2)), using the approximate analytical results obtained by cascading the approximate analytical expressions for the transmission matrices (section (3.3.3.4), eqns. (3.89), (3.90)) (uniform PBG + unperturbed microstrip line + uniform PBG), and using the approximate analytical expressions with the electrical position variable (section (3.3.4)). The prototype will be also fabricated employing a *LPKF* numerical milling machine, and its S parameters measured with our *HP* 8753D vector network analyzer. The S_{11} and S_{21} parameters obtained are depicted in Fig. 3.28. As it can be clearly seen a transmission peak of resonant nature appears in the middle of the rejected band.

To continue, the values for the resonance frequency, f_{res}, bandwidth at 3 dB of the

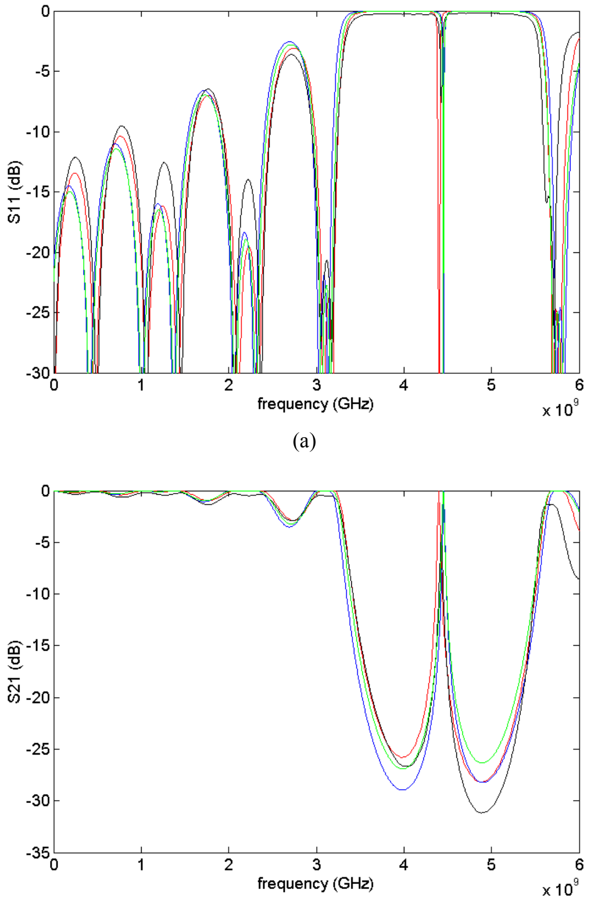

(a)

(b)

Figure 3.28: *(a) S_{11} and (b) S_{21} parameters for the defected PBG microstrip prototype of 8 periods designed as stated in section (3.6.3). They have been calculated through numerical solution of the coupled mode equations (red line), using the approximate analytical expressions for the transmission matrices and cascading them (blue line), and using the approximate analytical expressions for the transmission matrices with the electrical position variable (green line). The measurement results are also included for comparison (black line).*

	Numerical solution of coupled mode eqns.	Analytical solutions (z)	Analytical solutions (χ)	Measurements
f_{res} (GHz)	4.40	4.45	4.45	4.43
BW_{3dB} (MHz)	25.0	21.0	26.1	34.1
Q	176	211	170.5	130

Table 3.9: *Values for the resonance frequency, f_{res} , bandwidth at 3 dB of the resonance peak, BW_{3dB} , and quality factor of the resonator, Q , calculated from the frequency responses depicted in Fig. 3.28.*

resonance peak, BW_{3dB} , and quality factor of the resonator, Q , are obtained from the frequency responses previously calculated. All of them are given in Table 3.9.

As it can be seen in Fig. 3.28 and in Table 3.9, the agreement between the numerical solution of the coupled mode equations and the approximate analytical solutions obtained using the transmission matrices is very good. However it can be seen that the analytical solutions that employ the electrical position variable give more accurate predictions.

The agreement with the measurements is very good also. The discrepancies found in the level of the resonance peak and in the quality factor, Q, are due to the losses present in the constructed prototype. The losses are neglected in the analytical expressions. On the other hand, the small discrepancies present in the matching are due to the discontinuities introduced by the connector unions in the constructed prototype.

3.6.3.2. Complex amplitudes of the mode, $a^{+}(z)$, $a^{-}(z)$

In this section the complex amplitudes $a^{+}(z)$, $a^{-}(z)$ of the propagating mode (the microstrip or quasi-microstrip mode in our case), calculated along the defected PBG microstrip prototype designed as stated in section (3.6.3), will be given for a rejected frequency (f=4.9 GHz), Fig. 3.29, and for the resonance frequency (f=4.4 GHz), Fig. 3.30. The excitation taken has been the conventional one: a forward travelling wave of unitary amplitude at the input port ($a^{+}(z=0)=1$) and matching conditions at the output port ($a^{-}(z=L)=0$).

The complex amplitudes have been calculated through numerical solution of the coupled mode equations (section (3.2.2)).

From Fig. 3.29 it can be clearly seen that the complex amplitudes of the mode follow, for the frequencies that are actually rejected, the same evolution in the defected PBG as in the non-defected PBGs previously studied (see sections (3.6.1.3), (3.6.2.3)). However, the introduction of the defect opens up a transmission band (resonance peak) in the middle of the forbidden band, where the signal can be transmitted ideally without attenuation (in the ideal case of a lossless device). This happens because the defect supports a localized-defect-mode at the resonance frequency, allowing the transmission of energy at that frequency [JOA 95]. The effect can be seen in Fig. 3.30, where almost total transmission is achieved at the resonance frequency (the modulus of the complex amplitude associated to the forward travelling wave is equal to one at the output port), and the distribution of energy reveals that it is coupled to a localized mode associated to the defect.

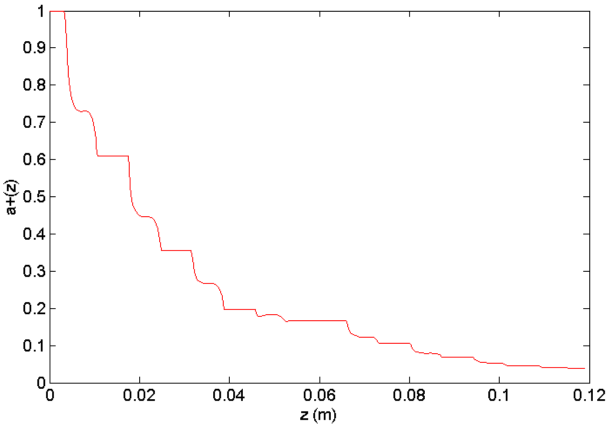

(a)

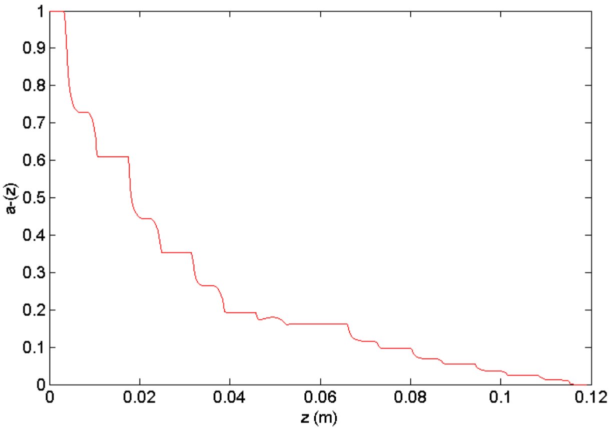

(b)

Figure 3.29: *Evolution of the modulus of the complex amplitudes of the mode, (a)* $a^{+}(z)$*, and (b)* $a^{-}(z)$*, along the defected PBG microstrip prototype designed as stated in section (3.6.3), for a rejected frequency (f=4.9 GHz). They have been calculated through numerical solution of the coupled mode equations.*

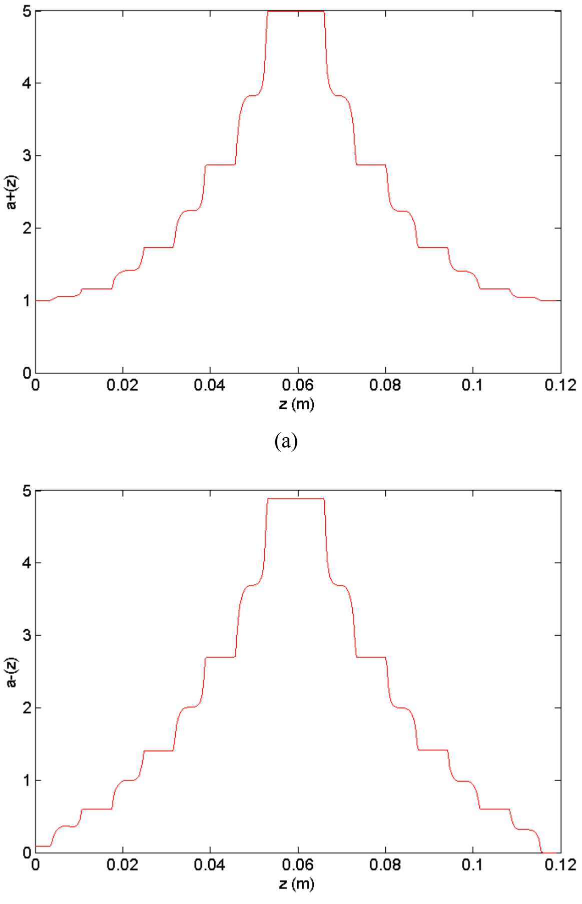

(a)

(b)

Figure 3.30: *Evolution of the modulus of the complex amplitudes of the mode, (a)* $a^{+}(z)$*, and (b)* $a^{-}(z)$*, along the defected PBG microstrip prototype designed as stated in section (3.6.3), for the resonance frequency (f=4.4 GHz). They have been calculated through numerical solution of the coupled mode equations.*

3.6.3.3. Fourier transform of the coupling coefficient

To finish the study of the defected PBG microstrip circuit with a pattern of circles, the Fourier transform of its coupling coefficient will be compared with its S_{11} (reflection) parameter. The relation between them is studied in section (3.5), and is given for the simplified case of structures with low reflectivity by eqn. (3.213). In Fig. 3.31 the evolution with the frequency of the S_{11} (reflection) parameter for the defected PBG microstrip device designed as stated in section (3.6.3) is given, calculated through the numerical solution of the coupled mode equations, section (3.2.2). Together with it, the estimate of the S_{11} parameter through a plain Fourier transform of the coupling coefficient (eqn. (3.213)), and through a plain Fourier transform of the coupling coefficient using the electrical position variable (eqn. (3.222)) are also represented. It is important to stress that these simple expressions that use a plain Fourier transform of the coupling coefficient give an approximation to the reflection (S_{11}) parameter accurate for structures with low reflectivity, but that still constitutes a first approach to the response of general structures. This fact can be seen in the results presented in Fig. 3.31, where the Fourier transform of the coupling coefficient gives a reasonable estimate for the reflection response, although when the reflectivity of the device is very high the estimated value can not be taken into account. Specifically, it is interesting to note that the presence of the resonance frequency is successfully predicted by the Fourier transform of the coupling coefficient, and even the exact value of this resonance frequency is quite accurately predicted by the Fourier transform with the electrical position variable. It can be also seen that, as before, the calculation using the electrical position variable provides more accurate results.

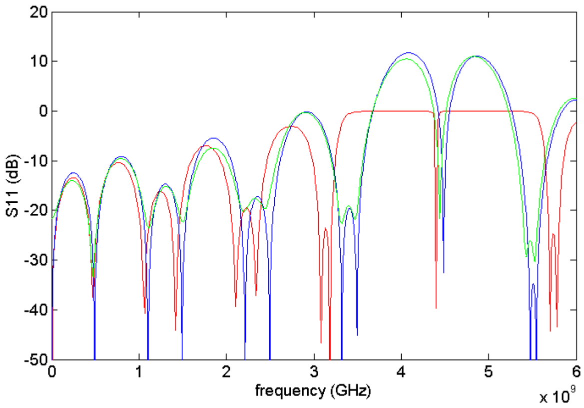

Figure 3.31: *S_{11} parameter for the defected PBG microstrip prototype designed as stated in section (3.6.3), with 8 periods. It has been calculated through numerical solution of the coupled mode equations (red line) and is compared to the estimates obtained realizing a plain Fourier transform of the coupling coefficient (blue line), and realizing a plain Fourier transform of the coupling coefficient using the electrical position variable (green line).*

CHAPTER 4

TECHNIQUES TO IMPROVE THE PERFORMANCE OF PBG STRUCTURES IN MICROSTRIP TECHNOLOGY

The frequency response of a PBG structure in microstrip technology features a wide rejected band whose central frequency is fixed by the periodicity of the periodic perturbation. However, the frequency response of a conventional PBG device includes also characteristics that can be detrimental in many applications: an important ripple appears in the passbands placed to the left and to the right of the rejected band; sometimes a wider rejected bandwidth can be needed; for some applications the circuit area required to implement the PBG structure can be too large; and for other applications the periodicity present in the frequency response (rejected bands at the harmonics of the design frequency) can be troublesome. In this chapter several techniques that allow to surpass this potential problems are proposed and successfully tested, giving rise to improved PBG microstrip structures.

4.1. Introduction

As it has been seen in chapter 1, the first approach proposed to produce a PBG structure in microstrip technology consisted in drilling a periodic pattern of cylinders in the substrate of the microstrip line, to locate implants of different materials within them or to leave them filled by air [QIA 97]. However, later it was found that PBG structures with even deeper and wider stopbands could be simply achieved by etching a periodic pattern of circles in the ground plane along the microstrip line. This approach is simpler to fabricate, compatible with the monolithic technology, and permits the PBG structure to be easily integrated with other microstrip components in the upper plane. As a first approximation, a PBG microstrip structure with three rows of same-size and equidistant circles, one of them etched in the ground plane just below the upper-plane conductor strip and the two others at both sides of it, was proposed [RAD 98]. Due to its advantages, this structure was chosen as the starting point for the research of our group into PBG structures for microstrip lines. A photograph of the upper plane and of the ground plane of a prototype is presented in Fig. 4.1. It has been constructed using a numerical milling machine in a Rogers RT/Duroid 6010 substrate, with dielectric constant ε_r=10.2 and substrate thickness h=1.27 mm. The period of the PBG structure has a value a=14.1 mm, the radius of the circle to period ratio is r/a=0.25, and the number of periods employed is 9. The strip conductor width is constant, w=1.2 mm, corresponding to a nominal characteristic impedance of 50 Ω. The prototype is a scaled version of the one presented in [RAD 98] in order to be measured with our *HP* 8753D vector network analyzer (up to 6 GHz). Its measured S parameters are given in Fig. 4.2.

One of the first contributions of our group was to show that similar behaviors for this two dimensional hole distribution, and for a lonely central row of circles placed behind the conductor strip, are achieved [FAL 99]. The resulting one dimensional PBG microstrip structures are studied in section (4.2). Due to the high confinement of the fields around the conductor strip of the microstrip line, their frequency response is almost identical to that of their 2D counterparts, but the circuit layout area is more compact.

As it was seen in chapter 3, sections (3.2.1) and (3.3.1), the system of coupled mode equations that characterize a PBG structure in microstrip technology can be simplified, introducing several reasonable approximations, to a form that is identical to that obtained when a uniform Fiber Bragg Grating (FBG) or a uniform optical periodic dielectric waveguide is studied by using the coupled mode theory [PAS 96, YAR 97, YAR 84]. Moreover, an equivalence model has been proposed by our group between

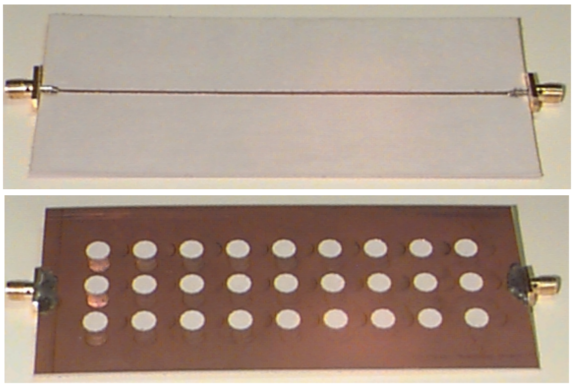

Figure 4.1: *Photograph of the upper plane and of the ground plane of a PBG microstrip prototype as it was originally proposed by Prof. Itoh at UCLA.*

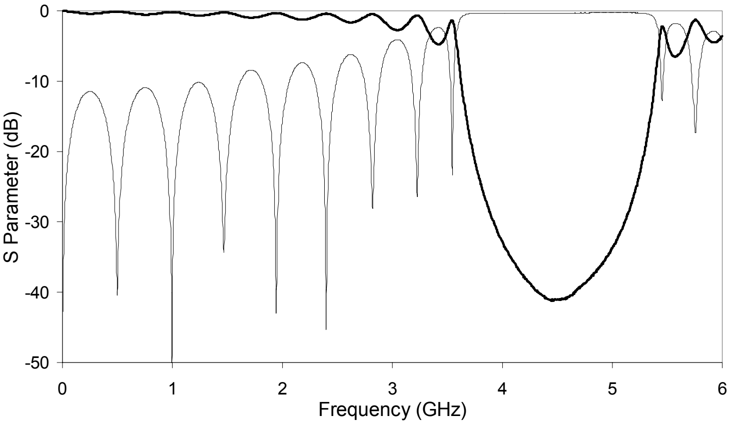

Figure 4.2: *Measured S_{11} (thin line) and S_{21} (thick line) parameters for the PBG microstrip prototype shown in the photographs of Fig. 4.1. It has been designed as originally proposed by Prof. Itoh at UCLA.*

the parameters of Fiber Bragg Gratings and PBG microstrip structures, in such a way that the equivalent pair of FBG and PBG microstrip circuit, feature the same frequency response, although centered at the corresponding operation frequency [LAS 99, ERR 00, ERR 02]. This facts suggest that a lot of ideas and techniques employed in the developed and mature field of Fiber Bragg Gratings could be easily and successfully translated to the novel and emerging field of PBG structures for microstrip lines.

One important problem of the frequency response of Fiber Bragg Gratings for filtering applications (rejection of a frequency band), is the presence of an important ripple (or from the reflection point of view sidelobes) in the pass band. The same problem arises in PBG microstrip structures (see Fig. 4.2). To surpass this difficulty, tapering techniques have been customarily employed in Fiber Bragg Gratings, achieving an important reduction in the ripple (and sidelobe) level [MIZ 93]. In section (4.3), it will be shown that a windowing function applied to the hole radii of a PBG microstrip structure, in such a way that the impedance mismatch diminishes towards the device endpoints, leads also to reduced ripple (sidelobes) levels in the passband, which may be critical in filtering applications [LOP 99a]. Different tapering functions will be systematically studied from the device performance point of view [ERR 00a].

In section (4.4), a non-equidistant hole-distribution in these PBG microstrip structures is considered. This is suggested by the linear change of the perturbation spatial frequency employed in the Linearly Chirped Fiber Bragg Gratings (LCFBGs) [HIL 97], achieving increased rejection bandwidths compared to the constant period structures [LAS 00]. Interesting design control over the group delay characteristic using these chirping techniques will be also shown later in chapter 5, section (5.6), where microstrip quadratic phase filters will be proposed for linearly chirped delaying, as in the case of LCFBGs, to perform real-time energy spectral density analysis and temporal processing of signals.

On the other hand, certain applications in microstrip technology, like high performance filters, require high rejection values in the stopbands and sharp cutoffs. However, to obtain them, it is necessary to include a large number of periods in the PBG microstrip structures. This has the drawback of resulting in circuits with large longitudinal dimension, which can certainly make unpractical their physical implementation. To solve this problem, a compact 2D hole-distribution for the PBG microstrip reflectors is proposed in section (4.5). As it can be seen in [RAD 98], the use of a single bend in the PBG microstrip device does not modify significantly its frequency behavior, which basically remains as for the straight PBG reflector. This bending feasibility leads to a 2D configuration in which the microstrip line presents multiple bends, following a similar structure as that of a meander line. The benefit of using this approach is that the PBG reflector has considerable length in a reasonable circuit area [FAL 99a]. The compactness results are very impressive but an additional periodicity (ripple) appears in the frequency response because the meander arrangement is a periodic structure itself. In section (4.5), several techniques are also employed to avoid this effect of unwanted ripple produced by the meander periodicity, which is added to the sidelobes due to the spatially limited PBG periodicity [LOP 00a]. These last ones, intrinsic to PBG devices, can be nearly eliminated through the tapering techniques commented above and studied in depth in section (4.3).

Until now, undesired frequencies in microstrip technology have been usually filtered using short-circuited stubs, one half-wavelength long, tuned at the frequency to be rejected. Alternatively, a chip capacitor placed to provide a transmission zero at the undesired frequency has been employed. These techniques have the drawback of being narrowband and of consuming valuable circuit layout area. PBG microstrip structures can be used to accomplish this filtering providing a broad rejected band. Furthermore, they can be easily integrated with other microstrip components in the upper plane to miniaturize the circuit configuration. However, in some designs, it is needed to eliminate more than one frequency. One interesting example is the tuning of the second and third harmonics in power amplifiers or oscillators [RAD 98a]. To perform this, various cascaded PBG microstrip structures, each one tuned at a different frequency, have to be used [RUM 98], enlarging the circuit longitudinal dimension. Furthermore, all the PBG microstrip structures described up to now with holes etched in the ground plane present a periodic frequency response. This fact can constitute a problem in some filtering applications. The replicas of the response at the harmonics of the design frequency can be eliminated whenever continuous patterns following a sinusoidal law, inspired by the continuous sinusoidal perturbation of FBGs, are employed [LOP 00b], as it will be seen in section (4.6). In the same way, compact multiple-frequency-tuned structures, based on superimposed PBGs, to perform simultaneously the rejection of all the undesired frequencies, can be achieved whenever a pattern that consists in the addition of multiple sine-functions, each one tuned at one of the frequencies to be rejected, is used [LAS 00a], as it will be further explained in section (4.6).

4.2. 1D PBG microstrip structures

The initial periodic patterns proposed to implement PBG structures for microstrip lines were two dimensional. Here we have focused our attention on the 2D pattern of Fig. 4.1. However, the operation of the resulting PBG microstrip circuit was 1D effective, since only the periodicity along the longitudinal dimension of the conductor strip was used. Moreover, due to the high confinement of the fields around the conductor strip of the microstrip line, the field levels outside the central row of circles of the periodic pattern will be very low. Finite Element three dimensional electromagnetic simulation of the PBG structure with two dimensional pattern confirms this fact, and reveals that field levels at the outer rows of the periodic pattern are negligible. This suggests that PBG microstrip structures consisting of only the central row of the pattern (1D) will have similar behaviour as a 2D structures. The advantage of a 1D implementation is a considerable reduction in the transverse size

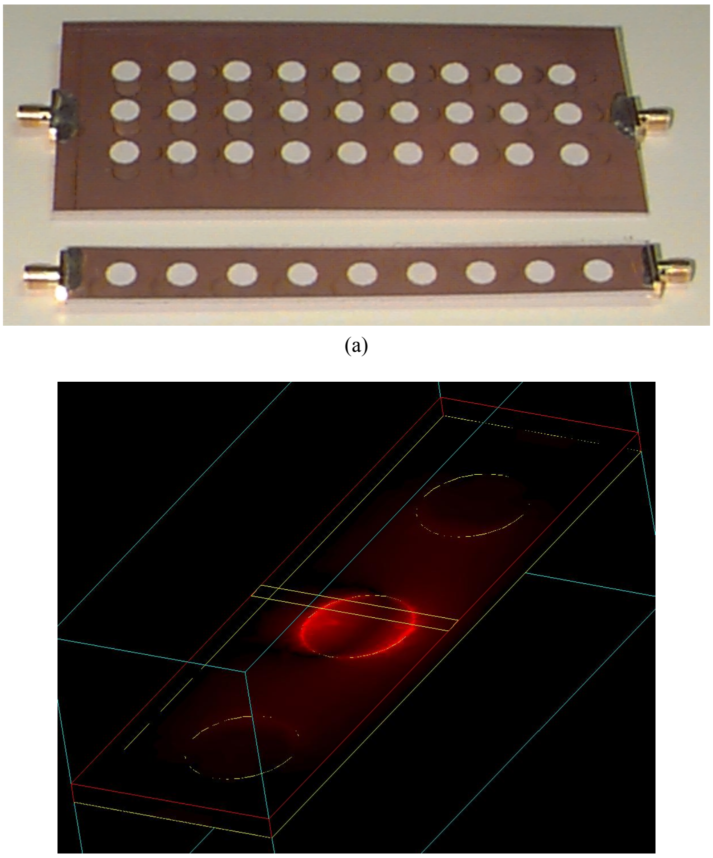
(a)

(b)

Figure 4.3: *2D and 1D PBG microstrip structure (a), and Finite Element simulation (b) of the electric field intensity in the 2D case confirming the negligible values in the outer rows of circles..*

of the reflector. To check the performance of the 1D PBG microstrip structures proposed, several prototypes have been fabricated using a numerical milling machine, and measured with an *HP* 8753D vector network analyzer. The S parameters obtained have been compared with those of their two dimensional counterparts, showing that the frequency response is virtually identical. In Fig. 4.3 a photograph of the 2D PBG microstrip structure presented in the previous section, and of its 1D counterpart is given. Both of them have the same design parameters (period of the PBG structure a=14.1 mm, radius of the circle to period ratio is r/a=0.25, and number of periods employed is 9), and have been implemented in the same substrate (Rogers RT/Duroid 6010, with dielectric constant ε_r=10.2 and substrate thickness h=1.27 mm). And both of them have almost identical frequency response (the one given in Fig. 4.2).

4.3. Tapered PBG microstrip structures

As it has been commented in section (4.1), one of the drawbacks of PBG structures in microstrip technology when employed in filtering applications is the significant ripple that appears in their pass-band (or from the reflection point of view the high sidelobe level of the frequency response). By using tapering techniques the ripple (and hence the sidelobe level) of the frequency response can be reduced in a noticeable way, as well as the rejected bandwidth is slightly increased. The tapering technique is applied modifying the radius of each circle according to its position in the structure, following a tapering function as in Fig. 4.4. The circle radii distribution will follow the next general expression:

$$r_i = r_{max} \cdot T(z_i) \tag{4.1}$$

being r_i the i-th circle radius, r_{max} the maximum circle radius that corresponds to the central one, $T(z)$ the tapering function, and z_i the distance between the i-th and the central circle. The improvement of the frequency response achieved through the application of a tapering function can be understood as a consequence of the progressive matching of the characteristic impedance of the Bloch wave towards the input and output characteristic impedances, that the tapering function produces.

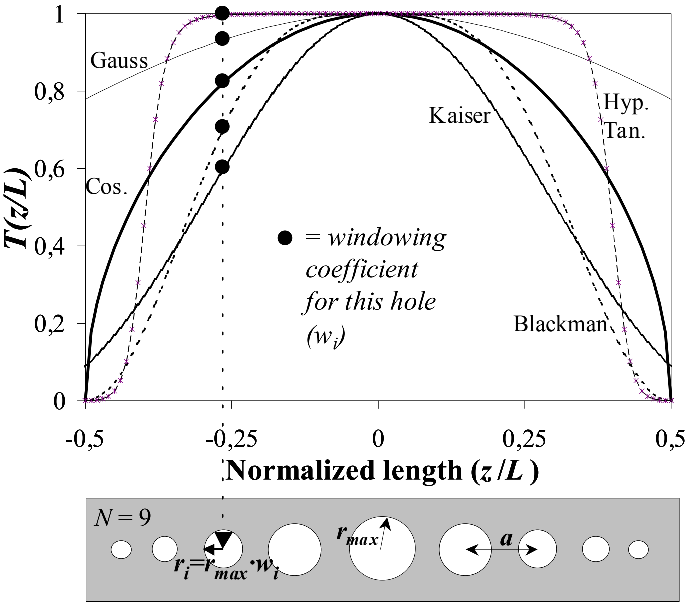

Figure 4.4: *Examples of windowing functions: Gauss, Cosine, Hyperbolic Tangent, Blackman, and Kaiser. The window name labels its corresponding profile.*

An example of tapered 1D and 2D PBG microstrip circuits can be seen in Fig. 4.5. Their design parameters are very similar to those employed in the previous sections. The substrate employed is a *Rogers RO3010*™, which is $h = 1.27$ mm-thick, and has a relative dielectric constant $\varepsilon_r = 10.2$. The conductor strip width on the upper plane is $w = 1.2$ mm, which corresponds to a characteristic impedance of 50 Ω in the conventional (unperturbed) microstrip line, and the period a is set to 14.1 mm to fix the central frequency of the rejected band at around 4 GHz through the Bragg condition of eqn. (3.70) of chapter 3:

$$f_{max} = \frac{c}{2 \cdot \sqrt{\varepsilon_{eff}} \cdot a} \tag{4.2}$$

where for the sake of simplicity ε_{eff} has been taken as the effective dielectric constant at 4 GHz of the unperturbed microstrip line (calculated using *Agilent Linecalc*™ or formulae in [YAM 79]).

For the prototypes of Fig. 4.5 a Hamming window (similar to a Blackman window with α fixed to –2) has been employed (but discarding the first and last samples), with a maximum radius to period ratio equal to r_{max}/a=0.3. Their S parameters have been measured with an *HP* 8753D vector network analyzer, obtaining again identical results for the 1D and the 2D prototypes. They are given in Fig. 4.6. As it can be seen, the ripple in the pass band (and hence the sidelobe level) is significantly reduced in the tapered microstrip structure. At the same time, the rejected bandwidth is slightly increased, but the rejection level achieved decreases when compared to the non-tapered PBG device (Fig. 4.1, Fig. 4.2).

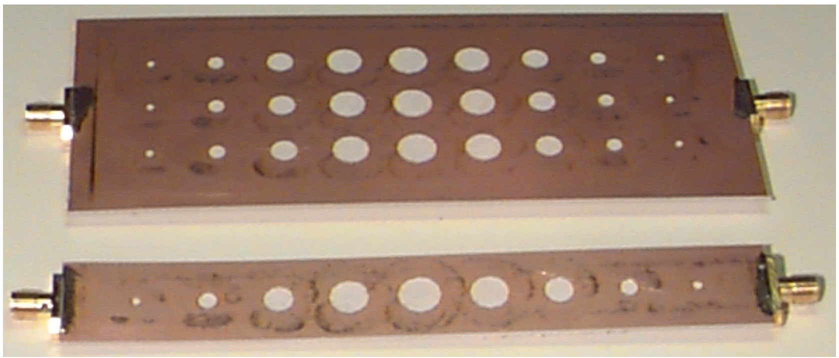

Figure 4.5: *Photograph of the ground plane of a two dimensional and a one dimensional tapered PBG microstrip structure.*

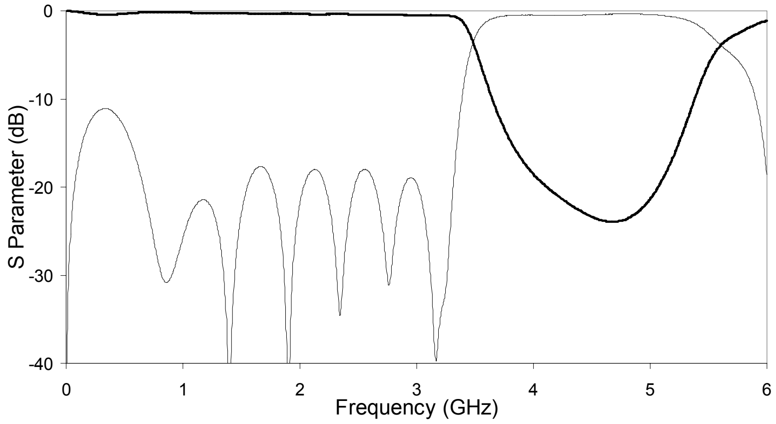

Figure 4.6: *Measured S_{11} (thin line) and S_{21} (thick line) parameters for the tapered PBG microstrip prototype shown in the photograph of Fig. 4.5.*

To continue our study, the frequency responses of several tapered PBG microstrip circuits with one row of holes etched in the ground plane below the upper conductor strip, will be analyzed, comparing different windowing functions and their effects on the rejection level, rejected bandwidth, sidelobe level and cutoff sharpness of the main stopband. Special attention is paid to optimize the sidelobe suppression ratio, which may be critical in some filtering applications, but without failing to attend the evolution of the rest of the frequency features.

The comparative study has been carried out for the Blackman, Cosine, Gauss, Hyperbolic Tangent, and Kaiser windows, because they are commonly used in optical diffraction gratings, and because of the extent of tapering profiles they comprise, as it can be seen in Fig. 4.4. These windowing functions, *T*, are analytically given in eqns. (4.3) to (4.7).

Blackman: $$T(z/L) = \frac{1+(1+\alpha)\cdot\cos\left(\frac{2\pi z}{L}\right)+\alpha\cdot\cos\left(\frac{4\pi z}{L}\right)}{2+2\alpha}, \text{with } \alpha = \text{-}0.2 \qquad (4.3)$$

Cosine: $$T(z/L) = \left(\cos\left(\pi\frac{z}{L}\right)\right)^{\alpha}, \text{with } \alpha = 0.5 \qquad (4.4)$$

Gauss: $$T(z/L) = \exp\left(-4\alpha\cdot\left(\frac{z}{L}\right)^2\right), \text{with } \alpha = 0.25 \qquad (4.5)$$

Hyperbolic Tangent: $$T(z/L) = 0.5\left(1+\tanh\left[4\cdot\left(1-2\cdot\left|2\frac{z}{L}\right|^{\alpha}\right)\right]\right), \text{with}\,\alpha = 3 \qquad (4.6)$$

Kaiser: $$T(z/L) = \frac{I_o(\alpha\sqrt{1-(2z/L)^2})}{I_o(\alpha)}, \text{with}\,\alpha = 4 \qquad (4.7)$$

In eqn. (4.6), *tanh* is the Hyperbolic Tangent function and, in eqn. (4.7), I_o is the first-class modified Bessel function. In eqns. (4.3) to (4.7), z/L is the normalized longitudinal position in the circuit, being L the device length and $z = 0$ its central point.

The frequency responses of the tapered PBG microstrip structures, all of them simulated using *Agilent Momentum and Advanced Design System*™ software, have been compared analyzing: the rejection level, defined as the minimum value of the $|S_{21}|$-parameter in the stopband; the 3-dB bandwidth of the stopband (viewed in $|S_{11}|$-parameter); the main lobe to sidelobe (MLSL) ratio, defined as the quotient between the maximum rejection values of the stopband and the first sideband (viewed in $|S_{11}|$-parameter); and the stopband cutoff sharpness (a kind of 'shape factor' of the frequency response), defined as the ratio between the 3-dB bandwidth (BW_{3dB}) and the bandwidth between the first zeroes (BW_{∞}) (viewed again in $|S_{11}|$-parameter). These four criteria seem to provide good insight into the circuit frequency behavior as it changes when the physical parameters are modified. When any ground plane etching is present, the available version 2001 of the simulation software package *Agilent Momentum* and *ADS*™ is not able to take properly into account conductor and dielectric losses yet. This causes the measured and conductor-and-dielectric lossless simulated results to differ slightly, mainly as frequency is higher.

Three different scenarios are going to be considered to account for the windowing effects: *case a*) the maximum hole radius in the structure is fixed and the number of periods is variable; *case b*) its reciprocal: the number of periods is fixed and the maximum hole-radius changes. A third situation (*case c*) is finally considered when the analysis is carried out sweeping N_{eq}, the equivalent number of periods. It is interesting to note that a similar concept (the effective length, L_{eff}) was already introduced in chapter 3, section (3.3.5), when theoretically studying ideally tapered PBG microstrip structures.

Case a) Fixed maximum hole radius and variable number of periods

When the ratio r_{max}/a, being r_{max} the largest hole radius, is set to 0.25 and the number of periods, N, varies, the resulting rejection level, bandwidth, MLSL value and stopband cutoff sharpness are shown in Fig. 4.7 for some of the windows of Fig. 4.4. (The device length, L, is always N times a).

As the number of periods in the structure increases, the wave interference at the Bragg frequency is reinforced and therefore the rejection level is increased with N, Fig. 4.7(*a*), for all windows. At the remaining frequencies the phase-matching condition for back-reflection is worse satisfied and hence the bandwidth is reduced, Fig. 4.7(*b*), and the stopband becomes steeper offering better selectivity, Fig. 4.7(*d*). The MLSL level changes slowly when the number of periods varies, in comparison with the same change when the tapering function varies, Fig. 4.7(*c*), because the MLSL level is strongly affected by the impedance mismatch at the boundaries of the structure, resulting in low finesse Fabry-Perot-type resonances. This way, the MLSL level primarily depends on the shape of each tapering function and less on the number of periods. In fact, as it was seen in chapter 3, section (3.5), the frequency behavior is intimately related to the Fourier Transform of the coupling coefficient, and hence to the windowing function in Fig. 4.4 between $z/L = -0.5$ and $z/L = 0.5$. This implies that smoother tapers (like the Cosine, Blackman or Kaiser), in contrast with other more square-like windows (like the Gauss or Hyperbolic Tangent), have a better MLSL ratio as well as this ratio is approximately independent of N. Therefore, the worst MLSL is always obtained when the non-tapered structure is chosen. The Hyperbolic Tangent window improves very slightly this value, whereas for the Cosine window an improvement of ~13 dB is achieved; the best MLSL values are given by the Kaiser window with a 25 dB-improvement with respect to the non-tapered structure. However, the bands are less steep for windows with better MLSL levels, and the rejection values smaller because as the window is smoother the wave interference is weaker at all frequencies. In the same way, it is also expected a wider bandwidth as the window is smoother, either from this reasoning or from the Fourier Transform of the tapering function. However, this is not apparent from Fig. 4.7(*b*), where less steep stopbands in the tapered cases partially mask the bandwidth increasing with respect to the non-tapered case. Perhaps, these spurious consequences coming along with greatly reinforced sidelobe suppression cause the filter to behave worse than expected in a specific application and, in general, a trade-off has always to be met between all frequency requirements. The concept of equivalent number of periods of the third scenario (case *c*) of this section will be then especially useful.

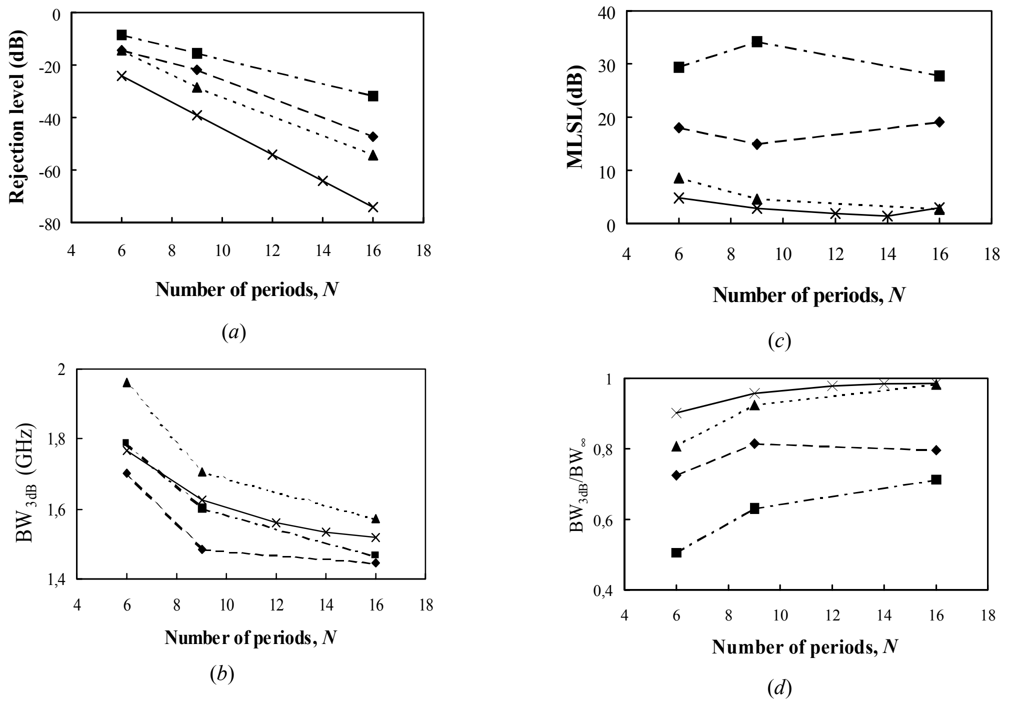

Figure 4.7: *Rejection level (a), bandwidth (b), main lobe to sidelobe ratio (c) and cutoff sharpness (d), as a function of the number of periods, N, when r_{max}/a = 0.25, for different windowing functions (see legend on the left). The Uniform-windowed case should be understood as the non-tapered case.*

Case b) Fixed number of periods and variable maximum hole-radius

In this case, the number of periods is fixed to N = 9 and the ratio r_{max}/a varies. An increasing r_{max}/a results in higher rejection level, 3 dB-bandwidth, and stopband cutoff sharpness, but in a decreasing MLSL value for all windows due to wave reinforcing at all frequencies. These trends can be observed in Fig. 4.8. Then, it is understandable that the non-tapered case gives, for all the r_{max}/a ratios, the maximum rejection level, Fig. 4.8(*a*), and the sharpest cutoff, Fig. 4.8(*d*), but also the worst MLSL level (worst impedance matching at the endpoints), Fig. 4.8(*c*). As explained in the first case or *case a*, tapering weakens the wave interference and broader bandwidths should be expected whenever the electrical parameter modulation is windowed. However, bandwidth broadening comes along with cutoff smoothing and, in Fig. 4.8(*b*), the curves are not apparently ordered from squared to more rounded windows and from narrower to broader bandwidth, respectively, just as neither occurs in Fig. 4.7(*b*) using the same reasoning. On the other hand, in Fig. 4.8(*a*), (*c*) and (*d*), as long as smoother windows are used, lower rejection level, higher MLSL value, and poorer cutoff sharpness, respectively, are obtained due to the wave weakening with respect to the non-tapered case. This way, lower rejection levels are achieved with the Gauss and Hyperbolic Tangent windows but improving the MLSL level only in a few dBs in the best case. The same MLSL level is attained approximately with the Blackman and Cosine windows for all the r_{max}/a ratios, but the rejection level of the Cosine taper is always better than that of the Blackman window. Moreover, with the Kaiser window the MLSL level is highly improved without a significant reduction in rejection level compared to the Blackman window. The Kaiser window allows using greater r_{max}/a ratios to obtain the same rejection level than a non-tapered structure, while keeping the sidelobes within lower values. For example, a device tapered with a Kaiser window with $N = 9$ and $r_{max}/a = 0.35$ offers a rejected level of ~-28.6 dB, similar to the rejection level (-25.9 dB) of a non-tapered device of 9 periods and $r_{max}/a = 0.2$, whilst significantly improving the MLSL value (~22 dB for the Kaiser window and ~4.5 dB for the non-tapered case). Besides, the bandwidth is broader (around 2.25 GHz compared to 1.25 GHz, approximately, for the non-tapered case), although the shape factor of the frequency response is worse.

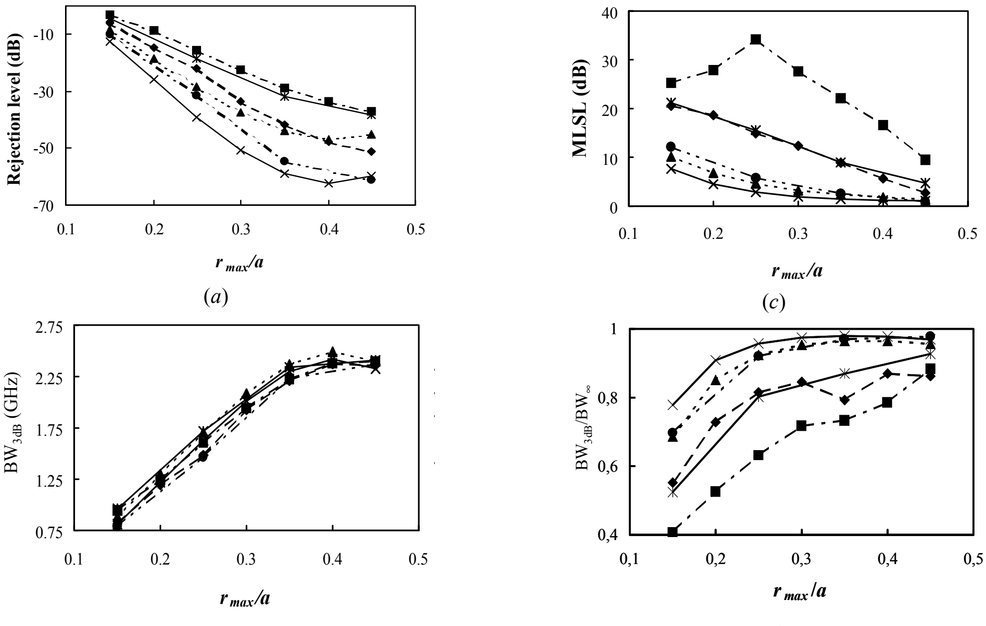

Figure 4.8: *Rejection level (a), bandwidth (b), main lobe to sidelobe ratio (c) and cutoff sharpness (d), as a function of r_{max}/a, when $N = 9$, for different windowing functions (see legend on the left). The uniform-windowed case should be understood as the non-tapered case.*

Case c) Comparison between windows with the same equivalent number of periods

As it can be inferred from both *cases a* and *b*, any change in either the hole radii or the device length affects all the parameters of interest of the frequency response, whichever the windowing function is being used. Then, it is not easy to arrive at a final conclusion on whether a change in the window, number of holes or maximum hole radius benefits or not the global frequency response without having in mind particular design objectives and very often, as it was said before, some trade-off has to be met between all of them. However, to facilitate the design of the PBG device to assure certain frequency characteristics as well as to make easier the comparison between different windowing functions, an equivalent number of periods, N_{eq}, is defined in eqn. (4.8) inspired in the equivalent length used in windowed optical diffraction gratings [PAS 96a], and introduced in chapter 3, section (3.3.5), when theoretically studying ideally tapered PBG microstrip structures.

$$N_{eq} = N \cdot \int_{-0.5}^{0.5} T(z/L)d(z/L) = N \cdot A_{eq} \tag{4.8}$$

where *T(z/L)* is the windowing function along the longitudinal *z*-axis, and A_{eq} represents the area under the tapering function. The values of A_{eq} for different windows are shown in Table 4.1.

Window	A_{eq}
Uniform (non-tapered case)	1
Gauss	0.92
Hyperbolic Tangent	0.79
Cosine	0.76
Blackman	0.63
Kaiser	0.61

Table 4.1: *Values of A_{eq} for different windowing functions.*

A PBG structure tapered with any of those windows registered in Table 4.1 or other ones, and with maximum hole-radius to period ratio r_{max}/a and N periods, will show approximately the same rejection level and bandwidth than a non-tapered structure with N_{eq} holes of the same size as the largest in the tapered structure. This can be verified in Fig. 4.9(*a*) and Fig. 4.9(*b*), where the rejection level and bandwidth, respectively, for non-tapered devices of different *r*/*a* ratios are shown with solid lines as functions of N_{eq} (that equals *N* in this case), along with the same parameters for all the windows (Blackman, Cosine, Hyperbolic Tangent, Gauss, and Kaiser) with the same r_{max}/a ratios and for different number of periods, plotted as isolated points. The 3 dB bandwidth of the tapered devices in Fig. 4.9(*b*), are slightly below those ones for their equivalent non-tapered structures because of less steep cutoffs using tapering. It is worth noting that N_{eq} may result in a non-integer number of periods and hence in an unreal equivalent non-tapered structure, but, nevertheless, it is a valuable parameter to be used in the design and comparison of windowed structures.

The MLSL level, Fig. 4.9(*c*), is always better for a tapered structure than for the non-tapered case, when they have the same equivalent number of periods and, consequently, the same rejection level and bandwidth. As counterpart, the tapered structure with reduced sidelobes has larger physical length than the non-tapered one

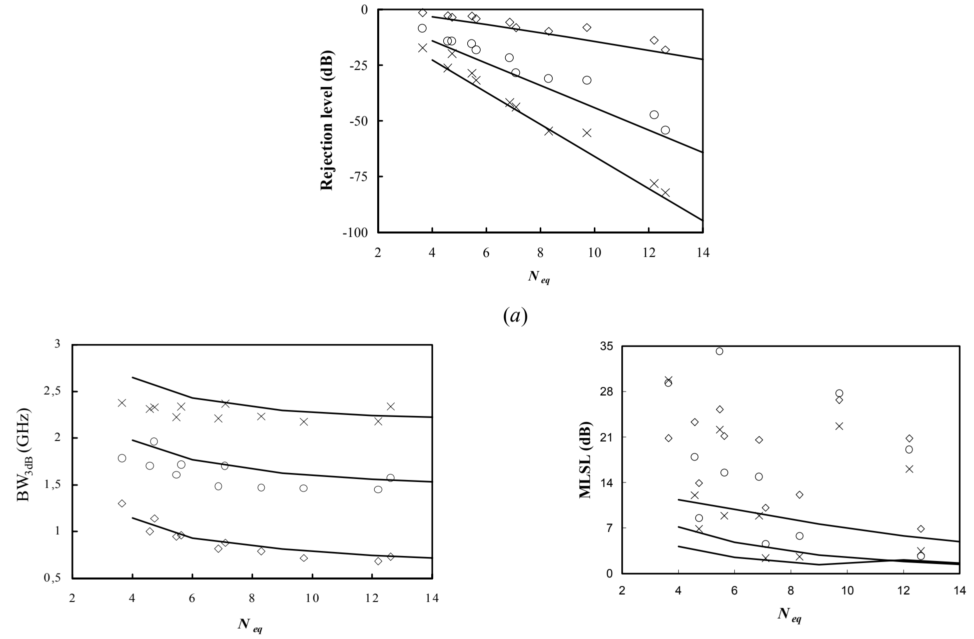

(*a*)

(*b*)

(*c*)

Legend:

— Non-tapered *r*/*a* = 0.15

◇ Tapered r_{max}/a = 0.15

— Non-tapered *r*/*a* = 0.25

○ Tapered r_{max}/a = 0.25

— Non-tapered *r*/*a* = 0.35

× Tapered r_{max}/a = 0.35

Figure. 4.9: *Rejection level (a), bandwidth (b) and main lobe to sidelobe ratio (c) as a function of the equivalent number of periods,* N_{eq} *, for* $r_{max}/a = 0.15$, $r_{max}/a = 0.25$ *and* $r_{max}/a = 0.35$, *with isolated points for different tapered cases and with solid lines* for *the non-tapered case (see legend on the left).*

since, for the tapered case, $N_{eq}<N$. The Cosine window offers the best compromise between length and MLSL value, while the Hyperbolic Tangent and Blackman windows are poorer because they need longer structures than the non-tapered and the Cosine-windowed cases, respectively, to offer similar MLSL values. The best MLSL value is always achieved with the Kaiser window, but it needs structures $1/A_{eq} = 1.6$ times longer than the non-tapered ones to obtain the same rejection level and bandwidth. At the opposite side, the Gauss window is only 1.09 times longer but improves the MLSL value in a limited way.

Observing Fig. 4.9(*c*), perturbation depth and length seem to be inversely proportional one another for a fixed MLSL level, consistent with the known behavior of FBGs.

In view of Fig. 4.7 to Fig. 4.9, some general conclusions can be drawn out on tapering techniques for PBG structures in microstrip technology. For a given window, for example, to achieve a better rejection level and a sharper band the number of periods, N, or the ratio r_{max}/a has to be increased, while to obtain a broader bandwidth one can reduce N or increase r_{max}/a. The MLSL level for each window does not depend on N and decreases when the r_{max}/a ratio increases. On the other hand, for the same number of periods, N, and r_{max}/a ratio, improving the rejection level or cutoff sharpness implies to choose a window with a higher A_{eq} (more square-like), and increasing the bandwidth or the MLSL level implies the opposite. Finally, to obtain a device with the same rejection level and bandwidth as a non-tapered structure but with lower sidelobes, a tapered device with N/A_{eq} periods is needed, being N the number of periods for the non-tapered case and A_{eq} the corresponding area under the windowing function of Table 4.1. The tapered structure has to be $1/A_{eq}$ times longer and, in general, its reflected band has smoother edges, depending on the windowing function. However, edges can be made sharper either by increasing a bit more the number of holes, making at the same time the bandwidth a bit narrower, or by enlarging the holes and, hence, decreasing a little the MLSL level.

4.4. Chirped PBG microstrip structures

The well known chirping techniques developed for Fiber Bragg Gratings [HIL 97], find also an application in this section originating PBG microstrip structures with a ground plane etched with linearly distributed holes making wider the rejected bandwidth to perform, for instance, broadband filtering of undesired frequencies, overcoming the narrowband techniques commonly used until now. Such a kind of devices tuned at a spatially varying frequency, could be also conceived to carry out some interesting phase filtering, for example, to reorder linearly in time the frequency components of an input signal. This linearly chirped delaying is similar to that of Linearly Chirped Fiber Bragg Gratings (LCFBGs) and will be studied in chapter 5, section (5.6) for PBG microstrip devices with continuous patterns to perform real-time energy spectral density analysis.

Chirping 1-D PBG microstrip structures with a row of holes etched in the ground plane will produce a device in which the distance between the centers of adjacent holes (period *a*) is not constant, but follows a linear function with the position in the structure. Figure 4.10 displays a geometrical comparison between chirped (on the right) and non-chirped (on the left) devices. The structure period, a_k, is given by eqn. (4.9) as a function of its position in the device:

$$a_k = a_0 \cdot \left(1 - k \cdot C \cdot \frac{a_0}{\pi}\right) \tag{4.9}$$

being a_0 the period corresponding to the central hole of the structure, *C* the chirp parameter, and $k = 0, \pm 1, \pm 2, \ldots$

The rate of the slowly varying periodicity is fixed by *C* (m^{-2}).

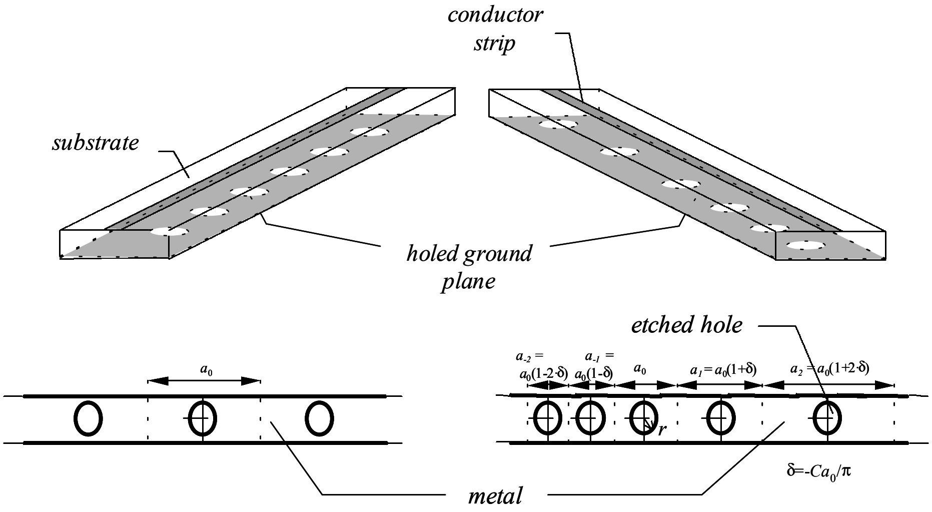

Figure 4.10: *Chirped (right), and non-chirped (left) 1-D PBG microstrip structure*

The central frequency of the rejected band for a non-chirped PBG microstrip structure is determined by the period of the structure through the Bragg condition of eqn. (4.2). To have a design central frequency, f_d, of 2.5 GHz, this period is calculated and results in 23.9 mm for the *Rogers RO3010*™ substrate $h = 1.27$ mm-thick with

$\varepsilon_r = 10.2$ and a conductor strip width of $w = 1.2$ mm (corresponding to a characteristic impedance of $Z_0 = 50\ \Omega$ for a conventional microstrip line). This low-design frequency has been chosen in order to measure the device response with our vector network analyzer, up to 6 GHz, being able to capture also the bandwidth increasing. Chirping techniques will be applied in such a way that only the central period will correspond to the central frequency and will have the calculated value $a_0 = 23.9$ mm (a_k will then take higher or lower values than a_0, depending on its position with respect to a_0 in Fig. 4.10).

As it is well known from the studies realized previously in FBGs [HIL 97], these chirping techniques, while increasing the rejected bandwidth, introduce a growing ripple in the rejected band. In chirped structures, there exists a position dependence of

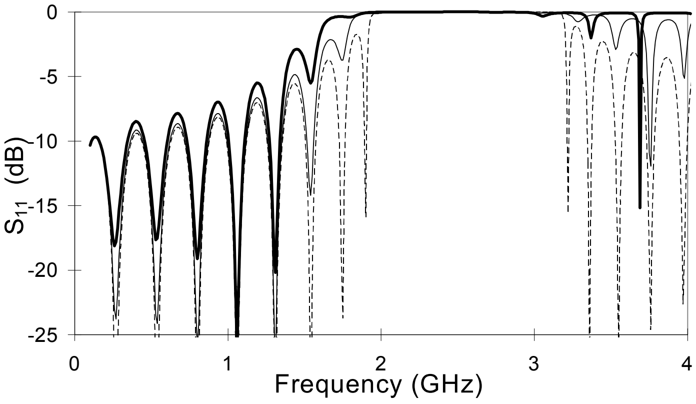

(*a*)

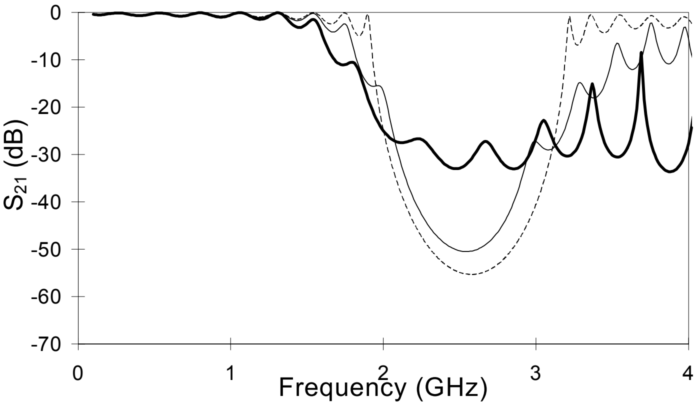

(*b*)

Figure 4.11: *Simulated (a) $|S_{11}|$- and (b) $|S_{21}|$-parameters for: the non-chirped 1-D PBG microstrip structure (dashed line); the chirped 1-D PBG microstrip structure with* C = *–5.5 (thin solid line); and the chirped 1-D PBG microstrip structure with* C = *–11 (thick solid line).*

the resonance frequency, like in eqn. (4.9). Thus, as a pulse propagates through the device, each frequency is reflected back to the input only in a narrow segment within the structure. This could create new different long-path Fabry-Perot-type resonances between that position and the mismatched boundaries of the circuit. This drawback can be surmounted using tapering techniques as those in section (4.3) to achieve wide but smooth rejected bands, simultaneously, with flat passbands at both sides. Then, chirped and tapered PBG microstrip devices will have a varying periodicity following eqn. (4.9) and a varying circle radius distribution following a windowing function.

Firstly, three different non-tapered structures with $N = 9$ circles and a radius, r, given by a r/a_0 ratio of 0.25 are analyzed. The first structure has $C = 0$, which corresponds to a conventional PBG microstrip reflector of constant period a_0. The second one has

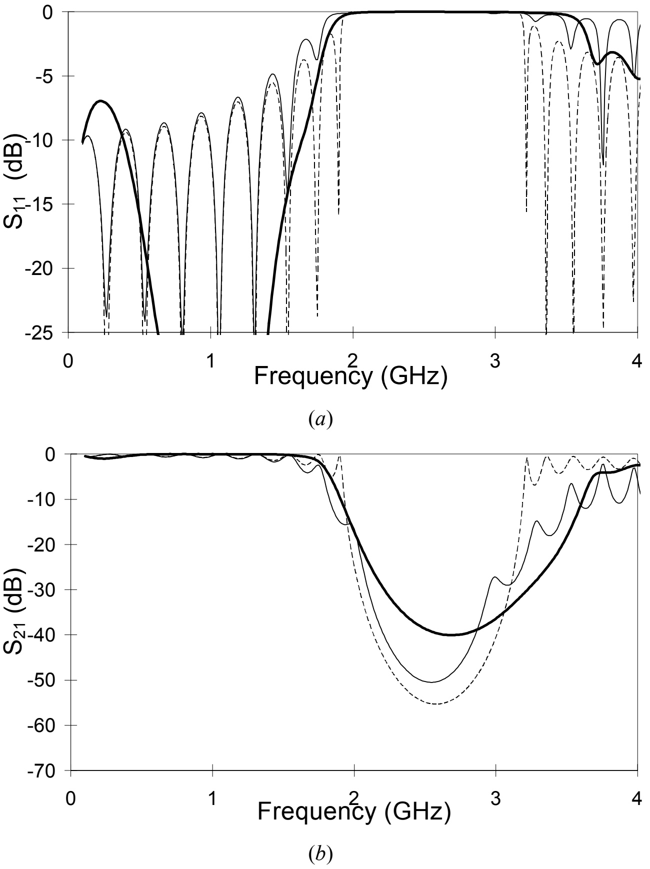

Figure 4.12: *Simulated (*a*) $|S_{11}|$- and (*b*) $|S_{21}|$-parameters for: the non-chirped 1-D PBG microstrip structure (dashed line); the chirped 1-D PBG microstrip structure with* C = *–5.5 (thin solid line); and the tapered and chirped 1-D PBG microstrip structure with* C = *–5.5 (thick solid line).*

been designed using a chirp parameter $C = -5.5$, while the third one has $C = -11$. Preliminary full-wave electromagnetic simulations are performed for all the microstrip circuits. The $|S_{11}|$-parameters for the three structures are depicted in Fig. 4.11(*a*).

Note in Fig. 4.11(*a*) the increasing bandwidth of the rejected band at the design frequency, f_d, as the chirp coefficient is bigger, comparing the non-chirped structure in dashed line with the chirped ones using $C = -5.5$ in thin solid line, and $C = -11$ in thick solid line. This broader bandwidth for the chirped structures can be also seen in Fig. 4.11(*b*) from the $|S_{21}|$-parameter point of view. It must be also noted that a growing ripple appears in the response, together with a reduction in the rejection level (due to a weaker wave interference at the central frequency because of chirping and, hence, because of the spatially-varying frequency-tuning of the structure), as the chirp parameter is increased. To further continuing with this comparison, a chirped and tapered PBG microstrip device with chirp parameter $C = -5.5$, $N = 9$ holes, and a Gaussian windowing function, eqn. (4.5), with $\alpha = 0.5$, has been also simulated. To compensate for the reduction in the rejection level due to chirping and tapering, the r_{max}/a_0 ratio has been increased to 0.4 in this case. Its performance, in thick solid line, is compared in Fig. 4.12(*a*) and (*b*), in $|S_{11}|$- and $|S_{21}|$-parameters respectively, with the conventional (non-chirped and non-tapered), in dashed line, and the chirped but non-tapered, in thin solid line, devices presented above. An impressive smoothing effect can be observed in the frequency response of the tapered device, compared to the chirped but non-tapered one, obtaining a very promising wide and non-rippled rejected band with flat passbands at both sides.

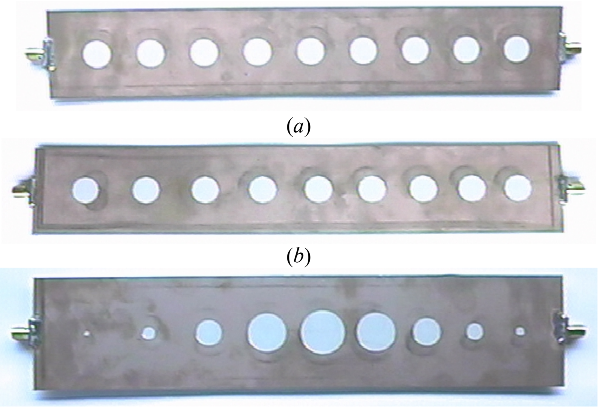
(*a*)

(*b*)

(*c*)

Figure 4.13: *Photographs of the fabricated prototypes: (a) non-chirped 1-D PBG microstrip structure; (b) chirped 1-D PBG microstrip structure with C = –5.5; and (c) tapered and chirped 1-D PBG microstrip structure with C = -5.5.*

The last three prototypes of Fig. 4.12 have been fabricated using a *LPKF Protomat 93s*™ numerical milling machine (see photographs in Fig. 4.13). For the measurements of the devices a *HP 8753-D*™ Vector Network Analyzer is used. The *Rogers RO3010*™ substrate has loss tangent $\tan\delta = 0.0026$, metal conductivity $\sigma = 5.8 \cdot 10^7$ S · m^{-1}, and metal thickness $t = 35\,\mu$m.

In Fig. 4.14(*a*) and (*b*) the measured $|S_{11}|$- and $|S_{21}|$-parameters, respectively, are depicted for the non-tapered and non-chirped structure, in dashed line, and for the chirped structures (tapered, thick solid line, and non-tapered, thin solid line) with C = –5.5. Good agreement is found between the measurements and the full-wave (conductor-and-dielectric lossless) simulated data of Fig. 4.12.

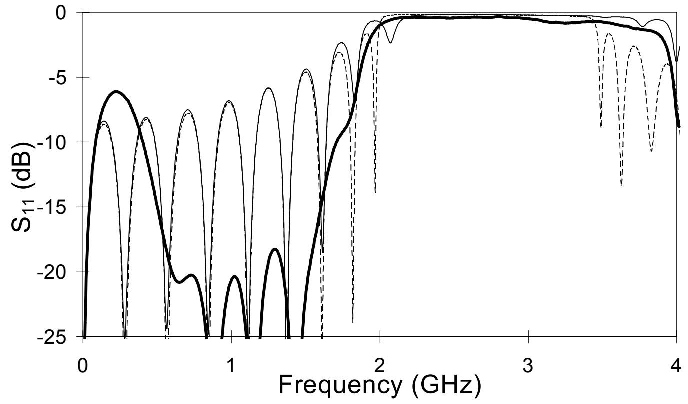

(*a*)

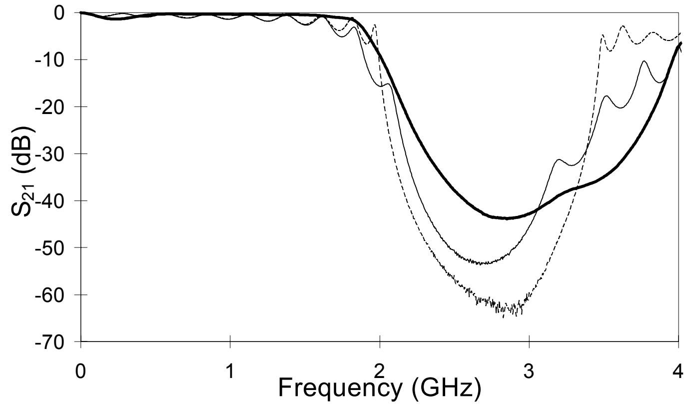

(*b*)

Figure 4.14: *Measured (a)* $|S_{11}|$ *- and (b)* $|S_{21}|$ *-parameters for: the non-chirped 1-D PBG microstrip structure (dashed line); the chirped 1-D PBG microstrip structure with* C *= –5.5 (thin solid line); and the tapered and chirped 1-D PBG microstrip structure with* C *= –5.5 (thick solid line).*

In particular, the measurements also show the increased bandwidth in the chirped structures compared to the non-chirped circuit, and the rejection level reduction experimented in the rejected band due to chirping. Note also the ripple that arises in the chirped but non-tapered device and the impressive smoothing effect achieved by windowing the electrical parameter modulation.

4.5. Compact PBG microstrip structures

As the number of periods in a 1D PBG microstrip reflector is increased, higher rejection values and sharper cutoffs in the stopband were shown in section (4.3) to be achieved. Whenever a high performance rejected-band filter is needed, a PBG microstrip reflector seems to be a good choice. However, the required number of periods could be quite large in order to obtain these frequency characteristics, making unpractical the physical implementation of the device. In this section, more compact structures are proposed using extensively the bending feasibility of PBG microstrip reflectors [RAD 98], this way allowing a large number of periods in a reasonable circuit layout area. A PBG microstrip reflector using a meander-like topology leads to a doubly periodic structure: a periodic pattern of holes etched in the ground plane (the PBG structure), and the meander arrangement itself that also introduces a new source of frequency ripple. In this section, different methods to reduce the undesirable frequency ripple originated by the new periodicity introduced by meandering the circuit are proposed too (this ripple is added to the sidelobes due to the spatially-limited PBG periodicity, which are nearly avoidable using the tapering techniques of section (4.3)). One method consists in chamfering the corners of the upper conductor strip to achieve better-matched bends. This matching weakens the effect of the meander periodic structure, and tends to flatten the passbands. Tuning the bent segments by lengthening introduces a phase factor and shifts the ripple peaks (i.e., the stopbands of the new periodicity) to a more optimal position depending on the application. A third method researches into different meander layouts to find arrangements that provide flatter passbands in the global response near the rejected frequency band, although they require the use of more bends, giving rise to slightly higher losses and more rectangular (less compact) circuits.

In this section, the PBG microstrip reflectors are implemented by etching circles in the ground plane. However, these compacting techniques could be also applied on PBG microstrip devices with continuous patterns, and even on microstrip lines with varying strip width. The separation between the centers of neighboring circles defines the period, *a*, of the structure, and, therefore, through the Bragg condition of eqn. (4.2), the central frequency of the rejected band for a given substrate. For the typical *Rogers RO3010™* substrate 1.27 mm-thick with relative dielectric constant $\varepsilon_r = 10.2$, the spatial periodicity is set to $a = 15.5\,\text{mm}$ to have the design frequency centered around 3.9 GHz, being $w = 1.2\,\text{mm}$ the conductor strip width for 50Ω-input and output ports. Before etching the periodic pattern, it is necessary to define the topology of the meander PBG device. There are several ways to insert bends in the conductor strip, depending on the separation between contiguous lines. Since there exists a high confinement of the fields around the conductor strip, the distance between contiguous lines is chosen as the minimum amount necessary to preserve the spatial periodicity, *a*, in the bent segments of the structure, obtaining in this way a very compact arrangement, as that in Fig. 4.15. It is apparent from this figure the existence of a double periodicity. On the one hand, it can be seen the periodicity already present in straight PBG structures with equally spaced holes (with period *a*), and, on the other hand, the meander arrangement constitutes another periodic structure itself (with period 5*a*, in this example).

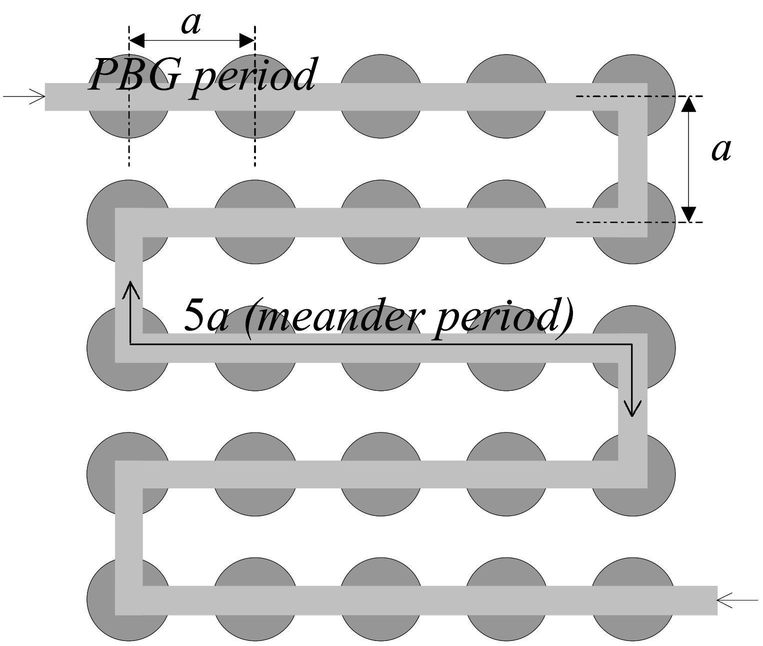

Figure 4.15: *Schematic representation of the proposed compact PBG microstrip structure. The periodic pattern of circles is etched in the ground plane of the microstrip line. In the top plane, the strip conductor follows a meander-type trace*

Firstly, two prototypes have been designed: a conventional (straight) PBG reflector with $N = 25$ periods and a radius to period ratio, r/a=0.25, and a compact (meandered) PBG reflector with the same hole-size, r, period a, and a 5×5 hole-distribution as that depicted in Fig. 4.15. The simulated $|S_{21}|$-parameters for the straight and compact PBG microstrip devices are compared in Fig. 4.16. The results reveal that the meander PBG circuit behaves (from the point of view of rejection level, bandwidth, and cutoff sharpness in the stopband) in a similar way as the conventional (straight) PBG microstrip reflector with the same parameter set (period, a, radius, r, and number of periods, N), solid and dotted line respectively, but its physical dimensions are considerably more reasonable. The most relevant differences between both responses are the narrow stopbands periodically registered in the compact case.

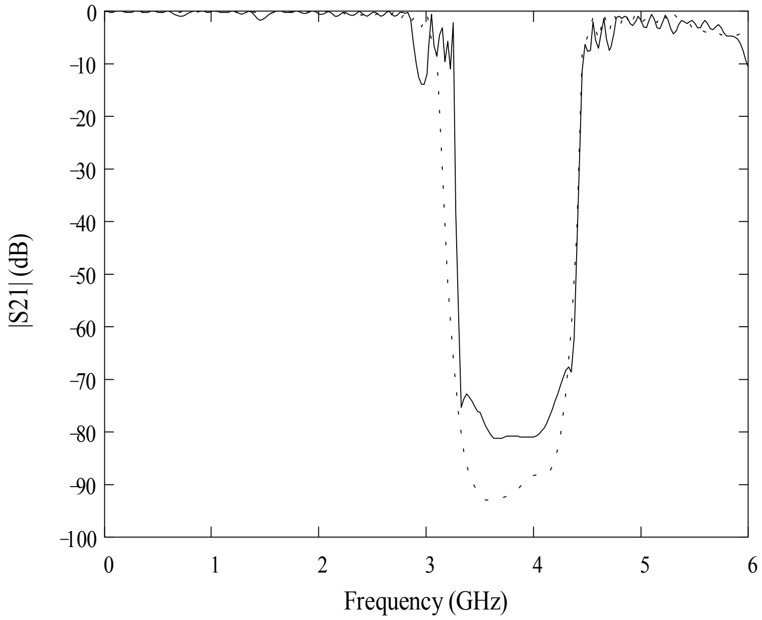

Figure 4.16: *Simulated $|S_{21}|$-parameters for the compact PBG microstrip reflector (solid line) and for the conventional (straight) PBG microstrip reflector (dotted line), both designed with the same parameters (structure period a = 15.5 mm, hole-radius to period ratio r/a = 0.25, and number of periods N = 25 (5×5)).*

As it can be seen in Fig. 4.17, these spurious stopbands are due to the periodic meander arrangement itself: the solid line is again the compact PBG reflector response, and the dotted line is the behavior of its associated conductor strip on its own with a non-holed ground plane.

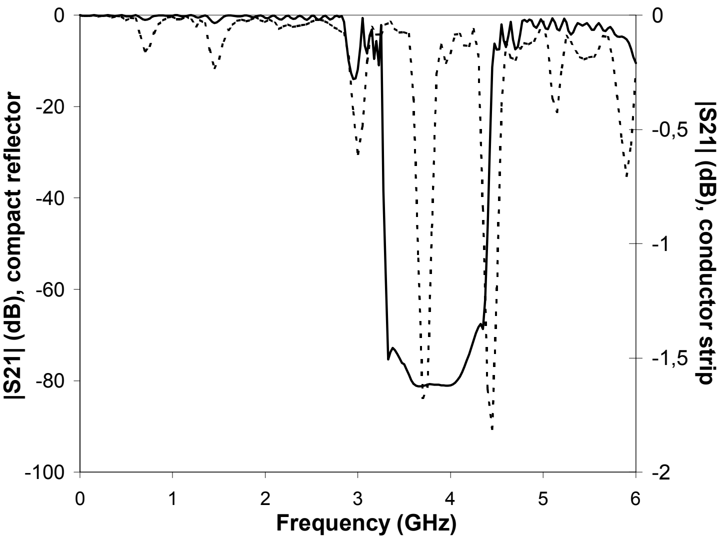

Figure 4.17: *Simulated* $|S_{21}|$ *-parameters for the compact PBG microstrip reflector (solid line) and for its associated conductor strip on its own with a non-holed ground plane (dotted line). The design parameters are: structure period a = 15.5 mm, hole-radius to period ratio r/a = 0.25 and number of periods N =5×5.*

The compact PBG prototype has been constructed and measured. See Fig. 4.18 for photographs of both its upper plane strip arrangement and its etched ground plane showing the 5×5 hole-distribution. The measurement is depicted in Fig. 4.19 in $|S_{11}|$-and $|S_{21}|$-parameters. A good agreement is obtained between the measurement and the (conductor-and-dielectric lossless) simulation in Fig. 4.16 or Fig. 4.17.

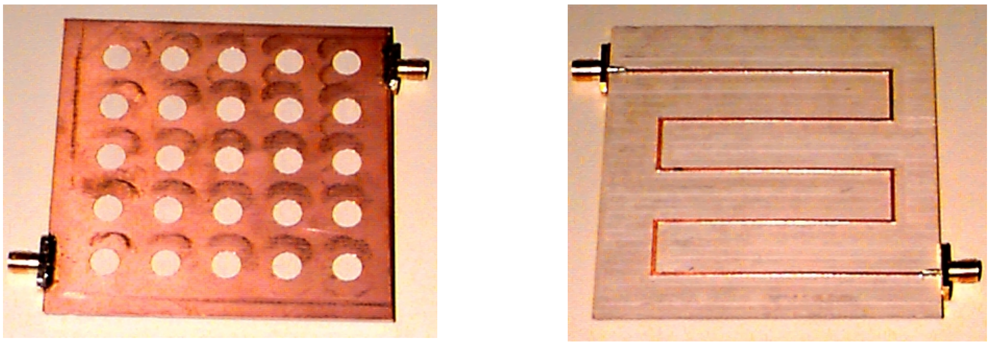
(*a*) (*b*)

Figure 4.18: *Photograph of the compact PBG microstrip reflector prototype;(a) ground plane and (b) upper plane.*

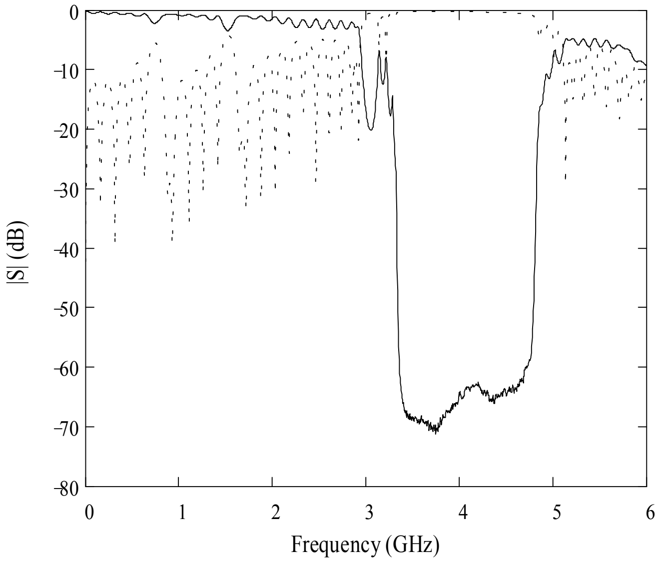

Figure 4.19: *Measured* $|S_{21}|$ *-parameter (solid line) and* $|S_{11}|$ *-parameter (dotted line) for the compact PBG microstrip reflector prototype of Fig. 4.18.*

Regarding the radiation and scattering losses that are expected to appear in a meander configuration, the simulations performed, Fig. 4.20, reveal that they are increased with respect to the values obtained for the straight PBG reflector case, but still maintained within low levels.

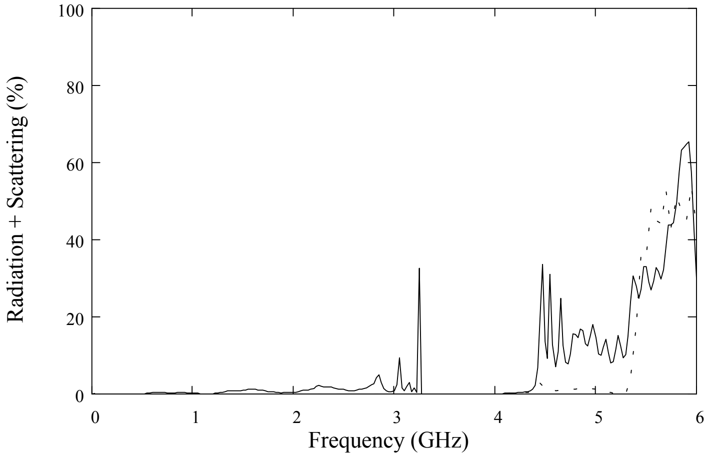

Figure 4.20: *Simulated scattering and radiation losses (in percent) for the compact PBG microstrip reflector (solid line) and for the conventional (straight) PBG microstrip reflector (dotted line).*

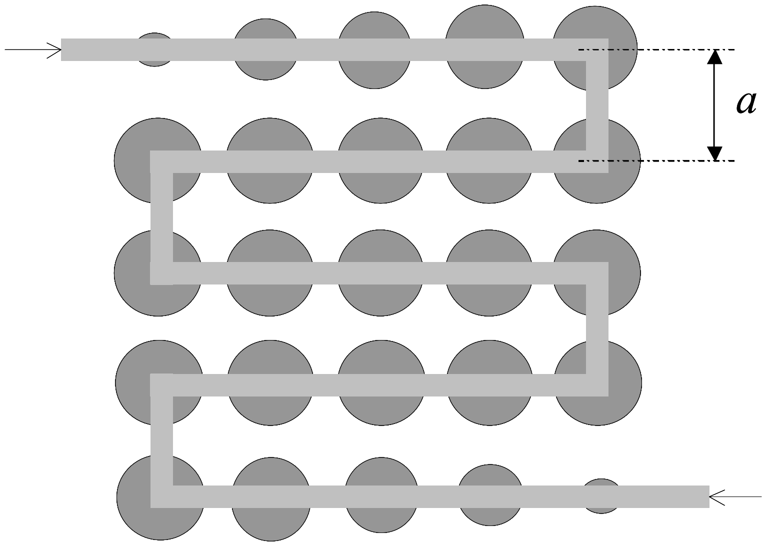

Figure 4.21: *Schematic representation of the compact PBG microstrip with tapered input and output holes.*

Tapering the hole-radii as in section (4.3), see Fig. 4.21, the sidelobes due to the spatially-limited PBG periodicity are nearly eliminated helping to achieve very well flattened passbands, and the attention can be focused on ways to eliminate the ripple due to the meander periodicity. This ripple could be detrimental for some applications of the PBG reflectors, specially the peaks placed near the rejected band, as it will be seen in the example of bandpass filter that will be given in chapter 5, section (5.4). A Hamming window, similar to a Blackman window with α fixed to –2 in eqn. (4.3), is applied to the five first (device input) and the five last (device output) circles (due to the length of the reflector, there is no need to taper the whole structure, but only its input and output).

Chamfered bends could be employed at the corners of the upper strip with a 50 per cent mitering to achieve better matched bends and, moreover, lower losses due to scattering and radiation effects than for the non-chamfered bends [EDW 92], [GAR 94]. Matching weakens the effect of the meander periodic structure, and tends to flatten the passbands. PBG microstrip meander reflectors with optimally chamfered bends [GUP 96] have been also studied arriving at not much better results from the matching or power loss points of view. In Fig. 4.22, the simulated transmission responses for the conductor strip configurations on their own (non-holed ground plane) without chamfering (0% mitering), thick solid line, with 50% mitering, dotted line, and with optimal mitering, thin solid line, show that mitered bends achieve better-matched behaviors. All of them are assumed to have the layout associated with a 5×5 meander PBG reflector as in Fig. 4.21. Optimally chamfered bends have a chamfering factor [GUP 96], *M*, defined by eqn. (4.10):

$$M(\%) = 52 + 65 \cdot \exp(-1.35 \cdot w/h) \tag{4.10}$$

so M = 70.15 % in this case. In Fig. 4.23, the power losses due to scattering and radiation for PBG meander reflectors with windowed hole-radii and without chamfered bends, thick solid line, 50%-mitered bends, dotted line, and 70.15%-mitered bends, thin solid line, all of them simulated using the described 5×5 topology, are shown.

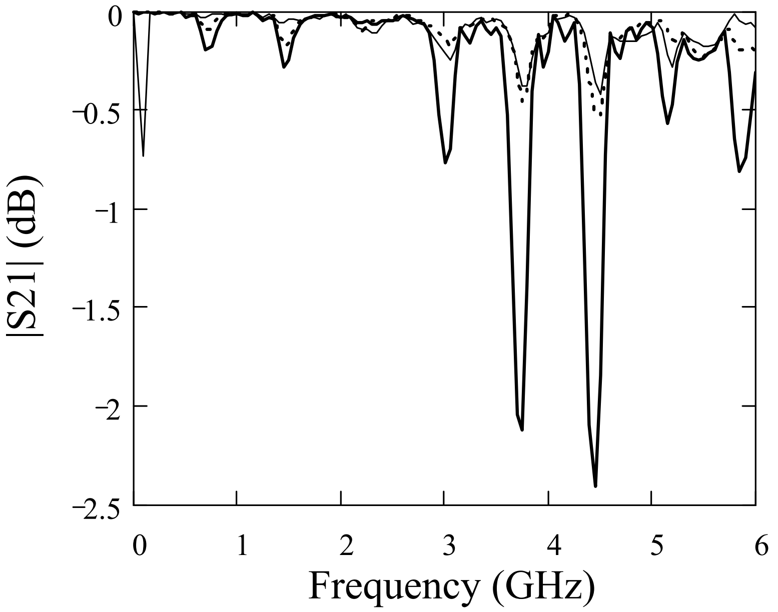

Figure 4.22: *Simulated transmission responses for conductor strip configurations without ground plane etching and with non-chamfered bends (thick solid line), 50%-mitered bends (dotted line), or 70.15%-mitered bends (thin solid line). All of them are assumed to have the layout that would be associated to a 5×5 meander PBG reflector.*

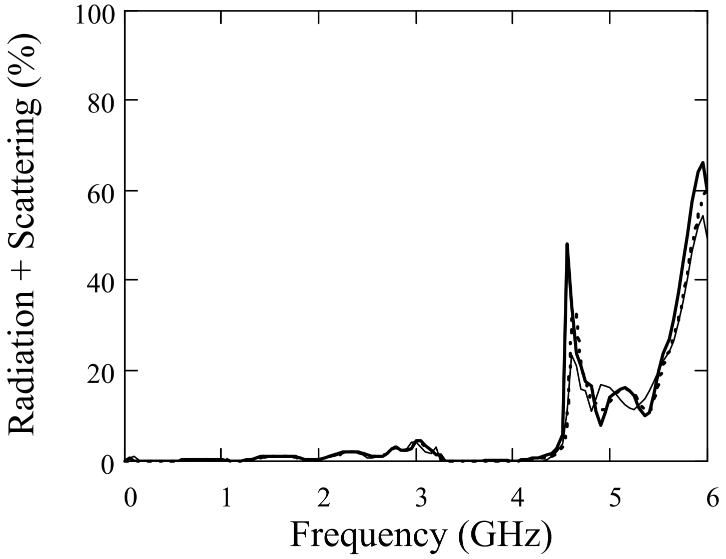

Figure 4.23: *Simulated power losses (in percent) due to radiation and scattering in 5×5 PBG microstrip meander reflectors with Hamming-windowed input and output, varying the chamfering factor of the bends: non-chamfered bends (thick solid line); 50%-mitered bends (dotted line); and 70.15%-mitered bends (thin solid line).*

As it can be seen in Fig. 4.22 and Fig. 4.23, the mitering is desired for better matching and less power losses but the amount of chamfering is not of great relevance. Moreover, any specific mitering amount to be implemented in the circuits is not a realistic situation in our case because of the tolerance in the fabrication process using a numerical milling machine, and a general 50%-mitering will be always considered in these compact PBG reflectors.

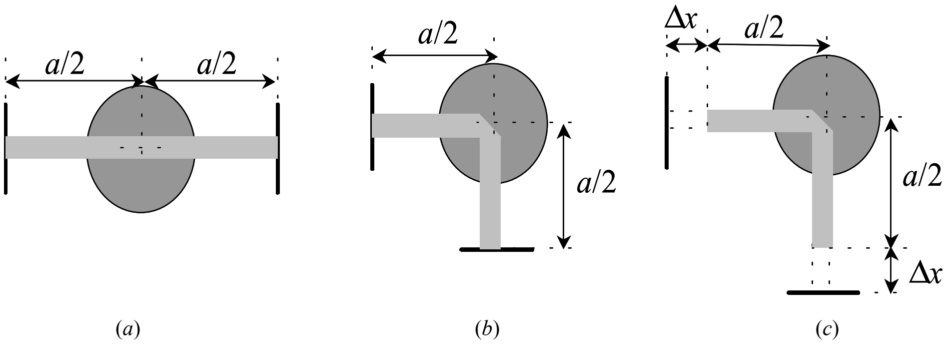

Figure 4.24: *Straight unitary period (a); bent unitary period (b). Demonstration of bend tuning through lengthening (c). a is the PBG periodicity.*

Once tapering and mitering are employed to smooth the influence of the sidelobes due to the PBG periodicity and the ripple due to the meander periodic structure, respectively, two more methods can be used to further combating the last one. The first solution consists in tuning the phase-shift in the bends by lengthening, which permits to move away the ripple to a more convenient frequency position. It seems plausible to choose a lengthening, Δx , like in Fig. 4.24(*c*), so that the phase behavior of a straight unitary period, Fig. 4.24(*a*), approximates that of a bent one, Fig. 4.24(*b*). This way, bend tuning would also create a shift in the central frequency of the rejected band, now closer to that of the straight PBG reflector. Due to the existence of the bend, the phase sign inversion between the input and output waves in the unitary period takes place at a different frequency as can be seen in Fig. 4.25. The length of the stretch, Δx , is calculated to obtain the same S_{21} phase in the bent and straight segments, resulting in $\Delta x = 0.4\text{ mm}$ for this case.

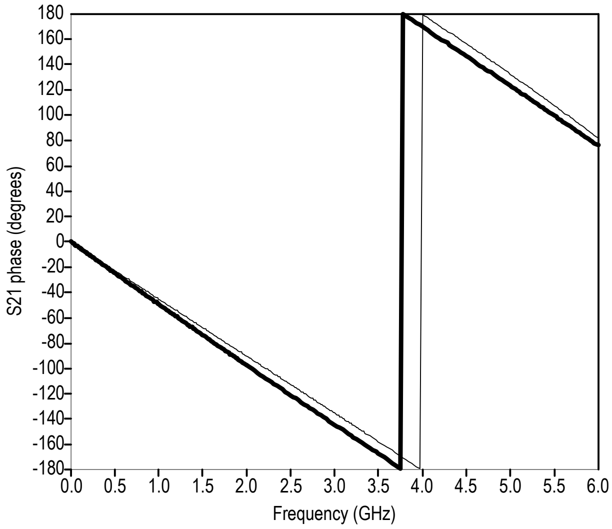

Figure 4.25: *Comparison between the simulated phase shift (in degrees) in the output wave respect to the input wave in a bent unitary period (thin solid line) and in a straight unitary period (thick solid line).*

In Fig. 4.26, the measured $|S_{21}|$-parameter of a 5×5 meander PBG reflector (see photograph in Fig. 4.27) is shown in two different situations: using tuned bends, solid line, and without tuned bends, dotted line. The meander PBG reflector with tuned bends has a frequency response with an attenuation in the peak present next to the lowest cutoff frequency of the rejected band, reduced in more than 4 dB in comparison with that appearing in the non-tuned case. On the other hand, in frequencies near the highest cutoff frequency of the rejected band the ripple increases. On the contrary, the meander PBG reflector without tuned bends shows a much better response in frequencies near the highest cutoff frequency of the rejected band than the meander reflector with tuned bends. However, as it has been already pointed out, its response at lower frequencies is worse.

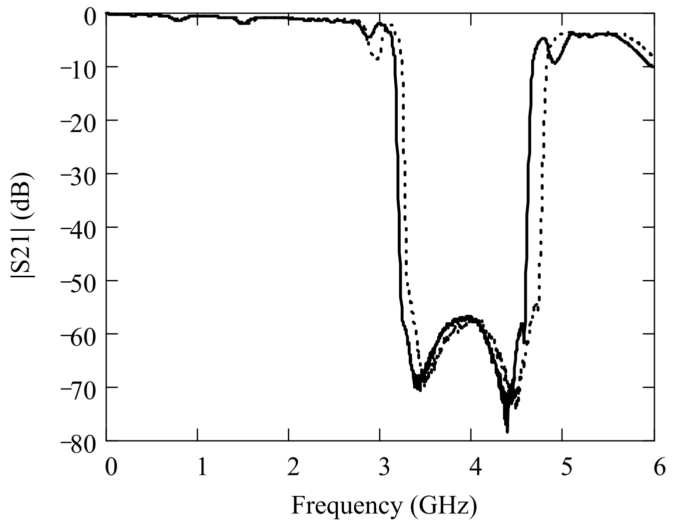

Figure 4.26: *Relationship between measured transmission responses for a 5×5 meander PBG reflector with tuned bends (solid line) and for a 5×5 meander PBG reflector with non-tuned bends (dotted line).*

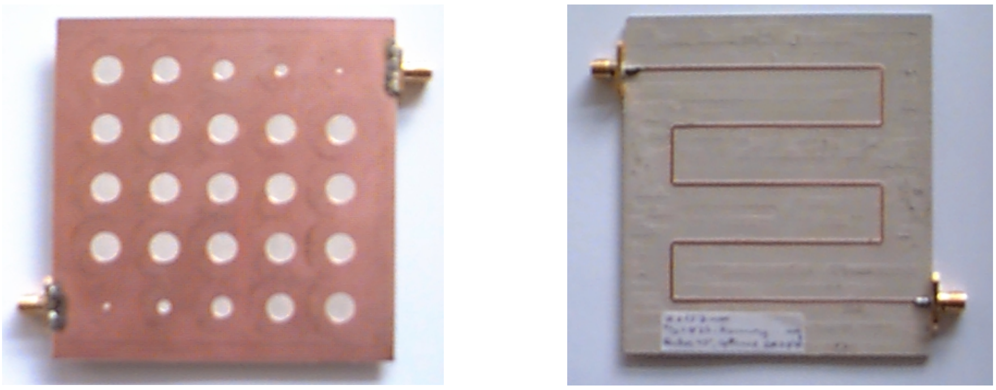

(*a*) (*b*)

Figure 4.27: *Photograph of the ground plane (a) and upper plane (b) of a 5×5 meander PBG reflector showing mitering and tapering.*

Since the meander arrangement is the determining fact in the generation of the frequency ripple, another solution based on altering the meander trace is proposed to reduce this ripple in the compact PBG reflector response. An isolated bend as in Fig. 4.24(*b*) introduces power losses, both through radiation and generation of surface waves. This means that the new configurations should have the minimum amount of bends as possible. On the other hand, the meander periodicity should be as short as possible in order to separate greatly the resonant frequencies. This will allow getting a reflector with flatter passbands at both sides of the rejected band. This way, in the new configurations, a trade-off must be met between a minimum number of bends and short meander periods. Moreover, a wave traversing an isolated bend presents an asymmetric distribution of fields depending on the direction of rotation (either rightward or leftward). To cancel this asymmetric behavior, the same amount of bends in each direction (same number of left-angled and right-angled bends) is recommended.

A prototype with good frequency behavior is achieved within a small circuit layout area, when $3a$-long meander periods are used. This way, it is possible to combine short meander periods, and hence a ripple far away from the rejected band, along with a minimum number of bends for low radiation and scattering losses. For example, to implement a 24-period reflector, the best configuration found consists of 3×8 periods, each bend turning to the right or to the left depending on the previous bend direction of rotation (either leftward or rightward, respectively) to compensate for the asymmetric field distribution (see photograph in Fig. 4.28). Using this novel configuration, the measured $|S_{21}|$-parameter of the reflector is improved in its flatness near the rejected band, obtaining almost the same rejection value, rejected bandwidth, and cutoff sharpness as the 5×5 configuration (see Fig. 4.29). As commented above,

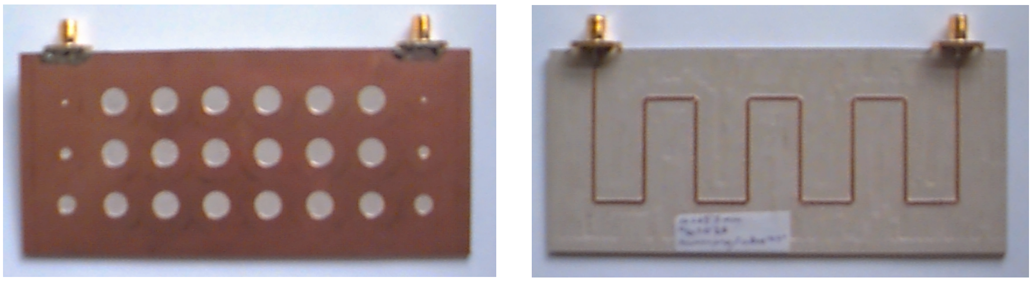

(*a*) (*b*)

Figure 4.28: *Photograph of the ground plane (a) and upper plane (b) of a 3×8 meander PBG reflector.*

although each bend introduces some radiation and scattering losses, and hence the more bends are, the more losses are expected, they are also maintained at low levels in this trade-off case. It can be seen in Fig. 4.30, where the simulated scattering and radiation power losses for the 3×8 and 5×5 meander reflectors are shown.

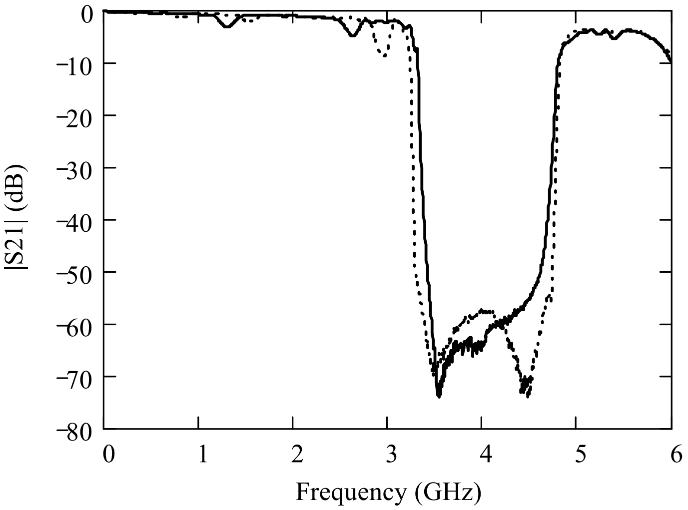

Figure 4.29: *Measured* $|S_{21}|$ *-parameters for the 24-period —3×8— (solid line) and 25-period —5×5— (dotted line) compact PBG microstrip reflectors*

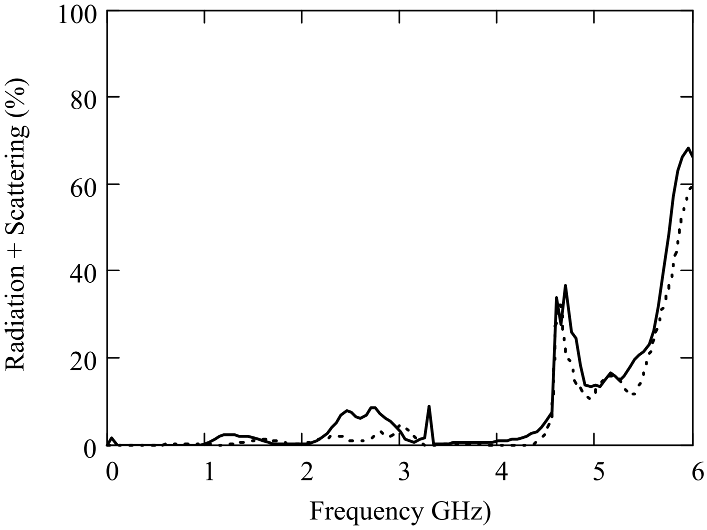

Figure 4.30: *Simulated scattering and radiation power losses given in percent for the 3×8 meander PBG reflector (solid line) and the 5×5 meander PBG reflector (dotted line).*

As it will be seen in chapter 5, section (5.4), promising configurations of bandpass filters could be obtained using two optimized meander PBG microstrip reflectors, as the ones studied in this section, placed in cascade and centered at different frequencies.

4.6. Continuous patterns: single and multiple frequency tuned PBG microstrip structures

In the previous sections, a discrete pattern of holes etched along the microstrip line ground plane was always considered. All the PBG microstrip structures proposed in those sections present a periodic frequency response, as corresponds to conventional periodic devices. This fact can constitute a problem in some filtering applications. However, as it will be seen in this section, the replicas of the response at the harmonics of the design frequency can be eliminated by employing continuous patterns following a sinusoidal law, inspired by the continuous sinusoidal perturbation of Fiber Bragg Gratings. Moreover, adding multiple sine-functions, as in superimposed FBGs [KAS 99], it is possible to perform simultaneously the rejection of multiple frequencies, each one corresponding to the constituent sine function whose spatial period is tuned at that frequency. Until now, to reject different frequencies with PBG structures, various conventional devices of discrete patterns [RUM 98] had to be cascaded enlarging the longitudinal dimension. Using these new multiple-frequency-tuned structures of continuous patterns, the different frequencies will find tuned periodic perturbations and, hence, all of them will be rejected at the same time, as it will be also proved in this section. This way, PBG microstrip structures are a good choice to accomplish the rejection of one or several undesired frequencies, providing broad rejected bands and being also easily integrated with other microstrip components in the upper plane to further miniaturizing the circuit configuration. These features surpass short-circuit stubs or chip capacitors usually employed for this purpose, since the later are narrowband and consume valuable circuit layout area.

It is well known in optics that the reflective frequency response of a periodically perturbed optical waveguide can be given, in a first estimation, as the Fourier Transform of its coupling coefficient [PER 96]. This fact has been rigorously demonstrated for PBG structures in microstrip technology in chapter 3, section (3.5), where an approximate and an exact expression for the relation between the coupling coefficient $K(z)$ and the reflection parameter $S_{11}(f)$, in terms of Fourier Transforms, have been found.

Therefore, it can be inferred that sinusoidal variations of the coupling coefficient in

PBG microstrip structures should yield to single-frequency-tuned frequency responses resulting from the Fourier Transformation of those (spatially-limited and usually windowed) sine functions. Moreover other appropriate periodic variations of the coupling coefficient could also yield to frequency responses in which the replicas at the harmonics of the design frequency are constrained within reduced levels. It is important to recall that as it was seen in chapter 2, section (2.3.2.1.1), the coupling coefficient of a PBG microstrip device with a periodic pattern etched in the ground plane is given by eqn. (2.90), and hence can be approximated as proportional to the derivative of the etched profile. This way, a PBG microstrip structure with a raised-sine or triangular pattern etched along its ground plane has a frequency response with a prominent rejected band at the design frequency and with strongly reduced rejection at the harmonics of it (at least for the first harmonic in the case of triangular pattern). In the same way, the microstrip line with an etched pattern consisting in the addition of multiple raised-sine functions is expected to have a response basically composed of rejected bands at the frequencies corresponding to the sinusoidal functions.

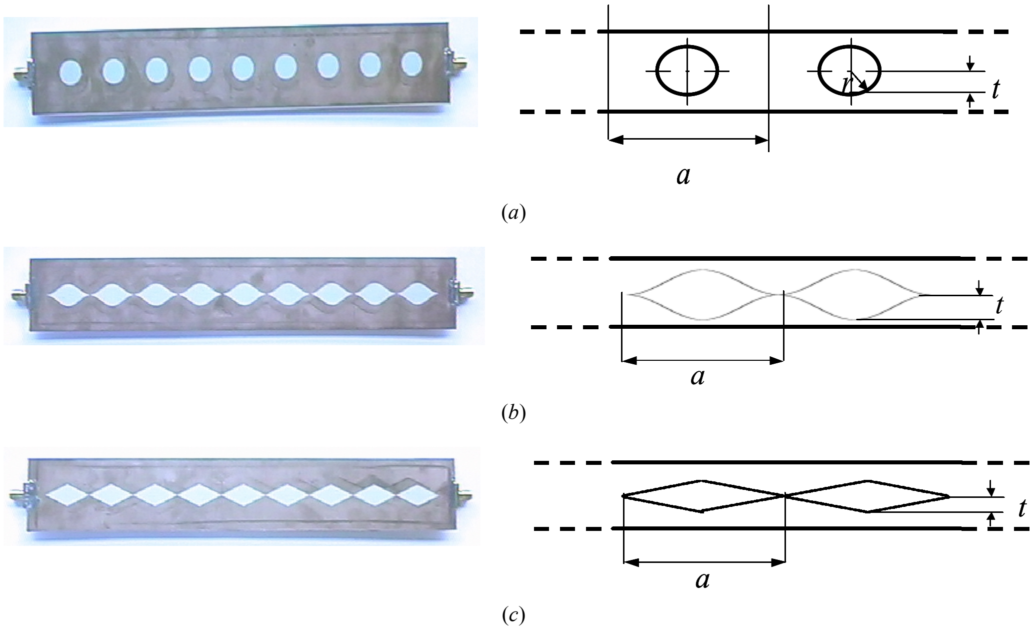

Figure 4.31: *Photographs (left) and schematics (right) for three different patterns etched in the ground plane: (a)discrete holes, (b) sinusoidal profile and (c) triangular profile. The structure period, a, and the maximum amplitude of each etched pattern, t, are shown. For the first case of holes, t is the circle radius r.*

To carry out a comparison between discrete and continuous profiles, a sinusoidal and a triangular profile have been chosen with the same parameters as for a conventional device with holes: $N = 9$ periods and $t/a = 0.25$, where a is the spatial period and t is the maximum amplitude of each etched pattern (see Fig. 4.31). In the discrete pattern of Fig. 4.31(*a*), t is the circle radius, r. The main rejected band of the three prototypes has been centered around 2.5 GHz in order to capture the first harmonic at 5 GHz with our vector network analyzer (up to 6 GHz). This requires a spatial period $a = 23.9$ mm for the *Rogers RO3010*™ substrate (relative dielectric constant $\varepsilon_r = 10.2$, and thickness $h = 1.27$ mm) with a conductor strip width $w = 1.2$ mm (corresponding to a characteristic impedance of $Z_0 = 50\ \Omega$ for a conventional microstrip line). Figures Fig. 4.32 to Fig. 4.34 show the simulated frequency behavior, in transmission and reflection, for the conventional PBG microstrip structure with a discrete pattern of holes, and for those ones with sinusoidal and triangular continuous patterns, respectively. The three prototypes have been also fabricated and the measurements are shown in Fig. 4.35 to Fig. 4.37. A good agreement between simulations and experimental results is obtained for all the devices. The main difference between the two types of structures (continuous and discrete ones) is the level of the rejected band at the harmonic of the design frequency, which is very high for the discrete PBG device (around –55 dB). The rejected band at the harmonic is almost suppressed for

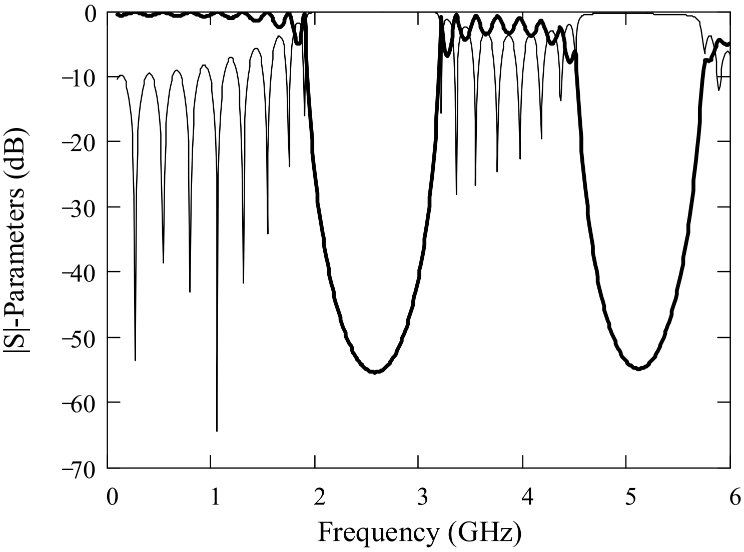

Figure 4.32: *Simulated* $|S_{11}|$ *(thin solid line) and* $|S_{21}|$ *(thick solid line) parameters for the discrete PBG microstrip structure with 9 circles etched in the ground plane, with a period a of 23.9 mm and r/a = t/a = 0.25.*

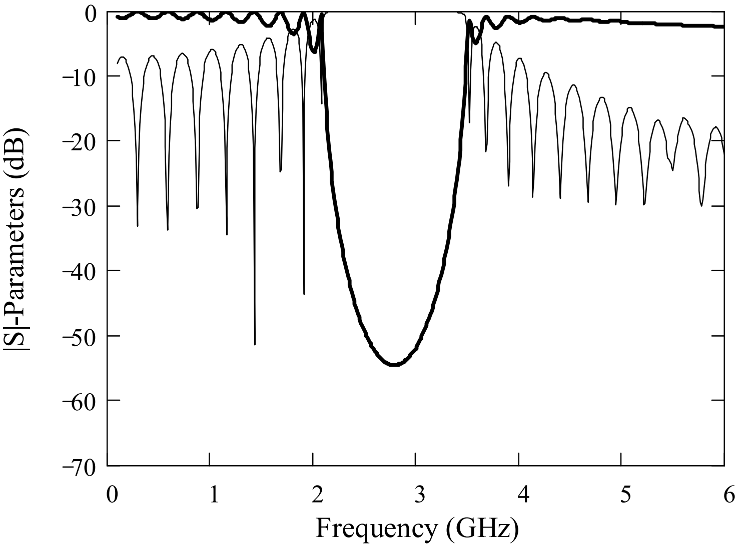

Figure 4.33: *Simulated* $|S_{11}|$ *(thin solid line) and* $|S_{21}|$ *(thick solid line) parameters for the PBG microstrip structure with 9 periods of a continuous sinusoidal pattern etched in the ground plane, a = 23.9 mm and t/a = 0.25.*

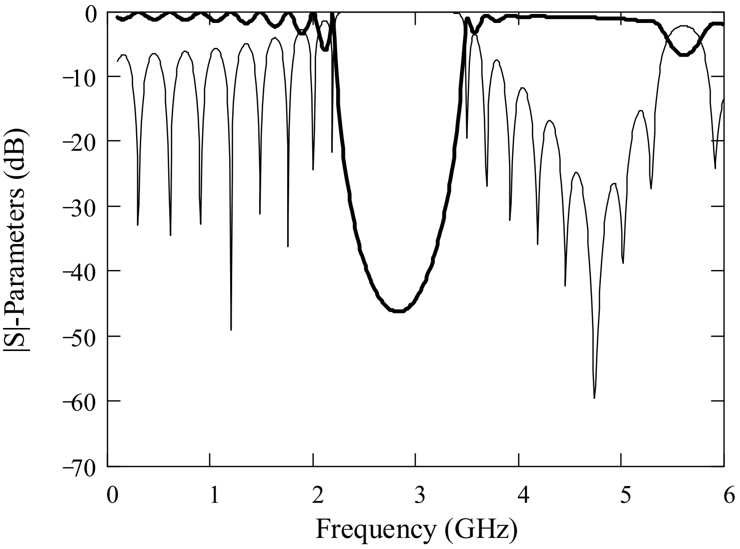

Figure 4.34: *Simulated* $|S_{11}|$ *(thin solid line) and* $|S_{21}|$ *(thick solid line) parameters for the PBG microstrip structure with 9 periods of a continuous triangular pattern etched in the ground plane, a = 23.9 mm and t/a = 0.25.*

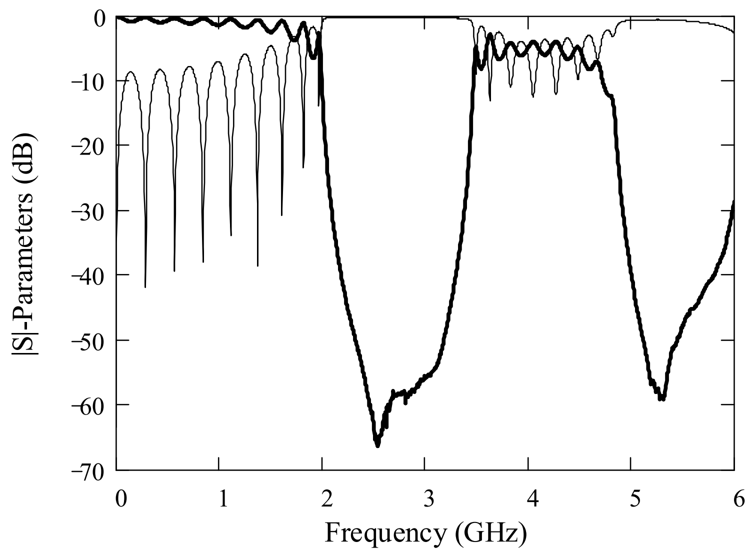

Figure 4.35: *Measured* $|S_{11}|$ *(thin solid line) and* $|S_{21}|$ *(thick solid line) parameters for the discrete PBG microstrip structure with 9 circles etched in the ground plane, with a period a of 23.9 mm and r/a = t/a = 0.25.*

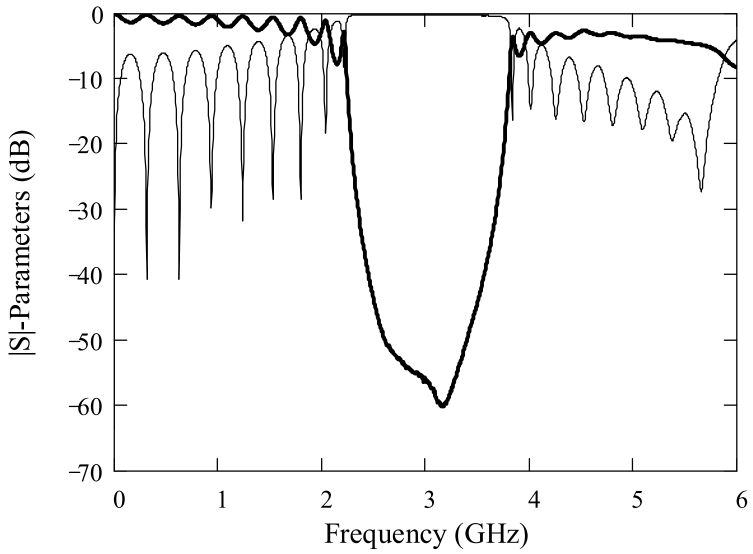

Figure 4.36: *Measured* $|S_{11}|$ *(thin solid line) and* $|S_{21}|$ *(thick solid line) parameters for the PBG microstrip structure with 9 periods of a continuous sinusoidal pattern etched in the ground plane, a = 23.9 mm and t/a = 0.25.*

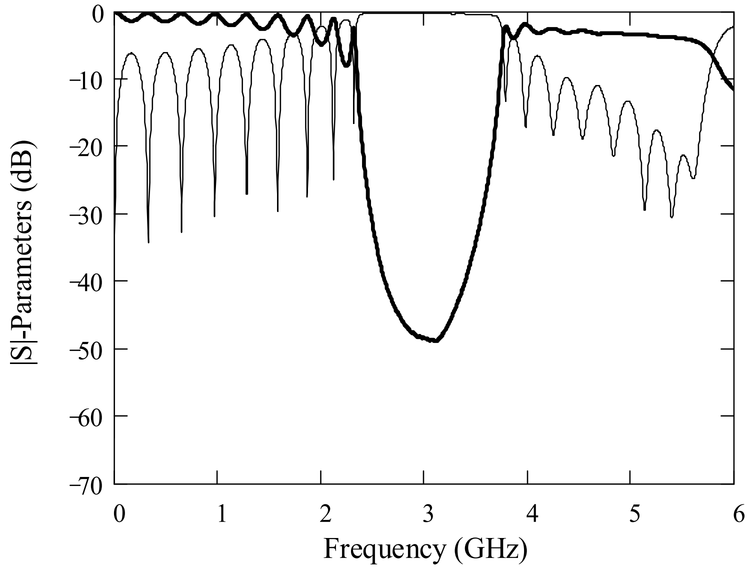

Figure 4.37: *Measured* $|S_{11}|$ *(thin solid line) and* $|S_{21}|$ *(thick solid line) parameters for the PBG microstrip structure with 9 periods of a continuous triangular pattern etched in the ground plane, a = 23.9 mm and t/a = 0.25.*

the sinusoidal structure (it presents a reduction around 50 dB compared to the discrete case) without significantly altering the main reflected band. Similarly, the triangular profile reduces the harmonic level in more than 45 dB but also the rejection amplitude of the main band (from more than –55 dB for the discrete and the sinusoidal patterns, to –50 dB).

Double- and triple-frequency-tuned PBG microstrip structures will be now designed, constructed and measured. The double-frequency-tuned PBG microstrip structure is designed with two added raised-sine functions: the first one has 9 periods of a_1 = 23.9 mm, and the second one has 14 periods of a_2 = 14.8 mm in order to have the rejected frequencies around 3 GHz and 4.5 GHz respectively. Both sine functions have t/a = 0.2. The triple-frequency-tuned PBG microstrip structure is designed with three added raised-sine functions. The first sine has 9 periods of a_1 = 23.9 mm, the second one has 11 periods of a_2 = 19.35 mm, and the third one has 14 periods of a_3 = 14.8 mm, to obtain their stopbands centered at 3 GHz, 4 GHz and 5 GHz, respectively. In all these cases the t/a ratio is fixed to 0.15. Note that the amplitude of each particular sine has been reduced in order to maintain the total amplitude of the ground plane perturbation in such values that radiation is kept in low levels. It must be also pointed

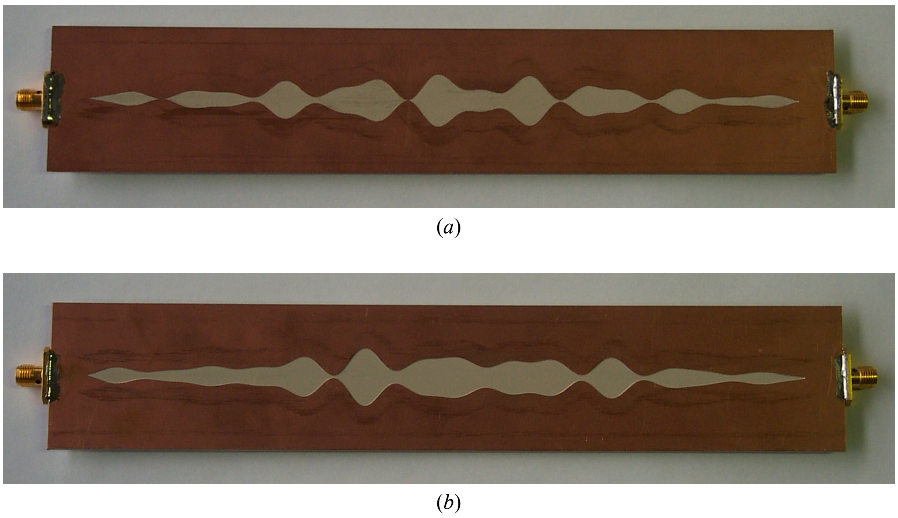
(*a*)

(*b*)

Figure 4.38: *Photograph of the ground plane of: (a) the double-frequency-tuned PBG microstrip structure. The pattern is formed by the addition of two Hamming-windowed raised-sine functions of periods* a_1 *= 23.9 mm,* a_2 *= 14.8 mm and peak amplitude to period ratio t/a = 0.2; (b) the triple-frequency tuned PBG microstrip structure. The pattern is formed by the addition of three Hamming-windowed raised-sine functions of periods* a_1 *= 23.9 mm,* a_2 *= 19.35 mm,* a_3 *= 14.8 mm and peak amplitude to period ratio t/a = 0.15.*

out that in both designs the patterns resulting from the addition of various sine functions are Hamming-windowed to achieve a low-rippled response at the passband.

The prototypes have been fabricated by means of a numerical milling machine. See Fig. 4.38 for photographs of both the double- (*a*) and the triple-frequency-tuned (*b*) PBG microstrip structures. The measurements are shown in Fig. 4.39 and Fig. 4.40, respectively. Both $|S_{11}|$ and $|S_{21}|$-parameters are given. Two rejected frequency bands centered at 2.85 GHz and 4.65 GHz are observed in Fig. 4.39 for the double-frequency-tuned structure. Rejection levels higher than 25 dB are shown for both stopbands. A flat and low-rippled passband is obtained at frequencies below 2 GHz. In Fig. 4.40 three rejected frequency bands corresponding to the triple-frequency-tuned device can be seen at 3 GHz, 3.85 GHz and 5 GHz, respectively. The achieved rejection levels are approximately 20 dB for the first and second one, and more than 16 dB for the last one. The reduction observed in the bandwidths and rejection levels compared with the double-frequency-tuned prototype is due to smaller *t*/*a* ratios. This filter has also a flat and low-rippled passband below 2 GHz. Measurements show that the proposed devices behave as multiple-frequency-tuned band reflectors, avoiding the

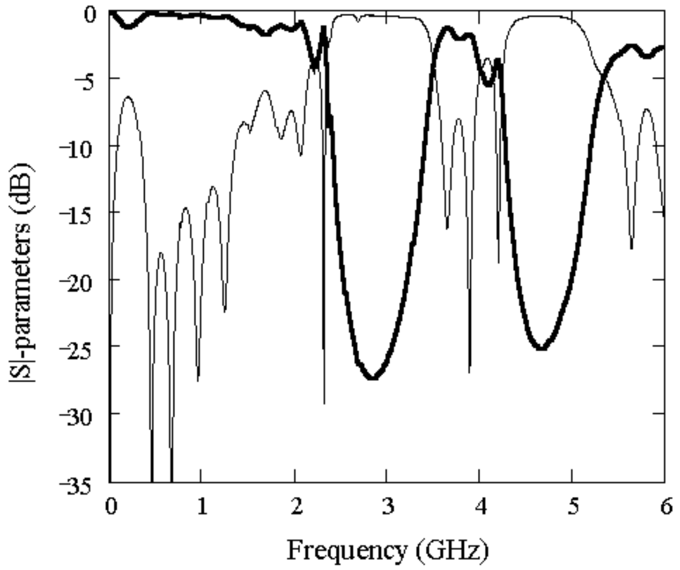

Figure 4.39: *Measured* $|S_{11}|$ *(thin solid line) and* $|S_{21}|$ *(thick solid line) parameters for the double-frequency-tuned PBG microstrip structure, as shown in Fig. 4.38(a). The two Hamming-windowed raised-sine functions have periods* a_1 *= 23.9 mm,* a_2 *= 14.8 mm and peak amplitude to period ratio t/a = 0.2. The total length of the device is 215.1 mm.*

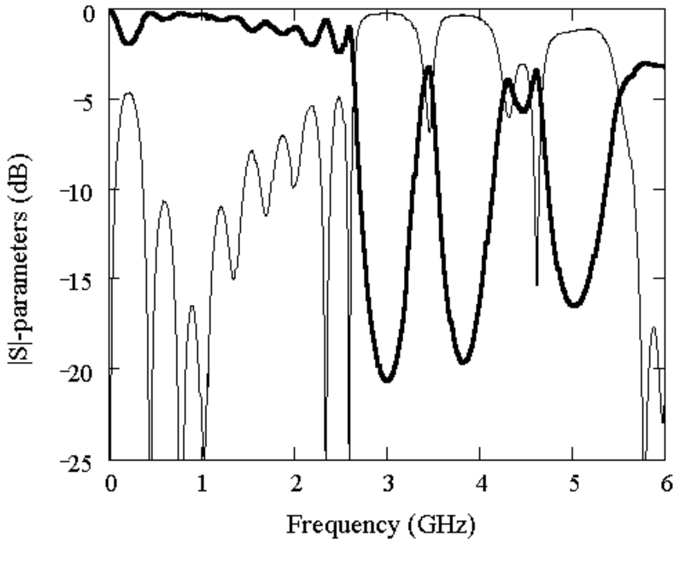

Figure 4.40: *Measured* $|S_{11}|$ *(thin solid line) and* $|S_{21}|$ *(thick solid line) parameters for the triple-frequency-tuned PBG microstrip structure, as shown in Fig. 4.38(b). The three Hamming-windowed raised-sine functions have periods* a_1 *= 23.9 mm,* a_2 *= 19.35 mm,* a_3 *= 14.8 mm and peak amplitude to period ratio t/a = 0.15. The total length of the device is 215.1 mm.*

need of cascading conventional PBG devices. A promising application of these novel devices can be the suppression of the second and third harmonic in power amplifiers and oscillators [RAD 98a].

4.7. Final remarks

The contents of this chapter have gone deep into the interpenetration between PBG microstrip devices and Fiber Bragg Gratings, and the application of some of the characteristic features of the refractive index modulation in FBGs on the electrical parameters of PBG microstrip devices has been systematically studied to improve the microwave device frequency behavior from different points of view. This way, in section (4.3), tapering the hole radii has led to larger ratios between the main rejected band and sidelobe rejections, which could be a critical aspect in some filtering applications, since smaller holes towards the device endpoints contribute to diminish the impedance mismatch at the boundaries of the structure. Different windowing functions have been compared from different points of view in several scenarios. The equivalent number of periods in a tapered structure, N_{eq}, seems to be a useful concept for the comparison and design of these windowed circuits. Thus, to obtain a device with the same rejection level and bandwidth as a non-tapered structure but with lower sidelobes, a tapered device with $N_{eq} = N/A_{eq}$ periods is needed, being N the number of periods in the non-tapered case, and $A_{eq} \leq 1$ the area under the tapering profile. The tapered structure has to be $1/A_{eq}$ times longer and, in general, its reflected band has less steep edges, as the taper is smoother. However, edges can be made sharper either by increasing a bit more the number of holes, making at the same time narrower the bandwidth, or by enlarging the holes and, hence, decreasing a little the mainlobe to sidelobe level. As it was said in this section (4.3), it is not easy to arrive at final conclusions on the best window shape, number of holes, or maximum hole-radius in order to determine whether those choices benefit or not the global frequency response, since all of them modify the frequency features altogether, and, very often, some trade-off has to be met for each particular application.

Broader bandwidths have been obtained in section (4.4), where the holes etched in the ground plane are not equidistant but follow a linear function with the position in the structure. In these chirped structures, the resonant frequency is dependent on the location and, hence, as a pulse propagates through the device the central frequency that is reflected back varies. Combining both chirping and tapering, a broad and non-rippled rejected band between two flat passbands can be obtained. The spatially varying frequency tuning of chirped structures is also the basic idea on which a device in the next chapter is based to perform phase filtering.

The bending feasibility of PBG microstrip reflectors has been used in section (4.5) to propose long structures in reasonable circuit layout areas. This way, high performance rejected-band filters with high rejection values and sharp cutoffs can be implemented. The meander-type arrangement, though, introduces a new periodic structure that is the source for a new frequency ripple. Different methods have been proposed to have control on the stopbands associated with this new periodicity: chamfering the corners of the upper conductor strip achieves better-matched bends that weaken the effect of the meander periodic structure; tuning the bends by lengthening shifts the ripple peaks to more convenient frequency positions; or modifying the way in which the holes are arranged can get flatter passbands at both sides of the main reflected band, especially when hole tapering is also used. Once two optimized compact (meander) PBG reflectors are designed, they could be cascaded to obtain bandpass filters with steep band edges and very high rejection at both sides of the passband, as it will be seen in one of the examples of the next chapter.

Smooth slots with continuously varying width in microstrip PBG structures have been presented in section (4.6) to avoid periodic frequency responses, which could be detrimental for some applications. This way, the use of continuous patterns following a sinusoidal law can eliminate the replicas of the response at the harmonics of the design frequency. Moreover, multiple-frequency-tuned structures to perform simultaneously the rejection of various undesired frequencies can be achieved, whenever a pattern consisting in the addition of multiple sine-functions, each one tuned at one of the frequencies to be rejected, is used. This avoids the need to cascade several PBG reflectors, which increase the circuit layout area. Then, PBG microstrip structures have been presented as a good choice to accomplish the rejection of one or several undesired frequencies, providing broad rejected bands and being also easily integrated with other microstrip components in the upper plane to further miniaturizing the circuit configuration. These features surpass short-circuit stubs or chip capacitors usually employed for this purpose, since these are narrowband and consume valuable circuit layout area.

CHAPTER 5

PRACTICAL APPLICATIONS OF PBG STRUCTURES IN MICROSTRIP TECHNOLOGY: EXAMPLES

In this chapter several examples of practical applications of PBG structures in microstrip technology are proposed and tested. The range of applications considered is quite wide, including the suppression of spurious bands and harmonics in passive and active circuits for enhanced out of band behaviour and higher efficiency, the implementation of enhanced lowpass filers and high rejection bandpass filters, the implementation of high-Q fully planar resonators, and the design of chirped delay lines to realize quadratic-phase filters with applications like real-time Fourier analysis. All of the examples presented show clearly the feasibility of the applications proposed, and almost all of them include fabricated prototypes and measured data. However, it is important to note that the range of possible applications for PBG structures in microstrip technology can be very wide, and here we are going to cover only some of them to show their potential.

5.1. Spurious passband suppression in passive devices

The first important application of PBG structures in microstrip technology that we are going to address is the suppression of spurious passbands in conventional passive devices. In this section several examples will be proposed and analyzed, showing the successful operation of this technique.

5.1.1. Lowpass filter and multisection transformer

In this section a conventional microstrip lowpass filter, implemented using the technique of stepped impedances, and a conventional microstrip multisection transformer will be designed and simulated. As it is well known, together with the desired passband, their frequency responses will include spurious passbands that we are going to eliminate introducing PBG structures. The resulting devices will require the same circuit layout area as the conventional ones, but will feature an improved frequency response without the undesired spurious passbands. It is important to note that in the particular case of the multisection transformer, the consideration of the second passband as a spurious passband depends really on the application. Here, we are going to eliminate it assuming that it is detrimental for the targeted application. However, the purpose of the example is only to show the feasibility of the elimination of undesired passbands in passive devices.

The procedure to design the conventional stepped impedance lowpass filter and the multisection transformer is well known and can be found in many microwave books (see for instance [POZ 98]). Here we are going to apply it to design an order 7 Butterworth lowpass filter, with cutoff frequency of 2.5 GHz, highest characteristic impedance of 80 Ω and lowest characteristic impedance of 20 Ω. In the same way, a multisection transformer with four sections, to connect a line with characteristic impedance of 20 Ω to a line with characteristic impedance of 80 Ω, will be designed using a binomial distribution. The transformer is designed to obtain optimum

Section (i)	**Z_{0i} (Ω)**	**W_i (mm)**	**L_i (mm)**
1	21.838	4.644	10.56
2	30.884	2.778	10.921
3	51.806	1.063	11.545
4	73.266	0.427	11.983

Table 5.1: *Characteristic impedances and physical dimensions for the multisection transformer (W_i and L_i represent the width and length, respectively, of the i-th section).*

Section (i)	**Z_{0i} (Ω)**	**W_i (mm)**	**L_i (mm)**
1	20	5.24	1.187
2	80	0.319	6.003
3	20	5.24	4.806
4	80	0.319	9.63
5	20	5.24	4.806
6	80	0.319	6.003
7	20	5.24	1.187

Table 5.2: *Characteristic impedances and physical dimensions for the lowpass filter (W_i and L_i represent the width and length, respectively, of the i-th section).*

matching at 2.5 GHz. Both circuits are implemented in a substrate 1.27 mm-thick, and with relative dielectric constant $\varepsilon_r = 10.2$. Their physical parameters are given in Table 5.1 for the multisection transformer, and in Table 5.2 for the lowpass filter.

The circuits are simulated using *Agilent Momentum* and *ADS* software. Their frequency response in transmission (S_{21} parameter) is given in Fig. 5.1 (red line) for the lowpass filter, and in Fig. 5.2 (red line) for the multisection transformer.

As it can be seen in Fig. 5.1, the frequency response of the lowpass filter includes a resonance peak (undesired spurious passband) placed around 5.4 GHz. In order to suppress it, a PBG structure is introduced in the ground plane of the microstrip line. The design frequency (frequency of maximum attenuation) of the PBG structure is governed by its periodicity, *a*, and can be calculated through the following expression obtained in chapter 3, section (3.3.3.2):

$$f_{max} = \frac{c}{2 \cdot a \cdot \sqrt{\varepsilon_{eff}}} \tag{5.1}$$

For the sake of simplicity the effective dielectric constant of the circuit, ε_{eff}, will be calculated taking the mean value of the effective dielectric constants of the different circuit sections. Using it, the period necessary to reject the frequencies placed around 5.4 GHz will be *a*=10.23 mm. Two different prototypes will be designed and simulated. The first one will have a discrete pattern of circles, with radius to period ratio *r/a*=0.488. The second one will employ a continuous pattern following a raised-sine, with amplitude to period ratio *r/a*=0.5. A sketch of the prototypes can be seen in Fig. 5.3, and their simulated transmission responses (S_{21} parameters) are given in Fig. 5.1 for the design with a discrete pattern of circles (blue line), and for the design with a continuous raised-sine pattern (pink line). As it can be seen in the frequency responses, the resonance peak is completely suppressed in both cases, while a good fundamental passband is still maintained.

Regarding the conventional multisection transformer, it can be seen in Fig. 5.2 (red line) that the frequency response includes a spurious passband placed around 7.5 GHz. In order to suppress it, a PBG structure will be again employed. This time, the period necessary to reject the frequency band placed around 7.5 GHz will be *a*=7.2 mm.

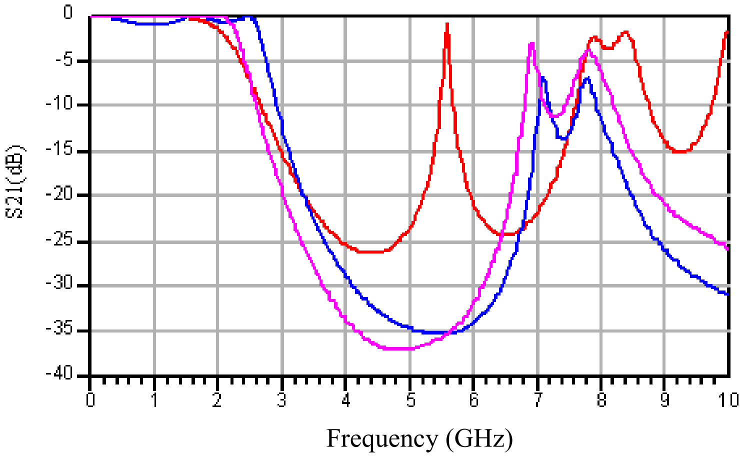

Figure 5.1: *Simulated frequency responses for the lowpass filter prototypes, including the conventional filter (red line), the filter with discrete PBG of circles (blue line), and the filter with continuous PBG of raised-sine pattern (pink line).*

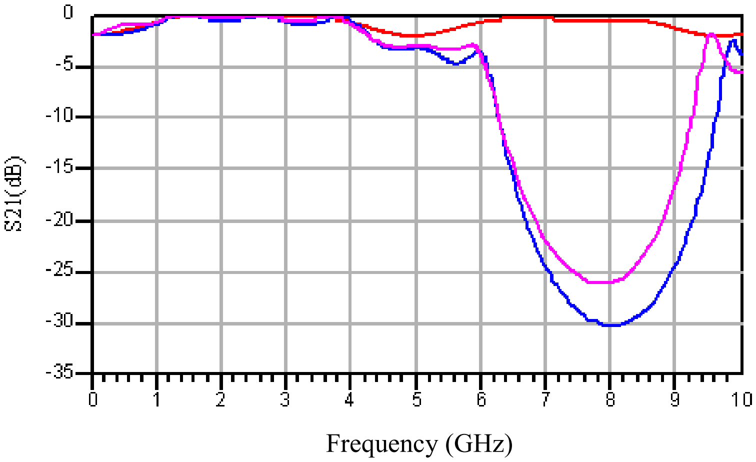

Figure 5.2: *Simulated frequency responses for the multisection transformer prototypes, including the conventional multisection transformer (red line), the transformer with discrete PBG of circles (blue line), and the transformer with continuous PBG of raised-sine pattern (pink line).*

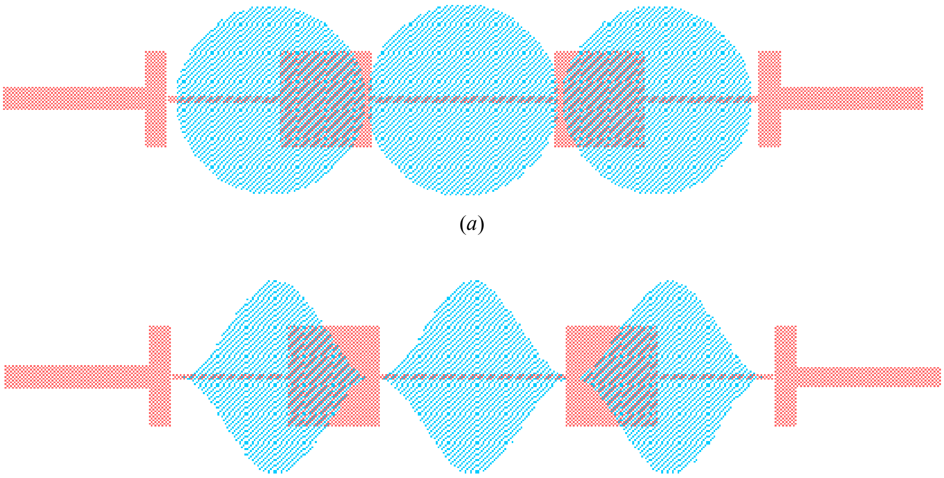

(*a*)

(*b*)

Figure 5.3: *Sketches of the lowpass filter prototypes with PBG constituted by a discrete pattern of circles (a), and with PBG constituted by a raised-sine pattern. The red parts represent the upper plane conductor strip, and the blue parts represent the area etched in the ground plane.*

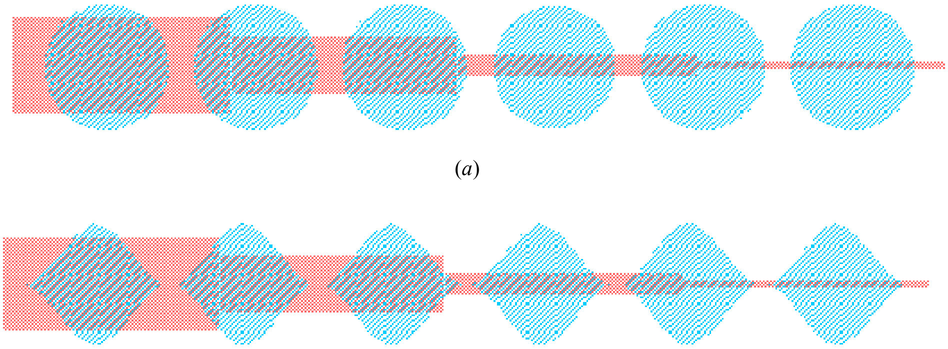

(*a*)

(*b*)

Figure 5.4: *Sketches of the multisection transformer prototypes with PBG constituted by a discrete pattern of circles (a), and with PBG constituted by a raised-sine pattern. The red parts represent the upper plane conductor strip, and the blue parts represent the area etched in the ground plane.*

Again, two different prototypes will be designed and simulated. The first one will have a discrete pattern of circles, with radius to period ratio *r/a*=0.4. The second one will employ a continuous pattern following a raised-sine, with amplitude to period ratio *r/a*=0.4. A sketch of the prototypes can be seen in Fig. 5.4, and their simulated transmission responses (S_{21} parameters) are given in Fig. 5.2 for the design with a discrete pattern of circles (blue line), and for the design with a continuous raised-sine pattern (pink line). As in the previous case, the suppression of the spurious passband achieved is very good, showing that PBG structures in microstrip technology can be successfully employed to suppress undesired passbands. It is important to remark that the introduction of the PBG structure in the ground plane has been done without altering the physical dimensions of the conventional circuit, and without requiring additional circuit layout area.

5.1.2. 'Wiggly-line' bandpass filter

In this section, the usefulness of some of the concepts developed up to now for PBG microstrip structures is broadened to other classical microstrip circuits. This broadening will be further extended in section (5.6), where the chirping and tapering techniques of the electrical parameter modulation will be applied on conventional microstrip lines with continuously varying strip width. Here, the strip width modulation of otherwise traditionally designed parallel-coupled-line microstrip bandpass filters is proposed in order to suppress their spurious passbands. It will be shown that employing a continuous modulation pattern that follows a sinusoidal law, as that of chapter 4, section (4.6), for the ground plane, the replica of the response at the harmonic of the design frequency can be eliminated, thereafter improving strongly the filter performance, provided that the sinusoidal perturbation period is tuned at the frequency band to reject. Moreover, if the strip width modulation is tuned simultaneously at several sine functions, as in multiple-frequency-tuned PBG microstrip circuits, then several harmonic passbands could be rejected, whenever the sine periods are appropriately tuned at these frequency-bands. This way, these coupled-line microstrip bandpass filters with sine-like modulated strip width have enhanced out-of-band behavior, whilst the main passband is virtually unaltered. This technique has important advantages over other alternative solutions described below, since the wiggle of the lines does not force the prototype parameters to be recalculated and it does not increase the circuit area. Moreover, these filters do not demand special fabrication processes or anything different to those requirements made for classical coupled-line microstrip filters.

Parallel coupled transmission line filters in microstrip and stripline technologies are very common for implementations of bandpass and bandstop filters with required bandwidths up to a 20% of the central frequency. The design equations for the coupled line parameters (space-gap between lines, and line widths and lengths) can be found in classical microwave books. This way, following a well-defined and systematic procedure, the required microstrip filter parameters can be easily derived for both Butterworth and Chebyshev prototypes [POZ 98]. As it has been said above, the fundamental limitation of these popular and simple techniques to implement filters is the presence of spurious passbands at the harmonics of the design frequency. To reject these harmonics, it has been usually necessary to cascade additional filters that can reject the spurious passbands. This solution, however, increases the filter layout area and introduces additional insertion losses. Within this context, more compact microstrip bandpass filters that achieve spurious passband suppression have been proposed by using a Uniplanar Compact Photonic Bandgap (UC-PBG) structure as a modified ground plane in a parallel-coupled-line microstrip filter [YAN 99]. The ground plane structure in [YAN 99] introduces a periodic perturbation that rejects the spurious passbands and, at the same time, acts as a slow wave structure that reduces the total physical size of the parallel-coupled-line microstrip filter itself, achieving a 20% of shortening in the reported results. However, this slow wave effect is achieved strongly in the even mode of the coupled-lines, but very weakly in the odd mode, increasing substantially the difference between the phase constant of the even and odd modes [YAN 00]. As it is well known, the difference between these phase constants produces spurious effects in the frequency response of the bandpass filter [EDW 92], giving rise in the discussed case to lower attenuation in the rejected band placed immediately at the right of the desired passband (around 20 dB in the results reported in [YAN 00]). Moreover, the design of the parallel-coupled-line filter must be completely recalculated involving the need of new graphs to relate the physical and electrical parameters of the coupled lines once the chosen UC-PBG structure is introduced in the ground plane [YAN 00]. This is not the case for the structures described in this section and the classical design methodology for coupled-line microstrip filters can be used, obtaining very effective rejection at the harmonic passband, while the design passband is kept almost unaltered [LOP 01].

Firstly, let’s consider a continuous and periodic perturbation of the cross section of a generalized waveguide, which results in a corresponding modulation of the wave impedance in the structure and yields to Bragg reflection in some frequency bands. As it was already said in section (4.6), this phenomenon has been extensively studied in optics, where it is well known that the frequency response in reflection of a periodically perturbed waveguide is given, in a first estimation, as the Fourier Transform of the mode-coupling coefficient [PER 96]. This fact has been rigorously demonstrated for PBG structures in microstrip technology in chapter 3, section (3.5), where an approximate and an exact expression for the relation between the coupling coefficient *K(z)* and the reflection parameter $S_{11}(f)$, in terms of Fourier Transforms, have been found. It is important to recall that following chapter 2, section (2.3.2.3), the coupling coefficient of a microstrip device can be approximated as proportional to the derivative of the characteristic impedance of the microstrip structure. This way, any smooth and periodic variation of those parameters (the coupling coefficient or the characteristic impedance) should yield to frequency responses mainly composed of rejected bands around those frequencies tuned at the spatial perturbation. This was applied in section (4.6) on PBG microstrip structures with continuous patterns etched in the ground plane to obtain non-periodic (single- or multiple-tuned) frequency responses, and it is the basic idea on which the present section relies to reject one or even several harmonic passbands in coupled-line microstrip filters.

Resonant Bragg mode coupling can be formulated for two generalized modes in an also generalized waveguide like that in Fig. 5.5, having a cross-section, *r(z)*, perturbed following a sinusoidal law as in eqn (5.2):

$$r(z) = r_0 + r_1 \cdot \cos(\Delta\beta \cdot z + \phi) \tag{5.2}$$

where *r(z)* is the waveguide cross-section perturbed along *z*, being *z* the propagation axis; r_0 is the mean value of the cross-section, and r_1 is the amplitude of the perturbation. $\Delta\beta$ is the difference between the unperturbed phase constants of the two interacting modes, and it is given here in eqn. (5.3):

$$\Delta\beta = \beta_1 - \beta_2 = \frac{2\pi}{\lambda_B} \tag{5.3}$$

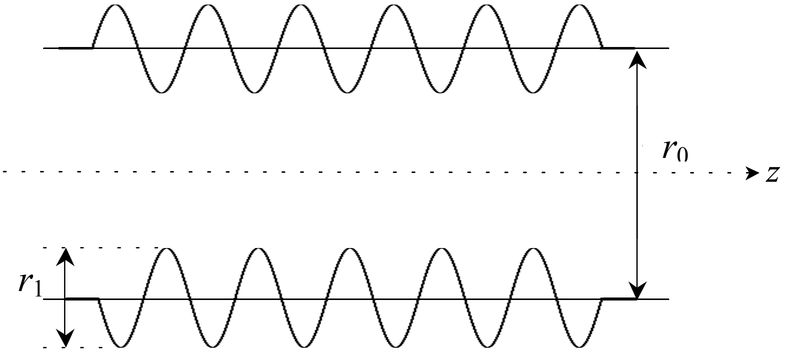

Figure 5.5: *Generalized waveguide with cross-section, r(z), perturbed following a sinusoidal law along the propagation axis, z.*

being λ_B the beat wavelength of the two modes, that is the period of the perturbation along the *z*-axis that makes the two modes satisfy the so-called resonance, coherence, or Bragg relationship. The initial phase ϕ in eqn. (5.2) can be adjusted for convenience. In principle, this includes any waveguide mode, and comprises backward and forward mode conversions.

The consequence of this perturbation is that for those frequencies at which the coherence relationship is held, a continuous transfer of energy between the two modes is guaranteed and the structure acts as a mode converter [KAT 98, THU 84]. Fourier integral transformation theory yields an additional general conclusion: the minimal length of the periodic structure for mode conversion must be on the order of the beat wavelength, λ_B, of the two modes of interest. The coherence relationship in eqn. (5.3) also guarantees that mode conversion to other unwanted modes that could be coupled by the waveguide perturbations suffers from a destructive interference.

In the case of two interacting modes, one forward and one backward, the last one is considered in eqn. (5.3) including a minus sign in its phase constant. This means that for Bragg reflection in the same but counter-propagating mode, the phase constant mismatch, $\Delta\beta$, must be two times the phase constant of the forward mode, as in eqn. (5.4):

$$\Delta\beta = \beta_1 - (-\beta_1) = 2 \cdot \beta_1 \tag{5.4}$$

A rigorous description of the previous concepts in the frame of the coupled mode theory (the cross-section method), for general non-uniform waveguides can be found in [KAT 98] for the case of bound modes. The generalized case of open waveguides including the continuous spectrum of modes is presented in [SHE 71].

The coupled mode theory can be formulated for the case of parallel-coupled microstrip lines [UYS 93], [ADA 69] (or PBG microstrip reflectors) with the same properties just discussed. To design the wiggly line filter, it can be taken advantage of this theory to calculate the period of the perturbation necessary to reject the first harmonic passband. Further studies could be also carried out to apply the full coupled mode theory to obtain the frequency response of the structure and, in this way, to characterize the harmonic reduction *vs.* the main passband distortion, for example as a function of the amplitude of the perturbation. This would help the designer in deciding, among other parameters, the amount of perturbation to use. However, this is beyond the scope of this thesis.

In Fig. 5.6 a conventional parallel-coupled-line bandpass filter (*a*) and a novel parallel-coupled-wiggly-line bandpass filter (*b*) for the same passband requirements are shown. Following the above considerations the new filter should exhibit, whenever the perturbation is properly designed, the same passband at the design frequency as the classical filter, but with an improved out-of-band behavior (harmonic suppression).

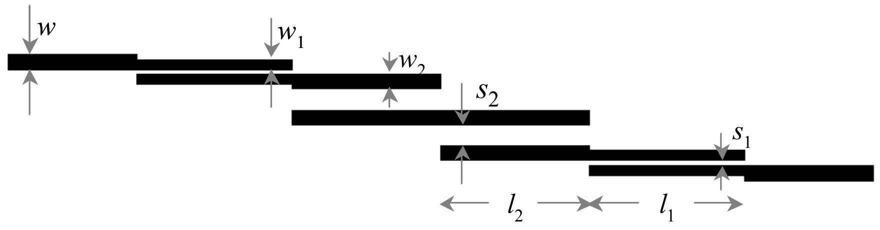

(*a*)

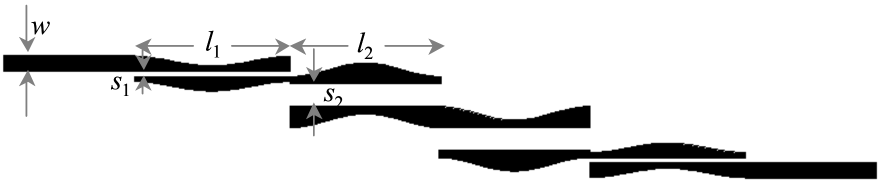

(*b*)

Figure 5.6: *(a) Classical parallel-coupled-line bandpass filter showing the typical design parameters: conductor strip widths,* w_i*, lengths of coupled-line sections,* l_i*, and separation between the coupled lines of each section,* s_i*; (b) Wiggly-line filter resulting after applying the strip width perturbation to (a).*

i	w_i***, mm***	s_i***, mm***	l_i***, mm***	$\varepsilon_{eff,e}$	$\varepsilon_{eff,o}$
1	0.75	0.42	11.98	7.244	5.354
2	1.09	1.70	11.54	7.448	6.086

Table 5.3: *Physical parameters for the order-3 Butterworth bandpass filter centered at 2.5 GHz with a 10% fractional bandwidth, being i, the section number;* w_i*, the strip width of the i-th section;* s_i*, the separation between the coupled lines of the i-th section; and* l_i *the length of the i-th section. The input and output port strip widths are w=1.2 mm (*$Z_0=50\Omega$*).* $\varepsilon_{eff,e}$ *and* $\varepsilon_{eff,o}$ *are the effective dielectric constants for the even and odd modes, respectively, in each section.*

To test the performance of this novel technique, an order-3 Butterworth bandpass filter centered at $f_d = 2.5\,\text{GHz}$, with a 10% fractional bandwidth (i.e., 250 MHz) will be designed. The substrate employed is the *Rogers RO3010*™ (with relative dielectric constant $\varepsilon_r = 10.2$, and thickness $h = 1.27\,\text{mm}$). The first stage in the design process of the wiggly line filter is to calculate a conventional parallel-coupled-line microstrip filter to meet the required specifications. The design equations to obtain the symmetrical layout parameters are very well known and they can be found in classical microwave books [POZ 98]. The layout dimensions for our case are given in Table 5.3 referred to the variables shown in Fig. 5.6 and to the effective dielectric constant of the even ($\varepsilon_{eff,e}$) and odd ($\varepsilon_{eff,o}$) modes in each section. Using these dielectric constants, the even and odd phase constants are calculated as in eqn. (5.5):

$$\beta_{e,o} = \frac{2 \cdot \pi \cdot f}{c} \cdot \sqrt{\varepsilon_{eff,e,o}} = \frac{2 \cdot \pi}{\lambda_{g,e,o}} \tag{5.5}$$

being $\lambda_{g,e}$, $\lambda_{g,o}$ the guided wavelengths of the even and odd modes, respectively, and *c* the light velocity in vacuum. Due to the non-ideal situation of having different phase constants for the even and odd modes, their mean value has to be taken to calculate the physical length of every section of coupled lines in order to have an electrical length of 90° ($\lambda_g/4$) at the design frequency.

The second stage in the design process is to calculate the period of the sinusoidal perturbation to adjust it to reject the harmonic passband at $2 \cdot f_d$ being f_d the design frequency. This case corresponds to backward coupling of the kind of Bragg reflection in the same but counter-propagating mode, so eqn. (5.4) is applicable and the coherence relationship reduces to eqn. (5.6):

$$\Delta\beta = 2 \cdot \beta_1 = \frac{2\pi}{\lambda_B} \tag{5.6}$$

Once more, due to the non-ideal situation of having different phase constants for the even and odd modes, their mean value is employed in eqn. (5.6). Neglecting the low dispersion existent for the fundamental mode in microstrip lines, the phase constant of the forward mode to be rejected at $2 \cdot f_d$ is simply calculated as two times the phase constant at the design frequency f_d:

$$\beta_1 = \beta(2 \cdot f_d) \cong 2 \cdot \beta(f_d) = 2 \cdot \frac{2 \cdot \pi}{\lambda_{gd}} \tag{5.7}$$

with λ_{gd} the guided wavelength at the design frequency. Introducing this result in the coherence relationship of eqn. (5.6), we obtain:

$$\Delta\beta = 2 \cdot \beta_1 = 2 \cdot \frac{4 \cdot \pi}{\lambda_{gd}} = \frac{2 \cdot \pi}{\lambda_B} \tag{5.8}$$

This means that the beat wavelength λ_B (the period of the perturbation necessary to satisfy the coherence relationship and, this way, to reject the mode) is equal to a quarter of the guided wavelength at the design frequency of the microstrip filter, as indicated in eqn. (5.9):

$$\lambda_B = \frac{\lambda_{gd}}{4} \tag{5.9}$$

It must be noted that every coupled line section of the filter will have its own mean phase constant value and therefore its own guided wavelength at the design frequency, λ_{gd}, but all of them will have the same electrical length of 90° at the design frequency, corresponding to $\lambda_{gd}/4$. This means that in every coupled line section a complete period of perturbation λ_B can be exactly accommodated.

The third and last stage in the design process consists in the introduction of the perturbation in the conventional filter previously designed. This perturbation will be introduced in an asymmetric way, modulating the outer edge of the coupled lines, but keeping the inner edge (coupling region) unaltered (constant distance between the coupled lines and straight shape), as can be seen in Fig. 5.6. This way, the conductor strip width variation, $w_i(z)$, in the i-th coupled line section can be expressed as in eqn. (5.10), where z varies from 0 to the beat wavelength at this coupled line section $\lambda_{B,i}$ (equal to the physical length of the section), and the initial phase is fixed alternatively to $0°$ and $180°$:

$$w_i(z) = w_i \cdot \left(1 + \frac{M(\%)}{100} \cdot \cos\left(\frac{2 \cdot \pi \cdot z}{\lambda_{B,i}} + \phi_i\right)\right) \tag{5.10}$$

being $w_i(z)$ the variable width of the conductor strips of the i-th coupled line section,

ϕ_i their initial phases ($0°$ or $180°$), w_i the constant widths calculated for the conventional filter, $\lambda_{B,i}$ the beat wavelength (the period of the sinusoidal perturbation for the i-th coupled line section), and M the strip-width modulation parameter expressed in percentage (see Fig. 5.6). The initial phase, ϕ, is optimized to maximize the rejection level achieved in the undesired passbands.

A systematic simulation of multiple prototypes with different perturbation amplitudes (different M) has been done to test the trade-off between the spurious passband rejection level and the preservation of the shape and matching of the main passband. Some prototypes have been also fabricated (see photographs in Fig. 5.7).

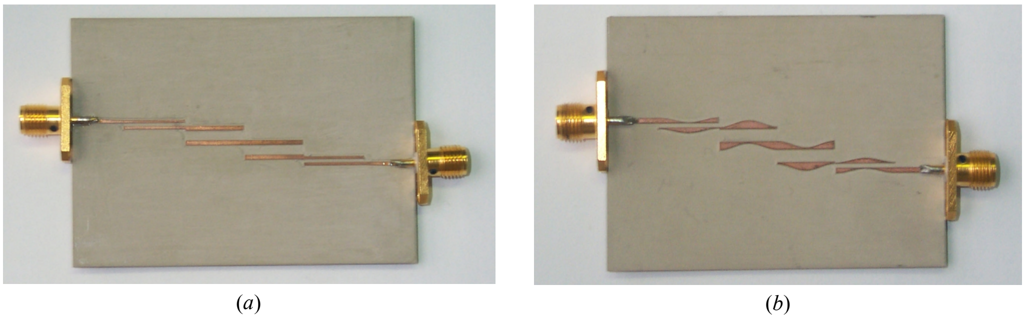
(*a*) (*b*)

Figure 5.7: *(a) Photograph of a classical coupled-line order-3 Butterworth bandpass microstrip filter centered at 2.5 GHz with a 10% fractional bandwidth; (b) Wiggly-line filter resulting after applying the strip width perturbation with* $M = 47.5\%$ *to (a).*

In Fig. 5.8 and Fig. 5.9, the simulated and experimental results, respectively, are presented for the conventional parallel-coupled-line microstrip filter and two parallel-coupled-wiggly-line prototypes with perturbations $M = 37.5\%$ and 47.5%. A very good agreement between simulations and experimental data has been obtained. It can be observed that the bigger the amplitude of the perturbation in the coupled lines, the higher the rejection level of the spurious passband. At the same time the return losses and shape of the main passband are maintained very similar in both the unperturbed and perturbed cases, offering this way a very satisfactory performance. As an example we can see that with a perturbation $M = 47.5\%$, a harmonic rejection of more than 40 dB is achieved in measurement, while the main passband is kept almost unaltered.

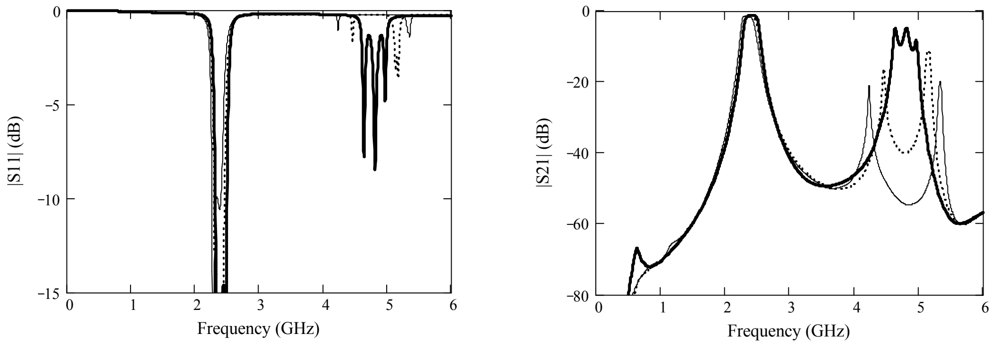

(*a*) (*b*)

Figure 5.8: *Simulated (a)* $|S_{11}|$ *- and (b)* $|S_{21}|$ *-parameters for a classical coupled-line order-3 Butterworth bandpass microstrip filter centered at 2.5 GHz with a 10% fractional bandwidth (thick solid line); for a wiggly-line filter with* $M = 37.5\%$ *(dashed line); and for a wiggly-line filter with* $M = 47.5\%$ *(thin solid line).*

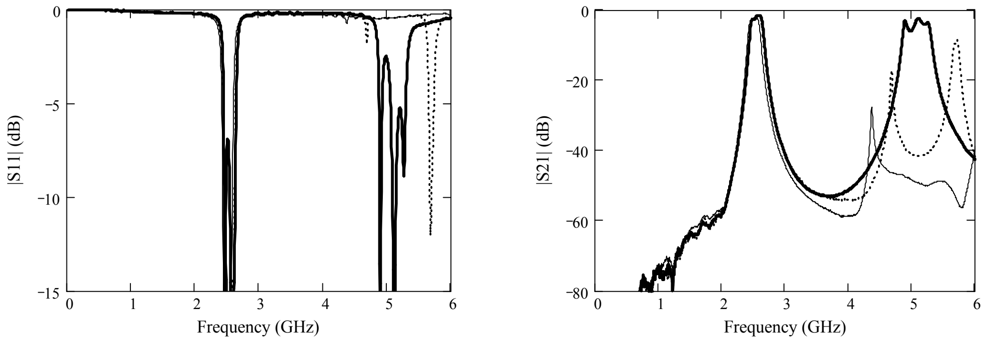

(*a*) (*b*)

Figure 5.9: *Measured (a)* $|S_{11}|$ *- and (b)* $|S_{21}|$ *-parameters for a classical coupled-line order-3 Butterworth bandpass microstrip filter centered at 2.5 GHz with a 10% fractional bandwidth (thick solid line); for a wiggly-line filter with* $M = 37.5\%$ *(dashed line); and for a wiggly-line filter with* $M = 47.5\%$ *(thin solid line).*

When the wiggle of the sections is tuned at multiple frequencies, suppression of multiple spurious passbands can be achieved. For instance, the first and second spurious passbands can be simultaneously suppressed in the classical order-3 Butterworth bandpass filter described above, if the strip width modulation of two sections is tuned at $2 \cdot f_d$, and that in the other two sections rejects $3 \cdot f_d$. In eqn. (5.7) β_1 can be generalized for the harmonic around $m \cdot f_d$, resulting in:

$$\beta_1 = m \cdot \frac{2\pi}{\lambda_{gd}} \tag{5.11}$$

and hence, the beat wavelength , λ_B, in eqn. (5.9) is:

$$\lambda_B = \frac{\lambda_{gd}}{2 \cdot m} \tag{5.12}$$

Depending on *m*, the number of periods that have to be accommodated in each section is different. To reject $2 \cdot f_d$ ($m = 2$) and $3 \cdot f_d$ ($m = 3$), a whole perturbation period and one and a half perturbation periods, respectively, have to inserted. Figure 5.10 is a photograph of the order-3 Butterworth bandpass filter where the wiggle of the two first sections, *i*=1 and 2, rejects $3 \cdot f_d$, and the wiggle of the two last ones, *i*=3 and 4, rejects $2 \cdot f_d$. The strip width modulation in each section follows the expression given in eqn. (5.10), employing the parameters of Table 5.4. Like in the previous example, the separation between the coupled lines in the *i*-th section, s_i, and the *i*-th section length, l_i, are the same as for the classical filter.

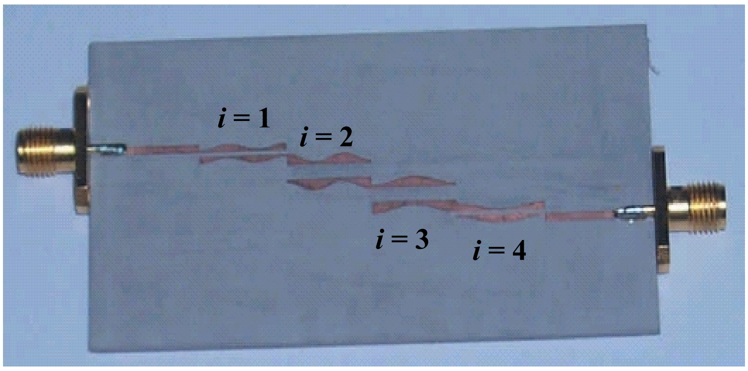

Figure 5.10: *Order-3 Butterworth bandpass microstrip filter centered at 2.5 GHz with a 10% fractional bandwidth. The strip widths in the classical filter are modulated so that the first and second spurious passbands are suppressed.*

i	w_i, mm	s_i, mm	l_i, mm	M_i(%)	ϕ_i (degrees)	Periods per section $l_i / \lambda_{B,i}$
1	0.75	0.42	11.98	50	90	1.5
2	1.09	1.70	11.54	50	270	1.5
3	1.09	1.70	11.54	50	90	1
4	0.75	0.42	11.98	50	270	1

Table 5.4: *Physical parameters for the order-3 Butterworth bandpass filter centered at 2.5 GHz with a 10% fractional bandwidth, with suppression of the first and second spurious passbands. The input and output port strip widths are 1.2 mm for a 50Ω-impedance.*

Figure 5.11(*a*) shows the simulated transmission parameters for the filter designed following the classical method (thin solid line) and for the wiggly-line filter of Fig. 5.10 (thick solid line). Figure 5.11(*b*) is a measurement of the wiggly-line filter transmission parameter. Note the reduction in the spurious passband levels, below –20 dB both in simulation and measurement for the first and second spurious passbands when the strip widths are modulated.

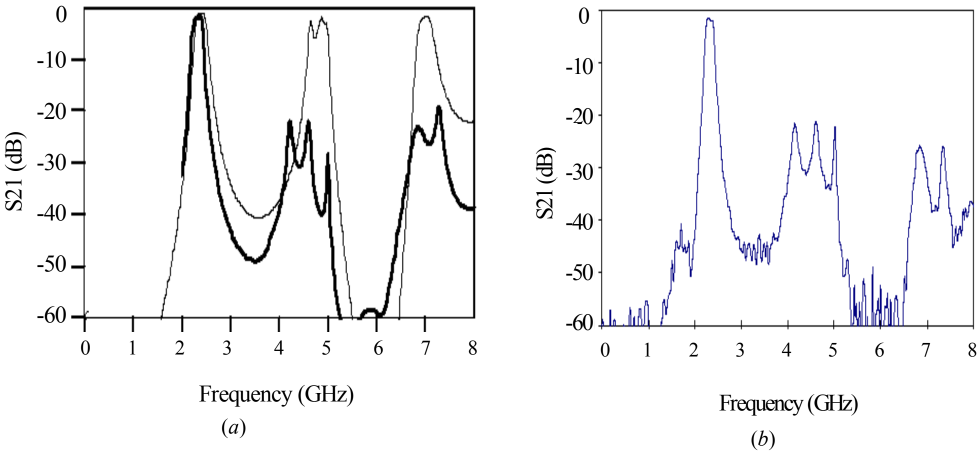

Figure 5.11: *(a) Simulated* $|S_{21}|$ *-parameter for a classical coupled-line order-3 Butterworth bandpass microstrip filter centered at 2.5 GHz with a 10% fractional bandwidth (thin solid line), and for the wiggly-line filter to reject the first and second spurious passbands (thick solid line); (b) measured* $|S_{21}|$ *-parameter for the wiggly-line filter.*

Similarly, an order-7 bandpass filter, centered at 2.5 GHz with a 10% fractional bandwidth, is designed so that the spurious passbands at $2\cdot f_d$, $3\cdot f_d$, $4\cdot f_d$ and $5\cdot f_d$, i.e. m = 2, 3, 4, and 5, are strongly suppressed. The physical filter parameters are now given in Table 5.5, and a photograph of the circuit is shown in Fig. 5.12. The modulation depth parameter M is now allowed to change from section to section.

i	***w_i*, *mm***	***s_i*, *mm***	***l_i*, *mm***	***M_i (%)***	***ϕ_i (degrees)***	*Periods per section* $l_i / \lambda_{B,i}$
1	0.47	0.27	12.34	87.5	270	1
2	1	0.9	11.67	75	90	1
3	1.09	1.77	11.53	50	270	1.5
4	1.10	2.15	11.51	50	90	1.5
5	1.10	2.15	11.51	50	90	2
6	1.09	1.77	11.53	50	270	2
7	1	0.9	11.67	75	90	2.5
8	0.47	0.27	12.34	75	90	2.5

Table 5.5: *Physical parameters for the order-7 Butterworth bandpass filter centered at 2.5 GHz with a 10% fractional bandwidth, with suppression of the four first spurious passbands. The input and output port strip widths are 1.2 mm for a 50Ω-impedance.*

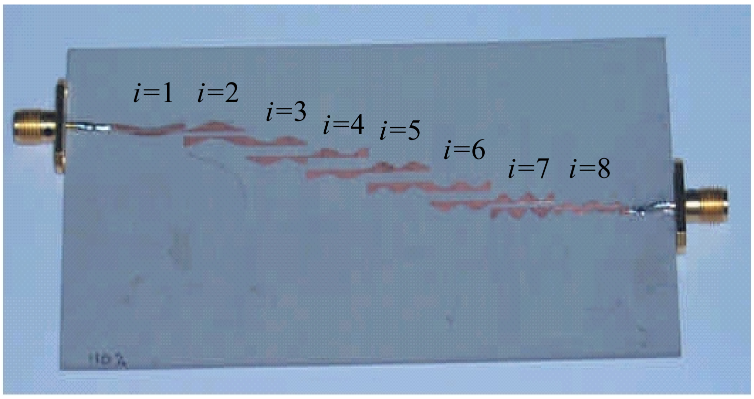

Figure 5.12: *Order-7 Butterworth bandpass microstrip filter centered at 2.5 GHz with a 10% fractional bandwidth. The strip widths in the classical filter are modulated so that the four first spurious passbands are suppressed.*

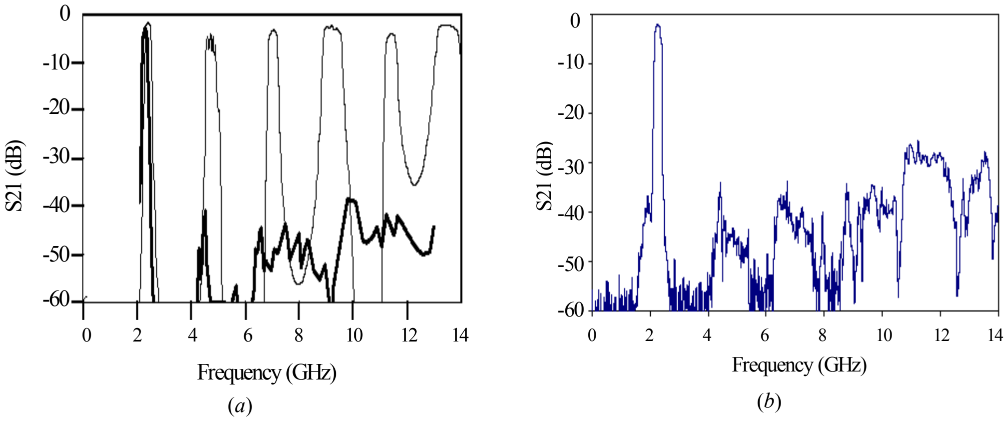

Figure 5.13: *(a) Simulated* $|S_{21}|$ *-parameter for a classical coupled-line order-7 Butterworth bandpass microstrip filter centered at 2.5 GHz with a 10% fractional bandwidth (thin solid line), and for the wiggly-line filter to reject the first four spurious passbands (thick solid line); (b) measured* $|S_{21}|$ *-parameter for the wiggly-line filter.*

In Fig. 5.13(*a*) it can be seen that the simulated levels of the spurious passbands are below –40 dB for the wiggly-line filter. Experimental results confirm a rejection level near –30 dB for all the spurious passbands, as can be seen in Fig. 5.13(*b*). The return losses, on the other hand, are better than –10 dB in the desired passband, being near 0 dB in the rejected bands.

To finish this section it can be concluded that varying continuously the strip widths of parallel-coupled-lines following a law of one or some consecutive sine-functions, one or several harmonic passbands could be rejected. These coupled-line bandpass microstrip filters with sine-like modulated strip width have enhanced out-of-band behavior, whilst the main passband is almost unaltered. This technique has important advantages over other alternative solutions as the use of a UC-PBG structure as a modified ground plane, since the wiggle of the lines does not force the prototype parameters to be recalculated and they do not demand special fabrication processes or anything different to those requirements made for classical coupled-line microstrip filters.

5.2. Harmonic suppression in active circuits: active antenna

In this section the performance of an active antenna in microstrip technology is notably improved by introducing PBG structures produced by etching the ground plane. The active antenna consists of a microwave oscillator directly feeding a patch antenna, and the aim of the PBG structure introduced is to suppress the harmonics present in the radiated power spectrum, increasing at the same time the power level in the fundamental frequency. As it will be seen, the introduction of the PBG structure is trouble-free, since it does not require a redesign of the circuit, and the circuit layout area needed will be maintained.

Up to now, the application of PBG structures for the reduction of harmonic content in the output signal of active circuits has been customarily limited to the addition in cascade of the PBG structure at the output of power amplifiers or mixers [RAD 98a], [HAN 99], [YAN 99a]. Recently, similar structures have been included in the input matching network of oscillators in order to provide harmonic tuning or a more selective resonator for phase noise reduction [XUE 01],[LEE 02].

However, the PBG structures employed for all the above mentioned designs are discrete. As it was demonstrated in chapter 4, section (4.6), and in references [LOP 00], [LAS 00a], these discrete PBG structures present a frequency response that rejects the desired frequency band and its harmonics. This is a limitation for harmonic cancellation in active circuits because if the structure is designed to reject the second harmonic at $2 \cdot f_0$, then the harmonics at $4 \cdot f_0$, $6 \cdot f_0$, etc.. (the even ones) will be rejected, but the odd ones (the third harmonic at $3 \cdot f_0$ and so on) will not be rejected [XUE 01].

To overcome this drawback, rejecting simultaneously the second and third harmonics, we propose to introduce a multiple-frequency-tuned PBG microstrip structure etched in the ground plane, as those proposed in chapter 4, section (4.6). It will be placed distributed along the whole oscillator circuit, and will follow a continuous pattern formed by the addition of two raised sines tuned at the frequencies to be rejected. As a result of it, an increase of the power in the fundamental oscillation and a rejection of the second harmonic will be observed as in [XUE 01], but this time the third harmonic will be also strongly reduced and the boost of the fundamental oscillation power will be larger.

The design of the active antenna in microstrip technology with a microwave oscillator and a patch antenna as terminating load is the first task to be solved. A medium power

Si BJT transistor, AT-42035, has been selected, operating at V_{CE}=8 V, and I_C=35 mA. The selected configuration is the common base transistor due to its higher instability. Following a classical oscillator design linear method [POZ 98], based upon the small signal S parameters, a stable oscillation can be obtained selecting the load network as indicated by eqn. (5.13) (see the schematic diagram of Fig. 5.14):

$$R_L = -\frac{R_{IN}}{3} \quad , \qquad X_L = -X_{IN} \tag{5.13}$$

the first term in eqn. (5.13) accounts for the evolution of the negative resistance in stable oscillation operation, whereas the second one, fixes the circuit resonance. The input impedance of the matching network (Z_T) can be transferred to the interface between the transistor and load network as:

$$\Gamma_{IN} = S_{11} + \frac{S_{12} \cdot S_{21} \cdot \Gamma_T}{1 - S_{22} \cdot \Gamma_T} \tag{5.14}$$

allowing the determination of the optimal matching network. It is important to recall that in this case the terminating load is constituted by a patch antenna designed to operate at the oscillation frequency.

This linear design method provides the resonance frequency value but no information can be extracted about the fundamental oscillation power level nor the harmonics levels.

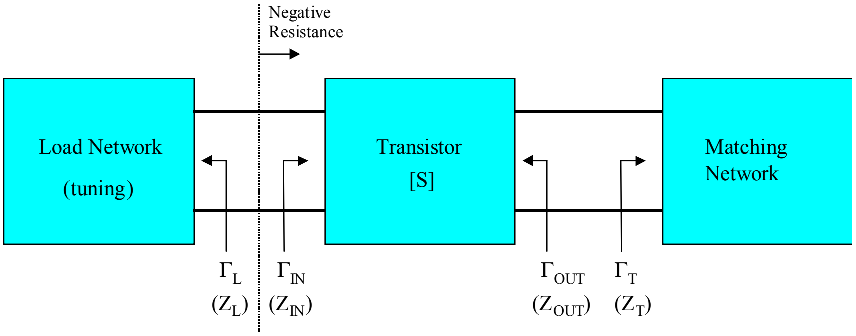

Figure 5.14: *Schematic diagram of transistor, load and matching networks of the oscillator.*

In our design, the oscillation frequency has been fixed to 4.5 GHz, and the prototype has been fabricated in a *Rogers RO3010* substrate (dielectric constant $\varepsilon_r = 10.2$, and thickness 1.27 mm), using a numerical milling machine. A photograph of the active antenna prototype is shown in Fig. 5.15.

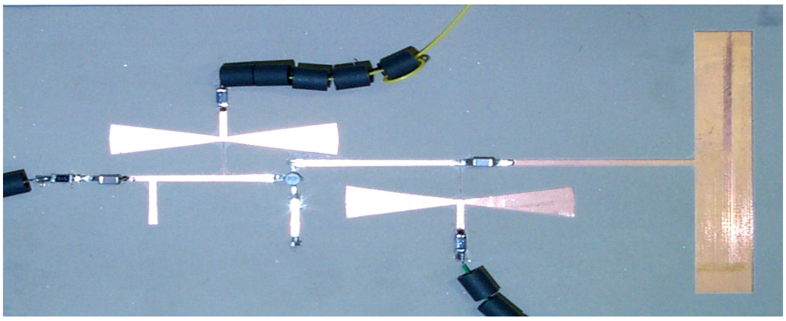

Figure 5.15: *Prototype of the classical active antenna in microstrip technology designed to operate at 4.5 GHz.*

The active antenna with PBG structure is designed by choosing the continuous PBG pattern in such a way that, for the fundamental frequency of oscillation, the introduced PBG perturbation does not change significantly the impedances seen by the transistor (the fundamental frequency of oscillation is placed at the passband of the PBG). Conversely, the rejected bands where the PBG provides high reflection are tuned to be centered around the second and third harmonics of the oscillator, at 9 GHz and 13.5 GHz in our case. The details of the PBG design process are given in chapter 4, section (4.6), and the periods of the added raised sines necessary in our case are a_1=6.2 mm (to reject the second harmonic) and a_2=4.1 mm (to reject the third harmonic). The amplitude of the perturbation to period ratio used (r_1/a_1 , r_2/a_2) is equal to 0.3 for both raised sines. The designed PBG structure has been simulated using *Agilent Momentum*, and its frequency response in transmission (S_{21} parameter) is given in Fig. 5.16.

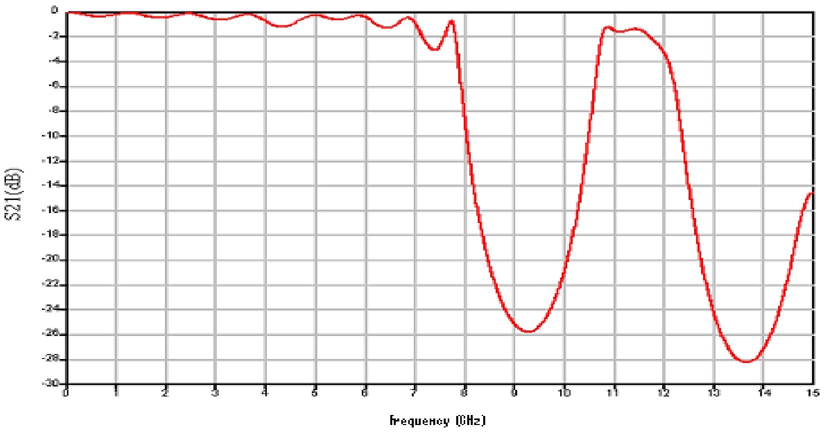

Figure 5.16: *Simulated frequency response in transmission of the designed multiple-frequency-tuned PBG structure. The total length of the simulated device is* $4 \cdot a_1$.

As it can be seen, the fundamental frequency of oscillation (4.5 GHz) is placed in the passband, and hence the PBG structure has very little effect over it. On the other hand, the second and third harmonics of the oscillator (9 GHz and 13.5 GHz) are placed in rejected bands, and therefore they will be strongly reflected by the PBG structure.

The multiple-frequency-tuned PBG pattern is etched in the ground plane of the otherwise classically designed microstrip active antenna, and the layout of the resulting active antenna with PBG is given in Fig. 5.17.

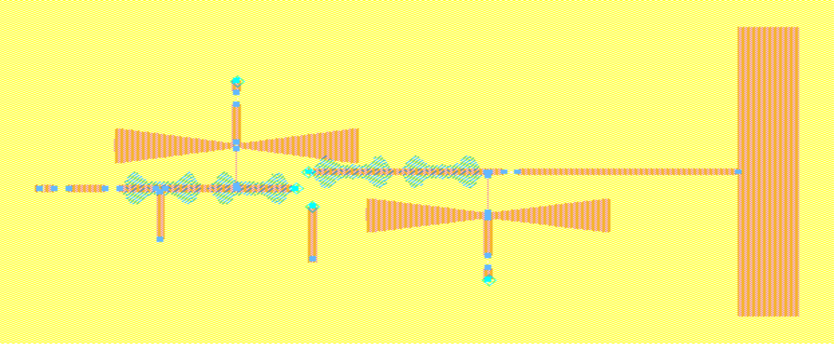

Figure 5.17: *Layout of the active antenna prototype with PBG, designed to operate at 4.5 GHz. The orange parts represent the upper plane conductor strip, and the blue parts represent the area etched in the ground plane.*

Both active antenna prototypes, with and without PBG etched in the ground plane, have been measured in the near field by means of an *Agilent* PSA E4440A Spectrum Analyzer and a rectangular horn antenna optimized for the fundamental oscillation. The experimental results are presented in Fig. 5.18, for the classical active antenna (blue line), and for the active antenna with PBG (red line). It can be seen, for the prototype with PBG, that the second harmonic has been reduced around 20 dB, and the third harmonic in at least 10 dB, as it was expected from the selective frequency behaviour of the PBG shown in Fig. 5.16. In addition, rejection levels of about 1 dB for the fourth harmonic, and 6 dB for the fifth one are achieved, probably due to the increase of radiation losses. Moreover, an increase of the fundamental oscillation power of around 3 dB is also achieved, due to the fact that the oscillation conditions have been changed with the introduction of the PBG.

It is important to note that the frequency dependency of the horn antenna gain is disregarded in our measurements, but obviously it has no effect in our comparative discussion.

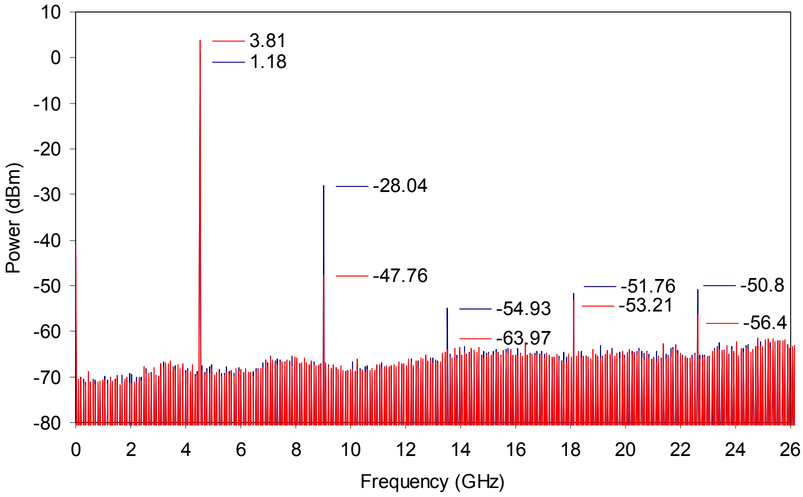

Figure 5.18: *Measured power spectrum for the classical active antenna (blue line) and for the active antenna with PBG (red line). The frequency dependency of the horn antenna gain is disregarded.*

To conclude this section it is important to remark that the benefits of introducing a PBG structure etched in the ground plane of a microstrip active antenna in order to suppress its second and third harmonic, have been experimentally demonstrated. An increase of the fundamental oscillation level has been also achieved.

The multiple-frequency-tuned PBG structure can be very useful for simultaneous rejection of the second and third harmonics in active circuits, and as it has been seen in the example of this section, it could be very easily introduced without requiring a redesign of the circuit or an increase in the circuit layout area.

5.3. Enhanced lowpass filter

In this section, stepped-impedance lowpass filters in microstrip technology have been designed by taking advantage of metal patterning of the front and back-side planes. It is shown that such an approach with etched holes in the ground plane for the high impedance sections permits one to alleviate some of the drawbacks associated with uniplanar impedance modulated filters with high geometric aspect ratios. Prototypes for the S and C-bands were fabricated by conventional low-cost printed circuit techniques and show improved performances in terms of rejection and bandwidth.

Novel portable and array-like communication-related applications are highly demanding of high performance compact filters with ever improved rejection over a broad band and low losses. In addition, such filters have to be manufactured in a low-cost and industrial-qualified technology which is now one of the driving forces for large volume market applications. This explains why microstrip technology is often preferred to intrinsically higher performance but also more critical technologies such as coplanar waveguides on free standing membranes defined by bulk micromachining [BLO 98], [DUP 99]. However, in practice microstrip technology, which is now very mature [GUP 96], requires a limited technological effort with printed-type processing techniques. One of the key figures of merit of microstrip filters is the impedance jump which is possible to realize on the front side of the circuit by patterning low (wide strip) and high (narrow strip) impedance sections. This impedance ratio is primarily defined by the geometrical aspect ratio keeping in mind some limitations associated to the increase of ohmic metallic losses and fabrication tolerances in narrow strips, and of radiation losses for large discontinuities. These considerations have been already recognized in the literature giving rise to new proposals based in majority on bulk micromachining techniques. By these means it is possible to locally modulate the permittivity of the substrate with air-like or semiconductor-like media giving rise to the so-called synthesized substrate technology [DRA 01].

The use of a periodic arrangement of air/high refractive index materials was also proposed for Photonic Band Gap (PBG) frequency selective devices in microstrip technology with the drilling of holes in the substrate while the strip width is maintained uniform. It was also demonstrated that etching the holes in the ground plane instead of in the substrate provided even better results [QIA 97], [RAD 98].

Here we are going to show that this last approach can be combined with a 2D½ scheme (ground plane etching coordinated with the upper strip width variations) so that some of the shortcomings in connection notably with the inherent losses of filters with a large number of sections can be overcome. We are going to demonstrate that such a two-side patterning technique is a high-performance and a low-cost alternative solution by fabricating and analyzing several prototypes, with constant periods or chirped patterns. These structures, designed for the S and C-band operation, exhibit higher performances in terms of rejection and bandwidth compared to conventional approaches [AKA 02].

Basically, two approaches can be investigated for the development of compact high-rejection filters on the modeling side. Both of them are based on a Bragg reflection concept which is implemented in the first approach via the drilling of holes within the substrate. The result of this is a large modulation of the refractive index (permittivity) constant, favorable to a high ratio between the low and high impedance sections. However, from the technological point of view, such an approach requires the development of specific technologies aimed at fabricating the holes. One solution is the drilling of holes through thin dielectric materials such as SU-8 or BCB films. The second approach involves the patterning of holes in the ground plane. Such a technology has demonstrated interesting performances with uniplanar structuring scheme provided that the holes are large enough with respect to the strip width on the front side whose value in this previous experimental works was kept constant. The filters in the present section were designed using *Agilent Advanced Design System (ADS)* software and *High Frequency Structure Simulator (HFSS)*. We decided to design several prototypes: (i) with constant-length impedance sections aimed at the demonstration of the underlying concepts and (ii) chirped devices with a Tchebyscheff design [KAR 02]. The electromagnetic simulations of these filters indicated that higher rejection and wider bandwidth are obtained with respect to their conventional counterpart even with a limited number of sections. On this basis, several prototypes were fabricated using a numerical milling machine in a Rogers Duroid 6010 substrate (1.27 mm-thick, and with dielectric constant of 10.2).

Figure 5.19 is a photograph of the front- and the back-side of a fabricated prototype. The width of the high impedance sections (with lengths l_3 and l_5) reinforced by the presence of holes in the ground plane is 0.4 mm. For the prototypes with constant-length sections ($l_2=l_3=l_4=l_5=l_6=7.1$ mm) the holes have a circular shape and a diameter of 7 mm, and the width of the low impedance sections (with lengths l_2, l_4, l_6) is 8 mm. On the other hand, for the chirped devices with Tchebyscheff design the holes have rectangular shape and a width of 8 mm, the low impedance sections have a width of 5 mm and the length of each section is variable as given in Table 5.6.

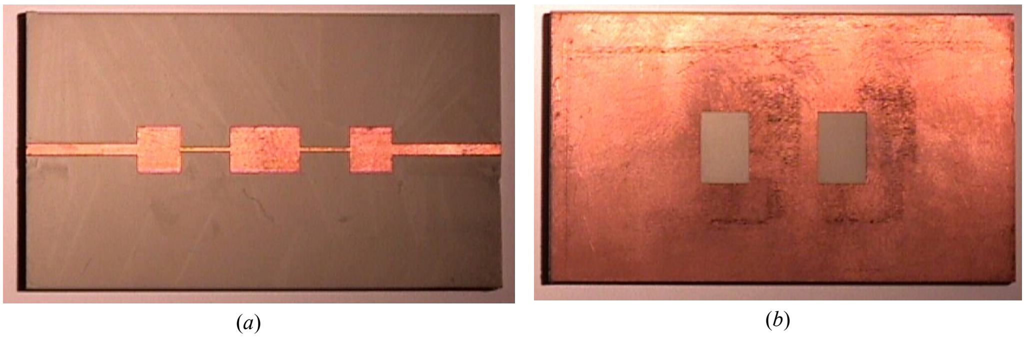
(*a*) (*b*)

Figure 5.19: *Photographs of the surface micromachined Tchebyscheff-type filter (a) front side (b) back side. Dimensions are given in Table 5.6.*

	l_1	l_2	l_3	l_4	l_5	l_6	l_7
(mm)	15	4.47	5.22	7.25	5.22	4.47	15

Table 5.6: *Lengths of the sections for the double side Tchebyscheff filter.*

For the RF assessment of the filters and in view of the low frequency pass band, necessary for the targeted application, simple SMA connectors were soldered on each side of the circuit. A Vector Network Analysis (VNA) was subsequently swept from 0.5 to 12GHz. Fig. 5.20 shows the frequency dependence of the transmission coefficient S_{21} for the prototype with constant-length sections. The frequency cutoff defined at 3dB bandwidth was around 1.5 GHz whereas the maximum of the rejection corresponding to the Bragg condition was at 3.6 GHz. At increasing frequencies, higher-order frequency passbands can be noticed in agreement with the theoretical analysis of periodic media. However, due to the fact that the structure is finite, instead of a pure passband, one can note the presence of discrete peaks which are the signature of the number of sections. This ripple in the passband of the filter with constant-length sections can be significantly improved by a chirp-like approach as it will be seen later. The thick line shows the theoretical frequency variations calculated using the HFSS software. The comparison between measured and calculated data is overall satisfactory, notably for the characteristic frequencies. In addition, it can be noticed that the second pass band, around 6 GHz, is relatively narrow, both stop bands practically overlapping. This result is particularly encouraging since very broadband rejection filters are of interest in modern telecommunication systems opening the possibility of an absolute overlapping of gaps via stub-like approach as will be seen later.

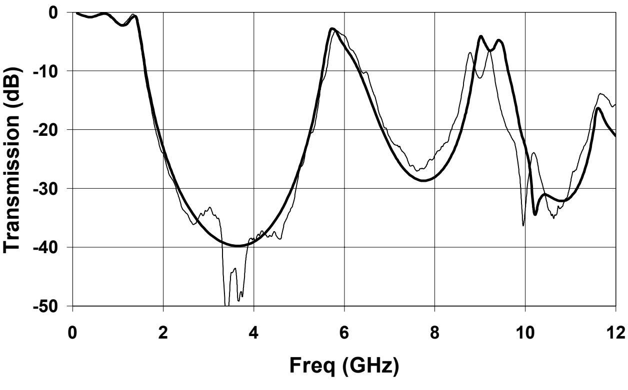

Figure 5.20: *Simulated (thick line) and experimental (thin line) variations versus frequency of* S_{21} *for a double side PBG microstrip filter with 5 constant-length sections.*

Regarding the chirped prototypes, the experimental and simulated results achieved with the Tchebyscheff-type 5 section filter with holes micromachined in the ground plane are plotted in Fig. 5.21 and compared to the corresponding conventional microstrip filter. For comparison, the key figures such as maximum ripple in the pass-band, cut-off frequency and number of sections were kept equal for the single and double side designs. Also we intentionally limit the number of sections to 5 for highlighting the improvements brought by the two side scheme. It can be seen that the introduction of holes significantly improved: (i) the rejection with 35 dB around 5 GHz for a PBG-like prototype instead of 22 dB for a conventional configuration, (ii) a dramatic increase of the bandwidth with only one peak of spurious transmission around 6.2 GHz. In contrast the conventional Tchebyscheff filter shows three peaks of transmission in the 5.5-7.5 GHz bandwidth which are more difficult to suppress.

In order to demonstrate the compactness offered by the double side topology filter we have realized a classical Tchebyscheff filter with the same passband ripple and the same rejection in the middle of the gap than the double sided 5 section filter. This classical Tchebyscheff filter has 7 sections and its total length is $L_{classical}$=36.27mm whereas the 5 section double side filter is only $L_{double\ side}$=26.6mm. It means, on this example, that to obtain the same rejection, the length of the classical filter is 36% longer than the double sided one (the filter that includes a PBG-like structure in its ground plane).

The origin of this improvement can be understood from the coordinated combination of the stepped-impedance filter implemented in the conductor strip, and the PBG perturbation etched in the ground plane.

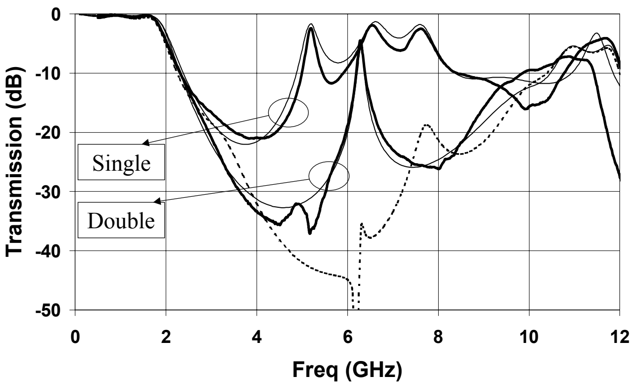

Figure 5.21: *Measured (thick line) and simulated (thin line) results for a conventional single side 5-section Tchebyscheff-type filter and the double side one. The double side filter with one stub (as explained later) is represented by the dotted line (simulation results).*

To have a further insight into the explanation of the resonant transmission at 6 GHz observed in Fig. 5.21 for the double side design, we first analyze the radiating term via the frequency dependence of $1-(|S_{11}|^2+|S_{21}|^2)$. A peak was clearly apparent at this characteristic frequency with around 50% losses. The mapping of the electric field given in Fig. 5.22 along the filtering cells at the center of the metallic strip shows that this spurious transmission peak reflects a quasi-stationary resonant regime resulting from the extra structuring of the ground plane. As shown in the dotted lines in Fig. 5.21, it can be demonstrated however that such a spurious transmission can be suppressed via an additional stub placed in the input section. With a stub width of 0.24 mm and a stub length of 4.75 mm, the bandwidth at – 20 dB extends over practically 5 GHz.

The concept of modulation of effective medium via surface micromachining of the ground plane (introduction of a PBG structure by etching the ground plane) is quite general and could be further extended with the implementation of slow wave periodic structures instead of devices fabricated from high permittivity substrate which are often very lossy. Such a periodic arrangement modifies the dispersion relation in a similar manner to that observed in transmission lines periodically loaded by discrete devices. From the technological point of view, especially with respect to the bulk micromachining version with a modification of the local permittivity by forming an air micro-cavity, it seems that the key advantage is the ease of fabrication. Despite the progress reported in the definition of air-filled cavity in semiconductor notably for a Silicon Based technology this kind of approach requires a film to sustain the metallic lines (polyimide, silicon nitride or silicon dioxide) which could be critical in an industrial environment.

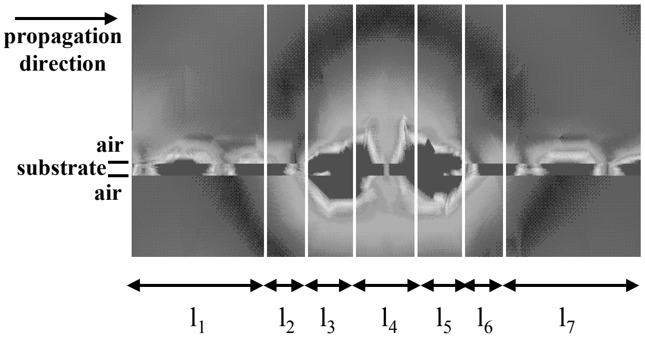

Figure 5.22: *Illustration of the quasi-stationary resonant transmission around 6.2GHz with an electric field mapping in the center of the metallic strip.*

To conclude this section it is important to remark that several microstrip lowpass filters have been designed, manufactured and RF characterized. The optimized prototypes have been obtained by using a two side patterning scheme (the stepped impedance conductor strip width variation, coordinated with a PBG structure etched in the ground plane) in order to strengthen the ratio between the impedance variation which is at the origin of the frequency selectivity. The prototypes under investigation were designed for S and C-bands application and more specifically for an electronically steerable antenna. The results obtained show that the frequency response of the stepped impedance microstrip lowpass filter is greatly improved by the introduction of the coordinated PBG structure in the ground plane.

5.4. High rejection bandpass filter

In this section we propose a new way to implement bandpass filters in microstrip technology. It consists on using two Photonic Bandgap (PBG) reflector structures (stopband filters) in cascade, tuned at different frequencies. In this way a bandpass with low attenuation is opened between the two rejected frequency bands. Optimizations of the PBG microstrip structures like those seen in chapter 4 will be used (tapering, compact arrangements) to obtain higher performance.

Here, specifically, two optimized meander PBG microstrip reflectors, like those designed in chapter 4, section (4.5), centered at different frequencies, and placed in cascade will be used. Very long reflectors and reasonable circuit layout area are compatible using the compact hole-arrangements studied in section (4.5). In this way, a flat passband can be opened between two deep rejected bands with sharp cutoffs. The advantage of this type of filter is that optimizing the behavior of each reflector individually, the filter parameters are highly improved. Specifically, the filter design parameters depend only on the frequency position of these reflectors (filter passband bandwidth) or on the individual reflectors (cut-off sharpness, rejection values, passband attenuation), which can be highly optimized. (Here, for example, using the meandering and tapering techniques described in chapter 4, section (4.5)) [LOP 99b].

Next, a bandpass filter centered around 4.1 GHz with a 600 MHz -3 dB bandwidth is designed. The first reflector is designed at 3.2 GHz, which implies a structure period $a = 18.9$ mm, and the second one is centered at 5.1 GHz, having a period $a = 11.7$ mm, in a *Rogers RO3010*™ substrate ($\varepsilon_r = 10.2$, thickness $h = 50$ mils, dielectric loss tangent $\tan\delta = 0.0026$ and conductor $\sigma = 5.8 \cdot 10^7$ S/m) and with $w = 1.2$mm-wide strips for 50Ω–input and output ports. Both reflectors follow a compact arrangement having 5×5 periods in the first case, and 3×9 periods in the second case. The bends have been optimized using chamfering techniques and the reflectors have been also tapered using a Hamming window to flatten their passbands as explained in section (4.5). The maximum radius to period ratio is 0.25. The total device dimensions are 15.5 cm × 11 cm. A flat passband can be expected for the 5×5 reflector on the right of its rejected band, as well as flat passbands for the 3×9 reflector at both sides of its rejected band (see chapter 4, section (4.5)). This way, the overlapping should yield to a flat passband between two profound and steep rejected bands. The (conductor-and-dielectric lossless) simulated results (obtained using *Agilent Momentum* and *ADS*) for this filter, Fig. 5.23, show a very promising flat passband with low attenuation (1 dB) between two very deep (80 dB and 70 dB of rejection) and very sharp (446 dB/GHz and 222 dB/GHz) stopbands. This prototype has been fabricated using a numerical milling machine (see photograph in Fig. 5.24) and measured with an HP 8753D vector network analyzer. Experimental data are shown in Fig. 5.25. A flat passband with an attenuation of 7 dB is measured around 4.4 GHz with a bandwidth of 450 MHz. The rejection values at both sides of the passband are around 52 dB for the lower stopband and 48 dB for the upper stopband. The cut-off sharpness is 520 dB/GHz and 400 dB/GHz, respectively. The differences found between the simulated and the experimental data can be attributed to the employment of a medium quality substrate with significant conductor and dielectric losses that are not taken into account in the simulations. Actually, to improve these experimental results, a higher quality substrate could be used.

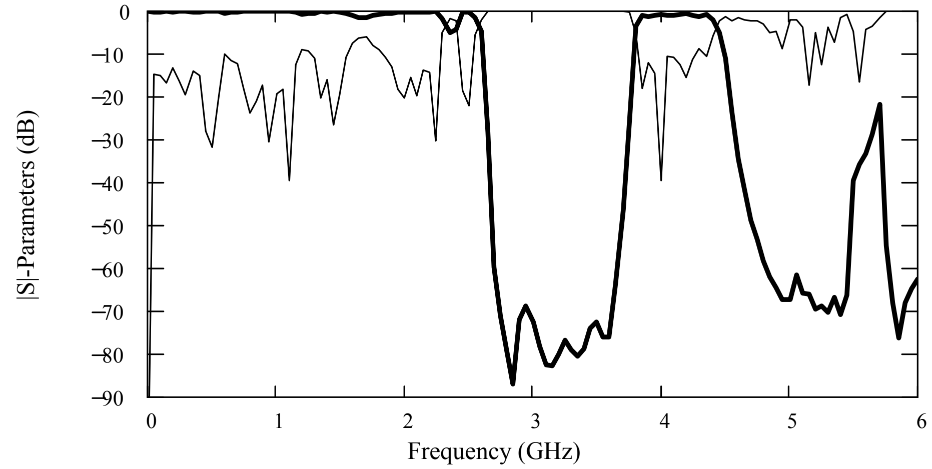

Figure 5.23: *Simulated* $|S_{11}|$*-parameter (thin line) and* $|S_{21}|$*-parameter (thick line) for the bandpass filter prototype formed by two compact PBG reflectors.*

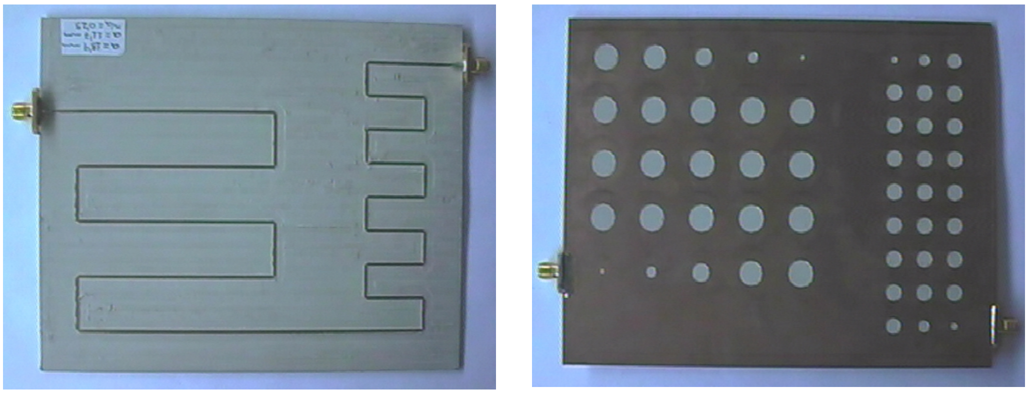

(*a*) (*b*)

Figure 5.24: *Photograph of the bandpass filter prototype formed by two cascaded compact PBG reflectors: upper plane (a) and ground plane (b).*

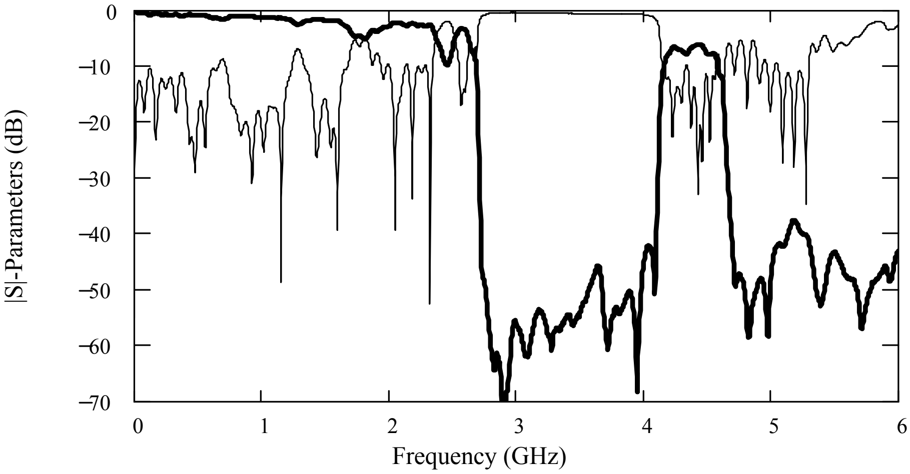

Figure 5.25: *Measured* $|S_{11}|$*-parameter (thin line) and* $|S_{21}|$*-parameter (thick line) for the bandpass filter prototype formed by two compact PBG reflectors.*

To conclude this section it is important to highlight that a novel technique to implement bandpass filters in microstrip technology has been proposed and successfully tested. It consists on the use of two PBG reflectors in cascade. The advantage of this type of filter is that design parameters depend only on the frequency position of its reflectors (filter bandwidth) or on the individual reflectors (cut-off sharpness, rejection values, passband attenuation), which can be highly optimized. Tapering techniques and compact arrangements have been used to improve the behavior of the filter obtained. The design frequency of our constructed prototype is "low" in order to measure it with our HP 8753 D network analyzer (up to 6 GHz). The physical dimensions obtained are large for these frequencies. Anyway, this design technique can be scaled to higher frequencies, obtaining smaller physical dimensions and maintaining the high performance.

5.5. High-Q PBG resonator

In this section a high-Q resonator based on a defected PBG microstrip structure will be designed and tested. To obtain the resonator, an optimized defect will be introduced in the middle of a uniform PBG structure. Here, the basic PBG microstrip device proposed in [RAD 98] and presented in chapter 4, section (4.1), (photograph in Fig. 4.1, and measurements in Fig. 4.2) will be used as starting point. It has been constructed using a numerical milling machine in a Rogers RT/Duroid 6010 substrate, (dielectric constant ε_r=10.2 and thickness h=1.27 mm). The period of the PBG structure has a value a=14.1 mm, producing a wide rejected band centered around f_{max}= 4 GHz, following eqn. (3.70) of chapter 3 (repeated as eqn. (5.1) in this chapter):

$$f_{max} = \frac{c}{2 \cdot \sqrt{\varepsilon_{eff}} \cdot a} \tag{5.1}$$

where for the sake of simplicity ε_{eff} has been taken as the effective dielectric constant at 4 GHz of the unperturbed microstrip line (calculated using *Agilent Linecalc*™ or formulae in [YAM 79]). The radius of the circle to period ratio is r/a=0.25, and the number of periods employed is 9. The strip conductor width is constant, w=1.2 mm, corresponding to a nominal characteristic impedance of 50 Ω.

A plain defect in the PBG structure would consist on the absence of a hole column, giving rise to a resonator structure formed by two uniform PBG reflectors with 4 period each, united by a 180º length microstrip transmission line. The length of this transmission line will be optimized to obtain better performance, giving rise to an "optimized defect". To achieve it, the response of the 4 period PBG reflector must be analyzed. A simulation has been realized for the 4 period PBG reflector, using *Agilent Momentum* and *ADS* software. The results are presented in Fig. 5.26. The reflectivity achieved in the rejected frequency band is adequate to employ this element as reflector (mirror) in the proposed PBG resonator.

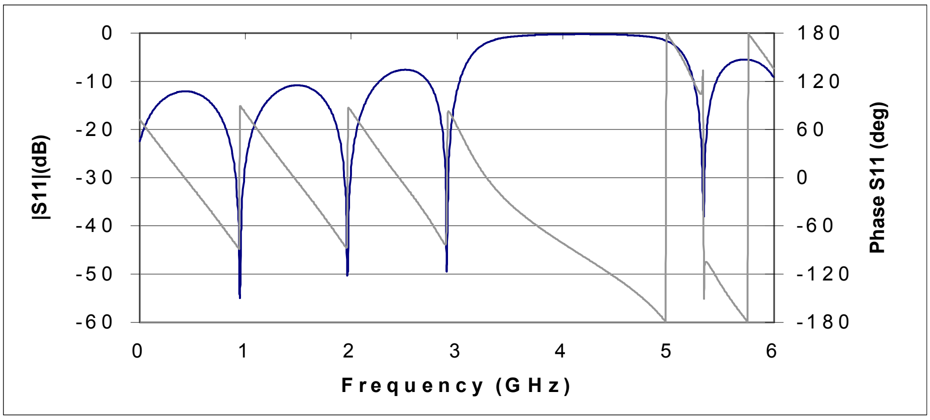

Figure 5.26: *Simulated S_{11} parameter for the 4 period PBG reflector of the resonator.*

As it has been explained, the resonator consists of two PBG reflectors separated by a 50 Ω microstrip transmission line that acts as a resonant cavity (see Fig. 5.27). This structure behaves in a similar manner as a Bragg Resonator. Therefore the resonant frequencies are the ones that fall in the reflected frequency band of the PBG reflectors and simultaneously satisfy the phase condition [BRA 83]:

$$\phi_{ref1}(f_{res}) + \phi_{ref2}(f_{res}) - 2 \cdot \beta(f_{res}) \cdot L = n \cdot 2\pi \tag{5.15}$$

being:

ϕ_{ref1}: phase of the reflection coefficient of the first reflector

ϕ_{ref2}: phase of the reflection coefficient of the second reflector

β : phase constant of the mode of interest in the "resonant cavity"

L : length of the microstrip transmission line that separates the two reflectors (length of the "resonant cavity")

n : an integer number (positive or negative)

Following eqn. (5.15), to design a PBG resonator we have to design and simulate first the PBG reflectors. That's why we have done it previously (see Fig. 5.26). The optimal frequency to design the resonator is the frequency at which the reflection coefficient in our reflectors is maximum. From the simulation (Fig. 5.26) it can be seen that this maximum reflection coefficient (maximum S_{11}) is obtained at a frequency f_{max} = 4.20 GHz, and the phase of the reflection coefficient (phase of the S_{11} parameter) at this frequency is $\phi(S_{11})$ = -95.849 °. Therefore to obtain an optimum design, the operating frequency of our resonator will be 4.20 GHz.

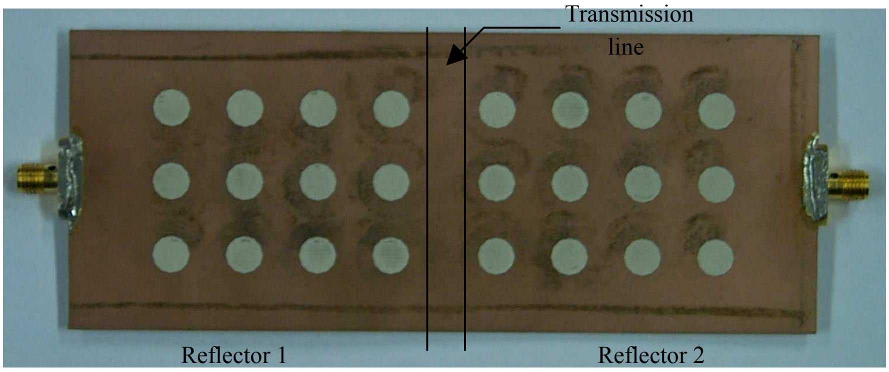

Figure 5.27: *Photograph of the PBG resonator prototype*

As we use two identical reflectors, the phase of their reflection coefficients will be equal, and following the simulated results we will have a value at the design frequency of: $\phi_{ref1} = \phi_{ref2} = -95.84^{\circ}$, so from eqn. (5.15), and taking $n = -1$, it can be obtained that the phase introduced by the microstrip transmission line must be $\beta \cdot L = 84.15^{\circ}$, that corresponds, for our substrate and design frequency, to a length L=6.25 mm.

The resulting PBG resonator will be formed, consequently, by two identical 4 period PBG reflectors, designed earlier, connected by a microstrip transmission line w=1.2 mm width (Z_0=50 Ω) and L=6.25 mm length (see [LOP 99]). The prototype has been produced in a substrate with $\varepsilon_r = 10.2$, loss tangent $\tan\delta = 0.0026$ and thickness $h = 50$ *mils*, by means of a numerical milling machine, and it is presented in Fig. 5.27.

The PBG resonator prototypes have been simulated with *Agilent Momentum* and *ADS* software. The measurements were taken using a HP^{TM} 8753D vector network analyzer.

In first place, the resonator obtained by introducing a plain defect in the PBG structure, as described previously in this section (180º length resonant cavity line), has been simulated. The results (Fig. 5.28) show that the performance obtained is not optimum, because the resonant frequency is notably shifted from the central frequency of the rejected band.

To place the resonant frequency at the center of the rejected band, the phase matching expression (eqn. (5.15)) presented before must be taken into account, and therefore the length of the transmission line must be optimized, as calculated previously. Now, the simulations and measurements of the optimized resonator (obtained previously by adjustment of the length of the resonant cavity transmission line) will be presented.

The first simulation with the resonant cavity line optimized (Fig. 5.29) has been realized in ideal conditions (i.e., without conductor and dielectric losses). The resonant frequency obtained with this simulation is f_{res}= 4.198 GHz, very close to the design

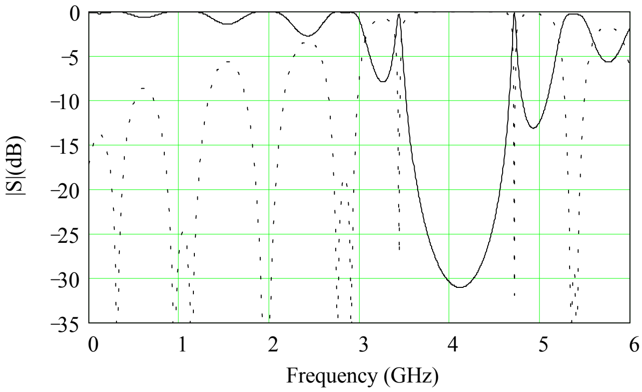

Figure 5.28: *Simulated S_{11} (dashed line) and S_{21} (solid line) parameters for the PBG resonator obtained by introducing a plain defect.*

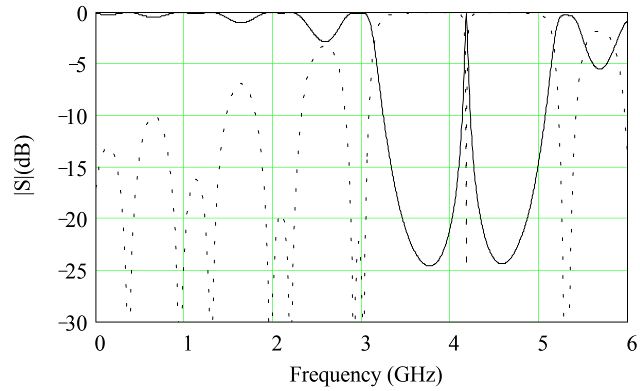

Figure 5.29: *Simulated S_{11} (dashed line) and S_{21} (solid line) parameters for the PBG resonator obtained by introducing an optimized defect. (The conductor and dielectric losses are neglected in this simulation).*

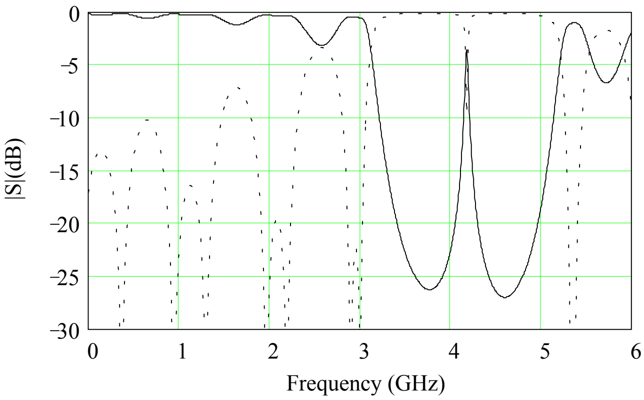

Figure 5.30: *Simulated S_{11} (dashed line) and S_{21} (solid line) parameters for the PBG resonator obtained by introducing an optimized defect. (The conductor and dielectric losses are taken into account in this simulation).*

frequency f_{design}= 4.20 GHz, and the value of $|S_{21}|$ at this frequency is –0.15dB also very close to the ideal value of 0dB.

The second simulation (Fig. 5.30) takes into account the losses in dielectric as well as in conductor. The obtained resonant frequency is similar to the last case (f_{res} = 4.21 GHz) but the S_{21} parameter at resonant frequency has a value of –3.50dB, which reveals that losses have a critical effect in resonator performance. Finally, the Q factor of the simulated resonators is 138.5 for the ideal case and 118.3 for the simulation accounting losses.

Regarding to the measurements, two circuits have been fabricated and measured. The first one is the 4 section PBG reflector of the resonator, and the other one is the optimized resonator.

The reflector measurements are presented in Fig. 5.31. The maximum reflectivity obtained is –0.21dB at a frequency of 4.248 GHz. Reasonable agreement is achieved between simulation and measurement, with a slight frequency shift where maximum reflectivity is obtained. Discrepancies between simulated and experimental data can be attributed to the absence of losses in the simulation, and to the moderate precision mesh used in the Momentum simulations for reasonable computing times.

For the PBG resonator, the measured resonant frequency is f_{res} = 4.42 GHz and the value of the $|S_{21}|$ parameter at this frequency is –4.85 dB, which can be seen in Fig. 5.32. Again a reasonable agreement is obtained between simulation and measurement, but there is a greater frequency shift than in the case of the reflector. This can be due to errors in the estimation of the phase of the reflectors, in our simulation. The value of the quality factor achieved in this measured case is Q = 129.2, similar to the values obtained in simulation.

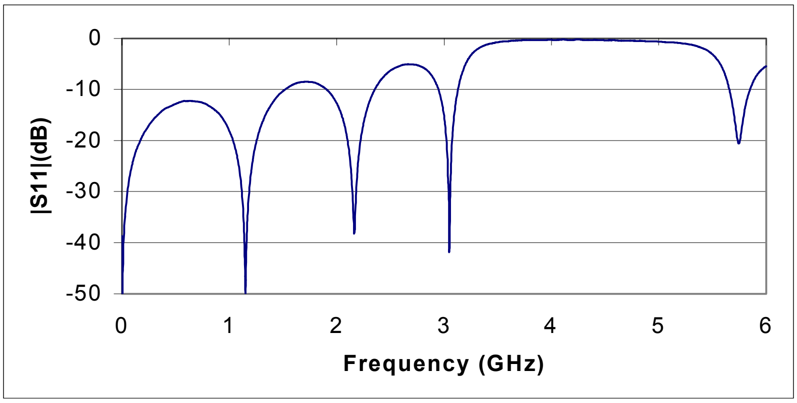

Figure 5.31: *Measured S_{11} parameter for the 4 period PBG reflector of the resonator.*

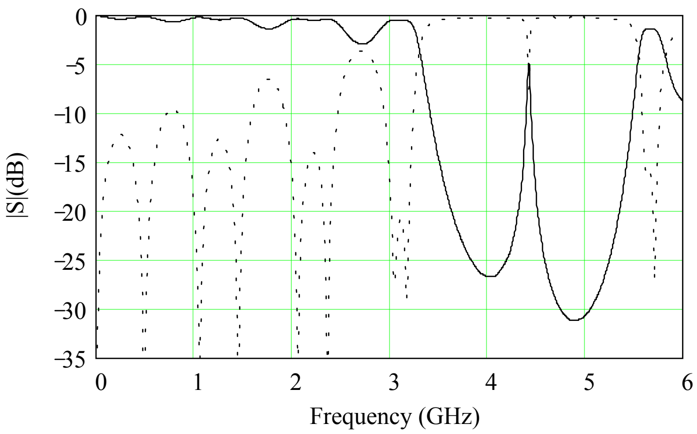

Figure 5.32: *Measured S_{11} (dashed line) and S_{21} (solid line) parameters for the PBG resonator obtained by introducing an optimized defect.*

The performance of the fabricated prototype could be improved if the 4 period PBG reflector is fabricated and its S_{11} phase measured, to redesign, using this value, the resonator.

To conclude this section it is interesting to remark that PBG resonators in microstrip technology obtained by introducing a defect in a uniform PBG reflector have been demonstrated both in simulation and measurement. A design approach has been proposed and successfully tested. The results demonstrate that it is not sufficient to produce a plain defect in the structure following [JOA 95] to obtain a good resonator, and therefore the resonator phase matching is critical in order to obtain good performance.

The value of the quality factor obtained by the so designed PBG resonator is promisingly high, considering the totally planar nature of the device. Substrate losses have demonstrated to be a key point to determine the real performance of the resonator. It is expected that the use of high quality low loss materials and optimized design techniques accounting losses in the resonator cavity will greatly improve the behavior of these structures. One very promising application for them would be the implementation of high performance planar oscillators.

5.6. Chirped delay lines

In this section we are going to study the use of PBG structures in microstrip technology to implement chirped delay lines (CDL), and a design method will be presented. The first approaches attempted used ground plane etching to implement the PBG structure in microstrip technology, following continuous patterns. However it was discovered that for this specific application better control over the circuit response was achieved implementing the structure by continuously varying the strip conductor width, so that the coupling location between the quasi-TEM microstrip mode and the same but counter-propagating mode is linearly distributed in frequency. In this way, as it was done in section (5.1.2), some of the concepts developed for PBG structures etched in the ground plane of a microstrip line are extended to the conductor strip width modulation.

High delay×bandwidth products, over frequency ranges of several gigahertzs, can be obtained following this procedure. Experimental data confirm the design method. Real-time Fourier analysis of wideband pulses can be performed using these CDLs.

A Chirped Delay Line (CDL) is a quadratic-phase filter whose frequency response $H(\omega) = A_0(\omega) \cdot \exp(-j \cdot \varphi_0(\omega))$, around a central frequency ω_0, is characterized by uniform insertion losses, $A_0(\omega)$, and a linear group-delay, $\dot{\varphi}_0 = d\varphi_0 / d\omega$, across the operating frequency-band. Different approaches have been followed to produce CDLs, mainly as components of compressive receivers [SKO 90]. Some of them are not simple to fabricate, while other ones do not meet easily the design specifications. Here, we report on a plain design method for CDLs in microstrip technology with continuously varying strip width to achieve closely the required frequency features, that is, the desired frequency range, delay versus frequency slope, and input/output impedance, and benefiting from fabrication on a mature technology and compatibility with monolithic circuits. This way, CDLs with very high time-bandwidth products (defined as the total delay excursion times the bandwidth), over ranges of several gigahertzs, can be obtained on high-dielectric-constant and thin substrates. Promising applications as the real-time spectral analysis of wideband signals can be envisaged using these devices [LAS 01a].

Let's see the microstrip CDL design. Let the characteristic impedance of a microstrip line be changed by a continuously changing profile, for example a non-uniform microstrip line with continuously varying strip width following a linearly frequency-modulated (chirped) continuous periodic function. Then, the phase-matching condition for resonant Bragg coupling between the quasi- TEM microstrip mode and the same but counter-propagating mode is ideally satisfied at only one position for each spectral frequency, from which it will be back-reflected. In fact, if the perturbation is linearly chirped then we will see that the mode-coupling location varies linearly in frequency and, as result, the reflection time is also a linear function of frequency.

Consider $Z_0(z)$ as the perturbed microstrip characteristic impedance given by $Z_0(z) = f_{\zeta(z)}(z)$, where $\zeta(z)$ represents the modulation of the local spatial angular frequency of a continuous periodic function $f(z)$, and z is the axis along which the microstrip CDL is extended from $z = -L/2$ to $z = L/2$, being L the device total length. We will show next that if $\zeta(z) = \zeta_0 + 2 \cdot C \cdot z$, then $Z_0(z)$ yields a mode-coupling location linearly distributed in spectral frequency. The parameter C (m^{-2}) fixes the variation rate of the local spatial frequency and $\zeta_0 = \zeta(z=0)$ is the value of the local spatial frequency at the device central point. The local spatial perturbation period *T(z)* is related to the previous parameter $\zeta(z)$ (local spatial angular frequency) as $T(z) = 2\pi/\zeta(z)$.

As it was seen in section (5.1.2), the Bragg condition states that the perturbation period for an angular frequency ω to be coupled to the counter-propagating quasi-TEM mode in a microstrip line can be estimated as $\lambda_g/2$ (π-rad phase-shift), being λ_g the guided wavelength at this frequency in the unperturbed (constant strip width) microstrip line. This condition was also seen from the point of view of the frequency of maximum reflectivity produced by a periodic perturbation of period T as:

$$f_{max} = \frac{c}{2 \cdot \sqrt{\varepsilon_{eff}} \cdot T} \Rightarrow \omega_{max} = 2 \cdot \pi \cdot f_{max} = \frac{\pi \cdot c}{\sqrt{\varepsilon_{eff}} \cdot T} \tag{5.1}$$

Then, the angular frequency locally reflected at z, $\omega_l(z)$, is found as:

$$\omega_l(z) = \frac{\zeta(z) \cdot c}{2 \cdot \sqrt{\varepsilon_{eff}\big|_{50\Omega}}} = \frac{c}{2 \cdot \sqrt{\varepsilon_{eff}\big|_{50\Omega}}} \cdot \left(\frac{2\pi}{a_0} + 2Cz \right) \propto z \tag{5.16}$$

if an impedance modulation around 50Ω is considered. $\varepsilon_{eff}\big|_{50\Omega}$ is the effective dielectric constant for a 50Ω-line at low-frequency regime (a quasi-static approximation is used), c is the speed of light in vacuum, and $a_0 = 2\pi/\zeta_0$ is the local spatial period at $z = 0$, which fixes the central operation frequency ω_0. Eqn. (5.16) anticipates that a linear spatial frequency modulation of the impedance provides a linear group delay in a bandwidth $\Delta\omega = \left|\omega_l(z=L/2) - \omega_l(z=-L/2)\right| = c \cdot |C| \cdot L \Big/ \sqrt{\varepsilon_{eff}\big|_{50\Omega}}$, around a central frequency $\omega_0 = c \cdot \pi \Big/ \left(a_0 \cdot \sqrt{\varepsilon_{eff}\big|_{50\Omega}} \right)$, and with a delay slope $|\ddot{\varphi}_0| = 2\sqrt{\varepsilon_{eff}\big|_{50\Omega}} \cdot L \big/ (c \cdot \Delta\omega)$, in units of s^2/rad, whose sign is the same as the sign of *C*. The delay slope is derived by taking into account that $\Delta\omega \cdot |\ddot{\varphi}_0|$ is the time-delay difference between the arrivals at the input of the extreme frequencies of the bandwidth, $\omega_l(z=-L/2)$ and $\omega_l(z=L/2)$, the former reflected at the input and the latter at the output of the device, respectively (path difference = 2·CDL length). Once the device length, *L*, and the variation rate of the local spatial frequency, *C*, in $f_{\zeta(z)}(z)$ have been fixed, we can straightforwardly test these design relationships by obtaining the single-mode loss-less behavior of the CDL, which provides valid information on the approximated operation frequency range and delay characteristic, by means of the approximated expression for the coupling coefficient obtained in chapter 2, section (2.3.2.3), from the characteristic impedance:

$$K(z) = \frac{1}{2} \cdot \frac{1}{Z_0} \cdot \frac{dZ_0}{dz} \tag{5.17}$$

and solving the simplified system of coupled mode equations (chapter 3, section (3.2)), valid for single mode operation. In this way, the S_{11} parameter at the input port, $z=-L/2$, is easily obtained assuming that the output port at $z=L/2$ is matched.

The function $f(z)$ is chosen to minimize the frequency interference of the spurious reflected bands, at the harmonics of ω_0, on the main band since low-rippled response is a requirement for a CDL. If $f(z) = 50 \cdot \exp(\sin(2\pi \cdot z/a_0))$ for a non-chirped impedance modulation (i.e., $Z_0(z) = f(z)$) around 50Ω with a spatial periodicity a_0, then $S_{11}(\omega, z=-L/2)$ can be analytically shown, using eqn. (5.17) and the simplified system of coupled mode equations, to be a single-frequency-tuned response mainly confined in the nearness of the central frequency ω_0, provided that $L >> a_0$ for high time-bandwidth products. This happens because the resulting coupling coefficient will be tuned at a single frequency, and hence will produce a single rejected band as it was seen in chapter 3. Any other election of the periodic function $f(z)$ would have led to frequency responses with reflected bands at $2 \cdot \omega_0, 3 \cdot \omega_0, \ldots$, although, if $f(z)$ is continuous and smooth, these replicas would be likely constrained to reduced levels.

Therefore, the impedance modulation finally implemented is

$$\begin{aligned} Z_0(z) &= 50\cdot\exp\left(A\cdot W(z)\cdot sin\left(\phi_{spatial}(z)\right)\right) = 50\cdot\exp\left(A\cdot W(z)\cdot sin\left(\int\zeta(z)\cdot dz\right)\right) = \\ &= 50\cdot\exp\left(A\cdot W(z)\cdot sin\left(2\pi/a_0\cdot z + C\cdot z^2 - C\cdot L^2/4\right)\right) \end{aligned} \tag{5.18}$$

since the spatial phase $\phi_{spatial}(z)$ relates to the spatial angular frequency $\zeta(z)$ through:

$$\phi_{spatial}(z) = \int\zeta(z)\cdot dz$$

where in eqn. (5.18) A (non-dimensional) is an amplitude factor and the integration constant is fixed to $-C\cdot L^2/4$ for 50Ω-input and output ports when L is a multiple of a_0. $W(z)$ is a windowing function for smoother input and output impedance transitions to avoid partially reflections from the extremes of the structure that give rise to different long-path Fabry-Perot like resonances, which cause undesirable rapid ripple to appear around the mean values in the magnitude and group-delay vs. frequency patterns degrading the CDL performance. Furthermore, both negative values of C, which imply upper (higher loss) frequencies to be reflected in first place, and asymmetric $W(z)$, which compensates for the longer lossy round trips of lower frequencies (conductor losses, $\propto\sqrt{\omega}$, are much more significant than dielectric losses, $\propto\omega$, for most microstrip substrates), can be proved to lead to better equalized reflection losses across the operation band if full-wave electromagnetic simulations are performed (in our case using the commercially available *Agilent Momentum* software). Parasitic effects in microstrip like radiation losses and surface-wave propagation are maintained within negligible values due to the smooth rounded strip shape.

Now, we are going to present an example of microstrip CDL with linearly chirped impedance modulation around 50Ω using a medium quality *Rogers RO3010* substrate ($\varepsilon_r = 10.2$, and thickness $h = 1.27\,\text{mm}$). The design frequency characteristics are: operation around 9 GHz, 12 GHz-bandwidth, and –0.5 ns/GHz ($\ddot{\varphi}_0 \cong -0.08\,\text{ns}^2/\text{rad}$)-delay slope. The next parameter set fulfills the response: $a_0 = 6.4$ mm, $L = 50\cdot a_0$, and $C = -2080\,\text{m}^{-2}$. The asymmetric tapering function $W(z)$ is gaussian:

$$W(z) = \exp\left(-4\cdot\left((z - L/4)/L\right)^2\right)$$

and $A = 0.4$.

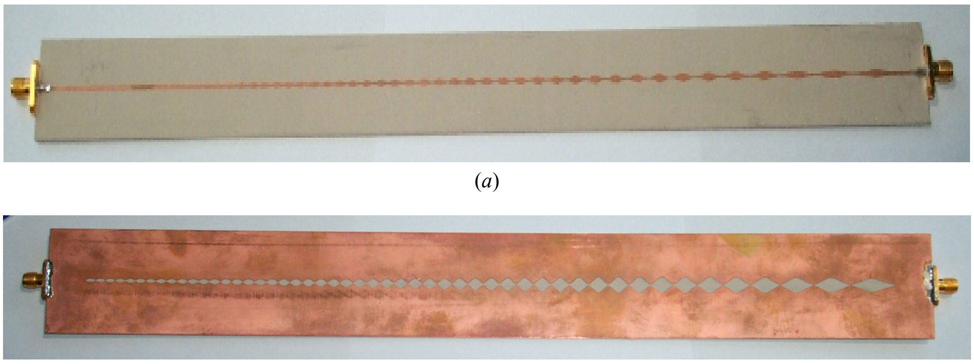

(*a*)

(*b*)

Figure 5.33: *Photograph of the microstrip quadratic-phase filter designed and constructed in this section (a), and equivalent implementation as PBG structure (b).*

Once all the parameters in eqn. (5.18) have been fixed, we implement the impedance variation as a strip width modulation (see [POZ 98], for instance). As the impedance varies between 35 and 75Ω, the strip width changes between 0.5 and 2.5 mm approximately. It is interesting to note that an equivalent device could be implemented etching a perturbation in the ground plane, but its performance would be slightly worse. In Fig. 5.33 a photograph of the constructed prototype is given, together with an equivalent implementation as PBG structure. In Fig. 5.34 the S_{11} parameter obtained solving the simplified system of coupled mode equations (chapter 3, section (3.2)) using the coupling coefficient of eqn. (5.17) (loss-less and single-mode approximation) (dotted line) is compared with the simulation employing the commercial software (thin solid line) and the measurement of the prototype (thick solid line), showing that the CDL provides the required features of flat magnitude and linear group delay. The reflection losses are maintained around -3 dB over the entire bandwidth (dielectric loss tangent, $\tan\delta = 0.0026$, and metal conductivity $\sigma = 5.8 \cdot 10^7$ S/m). We decided to use an appropriate time-gating to subtract the mismatch effects of the connectors in the presented measurement because these effects are critical in broadband operation and, in the intended integrated solution, the input and output sections will be also microstrip lines.

Figure 5.35 shows the average internal power distribution, as relative brightness levels, for every frequency in the operation bandwidth as a function of the position in the CDL, $|a^+(z)|^2 + |a^-(z)|^2$, being $a^\pm$ the complex amplitudes of the quasi-TEM mode traveling in the forward (+) and backward (-) z-direction, as it was seen in chapter 3. A coupling-location linearly distributed in frequency is clearly observed as

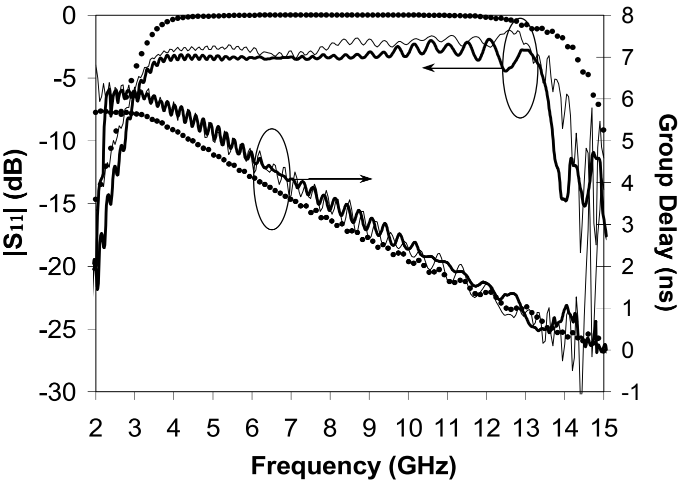

Figure 5.34: S_{11}*-parameter of the microstrip CDL (magnitude, left axis; and group delay, right axis) obtained by coupled mode theory approximation (loss-less) (dotted line), commercial software (thin solid line) and measurement (thick solid line).*

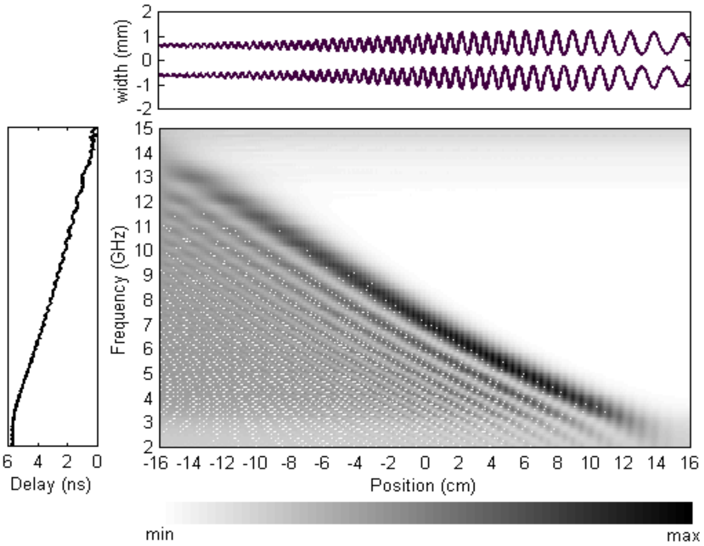

Figure 5.35: *Average internal power as a function of frequency and position in the CDL using the coupled mode theory approximation. Top: CDL strip pattern (not to scale). Left: group-delay*

well as higher frequencies being reflected back earlier than lower ones (negative *C*). This design method, shown here within the constrains of our equipment capabilities, can be applied on higher-dielectric-constant- and thinner substrates to obtain microstrip CDLs some centimeters long with time bandwidth products above several hundreds over very wide frequency ranges. The advantages of these devices are easiness of design, fabrication on a mature technology, and compatibility with monolithic circuits.

Interesting applications as real-time spectral analysis of wideband signals can be envisaged using these devices [LAS 01]. The plot at the bottom of Fig. 5.36 shows an ideal input rectangular pulse 0.6 ns-wide (dotted line), placed within the CDL bandwidth, together with the output pulse reflected from the CDL (solid line), calculated through a numerical simulation using the measured frequency response, both as normalized average power signals (then, only the envelopes of both microwave pulses, traveling on a carrier frequency at 8 GHz, are depicted). The normalized input and output energy spectral densities are the dotted and solid lines, respectively, at the upper left plot. The larger plot of Fig. 5.36 is a joint time-frequency representation of the energy distributions for both signals providing information of the temporal location of the spectral components. A Wigner-Ville distribution [QIA 96] was used in this case. A strong process of linear realignment in time is suffered by the input signal frequencies and, under the assumption of a high delay slope in the signal bandwidth, which is the case for these microstrip CDLs, a single dominant frequency exists at a given instant of time. This way, the output

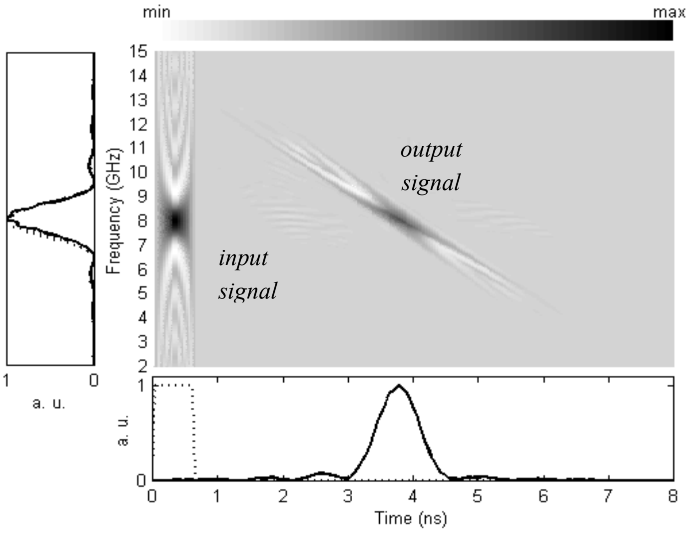

__Figure 5.36:__ Bottom: input signal to the CDL (dotted line) and simulation of the output reflected signal (solid line), given in normalized average power (arbitrary units). Top: joint time-frequency representation for the input and output signals (on the center), and normalized input (dotted line) and output (solid line) energy spectral densities (on the left).

closely reproduces the shape of the energy spectral density, $\sin^2(x)/x^2$, of the input signal on a time axis related to frequency by a linear axis-change given by the CDL delay slope.

To conclude this section we want to remark that it has been proposed an easy procedure to design microstrip CDLs with high time-bandwidth products, over frequency ranges of several gigahertzs, consisting in a continuously varying strip width so that the coupling location between the quasi-TEM microstrip mode and the same but counter-propagating mode is linearly distributed in frequency. Measurements have been provided verifying the design method. Real-time Fourier processing of wideband signals has been pointed out as a promising possible application for these devices.

CHAPTER 6

CONCLUSIONS AND FUTURE WORK-LINES

The main purpose of this thesis has been the study of PBG structures in microstrip technology, from the point of view of their analysis and design, and of their practical applications. To this end, the coupled mode theory has been rigorously formulated for them, providing very useful insight into their operation, and allowing their analysis and design through analytical solutions valid for uniform PBG devices, and fast numerical solutions for the general problem. Additionally, design techniques to improve the performance of PBG structures in microstrip technology have been proposed and successfully tested. And finally, a wide range of very promising applications for these structures, including many practical examples, have been proposed and demonstrated. The goals of the thesis have been successfully covered.
The main contributions of this work, together with the open work-lines, are the following:

- In chapter 2, the coupled mode theory has been rigorously applied to analyze open waveguides that can include metals, and in particular perturbed ground planes and strip conductors, covering all of our cases of interest. To formulate an accurate coupled mode theory suitable for microwave and millimeter wave devices, the cross-section method has been employed. The system of coupled mode equations obtained includes the discrete and the continuous spectrum modes, and takes into account all the phenomena (including the radiation), with no approximation involved. However, in this work, this system of coupled mode equations has been used only as an intermediate step to obtain the simplified system, valid for PBG microstrip devices, that will be actually solved. An open work-line would be to include in the system of coupled mode equations to be solved, the continuous spectrum modes. In this way, the radiation would be taken into account and the results would be more accurate. Moreover, the study of structures designed to radiate would be also possible. In the same way, it would be very interesting to explore the introduction of leaky modes, as a rephrasing of part of the continuous spectrum modes. Using them, it would be possible to explore the possibility of designing periodic mode converters, to transfer the energy from the fundamental microstrip mode to a leaky mode, in order to radiate it.

- In chapter 3, the system of coupled mode equations that characterizes the PBG structure in microstrip technology is notably simplified by realizing several reasonable approximations that will eventually lead to a simplified system of coupled mode equations that features analytical solutions for the case of uniform PBG structures. In this way, a comprehensive set of analytical expressions for the most important design parameters of PBG microstrip structures is furnished. The set of analytical expressions available cover a wide scope, ranging from the S parameters to the Bloch wave analysis, and constitutes a very useful and unique set of tools for the analysis and design of these PBG devices.

An also very important contribution of the coupled mode analysis of these devices is the fruitful link that it establishes between them and the Fiber Bragg Gratings (FBGs) in the optical regime. As a consequence, several ideas and techniques that are widely employed in the field of FBGs, can be transposed to the novel and emergent field of PBG structures for microstrip lines, to improve their performance and the range of applications.

- In chapter 4, several techniques to improve the performance of PBG structures for microstrip lines are introduced. The results obtained are very satisfactory. Specially promising are the novel continuous patterns proposed, that give rise to non-periodic frequency responses, as well as to multiple frequency tuned PBG devices. The origin of this novel patterns is in the relation that can be established, in terms of Fourier Transforms, between the coupling coefficient $K(z)$ produced by a PBG structure, and its reflection parameter $S_{11}(f)$. It is important to note, however, that to design these novel patterns only the approximate relation has been used. As it is seen in chapter 3, an exact relation between both parameters has been also obtained, and using it more sophisticated and accurate designs could be expected. The use of the exact relation between $K(z)$ and $S_{11}(f)$ to design PBG structures with a specific frequency response is a very interesting and promising work-line that should be addressed in the near future.

- In chapter 5, several examples of practical applications of PBG structures in microstrip technology are proposed and tested. All the designs studied show high potential. Specially interesting are the applications aimed to the suppression of spurious bands and harmonics in passive and active circuits for enhanced out of band behaviour and higher efficiency. An important open work-line is to continue exploring the benefits of using PBG structures with this aim, in conventional passive and active circuits. Other very interesting application proposed is the implementation of high-Q fully planar resonators. It is very difficult to obtain planar high-Q resonators in microstrip technology, and actually, sometimes, the introduction of dielectric resonators is necessary. PBG resonators could be a very interesting alternative. In fact, they constitute an also promising open work-line.

Electrically tunable PBG resonators have been already proposed, and it could be expected that the use of high quality low loss materials and optimized design techniques accounting for losses in the resonator cavity will greatly improve the behavior of these PBG devices. Additionally, cascaded PBG resonators could be employed for the synthesis of PBG bandpass filters.

Other important application studied is the design of chirped delay lines to realize quadratic-phase filters with applications like real-time Fourier analysis. A wealth of research work can be done in this area that takes advantage of the phase response of PBG structures.

To finish this chapter it is important remark that a very interesting open work-line, that is already being exploited by our group, is the introduction of PBG structures in other planar microwave and millimeter wave technologies. Specially promising are the applications in coplanar waveguide technology. There, we have proposed the use of PBG structures to eliminate the spurious passbands that appear in coplanar waveguides periodically loaded with reactive elements and employed to implement low-pass filters, phase shifters or frequency multipliers [FER 02]. This work is being done in cooperation with the Electronic Engineering Department of the Universitat Autònoma de Barcelona, and the results obtained are really encouraging, confirming that in the future the application of PBG structures to planar microwave technologies will in no way be limited to the microstrip technology. Fortunately, most of the results and techniques of this thesis, although developed for PBG structures in microstrip technology, can be very easily translated to other planar circuit technologies.

REFERENCES

[ADA 69] J. E. Adair and G. I. Haddad, "Coupled-mode analysis of nonuniform coupled transmission lines," *IEEE Transactions on Microwave Theory and Techniques*, vol. 17, no. 10, pp. 746-752, October 1969.

[AIK 89] M. Aikawa, H. Ogawa, “Double-Sided MIC’s and their applications,” *IEEE Transactions on Microwave Theory ands Techniques*, vol. 37, no. 2, pp. 406-413, February 1989.

[AKA 02] T. Akalin, M. A. G. Laso, E. Delos, T. Lopetegi, O. Vanbésien, M. Sorolla, and D. Lippens, “High performance double-sided microstrip PBG filter,” to be published in *Microwave and Optical Technology Letters*, October 2002 issue.

[BLO 98] P. Blondy, A. R. Brown, D. Cros, and G. M. Rebeiz, “Low-Loss Micromachined Filters for Millimeter-Wave Communication Systems,” *IEEE Transactions on Microwave Theory Techniques*, vol. 46, pp. 2283-2288, 1998.

[BOL 50] E. F. Bolinder, “Fourier transforms in the theory of inhomogeneous transmission lines,” *Proceedings of the I.R.E.*, vol. 38, pp. 1354, November 1950.

[BOL 56] E. F. Bolinder, “Fourier transforms and tapered transmission lines,” *Proceedings of the I.R.E.*, vol. 44, pp. 557, April 1956.

[BRA 83] V. L. Bratman, G. G. Denisov, N. S. Ginzburg, and M. I. Petelin, “FEL’s with Bragg Reflection Resonators: Cyclotron Autoresonance Masers versus Ubitrons”, *IEEE Journal of Quantum Electronics*, vol. 19, no. 3, pp. 282-296, March 1983.

[BRI 53] L. Brillouin, *Wave Propagation in Periodic Structures: electric filters and crystal lattices*, Second Edition, New York, NY: Dover Publications, 1953.

[BRO 95] E. R. Brown and O. B. McMahon, “Large electromagnetic stop bands in metallodielectric photonic crystals,” *Applied Physics Letters*, vol. 67, no. 15, pp. 2138-2140, October 1995.

[CAR 86] A. B. Carlson, *Communication Systems: an introduction to signals and noise in electrical communication*, Third Edition, New York-Madrid: McGraw-Hill, 1986.

[COC 98] R. Coccioli, W. R. Deal, and T. Itoh, "Radiation characteristics of a patch antenna on a thin PBG substrate," *IEEE Antennas and Propagation International Symposium*, pp. 656-659, Atlanta, GA, June 21-26, 1998.

[COC 99] R. Coccioli, F. R. Yang, K. P. Ma, and T. Itoh, "Aperture coupled patch antenna on UC-PBG substrate," *IEEE Transactions on Microwave Theory and Tech*niques, vol. 47, no. 11, pp. 2123-2130, November 1999.

[COL 91] R. E. Collin, *Field Theory of Guided Waves,* Second Edition, New York, NY: IEEE Press, 1991.

[COL 92] R. E. Collin, *Foundations for microwave engineering*, Second Edition, Singapore: McGraw Hill, 1992.

[DRA 01] R. F. Drayton, S. P. Pacheco, J. Wang, J-G. Yook, and L. P. B. Katehi, "Micromachined Filters on Synthesized Substrates," *IEEE Transactions on Microwave Theory Techniques*, vol. 49, pp. 308-314, 2001.

[DUP 99] O. Dupuis, J. Carbonell, P. Mounaix, O. Vanbésien and D. Lippens, "Micromachined coplanar transmission lines in a GaAs technology," *Microwave and Optical Technology Letters*, vol. 20, pp. 106-110, 1999.

[EDW 92] Terry Edwards, *Foundations for Microstrip Circuit Design*, Second Edition, Chichester, England: John Wiley & Sons Ltd., 1992.

[EDW 00] Terry Edwards, *Foundations of Interconnect and Microstrip Design*, Third Edition, Chichester, England: John Wiley & Sons Ltd., 2000.

[ERR 00] M. J. Erro, M. A. G. Laso, T. Lopetegi, D. Benito, M. J. Garde, and M. Sorolla, "Modeling and testing of uniform fiber Bragg gratings using 1-D photonic bandgap structures in microstrip technology," *Journal of Fibre and Integrated Optics*, vol. 19, no. 4, pp. 311-325, September 2000.

[ERR 00a] M. J. Erro, M. A. G. Laso, T. Lopetegi, D. Benito, M. J. Garde, and M. Sorolla, "Optimization of tapered bragg reflectors in microstrip technology," *International Journal of Infrared and Millimeter Waves*, vol. 21, no. 2, pp.231- 245, February 2000.

[ERR 02] M. J. Erro, M. A. G. Laso, T. Lopetegi, D. Benito, M. J. Garde, and M. Sorolla, "Analysis and Design of Electromagnetic Crystals in Microstrip Technology using a Fiber Grating Model," *Optical and Quantum Electronics*, vol. 34, pp. 297-310, 2002.

[FAL 99] F. Falcone, T. Lopetegi, and M. Sorolla, "1-D and 2-D Photonic Bandgap Microstrip Structures," *Microwave and Optical Technology Letters,* vol. 22, pp. 411-412, Sep. 1999.

[FAL 99a] F. Falcone, T. Lopetegi, M. Irisarri, M. A. G. Laso, M. J. Erro, and M. Sorolla, "Compact Photonic Bandgap Microstrip Structures," *Microwave and optical Technology Letters*, vol 23, no. 4, pp. 233-236, November 1999.

[FAN 96] S. Fan, P. R. Villeneuve, and J. D. Joannopoulos, “Large omnidirectional band gaps in metallodielectric photonic crystals,” *Physical Review B (Condensed Matter)*, vol. 54, no. 16, pp. 11245-11251, October 1996.

[FEC 99] R. Feced, M. N. Zervas, and M. Muriel, “An efficient inverse scattering algorithm for the design of nonuniform Fiber Bragg Gratings”, *IEEE Journal of Quantum Electronics*, vol. 35, no. 8, August 1999.

[FEL 73] L. Felsen and N. Marcuvitz, *Radiation and Scattering of Waves*, Englewood Cliffs, NJ: Prentice Hall, 1973.

[FRI 56] B. Friedman, *Principles and Techniques of Applied Mathematics,* New York, NY: Wiley, 1956.

[FU 01] Y. Q. Fu, G. H. Zhang, and N. C. Yuan, “A novel PBG coplanar waveguide,” *IEEE Microwave and Wireless Components Letters*, vol. 11, no. 11, pp. 447-449, November 2001.

[GAR 94] Fred Gardiol, *Microstrip circuits*, John Wiley & Sons, Inc., New York, NY, 1994.

[GAU 97] G. P. Gauthier, A. Courtay, and G. M. Rebeiz, “Microstrip antennas on synthesized low dielectric constant substrates,” *IEEE Transactions on Antennas & Propag*ation, vol. 45, no. 8, pp. 1310-1314, Aug. 1997.

[GET 83] W. J. Getsinger, “Measurement and modeling of the apparent characteristic impedance of microstrip,” *IEEE Transactions on Microwave Theory and Techniques*, vol. 31, no. 8, pp. 624-632, August 1983.

[GUP 96] K. C. Gupta, R. Garg, I. Bahl, P. Bhartia, *Microstrip lines and slotlines*, Second Edition, Boston – London: Artech House, 1996.

[HAU 91] H. A. Haus, and W. Huang, “Coupled-mode theory,” *Proceedings of the IEEE*, *Special Issue on Electromagnetics*, vol. 79, no. 10, pp. 1505-1518, October 1991.

[HAN 99] C. Y. Hang, V. Radisic, Y. Qian, and T. Itoh, “High efficiency power amplifier with novel PBG ground plane for harmonic tuning,” *1999 IEEE MTT-S International Microwave Symposium*, Anaheim, CA, June 1999, pp. 807-810.

[HIL 97] K.O. Hill and G. Meltz, “Fiber Bragg grating technology fundamentals and overview”, *Journal of Lightwave Technology*, vol. 15, no. 8, Aug. 1997.

[HO 94] K. M. Ho, C. T. Chan, C. M. Soukoulis, R. Biswas, and M. Sigalas, “Photonic band gaps in three dimensions: new layer-by-layer periodic structures,” *Solid State Commun.*, vol. 89, pp. 413, 1994.

[HON 01] J. S. Hong, and M. J. Lancaster, *Microstrip Filters for RF/Microwave applications*, New York, NY: John Wiley & Sons, Inc., 2001.

[HOR 99] Y. Horii and M. Tsutsumi, "Harmonic control by photonic bandgap on microstrip patch antenna," *IEEE Microwave Guided Wave Lett*ers, vol. 9, no. 1, pp. 13-15, January 1999.

[ITO 80] T. Itoh, "Spectral domain immitance approach for dispersion characteristics of generalized printed transmission lines," *IEEE Transactions on Microwave Theory and Techniques*, vol. 28, no. 7, pp. 733-736, July 1980.

[ITO 01] T. Itoh, G. Haddad, and J. Harvey, *RF Technologies for Low Power Wireless Communications*, New York, NY: John Wiley & Sons, 2001.

[JI 00] Y. Ji, X. S. Yao, and L. Maleki, "High-Q whispering gallery mode dielectric resonator bandpass filter with microstrip line coupling and photonic bandgap mode-suppression," *IEEE Microwave and Guided Wave Letters,* vol. 10, no. 8, pp. 310-312, August 2000.

[JOA 95] J. D. Joannopoulos, R. D. Meade, and J. N. Winn, *Photonic Crystals: Molding the flow of light*, Princeton, NJ: Princeton University Press, 1995.

[JOH 87] S. John, "Strong localization of photons in certain disordered dielectric superlattices," *Physical Review Letters,* vol. 58, pp. 2486-2489, 1987.

[KAR 02] N. C. Karmakar, "Improved Performance of Photonic Band-Gap Microstriplines Structures with the use of Chebyshev Distributions," *Microwave and Optical Tecnology Letters*, vol. 33, pp. 1-5, 2002.

[KAS 99] R. Kashyap, *Fiber Bragg Gratings*, San Diego-London: Academic Press, 1999.

[KAT 57] B. Z. Katsenelenbaum, "On the theory of nonuniform waveguides with slowly changing parameters," *Proceedings of the International Conference on Ultra high-frequency circuits and antennas*, Paris, France, October 1957.

[KAT 61] B. Z. Katsenelenbaum, *Theory of nonuniform waveguides with slowly varying parameters* (in Russian), Moscow, USSR: published by the former Soviet Union Academy of Sciences, Izd. Akad. Nauk. SSSR, 1961.

[KAT 98] B. Z. Katsenelenbaum, L. Mercader, M. Pereyaslavets, M. Sorolla, and M. Thumm, *Theory of nonuniform waveguides – the cross-section method*, London, UK: IEE Electromagnetic Waves Series, 44, 1998.

[KAZ 59] Y. I. Kaznacheev, "Broadband telecommunications using waveguides," (in Russian) Publication of the Academy of Sciences of USSR, Moscow.

[KES 96] M. P. Kesler, J. G. Maloney, and B. Shirley, "Antenna design with the use of photonic bandgap materials as all dielectric planar reflectors," *Microwave and Optical Technology Letters*, vol. 11, no. 4, pp. 169-174, March 1996.

[KIS 49] G. V. Kisun'ko, *Electrodynamics of hollow systems* (in Russian), Leningrad, USSR: Publishing House VKAS, 1949.

[KIM 00] T. Kim, and C. Seo, "A novel photonic bandgap structure for low-pass filter of wide stopband," *IEEE Microwave and Guided Wave Letters,* vol. 10, no. 1, pp. 13-15, January 2000.

[KIM 00a] C. S. Kim, J. S. Park, D. Ahn, and J. B. Lim, "A novel 1-D periodic defected ground structure for planar circuits," *IEEE Microwave and Guided Wave Letters,* vol. 10, no. 4, pp. 131-133, April 2000.

[KOB 92] M. Kobayashi, N. Sawada, "Analysis and Synthesis of tapered microstrip transmission lines," *IEEE Transactions on Microwave Theory and Techniques*, vol. 40, no. 8, pp. 1642-1646, August 1992.

[KOG 72] H. Kogelnik and C. V. Shank, "Coupled-Wave theory of distributed feedback lasers," *Journal of Applied Physics*, vol. 43, no. 5, pp. 2327-2335, May 1972.

[KOG 76] H. Kogelnik, "Filter response of nonuniform almost-periodic structures," *Bell System Technical Journal*, vol. 55, no. 1, pp. 109-126, January 1976.

[KOS 86] M. Koshiba and M Suzuki, "Vectorial wave analysis in dielectric waveguides for optical integrated circuits using equivalent network approach," *IEEE Journal of Lightwave Technology*, vol. 4, pp. 656-664, June 1986.

[KOV 86] N. F. Kovalev, "The theoretical basis for the transverse-section method in the theory of irregular waveguides," *Soviet Journal of Communication Technology and Electronic*, vol. 31, no. 1, pp. 60-64, 1986.

[LAS 99] M. A. G. Laso, M. J. Erro, D. Benito, M. J. Garde, T. Lopetegi, F. Falcone, and M. Sorolla, "Analysis and design of 1-D photonic bandgap microstrip structures using a fibre grating model," *Microwave and Optical Technology Letters,* vol. 22, no. 4, pp. 223-226, August 1999.

[LAS 00] M. A. G. Laso, T. Lopetegi, M. J. Erro, D. Benito, M. J. Garde and Mario Sorolla, "Novel wideband photonic bandgap microstrip structures," *Microwave and Optical Technology Letters*, vol. 24, no. 5, pp. 357-360, March 2000.

[LAS 00a] M. A. G. Laso, T. Lopetegi, M. J. Erro, D. Benito, M. J. Garde, and M. Sorolla, "Multiple-frequency-tuned Photonic Bandgap microstrip structures," *IEEE Microwave and Guided Wave Letters*, vol. 10, no. 6, pp. 220-222, June 2000.

[LAS 01] M. A. G. Laso, T. Lopetegi, M. J. Erro, M. Castillo, D. Benito, M. J. Garde, M. A. Muriel, M. Sorolla, and M. Guglielmi, "Real-time spectrum analysis in microstrip technology," *Proceedings of the 31st European Microwave Conference*, London, UK, Sep. 25-27th, 2001.

[LAS 01a] M. A. G. Laso, T. Lopetegi, M. J. Erro, D. Benito, M. A. Muriel, M. Sorolla, and M. Guglielmi, “Chirped Delay Lines in Microstrip Technology,” *IEEE Microwave and Wireless Components Letters*, vol. 11, no. 12, pp. 486-488, December 2001.

[LEE 02] Y. T. Lee, J. S. Lim, J. S. Park, D. Ahn, and S. Nam, “A Novel Phase Noise Reduction Technique in Oscillators Using Defected Ground Structure”, *IEEE Microwave and Wireless Components Letters*, vol. 12, no. 2, pp. 39-41, February 2002.

[LEO 02] K. M. K. H. Leong, A. C. Guyette, B. Elamaran, W. A. Shiroma, and T. Itoh, “Coupling suppression in microstrip lines using a bi-periodically perforated ground plane,” *IEEE Microwave and Wireless Components Letters*, vol. 12, no. 5, pp. 169-171, May 2002.

[LOP 99] T. Lopetegi, F. Falcone, and M. Sorolla, "Bragg reflectors and resonators in microstrip technology based on Electromagnetic Crystal structures," *International Journal of Infrared and Millimeter Waves*, vol. 20, no. 6, pp. 1091-1102, June 1999.

[LOP 99a] T. Lopetegi, F. Falcone, B. Martínez, R. Gonzalo, and M. Sorolla, “Improved 2-D photonic bandgap structures in microstrip technology,” *Microwave and Optical Technology Letters,* vol. 22, no. 3, pp. 207-211, August 1999.

[LOP 99b] T. Lopetegi, M. A. G. Laso, M. J. Erro, F. Falcone, and M. Sorolla, “Bandpass filter in microstrip technology using photonic bandgap reflectors”, Proceedings of the *29th European Microwave Conference*, pp. 337-340, October 1999, Munich, Germany.

[LOP 00] T. Lopetegi, M. A. G. Laso, M. J. Erro, D. Benito, M. J. Garde, F. Falcone and M. Sorolla, “Novel photonic bandgap microstrip structures using network topology,” *Microwave and Optical Technology Letters*, vol. 25, no. 1, pp. 33-36, April 2000.

[LOP 00a] T. Lopetegi, M. A. G. Laso, M. Irisarri, M. J. Erro, F. Falcone, and M. Sorolla, "Optimization of compact Photonic Bandgap microstrip structures," *Microwave and Optical Technology Letters*, vol. 26, no. 4, pp. 211-216, August 2000.

[LOP 00b] T. Lopetegi, M. A. G. Laso, M. J. Erro, D. Benito, M. J. Garde, F. Falcone and M. Sorolla, “Novel photonic bandgap microstrip structures using network topology,” *Microwave and Optical Technology Letters*, vol. 25, no. 1, pp. 33-36, April 2000.

[LOP 01] T. Lopetegi, M. A. G. Laso, J. Hernández, M. Bacaicoa, D. Benito, M. J. Garde, M. Sorolla, and M. Guglielmi, “New Microstrip “Wiggly-Line” Filters With Spurious Pass-band Suppression”, *IEEE Transactions on Microwave Theory and Techniques*, vol. 49, no. 9, pp. 1593-1598, September 2001.

[MA 98] K. P. Ma, F. R. Yang, Y. Qian, and T. Itoh, “Nonleaky conductor-backed CPW using a novel 2D PBG lattice,” *Asia-Pacific Microwave Conference (APMC’98) Digest*, pp. 509-512, December 1998.

[MA 99] K. P. Ma, J. Kim, F. R. Yang, Y. Qian, and T. Itoh, “Leakage suppression in stripline circuits using a 2-D photonic bandgap lattice,” *1999 IEEE MTT-S International Microwave Symposium,* Anaheim, CA, June 1999, pp. 73-76.

[MAR 74] D. Marcuse, *Theory of Dielectric Optical Waveguides*, New York, NY: Academic Press, 1974.

[MAR 91] D. Marcuse, *Theory of Dielectric Optical Waveguides*, Second Edition, San Diego, CA: Academic Press, 1991.

[MAR 02] F. Martín, F. Falcone, J. Bonache, T. Lopetegi, M. A. G. Laso, and M. Sorolla*, “*New periodic-loaded electromagnetic bandgap coplanar waveguide with complete spurious passband suppression,” to be published in *IEEE Microwave and Wireless Components Letters*, in November 2002 issue.

[MIL 54] S. E. Miller, “Waveguide as a communication medium,” *The Bell System Technical Journal*, vol. 33, pp. 1209-1265, 1954.

[MIL 54a] S. E. Miller, “Coupled wave theory and waveguide applications,” *The Bell System Technical Journal*, vol. 33, no.3, pp. 661-719, May 1954.

[MIL 68] S. E. Miller, “On solutions for two waves with periodic coupling,” *The Bell System Technical Journal*, pp. 1801-1822, October 1968.

[MIZ 93] V. Mizrahi and J.E. Sipe, “Optical properties of photosensitive fiber phase gratings”, *Journal of Lightwave Technology*, vol. 11, no. 10, pp. 1513-1517, Oct. 1993.

[MON 93] M. Mongiardo and T. Rozzi, “Continuous spectrum, characteristic modes, and leaky waves of open waveguides,” *IEEE Transactions on Microwave Theory and Techniques*, vol. 41, no. 8, pp. 1329-1335, August 1993.

[NAI 84] N. V. Nair, and A. K. Mallick, “An analysis of a width-modulated microstrip periodic structure,” *IEEE Transactions on Microwave Theory and Techniques*, vol. 32, no. 2, pp. 200-204, February, 1984.

[NIK 76] V. V. Nikolski, *Electrodinámica y propagación de ondas de radio*, Moscú, Rusia: Editorial Mir, 1976.

[OLI 63] A. A. Oliner, *Radiating periodic structures: analysis in terms of k vs. β diagrams*, Short Course on Microwave Field and Network Techniques, Polytechnic Institute of Brooklyn, 1963.

[OTH 99] A. Othonos, K. Kalli, *Fiber Bragg Gratings: fundamentals and applications in telecommunications and sensing*, Boston-London: Artech House, 1999.

[OZB 96] E. Özbay, "Layer-by-layer photonic crystals from microwave to far-infrared frequencies," *Journal of the Optical Society of America B*, vol. 13, no. 9, pp. 1945-1955, September 1996.

[PAS 96] D. Pastor, "Redes de difracción sobre fibra óptica para procesamiento de señales fotonicas" Doctoral Thesis, Universidad Politécnica de Valencia, Spain, 1996.

[PAS 96a] D. Pastor, J. Capmany, D. Ortega, V. Tatay, and J. Martí, "Design of apodized linearly chirped fiber gratings for dispersion compensation", *Journal of Lightwave Technology*, vol. 14, no. 11, pp. 2581-2588, Nov. 1996.

[PER 96] E. Peral, J. Capmany, and J. Martí, "Iterative solution to the Gel'Fand-Levitan-Marchenko coupled equations and application to synthesis of fiber gratings," *IEEE Journal of Quantum Electronics,* vol. 32, no. 12, pp. 2078-2084, December 1996.

[POZ 98] D. M. Pozar, *Microwave Engineering*, Second Edition, Reading, MA: Addison-Wesley, 1998.

[QIA 96] S. Qian and D. Chen, *Joint Time-Frequency Analysis: Methods and Applications*, Prentice-Hall, Englewood Cliffs, NJ, 1996.

[QIA 97] Y. Qian, V. Radisic, and T. Itoh, "Simulation and experiment of photonic band-gap structures for microstrip circuits," *Proceedings of the 1997 Asia-Pacific Microwave Conference*, Hong Kong, December 1997, pp. 585-588.

[QIA 98] Y. Qian, D. Sievenpiper, V. Radisic, E. Yablonovitch, and T. Itoh, "A novel approach for gain and bandwidth enhancement of patch antennas," *IEEE RAWCON. Symposium Dig*est, pp. 221-224, Colorado Springs, CO, Aug. 9-12, 1998.

[QIA 98a] Y. Qian, F. R. Yang, and T. Itoh, "Characteristics of microstrip lines on a uniplanar compact PBG ground plane," *Proceedings of the 1998 Asia-Pacific Microwave Conference*, pp. 589-592, Yokohama (Japan), December 1998.

[RAD 98] V. Radisic, Y. Qian, R. Coccioli, T. Itoh, "Novel 2-D Photonic Bandgap structure for microstrip lines," *IEEE Microwave and Guided Wave Letters*, vol. 8, no. 2, pp. 69-71, February 1998.

[RAD 98a] V. Radisic, Y. Qian, and T. Itoh, "Broad-band power amplifier using dielectric photonic bandgap structure," *IEEE Microwave Guided Wave Letters,* vol. 8, no.1, pp. 13-14, January 1998.

[RAD 98b] V. Radisic, Y. Qian, and T. Itoh, "Novel architectures for high-efficiency amplifiers for wireless applications," *IEEE Transactions on Microwave Theory and Techniques*, vol. 46, no. 11, pp. 1901-1909, November 1998.

[RAD 98c] V. Radisic, Y. Qian, and T. Itoh, “Broadband power amplifier integrated with slot antenna and novel harmonic tuning structure,” *1998 IEEE MTT-S International Microwave Symposium,* Baltimore, MD, June 1998, pp. 1895-1898.

[REI 59] G. Reiter, “Generalized telegraphist’s equation for waveguides of varying cross-section,” *Proceedings of the IEE*, vol. 106B, suppl. 13, pp. 54-57, 1959.

[ROZ 87] T. Rozzi and S. Hedges, “Rigorous analysis and network modeling of inset dielectric guide,” *IEEE Transactions on Microwave Theory and Techniques*, vol. 35, no. 9, pp. 823-834, September 1987.

[ROZ 92] T. Rozzi and P. D. Sewell, “The continuous spectrum of open waveguides of nonseparable cross section,” *IEEE Transactions on Antennas and Propagation*, vol. 40, no. 11, pp. 1283-1291, November 1992.

[ROZ 92a] T. Rozzi, G. Gerini, and M. Righi, “Radiation modes of slotline with application to millimetric circuits,” *Proceedings of the IEEE Microwave Theory and Techniques Symposium*, Albuquerque, NM, June 1992, pp. 503-506.

[ROZ 95] T. Rozzi and G. Cerri, “Radiation modes of open microstrip with applications,” *IEEE Transactions on Microwave Theory and Techniques*, vol. 43, no. 6, pp. 1364-1370, June 1995.

[ROZ 97] T. Rozzi and M. Mongiardo, *Open Electromagnetic Waveguides*, London, UK: IEE Electromagnetic Waves Series, 43, 1997.

[RUM 98] I. Rumsey, M. Piket-May, and P. K. Kelly, "Photonic bandgap structures used as filters in microstrip circuits," *IEEE Microwave and Guided Wave Letters*, vol. 8, no. 10, pp. 336-338, October 1998.

[SCH 55] S. A. Schelkunoff, “Conversion of Maxwell’s equations into generalized telegraphist’s equations ,” *Bell Systems Technical Journal*, vol. 34, pp. 995-1043, 1955.

[SHA 00] L. F. Shampine, J. Kierzenka, and M. W. Reichelt, “Solving boundary value problems for ordinary differential equations in Matlab with bvp4c,” available at ftp:// ftp.mathworks.com/pub/doc/papers/bvp/.

[SHE 71] V. V. Shevchenko, *Continuous Transitions in Open Waveguides – Introduction to the Theory*, Boulder, CO: The Golem Press, 1971.

[SHE 00] V. V. Shevchenko, Private Communication, 2000.

[SIE 98] D. Sievenpiper, E. Yablonovitch, J. N. Winn, S. Fan, P. R. Villeneuve, and J. D. Joannopoulos, “3D metallodielectric photonic crystals with strong capacitive coupling between metallic islands,” *Physical Review Letters*, vol. 80, no. 12, pp. 2829-2832, March 1998.

[SIE 98a] D. Sievenpiper and E. Yablonovitch, “Eliminating surface currents with metallodielectric photonic crystals,” *IEEE MTT-S Symposium Digest*, pp. 663-666, Baltimore, MD, June 7-12, 1998.

[SKO 90] M. Skolnik, *Radar Handbook*, Second Edition, McGraw-Hill, Inc., NY, 1990.

[SMI 99] G. S. Smith, M. P. Kesler, and J. G. Maloney, “Dipole antennas used with all-dielectric, woodpile photonic-bandgap reflectors: gain, field patterns, and input impedance,” *Microwave and Optical Technology Letters*, vol. 21, no. 3, pp. 191-196, May 1999.

[SNY 71] A. W. Snyder, “Mode propagation in a non-uniform cylindrical medium,” *IEEE Transactions on Microwave Theory and Techniques*, vol. 19, pp. 402-403, 1971.

[SNY 72] A. W. Snyder, “Coupled-mode theory for optical fibers,” *Journal of the Optical Society of America*, vol. 62, pp. 1267-1277, 1972.

[SNY 83] A. W. Snyder and J. D. Love, *Optical Waveguide Theory*, London, UK: Chapman & Hall, 1983.

[SON 85] G. H. Song, S. Y. Shin, “Design of corrugated waveguide filters by the Gel’fand-Levitan-Marchenko inverse-scattering method,” *Journal of the Optical Society of America A*, vol. 2, no. 11, pp.1905-1915, November 1985.

[SPO 79] F. Sporleder, and H. G. Unger, *Waveguide tapers, transitions and couplers,* London, UK: Peter Peregrinus Ltd., 1979.

[STE 51] A. Stevenson, “General theory of electromagnetic horns,” *Journal of Applied Physics*, vol. 22, pp. 1447-1454, 1951.

[TEM 99] B. Temelkuran and E. Özbay, “Experimental demonstration of photonic crystal based waveguides,” *Applied Physics Letters*, vol. 74, no. 4, pp. 486- 488, January 1999.

[THU 84] M. Thumm, “High-power millimeter-wave mode converters in overmoded circular waveguides using periodic wall perturbations,” *International Journal of Electronics*, vol. 57, no. 6, pp. 1225-1246, 1984.

[UNG 58] H. G. Unger, “Circular waveguide taper of improved design,” *Bell Systems Technical Journal*, vol. 37, pp. 899-912, 1958.

[UYS 93] S. Uysal, *Nonuniform Line Microstrip Directional Couplers and Filters*, Artech House, Boston – London, 1993.

[VAS 85] Charles Vasallo, *Théorie des Guides d’Ondes Électromagnétiques*, vol. 1, Eyrolles, Paris, 1985.

[WOH 66] M. R. Wohlers, “A realizability theory for smooth lossless transmission lines,” *IEEE Transactions on Circuit Theory*, vol. 13, no. 4, pp. 356-363, December 1966.

[XIA 01] G. Xiao, K. Yashiro, N. Guan, and S. Ohkawa, "An effective method for designing nonuniformly coupled transmission-line filters," *IEEE Transactions on Microwave Theory and Techniques*, vol. 49, no. 6, pp. 1027-1031, June 2001.

[XUE 00] Q. Xue, K. M. Shum, and C. H. Chan, "Novel 1-D microstrip PBG cells," *IEEE Microwave and Guided Wave Letters*, vol. 10, no. 10, pp. 403-405, October 2000.

[XUE 01] Q. Xue, K. M. Shum, and C. H. Chan, "Novel Oscillator Incorporating a Compact Microstrip Resonant Cell", *IEEE Microwave and Wireless Components Letters*, vol. 11, no. 5, pp. 202-204, May 2001.

[YAB 87] E. Yablonovitch, "Inhibited spontaneous emission in solid-state physics and electronics," *Physical Review Letters,* vol. 58, pp. 2059-2062, 1987.

[YAM 79] E. Yamashita, K. Atsuki, and T. Ueda, "An approximate dispersion formula of microstrip lines for computer-aided design of microwave integrated circuits," *IEEE Transactions on Microwave Theory Techniques*, vol. 27, pp. 1036-1038, 1979.

[YAM 87] M. Yamada, K. Sakuda, "Analysis of almost-periodic distributed feedback slab waveguides via a fundamental matrix approach," *Applied Optics*, vol. 26, no. 16, pp. 3474-3478, August 1987.

[YAN 98] F. R. Yang, Y. Qian, R. Coccioli, and T. Itoh, "A novel low-loss slow-wave microstrip structure," *IEEE Microwave and Guided Wave Letters,* vol.8, no. 11, pp. 372-374, November 1998.

[YAN 98a] F. R. Yang, Y. Qian, and T. Itoh, "A novel compact microstrip bandpass filter with intrinsic spurious suppression," *Asia-Pacific Microwave Conference (APMC'98) Dig*est, pp. 593-596, December 1998.

[YAN 99] F. R. Yang, K. P. Ma, Y. Qian, and T. Itoh, "A Uniplanar Compact Photonic-Bandgap (UC-PBG) Structure and Its Applications for Microwave Circuits," *IEEE Transactions on Microwave Theory and Techniques*, vol. 47, no. 8, pp. 1509-1514, August 1999.

[YAN 99a] F. R. Yang, Y. Qian, and T. Itoh, "A novel uniplanar compact PBG structure for filter and mixer applications," *1999 IEEE MTT-S International Microwave Symposium,* Anaheim, CA, June 1999, pp. 919-922.

[YAN 99b] F. R. Yang, K. P. Ma, Y. Qian, and T. Itoh, "A novel TEM waveguide using uniplanar compact photonic-bandgap (UC-PBG) structure," *IEEE Transactions on Microwave Theory and Techniques*, vol. 47, no. 11, pp. 2092-2098, November 1999.

[YAN 00] F. R. Yang, R. Coccioli, Y. Qian, and T. Itoh, “Analysis and Application of Coupled Microstrips on Periodically Patterned Ground Plane,” *IEEE MTT-S Symposium Digest*, Boston, MA, June 11-16, 2000, pp. 1529-1531.

[YAR 73] A. Yariv, “Coupled-mode theory for guided-wave optics,” *IEEE Journal of Quantum Electronics*, vol. 9, no. 9, pp. 919-933, September 1973.

[YAR 77] A. Yariv, M. Nakamura, “Periodic structures for integrated optics,” *IEEE Journal of Quantum Electronics*, vol. 13, no. 4, pp. 233-253, April 1977.

[YAR 84] A. Yariv, P. Yeh, *Optical Waves in Crystals*, New York: John Wiley & Sons, 1984.

[YAR 97] A. Yariv, *Optical Electronics in Modern Communications*, Fifth Edition, New York-Oxford: Oxford University Press, 1997.

[YOO 01] J. Yoon, and C. Seo, “Improvement of broadband feedforward amplifier using photonic bandgap,” *IEEE Microwave and Wireless component Letters*, vol. 11, no. 11, pp. 450-452, November 2001.

APPENDIX A

EQUIVALENT VOLTAGE AND CURRENT MODEL FOR A WAVEGUIDE MODE AND DERIVATION FROM IT OF THE COUPLED MODE EQUATIONS

A.1. Equivalent voltage and current for a waveguide mode

As it is well known, if a mode is TEM, its associated voltage V and current I can be defined in a unique way. In that case the definition of the characteristic impedance of the mode, Z_0, is also unique. If, on the other hand, the mode is non-TEM, there are many different ways to define equivalent voltage, current and characteristic impedance for it, since these quantities only have full physical meaning for TEM modes, and should be seen only as "equivalent" parameters for non-TEM modes. However, in order to obtain the most useful equivalent parameters for non-TEM modes, it is desirable to satisfy the following considerations [POZ 98]:

a) Voltage and current are only defined for a particular waveguide mode, and are defined so that the voltage is proportional to the transverse electric field, and the current is proportional to the transverse magnetic field.
b) In order to be used in a manner similar to voltages and currents of circuit theory, the equivalent voltages and currents should be defined so that their product gives the power flow of the mode.
c) The ratio of the voltage to the current for a single forward travelling wave should be equal to the characteristic impedance of the mode. This impedance may be chosen arbitrarily. However, as it is commented in section (2.3.2.3), the best election for Z_0 is the one that achieves the best characterization of the propagation of the mode along the nonuniform waveguide, in terms of reflection produced by

the discontinuities that can exist along the waveguide, and that can be calculated using the circuit theory.

As it can be seen in chapter 2, section (2.2), the total transversal electric field, and the total transversal magnetic field, can be expanded as a function of the complex amplitudes of the mode in the following way:

$$\begin{aligned}\hat{\vec{E}}_t(x,y,z) &= a^+ \cdot \vec{E}_t^+(x,y) + a^- \cdot \vec{E}_t^-(x,y)\\ \hat{\vec{H}}_t(x,y,z) &= a^+ \cdot \vec{H}_t^+(x,y) + a^- \cdot \vec{H}_t^-(x,y)\end{aligned} \tag{A.1}$$

It is important to note that following a) we are working only with one discrete spectrum mode (and its forward and backward travelling waves). Taking into account the relation existent between the fields of the forward and backward travelling waves associated to the same mode, eqns. (2.14), the expressions for the transversal fields can be rewritten as:

$$\begin{aligned}\hat{\vec{E}}_t(x,y,z) &= \vec{E}_t^+(x,y) \cdot \left(a^+ - a^-\right)\\ \hat{\vec{H}}_t(x,y,z) &= \vec{H}_t^+(x,y) \cdot \left(a^+ + a^-\right)\end{aligned} \tag{A.2}$$

On the other hand, the total equivalent voltage and current for the mode can be separated into the part associated to the forward travelling wave, and the part associated to the backward travelling wave:

$$\begin{aligned}V &= V^+ + V^-\\ I &= I^+ + I^-\end{aligned}$$

Defining the voltage and the current (following a)) in such a way that the voltage is proportional to the transverse electric field, and the current is proportional to the transverse magnetic field, we have:

$$\begin{aligned}\hat{\vec{E}}_t(x,y,z) &= \frac{\vec{E}_t^+(x,y)}{C_1} \cdot V = \frac{\vec{E}_t^+(x,y)}{C_1} \cdot \left(V^+ + V^-\right)\\ \hat{\vec{H}}_t(x,y,z) &= \frac{\vec{H}_t^+(x,y)}{C_2} \cdot I = \frac{\vec{H}_t^+(x,y)}{C_2} \cdot \left(I^+ + I^-\right)\end{aligned} \tag{A.3}$$

and combining eqns. (A.2) and (A.3) it is obtained:

$$\begin{aligned}V^+ &= C_1 \cdot a^+ \quad ; \quad V^- = -C_1 \cdot a^-\\ I^+ &= C_2 \cdot a^+ \quad ; \quad I^- = C_2 \cdot a^-\end{aligned} \tag{A.4}$$

On the other hand, in order to satisfy b), the power flow carried by the mode and calculated using the transversal electric and magnetic fields must be the same to that calculated using the equivalent voltage and current. Let's see.

We are going to limit our study to propagating modes (cut-off or evanescent modes will not be taken into account in this study). Following section (2.2.2.3) it can be seen that the complex power flow carried by a forward propagating mode (of the discrete spectrum) will be:

$$\begin{aligned} P^{+} &= \frac{1}{2}\cdot\iint_S \hat{\vec{E}}\times\hat{\vec{H}}^{*}\cdot\hat{z}\cdot dS = \frac{1}{2}\cdot\left|a^{+}\right|^{2}\cdot\iint_S \left(E_x^{+}\cdot H_y^{+^*} - H_x^{+^*}\cdot E_y^{+}\right)\cdot dS = \\ &= \frac{1}{2}\cdot\left|a^{+}\right|^{2}\cdot\iint_S \vec{E}^{+}\times\vec{H}^{+}\cdot\hat{z}\cdot dS = \frac{1}{2}\cdot\left|a^{+}\right|^{2}\cdot N^{+} \end{aligned} \tag{A.5}$$

where the convention for the mode fields (valid for propagating modes) given by eqn. (2.12), and the normalization for the fields of the discrete spectrum modes (eqn. (2.25a)) are used.

In the same way, the complex power flow for a forward propagating mode calculated using the equivalent voltage and current will have the following form:

$$P^{+} = \frac{1}{2}\cdot V^{+}\cdot I^{+^*} \tag{A.6}$$

Therefore, combining eqns. (A.5) and (A.6), the following expression must be satisfied:

$$\frac{1}{2}\cdot\left|a^{+}\right|^{2}\cdot N^{+} = \frac{1}{2}\cdot V^{+}\cdot I^{+^*}$$

and introducing eqns. (A.4) the expression can be rewritten as:

$$\frac{1}{2}\cdot\left|a^{+}\right|^{2}\cdot N^{+} = \frac{1}{2}\cdot C_1\cdot a^{+}\cdot C_2^{*}\cdot a^{+^*} \Rightarrow N^{+} = C_1\cdot C_2^{*} \tag{A.7}$$

On the other hand, following consideration c), the characteristic impedance, Z_0, will satisfy:

$$Z_0 = \frac{V^{+}}{I^{+}} = \frac{C_1\cdot a^{+}}{C_2\cdot a^{+}} \Rightarrow Z_0 = \frac{C_1}{C_2} \tag{A.8}$$

where eqns. (A.4) have been used.

Finally, combining eqns. (A.7) and (A.8), the values for C_1 and C_2 are readily calculated:

$$C_1 = \sqrt{N^+} \cdot \sqrt{Z_0}$$
$$C_2 = \frac{\sqrt{N^+}}{\sqrt{Z_0}}$$

and introducing them in eqns. (A.4) the sought equivalent voltage and current for a waveguide mode are obtained as a function of the complex amplitudes of the mode:

$$\begin{aligned} V^+ &= \sqrt{Z_0} \cdot \sqrt{N} \cdot a^+ \quad ; \quad V^- = -\sqrt{Z_0} \cdot \sqrt{N} \cdot a^- \\ I^+ &= \frac{1}{\sqrt{Z_0}} \cdot \sqrt{N} \cdot a^+ \quad ; \quad I^- = \frac{1}{\sqrt{Z_0}} \cdot \sqrt{N} \cdot a^- \end{aligned} \tag{A.9}$$

where N is the normalization of the mode and satisfies:

$$N = \left|N^+\right| = \left|N^-\right| \tag{A.10}$$

since N^+ is real and positive, due to the convention adopted for the mode fields (valid for propagating modes) given by eqn. (2.12), and N^+ and N^- satisfy eqn. (2.26a).
It is important to recall that the expressions for the equivalent voltage and current obtained, eqns. (A.9), are valid for a discrete spectrum mode that is in propagation. The cut-off modes and the continuous spectrum modes have not been considered in our deduction.

It is interesting to note that if the relation between the fields of the forward and backward travelling waves associated to the same i mode were:

$$\begin{aligned} E_x^{-i} &= E_x^{\,i} \quad ; \quad E_y^{-i} = E_y^{\,i} \quad ; \quad E_z^{-i} = -E_z^{\,i} \\ H_x^{-i} &= -H_x^{\,i} \quad ; \quad H_y^{-i} = -H_y^{\,i} \quad ; \quad H_z^{-i} = H_z^{\,i} \end{aligned} \tag{A.11}$$

instead of the one used in [KAT 98] and in this work (eqn. (2.14)), then the relation between the complex amplitudes of the mode a^+, a^-, and the equivalent voltage and current would be slightly different:

$$\begin{aligned} V^+ &= \sqrt{Z_0} \cdot \sqrt{N} \cdot a^+ \quad ; \quad V^- = \sqrt{Z_0} \cdot \sqrt{N} \cdot a^- \\ I^+ &= \frac{1}{\sqrt{Z_0}} \cdot \sqrt{N} \cdot a^+ \quad ; \quad I^- = \frac{-1}{\sqrt{Z_0}} \cdot \sqrt{N} \cdot a^- \end{aligned} \tag{A.12}$$

A.2. Derivation of the coupled mode equations from the equivalent voltage and current model

As it is well known from the circuit theory, voltage and current obey the following equations in a transmission line (or equivalently in a waveguide if equivalent parameters are being used):

$$\begin{aligned} \frac{dV}{dz} &= -Z' \cdot I \\ \frac{dI}{dz} &= -Y' \cdot V \end{aligned} \tag{A.13}$$

where Z' is the (equivalent) series impedance per unit length of the waveguide, and Y' is the (equivalent) shunt admittance per unit length of the waveguide. The phase constant β and the characteristic impedance Z_0 of the mode relate to these primary parameters as follows:

$$\begin{aligned} j \cdot \beta &= \sqrt{Z' \cdot Y'} \\ Z_0 &= \sqrt{\frac{Z'}{Y'}} \end{aligned} \tag{A.14}$$

For a nonuniform waveguide the phase constant β and the characteristic impedance Z_0 of the mode change with the axial distance z, and hence its equivalent quantities Z' and Y' will change also.

In order to obtain the coupled mode equations and the coupling coefficient from the voltage and current model for a discrete spectrum mode in propagation, the expression for the equivalent voltage and equivalent current as a function of the complex amplitudes of the mode, eqns. (A.9), will be substituted in eqns. (A.13). Since the equivalent voltage and current are defined for a single mode, the coupled mode equations and the coupling coefficient obtained will correspond to the case of single mode operation. This case has been rigorously studied in chapter 3, section (3.2).

From eqns. (A.9), the total equivalent voltage and current will have the following expressions:

$$\begin{aligned} V &= V^+ + V^- = \left(a^+ - a^-\right) \cdot \sqrt{N} \cdot \sqrt{Z_0} \\ I &= I^+ + I^- = \left(a^+ + a^-\right) \cdot \sqrt{\frac{N}{Z_0}} \end{aligned} \tag{A.15}$$

Substituting the expressions for the voltage and the current in the first equation of eqns. (A.13), we have:

$$\frac{d}{dz}\left(\sqrt{Z_0}\cdot\sqrt{N}\cdot\left(a^+ - a^-\right)\right) = -Z'\cdot\left(a^+ + a^-\right)\cdot\frac{\sqrt{N}}{\sqrt{Z_0}}$$

and assuming that the normalization of the mode N does not vary with z, the last equality can be rewritten as:

$$\frac{1}{2}\cdot\frac{1}{\sqrt{Z_0}}\cdot\frac{dZ_0}{dz}\cdot\left(a^+ - a^-\right) + \sqrt{Z_0}\cdot\left(\frac{da^+}{dz} - \frac{da^-}{dz}\right) = -Z'\cdot\left(a^+ + a^-\right)\cdot\frac{1}{\sqrt{Z_0}}$$

reorganizing the expression and using eqns. (A.14) it follows:

$$\frac{1}{2}\cdot\frac{1}{Z_0}\cdot\frac{dZ_0}{dz}\cdot\left(a^+ - a^-\right) + \frac{da^+}{dz} - \frac{da^-}{dz} = -j\cdot\beta\cdot\left(a^+ + a^-\right) \tag{A.16}$$

In the same way, substituting the expressions for the equivalent voltage and current of eqns. (A.15) into the second equation of eqns. (A.13), assuming that the normalization N does not vary with z, and using eqns. (A.14) it is obtained:

$$-\frac{1}{2}\cdot\frac{1}{Z_0}\cdot\frac{dZ_0}{dz}\cdot\left(a^+ + a^-\right) + \frac{da^+}{dz} + \frac{da^-}{dz} = -j\cdot\beta\cdot\left(a^+ - a^-\right) \tag{A.17}$$

The final step to obtain the coupled mode equations consist of adding and subtracting the last two eqns. (A.16) and (A.17).

Adding eqns. (A.16) and (A.17) it is obtained:

$$\frac{1}{2}\cdot\frac{1}{Z_0}\cdot\frac{dZ_0}{dz}\cdot\left(-2\cdot a^-\right) + 2\cdot\frac{da^+}{dz} = -j\cdot\beta\cdot\left(2\cdot a^+\right)$$

and subtracting them:

$$\frac{1}{2}\cdot\frac{1}{Z_0}\cdot\frac{dZ_0}{dz}\cdot\left(2\cdot a^+\right) - 2\cdot\frac{da^-}{dz} = -j\cdot\beta\cdot\left(2\cdot a^-\right)$$

Reorganizing the last two equations obtained they can be rewritten as:

$$\begin{aligned}\frac{da^+}{dz} &= -j\cdot\beta\cdot a^+ + \frac{1}{2}\cdot\frac{1}{Z_0}\cdot\frac{dZ_0}{dz}\cdot a^- \\ \frac{da^-}{dz} &= j\cdot\beta\cdot a^- + \frac{1}{2}\cdot\frac{1}{Z_0}\cdot\frac{dZ_0}{dz}\cdot a^+\end{aligned} \tag{A.18}$$

Comparing the resulting system of equations (eqns. (A.18)), with the simplified system of coupled mode equations obtained in chapter 3, section (3.2), and valid for single mode operation (eqns. (3.16), (3.17)), it can be seen that they are identical if the coupling coefficient K is calculated as:

$$K = \frac{1}{2} \cdot \frac{1}{Z_0} \cdot \frac{dZ_0}{dz}$$

Let's recall that following eqn. (3.13):

$$K = C^{+-} = C^{-+}$$

and therefore the coupling coefficients obtained from the voltage and current model have the following value:

$$K = C^{+-} = C^{-+} = \frac{1}{2} \cdot \frac{1}{Z_0} \cdot \frac{dZ_0}{dz} \tag{A.19}$$

It is important to recall that to deduce the coupled mode equations and the coupling coefficients from the voltage and current model, several assumptions have been made: single mode operation has been assumed, the normalization of the mode, N, is assumed to be constant with z, and it has been assumed that the mode of interest is a discrete spectrum mode that is in propagation along the nonuniform waveguide.

As it can be seen, if the characteristic impedance of the mode, Z_0, characterizes adequately the propagation of the mode along the nonuniform waveguide in terms of reflection produced by the variations of cross section, then the coupling coefficient $K = C^{+-} = C^{-+}$ can be approximated as indicated by eqn. (A.19) (provided that the assumptions detailed in the previous paragraph hold).

APPENDIX B

PROPERTIES OF THE SCATTERING MATRIX

B.1. Definitions

A two port network is represented in the following generic form for the calculation of its S-parameters or scattering matrix [POZ 98]:

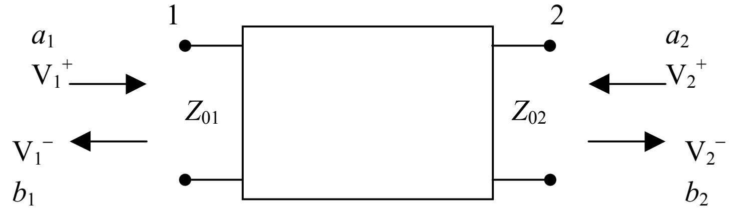

being Z_{0n} the characteristic impedance of the n port and

$$a_n = \frac{V_n^+}{\sqrt{Z_{0n}}} \qquad ; \qquad b_n = \frac{V_n^-}{\sqrt{Z_{0n}}} \tag{B.1}$$

From the definitions (B.1) it can be easily seen that the wave amplitudes a_n , b_n are valid to establish physically meaningful power relations, because the power flow is proportional to the square of their modulus.

The scattering matrix of a two port network relates the power and phase of the forward and backward travelling waves at the input and output ports of the network, in terms of the wave amplitudes a_n , b_n , in the following way:

$$\begin{bmatrix} b_1 \\ b_2 \end{bmatrix} = \begin{bmatrix} S_{11} & S_{12} \\ S_{21} & S_{22} \end{bmatrix} \cdot \begin{bmatrix} a_1 \\ a_2 \end{bmatrix} \tag{B.2}$$

fully characterizing the response of a linear (or linearized) time invariant network for single mode operation.

B.2. Reciprocal and lossless networks

If a network is reciprocal (passive and without anisotropic elements, i.e. no active devices, ferrites or plasmas) then the following relation will be satisfied [COL 92]:

$$[S] = [S]^t \tag{B.3}$$

that is

$$S_{ij} = S_{ji} \tag{B.4}$$

If a network is reciprocal and lossless then it will be satisfied that [COL 92]:

$$[S]^t \cdot [S]^* = [I_n] \tag{B.5}$$

Centering our study in a two port network we have from the previous eqn. (B.5):

$$\begin{gathered} |S_{11}|^2 + |S_{21}|^2 = 1 \\ |S_{22}|^2 + |S_{12}|^2 = 1 \end{gathered} \tag{B.6}$$

and since from eqn. (B.4):

$$S_{12} = S_{21} \tag{B.7}$$

we will also have:

$$|S_{11}| = |S_{22}| \tag{B.8}$$

From eqn. (B.5) it can be also seen that:

$$S_{11} \cdot S_{12}^* + S_{21} \cdot S_{22}^* = 0 \tag{B.9}$$

If we take:

$$S_{11} = |S_{11}| \cdot e^{j\cdot\theta_1} \quad ; \quad S_{22} = |S_{11}| \cdot e^{j\cdot\theta_2} \quad ; \quad S_{21} = S_{12} = \left(1 - |S_{11}|^2\right)^{\frac{1}{2}} \cdot e^{j\cdot\phi} \tag{B.10}$$

then eqn. (B.9) gives:

$$|S_{11}|\cdot\left(1-|S_{11}|^2\right)^{\frac{1}{2}}\cdot\left(e^{j\cdot\theta_1}\cdot e^{-j\cdot\phi}+e^{j\cdot\phi}\cdot e^{-j\cdot\theta_2}\right)=0$$

and therefore

$$\left(e^{j\cdot\theta_1}\cdot e^{-j\cdot\phi}+e^{j\cdot\phi}\cdot e^{-j\cdot\theta_2}\right)=0\Rightarrow e^{j\cdot(\theta_1+\theta_2)}=-e^{2\cdot j\cdot\phi}\Rightarrow\theta_1+\theta_2=2\cdot\phi-\pi\pm2\cdot\pi\cdot n$$

Thus

$$\phi=\frac{\theta_1+\theta_2}{2}+\frac{\pi}{2}+\mp\pi\cdot n \tag{B.11}$$

valid, as we have seen, for a reciprocal lossless two port network, with the definitions of eqn. (B.10).

B.3. Symmetrical networks

If a two port network is symmetrical, then the following relations will be satisfied:

$$\begin{aligned}S_{11}&=S_{22}\\S_{21}&=S_{12}\end{aligned} \tag{B.12}$$

APPENDIX C

PROPERTIES OF THE TRANSMISSION MATRIX

C.1. Definitions

A two port network is represented in the following generic form for the calculation of its transmission matrix (or more exactly of its wave amplitude transmission matrix) [COL 92]:

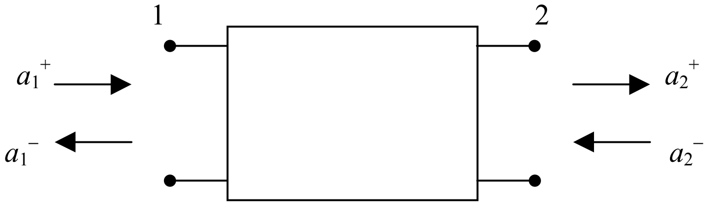

The transmission matrix relates the forward and backward travelling waves at the input and output ports of the device in terms of the wave amplitudes a_n^+, a_n^-, in the following form:

$$\begin{bmatrix} a_1^+ \\ a_1^- \end{bmatrix} = \begin{bmatrix} A_{11} & A_{12} \\ A_{21} & A_{22} \end{bmatrix} \cdot \begin{bmatrix} a_2^+ \\ a_2^- \end{bmatrix} \tag{C.1}$$

Once we know the transmission matrix of a linear (or linearized) time invariant network, its response is fully characterized for single mode operation.

Using the relations obtained in chapter 3, eqn. (3.26), and eqn. (B.2) we can also express the relationship between the wave amplitudes a_1^+, a_1^-, a_2^+, a_2^-, as a function of the S-parameters:

$$\begin{aligned} -\sqrt{N_1}\cdot a_1^- &= S_{11}\cdot\sqrt{N_1}\cdot a_1^+ + S_{12}\cdot\left(-\sqrt{N_2}\right)\cdot a_2^- \\ \sqrt{N_2}\cdot a_2^+ &= S_{21}\cdot\sqrt{N_1}\cdot a_1^+ + S_{22}\cdot\left(-\sqrt{N_2}\right)\cdot a_2^- \end{aligned} \tag{C.2}$$

Reorganizing eqn. (C.2) to put it in the same form as eqn. (C.1), we obtain that:

$$\begin{bmatrix} a_1^+ \\ a_1^- \end{bmatrix} = \begin{bmatrix} \dfrac{\sqrt{N_2}}{\sqrt{N_1}}\cdot\dfrac{1}{S_{21}} & \dfrac{\sqrt{N_2}}{\sqrt{N_1}}\cdot\dfrac{S_{22}}{S_{21}} \\ \dfrac{\sqrt{N_2}}{\sqrt{N_1}}\cdot\left(\dfrac{-S_{11}}{S_{21}}\right) & \dfrac{\sqrt{N_2}}{\sqrt{N_1}}\cdot\left(S_{12}-\dfrac{S_{11}\cdot S_{22}}{S_{21}}\right) \end{bmatrix}\cdot\begin{bmatrix} a_2^+ \\ a_2^- \end{bmatrix}$$

and therefore

$$\begin{aligned} A_{11} &= \frac{\sqrt{N_2}}{\sqrt{N_1}}\cdot\frac{1}{S_{21}} \\ A_{12} &= \frac{\sqrt{N_2}}{\sqrt{N_1}}\cdot\frac{S_{22}}{S_{21}} \\ A_{21} &= \frac{\sqrt{N_2}}{\sqrt{N_1}}\cdot\left(\frac{-S_{11}}{S_{21}}\right) \\ A_{22} &= \frac{\sqrt{N_2}}{\sqrt{N_1}}\cdot\left(S_{12}-\frac{S_{11}\cdot S_{22}}{S_{21}}\right) \end{aligned} \tag{C.3}$$

where $N_n = \left|N_n^+\right| = \left|N_n^-\right|$, is the normalization of the mode at the *n* port.

C.2. Reciprocal networks

If a network is reciprocal (passive and without anisotropic elements, i.e. no active devices, ferrites or plasmas), then eqn. (B.4) will hold implying that $S_{21} = S_{12}$, and hence:

$$\begin{vmatrix} A_{11} & A_{12} \\ A_{21} & A_{22} \end{vmatrix} = \frac{N_2}{N_1}\cdot\frac{1}{S_{21}}\cdot\left(S_{21}-\frac{S_{11}\cdot S_{22}}{S_{21}}\right)-\frac{N_2}{N_1}\cdot\left(\frac{-S_{11}}{S_{21}}\cdot\frac{S_{22}}{S_{21}}\right)=\frac{N_2}{N_1}\Rightarrow$$

$$\Rightarrow\begin{vmatrix} A_{11} & A_{12} \\ A_{21} & A_{22} \end{vmatrix} = \frac{N_2}{N_1} \tag{C.4}$$

As a consequence, if we have a reciprocal network and the normalization at the input and output ports is the same, the determinant of its transmission matrix is equal to 1 [COL 92].

C.3. Reciprocal and lossless networks

If a network is reciprocal and lossless then eqns. (B.10) and (B.11) hold, and using them the transmission matrix expressed as a function of the S-parameters (C.3) can be rewritten as:

$$\frac{\sqrt{N_2}}{\sqrt{N_1}} \cdot \frac{1}{\left(1-|S_{11}|^2\right)^{\frac{1}{2}}} \cdot \begin{bmatrix} e^{-j\cdot\left(\frac{\theta_1+\theta_2}{2}+\frac{\pi}{2}\mp n\cdot\pi\right)} & |S_{11}|\cdot e^{-j\cdot\left(\frac{\theta_1}{2}-\frac{\theta_2}{2}+\frac{\pi}{2}\mp n\cdot\pi\right)} \\ |S_{11}|\cdot e^{-j\cdot\left(-\frac{\theta_1}{2}+\frac{\theta_2}{2}-\frac{\pi}{2}\mp n\cdot\pi\right)} & e^{-j\cdot\left(-\frac{\theta_1+\theta_2}{2}-\frac{\pi}{2}\mp n\cdot\pi\right)} \end{bmatrix} \tag{C.5}$$

Identifying terms it can be seen that if the normalizations at the input and output ports, N_1 , N_2 , of a reciprocal and lossless network are equal, or are real numbers or at least their quotient is a real number, then the transmission matrix parameters will satisfy:

$$\begin{aligned} A_{11} &= A_{22}{}^{*} \\ A_{21} &= A_{12}{}^{*} \end{aligned} \tag{C.6}$$

and the form of the transmission matrix will be:

$$\begin{bmatrix} A_{11} & A_{21}{}^{*} \\ A_{21} & A_{11}{}^{*} \end{bmatrix} \tag{C.7}$$

To obtain these last relations it is important to take into account that in the terms $e^{j\cdot\pi\cdot n}$ the sign of the exponent has no importance because the value of the term is exactly the same with positive or negative sign in the exponent.

Author's publications related to the thesis

Journal papers

- Txema Lopetegi, Miguel A. G. Laso, Maria J. Erro, Mario Sorolla, and Manfred Thumm, "Analysis and Design of Periodic Structures for Microstrip Lines by Using the Coupled Mode Theory," to be published in *IEEE Microwave and Wireless Components Letters*, in November 2002 issue.

- Ferran Martín, Francisco Falcone, Jordi Bonache, Txema Lopetegi, Miguel A.G. Laso, and Mario Sorolla, "New periodic-loaded electromagnetic bandgap coplanar waveguide with complete spurious passband suppression," to be published in *IEEE Microwave and Wireless Components Letters*, in November 2002 issue.

- T. Akalin, M. A. G. Laso, E. Delos, T. Lopetegi, O. Vanbésien, M. Sorolla, and D. Lippens, "High performance double-sided microstrip PBG filter," to be published in *Microwave and Optical Technology Letters*, October 2002 issue.

- F. Falcone, T. Lopetegi, M. A. G. Laso, M. Sorolla, "Novel Photonic Crystal Waveguide in Microwave Printed Circuit Technology," to be published in *Microwave and Optical Technology Letters*, September 2002 issue.

- Miguel A. G. Laso, María J. Erro, Txema Lopetegi, María J. Garde, David Benito y Mario Sorolla, "Cristales Fotónicos: Estructuras periódicas para el control de la propagación electromagnética," to be published in *Mundo Electrónico*, in December 2002 issue.

- F. Hirtenfelder, T. Lopetegi, M. Sorolla, L. Sassi, "Designing components containing photonic bandgap structures using time domain field solvers," *Microwave Engineering*, pp. 23-29, March 2002.

- M. A. G. Laso, T. Lopetegi, M. J. Erro, D. Benito, M. A. Muriel, M. Sorolla, and M. Guglielmi, "Chirped Delay Lines in Microstrip Technology," *IEEE Microwave and Wireless Components Letters*, vol. 11, no. 12, pp. 486-488, December 2001.

- T. Lopetegi, M. A. G. Laso, J. Hernández, M. Bacaicoa, D. Benito, M. J. Garde, M. Sorolla, and M. Guglielmi, "New Microstrip "Wiggly-Line" Filters With Spurious Pass-band Suppression", *IEEE Transactions on Microwave Theory and Techniques*, vol. 49, no. 9, pp. 1593-1598, September 2001.

- T. Lopetegi, M. A. G. Laso, R. Gonzalo, M. J. Erro, F. Falcone, D. Benito, M. J. Garde, P. de Maagt, and M. Sorolla, "Electromagnetic Crystals in Microstrip Technology," *Optical and Quantum Electronics*, vol. 34, no. 1-3, pp. 279-295, January - March 2002.

- M. J. Erro, M. A. G. Laso, T. Lopetegi, D. Benito, M. J. Garde, and M. Sorolla, "Analysis and Design of Electromagnetic Crystals in Microstrip Technology using a Fiber Grating Model," *Optical and Quantum Electronics*, vol. 34, no. 1-3, pp. 297-310, January - March 2002.

- T. Akalin, M. A. G. Laso, T. Lopetegi, O. Vanbésien, M. Sorolla, and D. Lippens, "PBG-type microstrip filters with one and two side patterns," *Microwave and Optical Technology Letters*, vol. 30, no. 1, pp. 69-72, July 2001.

- M. A. G. Laso, T. Lopetegi, M. Bacaicoa, J. Hernández, R. Gonzalo, and M. Sorolla, "Arrangements of via-holes in microstrip lines as metallodielectric periodic structures," *Microwave and Optical Technology Letters*, vol. 26, no. 6, pp. 372-379, September 2000.

- M. J. Erro, M. A. G. Laso, T. Lopetegi, D. Benito, M. J. Garde, and M. Sorolla, "Modeling and testing of uniform fiber Bragg gratings using 1-D photonic bandgap structures in microstrip technology," *Journal of Fibre and Integrated Optics*, vol. 19, no. 4, pp. 311-325, September 2000.

- T. Lopetegi, M. A. G. Laso, M. Irisarri, M. J. Erro, F. Falcone, and M. Sorolla, "Optimization of compact Photonic Bandgap microstrip structures," *Microwave and Optical Technology Letters*, vol. 26, no. 4, pp. 211-216, August 2000.

- M. A. G. Laso, T. Lopetegi, M. J. Erro, D. Benito, M. J. Garde, and M. Sorolla, "Multiple-frequency-tuned Photonic Bandgap microstrip structures," *IEEE Microwave and Guided Wave Letters*, vol. 10, no. 6, pp. 220-222, June 2000.

- T. Lopetegi, M. A. G. Laso, M. J. Erro, D. Benito, M. J. Garde, F. Falcone and M. Sorolla, “Novel photonic bandgap microstrip structures using network topology,” *Microwave and Optical Technology Letters*, vol. 25, no. 1, pp. 33-36, April 2000.

- M. J. Erro, M. A. G. Laso, T. Lopetegi, D. Benito, M. J. Garde, and M. Sorolla, “Optimization of tapered bragg reflectors in microstrip technology,” *International Journal of Infrared and Millimeter Waves*, vol. 21, no. 2, pp.231- 245, February 2000.

- M. A. G. Laso, T. Lopetegi, M. J. Erro, D. Benito, M. J. Garde and Mario Sorolla, “Novel wideband photonic bandgap microstrip structures,” *Microwave and Optical Technology Letters*, vol. 24, no. 5, pp. 357-360, March 2000.

- J. Tirapu, T. Lopetegi, M. A. G. Laso, M. J. Erro, F. Falcone, and M. Sorolla, “Study of the Delay Characteristics of 1-D Photonic Bandgap Microstrip Structures,” *Microwave and Optical Technology Letters*, vol. 23, no. 6, pp. 346-349, December 1999.

- F. Falcone, T. Lopetegi, M. Irisarri, M. A. G. Laso, M. J. Erro, and M. Sorolla, "Compact Photonic Bandgap Microstrip Structures," *Microwave and optical Technology Letters*, vol 23, no. 4, pp. 233-236, November 1999.

- F. Falcone, T. Lopetegi, and M. Sorolla, “1-D and 2-D Photonic Bandgap Microstrip Structures,” *Microwave and Optical Technology Letters,* vol. 22, no. 6, pp. 411-412, September 1999.

- M. A. G. Laso, M. J. Erro, D. Benito, M. J. Garde, T. Lopetegi, F. Falcone, and M. Sorolla, “Analysis and design of 1-D photonic bandgap microstrip structures using a fibre grating model,” *Microwave and Optical Technology Letters,* vol. 22, no. 4, pp. 223-226, August 1999.

- T. Lopetegi, F. Falcone, B. Martínez, R. Gonzalo, and M. Sorolla, “Improved 2-D photonic bandgap structures in microstrip technology,” *Microwave and Optical Technology Letters,* vol. 22, no. 3, pp. 207-211, August 1999.

- T. Lopetegi, F. Falcone, and M. Sorolla, "Bragg reflectors and resonators in microstrip technology based on Electromagnetic Crystal structures," *International Journal of Infrared and Millimeter Waves*, vol. 20, no. 6, pp. 1091-1102, June 1999.

International conferences

- T. Lopetegi, M. A. G. Laso, M. J. Erro, J. A. Leo, M. Sorolla, "Application of the coupled mode theory to the analysis and design of PBG structures in microstrip technology," Proceedings of the *32nd European Microwave Conference*, September 2002, Milan, Italy.

- M. A. G. Laso, D. Benito, T. Lopetegi, M. J. Erro, M. J. Garde, M. A. Muriel, M. Sorolla, and M. Guglielmi, "Microstrip chirped Delay Lines based on Photonic Band-Gap structures," Proceedings of the *32nd European Microwave Conference*, September 2002, Milan, Italy.

- Ferran Martín, Francisco Falcone, Jordi Bonache, Txema Lopetegi, Miguel A. G. Laso, and Mario Sorolla, "New PBG nonlinear distributed structures: application to the optimization of millimeter wave frequency multipliers," Proceedings of the *27th International Conference on Infrared and Millimetre-Waves*, September 2002, San Diego, California.

- M. A. G. Laso, T. Lopetegi, M. J. Erro, M. Castillo, D. Benito, M. J. Garde, M. A. Muriel, M. Sorolla, and M. Guglielmi, "Real-time spectrum analysis in microstrip technology," Proceedings of the *31st European Microwave Conference*, vol.2, pp. 237-240, September 2001, London, UK.

- F. Falcone, T. Lopetegi, M. A. G. Laso, R. Gonzalo, S. Arana, and M. Sorolla, "Novel 2d-electromagnetic crystal waveguide in microwave printed circuit technology," Proceedings of the *31st European Microwave Conference*, September 2001, vol.2, pp. 297-300, London, UK.

- F. Falcone, T. Lopetegi, M. A. G. Laso, and M. Sorolla, "Applications of novel 2D electromagnetic crystal waveguides in microwave printed circuit technology," Proceedings of the *26th International Conference on Infrared and Millimetre*

Waves, September 2001, Toulouse, France.

- M. A. G. Laso, T. Lopetegi, M. Bacaicoa, J. Hernández, M. J. Garde, and M. Sorolla, "Arrangements of via-holes in Microstrip Lines as Metallodielectric Periodic Structures", Proceedings of the *Asia-Pacific Microwave Conference 2000*, pp. 1257-1260, December 2000, Sydney, Australia.

- M. A. G. Laso, T. Lopetegi, R. Gonzalo, M. J. Erro, D. Benito, M. J. Garde, P. de Maagt, and M. Sorolla, "Applications of Electromagnetic Crystals in Microstrip Technology", Proceedings of the *30th European Microwave Conference*, pp. 108-111, October 2000, Paris, France.

- T. Lopetegi, M. A. G. Laso, M. J. Erro, R. Gonzalo, J. Tirapu, A. Marcotegui. D. Benito, M. J. Garde, and M. Sorolla, "Photonic Crystals in Microstrip Technology", presented at the *NATO ASI - Photonic Crystals and Light Localization*, June 2000, Crete, Greece.

- M. Anaya, J. A. Marcotegui, T. Lopetegi, M. A. G. Laso, and M. Sorolla, “Analysis of New Periodic Structures in Microstrip by FDTD”, Proceedings of the *European Congress on Computational Methods in Applied Sciences and Engineering (ECCOMAS),* September 2000, Barcelona.

- M. Irisarri, T. Lopetegi, M. A. G. Laso, M. J. Erro, D. Benito, M.J. Garde, and M. Sorolla, “Optimization of compact photonic bandgap microstrip structures”, Proceedings of the *Millennium Conference on Antennas and Propagation, (AP2000)*, 1A9, April 2000, Davos, Switzerland.

- T. Lopetegi, M. A. G. Laso, M. J. Erro, R. Gonzalo, J. Tirapu, A. Marcotegui, D. Benito, M. J. Garde, and M. Sorolla, “Electromagnetic Crystals in Microstrip Technology”, Technical Digest of the *International Workshop on Photonic and Electromagnetic Crystal Structures (PECS)*, W4-9, March 2000, Sendai, Japan.

- T. Lopetegi, M. A. G. Laso, M. J. Erro, D. Benito, M.J. Garde, F. Falcone, and M. Sorolla, “New Results in Microstrip Grating Technology”, invited conference in *7th International Symposium on Recent Advances in Microwave Technology (ISRAMT’99)*, pp. 507 - 510, December 1999, Málaga.

- T. Lopetegi, M. A. G. Laso, M. J. Erro, D. Benito, M.J. Garde, F. Falcone, and M. Sorolla, "Microstrip continuos gratings (MCGs)", Proceedings of the *7th International Symposium on Recent Advances in Microwave Technology (ISRAMT'99)*, pp. 601-604, December 1999, Málaga.

- T. Lopetegi, M. A. G. Laso, M. J. Erro, F. Falcone, and M. Sorolla, "Bandpass filter in microstrip technology using photonic bandgap reflectors", Proceedings of the *29th European Microwave Conference*, pp. 337-340, October 1999, Munich, Germany.

- M. J. Erro, T. Lopetegi**,** M. A. G. Laso, D. Benito, M.J. Garde, F. Falcone, and M. Sorolla, "Novel wideband photonic bandgap microstrip structures", Procedings of the *29th European Microwave Conference*, pp. 345-348, October 1999, Munich, Germany.

- M. A. G. Laso, M. J. Erro, T. Lopetegi, D. Benito, M. J. Garde, F. Falcone, and M. Sorolla, "Optimization of tapered photonic bandgap structures in microstrip", Proceedings of the *24th International Conference on Infrared and Millimeter Waves*, TH-D2, September 1999, Monterey, California.

- J. Tirapu, T. Lopetegi, F. Falcone, and M. Sorolla, "Dispersion Cancellation using 1-D Photonic Bandgap Microstrip Structures in Transmission", Proceedings of the *24th International Conference on Infrared and Millimeter Waves*, M-B4, September 1999, Monterey, California.

- M. J. Erro, M.A.G. Laso, D. Benito, M. J. Garde, T. Lopetegi, F. Falcone, and M. Sorolla, "Extended model based on the coupled-mode theory in fibre gratings for the analysis and design of 1-D photonic bandgap devices in microstrip technology", Proceedings of *SPIE's International Symposium on Optical Science, Engineering, and Instrumentation*, pp. 166-175, July 1999, Denver, Colorado.

- T. Lopetegi, F. Falcone, B. Martínez, I. Ederra, R. Gonzalo, and M. Sorolla, "Photonic Bandgap Resonator Structures in Microstrip". Proceedings of the *1998 Asia-Pacific Microwave Conference*, pp. 597-600, Yokohama (Japan), December 1998.

- F. Falcone, T. Lopetegi, B. Martínez, R. Gonzalo, and M. Sorolla, “New 1-D and 2-D Photonic Bandgap Structures in Microstrip”. Proceedings of the *XXVIII Moscow International Conference on Antenna Theory and Technology,* pp. 520-523, Moscow, September1998.

- T. Lopetegi, F. Falcone, B. Martínez, R. Gonzalo, and M. Sorolla, “Improved 2-D photonic bandgap microstrip structures”. Proceedings of the *23rd International Conference on Infrarred and Millimeter Waves*, pp. 197-198, Colchester (United Kingdom), September 1998.

National conferences

- A. González, T. Lopetegi, M. A. G. Laso, y M. Sorolla, “Antena activa en sustrato cristal electromagnético,” Libro de Actas del *XVII Simposium Nacional U.R.S.I.*, Septiembre 2002, Alcalá de Henares, Madrid.

- Ferran Martín, Francisco Falcone, Txema Lopetegi, Miguel A. G. Laso, Mario Sorolla, and Jordi Bonache, “Application of photonic bandgap structures in coplanar waveguide technology,” Libro de Actas del *XVII Simposium Nacional U.R.S.I.*, Septiembre 2002, Alcalá de Henares, Madrid.

- M. A. G. Laso, D. Benito, T. Lopetegi, M. J. Erro, M. J. Garde, M. A. Muriel, M. Sorolla, M. Guglielmi, “Filtros de fasse cuadrática en tecnología microstrip basados en estructuras de Band-Gap fotónico,” Libro de Actas del *XVII Simposium Nacional U.R.S.I.*, Septiembre 2002, Alcalá de Henares, Madrid.

- L. P. Cuevas, T. Lopetegi, M. A. G. Laso, D. Benito, M. J. Garde, M. Sorolla y M. Guglielmi, “Filtros de líneas acopladas en tecnología microstrip con eliminación de bandas espurias,” Libro de Actas del *XVI Simposium Nacional U.R.S.I.*, pp. 85-86, Septiembre 2001, Villaviciosa de Odón, Madrid.

- T. Akalin, M. A. G. Laso, T. Lopetegi, O. Vanbésien, M. Sorolla, and D. Lippens, "De la topologie micro-ruban vers les nouvelles structures periodiques pour le filtrage frequentiel", *IVemes Journees Nationales du Reseau Doctoral de Microelectronique*, 24-25 april 2001, Strasbourg, France.

- M. A. G. Laso, T. Lopetegi, M. J. Erro, D. Benito, M. J. Garde, and M. Sorolla, "Estructuras continuas de Bandgap Fotónico en tecnología microstrip con sintonía múltiple", Proceedings of the *XV Simposium Nacional U.R.S.I.*, pp. 257-258, Septiembre 2000, Zaragoza, Spain.

- M. A. G. Laso, T. Lopetegi, M. J. Erro, D. Benito, M. J. Garde y M. Sorolla, "Aplicación de técnicas para el aumento de ancho de banda a estructuras de bandgap fotónico en tecnología microstrip", *XIV Simposium Nacional U.R.S.I.*, pp. 75-76, Santiago de Compostela, Septiembre 1999.

- M.J. Asarta, A. Escudero, M. A. G. Laso, M. J. Erro, T. Lopetegi, D. Benito, M. J. Garde y M. Sorolla, "Análisis y diseño de estructuras de bandgap fotónico en microstrip usando un modelo equivalente de red de difracción óptica", Libro de Actas del *XIV Simposium Nacional U.R.S.I.*, pp. 83-84, Santiago de Compostela, Septiembre 1999.

- M. Ezcurra, R. Artieda, M.J. Erro, M.A.G. Laso, T. Lopetegi, D. Benito, M. J. Garde y M. Sorolla, "Estudio comparativo de las prestaciones obtenidas por distintas ventanas aplicadas a estructuras de bandgap fotónico en tecnología microstrip", Libro de Actas del *XIV Simposium Nacional U.R.S.I.*, pp. 73-74, Santiago de Compostela, Septiembre 1999.

- F. Falcone, T. Lopetegi, B. Martínez, R. Gonzalo y M. Sorolla, "Diseño de Estructuras de Bandgap Fotónico 2-D Optimizadas en Tecnología Microstrip". Libro de Actas del *XIII Simposium Nacional U.R.S.I.,* pp. 211-212*,* Pamplona, Septiembre 1998.